SERIES IN CONDENSED MATTER PHYSICS

MAGNETIC ANISOTROPIES IN NANOSTRUCTURED MATTER

PETER WEINBERGER

CRC Press
Taylor & Francis Group
A TAYLOR & FRANCIS BOOK

Magnetic Anisotropies in Nanostructured Matter

Series in Condensed Matter Physics

Series Editor:
D R Vij
Department of Physics, Kurukshetra University, India

Other titles in the series include:

Aperiodic Structures in Condensed Matter: ***Fundamentals and Applications***
Enrique Maciá Barber

Thermodynamics of the Glassy State
Luca Leuzzi, Theo M. Nieuwenhuizen

One- and Two-Dimensional Fluids: ***Properties of Smectic, Lamellar and Columnar Liquid Crystals***
A Jákli, A Saupe

Theory of Superconductivity: From Weak to Strong Coupling
A S Alexandrov

The Magnetocaloric Effect and Its Applications
A M Tishin, Y I Spichkin

Field Theories in Condensed Matter Physics
Sumathi Rao

Nonlinear Dynamics and Chaos in Semiconductors
K Aoki

Permanent Magnetism
R Skomski, J M D Coey

Modern Magnetooptics and Magnetooptical Materials
A K Zvezdin, V A Kotov

Series in Condensed Matter Physics

Magnetic Anisotropies in Nanostructured Matter

Peter Weinberger

CRC Press
Taylor & Francis Group
Boca Raton London New York

CRC Press is an imprint of the
Taylor & Francis Group, an **informa** business

A TAYLOR & FRANCIS BOOK

Chapman & Hall/CRC
Taylor & Francis Group
6000 Broken Sound Parkway NW, Suite 300
Boca Raton, FL 33487-2742

Printed in the United States of America on acid-free paper
10 9 8 7 6 5 4 3 2 1

International Standard Book Number-13: 978-1-4200-7265-5 (Hardcover)

Library of Congress Cataloging-in-Publication Data

Weinberger, P. (Peter)
Magnetic anisotropies in nanostructured matter / Peter Weinberger.
p. cm. -- (Series in condensed matter physics ; 2)
Includes bibliographical references and index.
ISBN 978-1-4200-7265-5 (hardcover : alk. paper)
1. Nanostructures. 2. Anisotropy. 3. Nanostructured materials--Magnetic properties. 4. Nanoscience. I. Title. II. Series.

QC176.8.N35W45 2009
620.1'1299--dc22 2008042181

Visit the Taylor & Francis Web site at
http://www.taylorandfrancis.com

and the CRC Press Web site at
http://www.crcpress.com

Contents

Biography

Peter Weinberger was for many years (1972 - October 2008) professor at the Vienna Institute of Technology, Austria, and consultant to the Los Alamos National Laboratory, Los Alamos, New Mexico, USA (1982 - 1998), and the Lawrence Livermore National Laboratory (1987 - 1995), Livermore, California, USA. For about 15 years, until 2007, he headed the Center for Computational Materials Science, Vienna.

He is a fellow of the American Physical Society and a receiver of the Ernst Mach medal of the Czech Academy of Sciences (1998). In 2004 he acted as coordinator of a team of scientists that became finalists in the Descartes Prize of the European Union.

He (frequently) spent time as guest professor or guest scientist at the H. H. Wills Physics Laboratory, University of Bristol, UK, the Laboratorium für Festkörperphysik, ETH Zürich, Switzerland, the Department of Physics, New York University, New York, USA, and the Laboratoire de Physique des Solides, Université de Paris-Sud, France.

Besides some 330 publications (about 150 from the *Physical Review B*), he is author or coauthor of three textbooks (Oxford University Press, Kluwer, Springer). He is also author of 4 non-scientific books (novels and short stories, in German).

Presently he heads the Center for Computational Nanoscience Vienna, an Internet institution with the purpose of facilitating scientific collaborations between Austria, the Czech Republic, France, Germany, Hungary, Spain, the UK and the USA in the field of theoretical spintronics and/or nanomagnetism.

Acknowledgments

This book is dedicated to all my former or present students and/or collaborators in the past 10 years:

Claudia Blaas, Adam Buruzs, Patrick Bruno, Corina Etz, Peter Dederichs, Peter Entel, Vaclav Drachal, Hubert Ebert, Robert Hammerling, Heike Herper, Silvia Gallego, Balazs Györffy, Jaime Keller, Sergej Khmelevskij, Josef Kudrnovsky, Bence Lazarovits, Peter Levy, Ingrid Mertig, Peter Mohn, Kristian Palotas, Ute Pustogowa, Irene Reichl, Josef Redinger, Chuck Sommers, Julie Staunton, Malcolm Stocks, Ilja Turek, Laszlo Szunyogh, Laszlo Udvardi, Christoph Uiberacker, Balasz Ujfalussy, Elena Vedmedenko, Andras Vernes, Rudi Zeller and Jan Zabloudil.

From each of them I learned a lot and profited considerably. In particular I am indebted to **Laszlo Szunyogh** for a long lasting scientific partnership concerning the fully relativistic Screened Korringa-Kohn-Rostoker project.

I am also very grateful to all my colleagues (friends) in experimentation with whom I had many, sometimes heated discussions:

Rolf Allenspach, Klaus Baberschke, Bret Heinrich, Jürgen Kirschner, Ivan Schuller and Roland Wiesendanger.

Last, but not least: books are never written without indoctrinations by others. Definitely **Simon Altmann** (Oxford) and **Walter Kohn** (S. Barbara) did (and still do) have a substantial share in this kind of intellectual "pushing".

1

Introduction

In here the key words in the title of the book, namely nanostructured matter and magnetic anisotropies, are critically examined and defined.

Nanosystems and *nanostructured matter* are terms that presently are very much *en vogue*, although at best semi-qualitative definitions of these expressions seem to exist. The prefix *nano* only makes sense when used in connection with physical units such as meters or seconds, usually then abbreviated by nm (nanometer) or ns (nanosecond):

$$\begin{array}{l} 1\ \text{Å} = 10^{-8}\text{cm} = 0.1\ \text{nm} \\ 1\ \text{nm} = 10^{-9}\text{m} \end{array}$$

Quite clearly the macroscopic pre-Columbian statue in Fig. 1.1 made from pure gold nobody would call a nanostructured system because in "bulk" gold the atoms are separated only by few tenths of a nanometer. Therefore, in

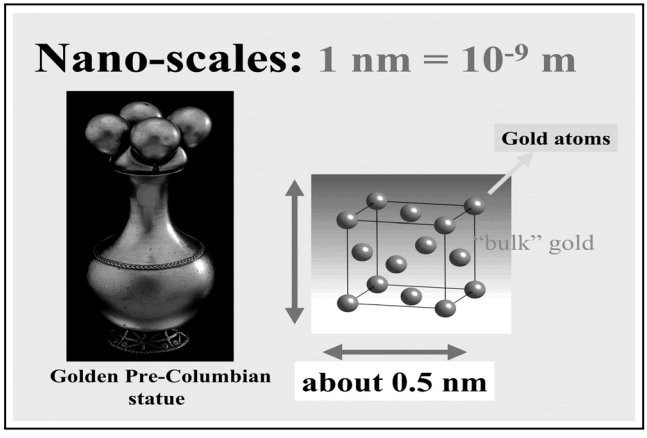

FIGURE 1.1: *Left:* *macroscopic golden artifact,* *right:* *microscopic structure of fcc Au.*

order to define nanosystems somehow satisfactorily the concept of functional units or functional parts of a solid system has to be introduced. *Functional* in this context means that particular physical properties of the total system are mostly determined by such a unit or part. In principle two kinds of nanosystems can be defined, namely solid systems in which the functional part is confined in one dimension by less than about 100 nm and those where the confinement is two-dimensional and restricted by about 10 - 20 nm. For matters of simplicity in the following, nanosystems confined in one dimension will be termed *1d-nanosystems*, those confined in two dimensions *2d-nanosystems*. Confinement in three dimensions by some length in a few nm does not make sense, because this is the realm of molecules (in the gas phase). In soft matter physics qualitative definitions of nanosystems can be quite different: so-called nanosized pharmaceutical drugs usually contain functional parts confined in length in all three directions, which in turn are part of some much larger carrier molecule. Since soft matter physics is not dealt with in this book, in the following a distinction between *1d-* and *2d-nanosystems* will be sufficient.

A diagram of a typical *1d-nanosystem* is displayed in Fig. 1.2 reflecting the situation, for example, of a magnetically coated metal substrate such as a few monolayers of Co on Cu(111). Systems of this kind are presently very much studied in the context of perpendicular magnetism. Very prominent examples

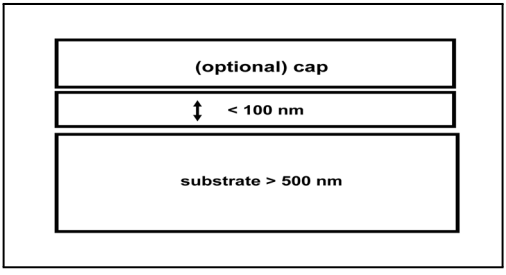

FIGURE 1.2: *Solid system, nanostructured in one dimension.*

of *1d-nanosystems* are magnetoresistive spin-valve systems, see Fig. 1.3, that consist essentially of two magnetic layers separated by a non-magnetic spacer. As can be seen from this figure the functional part refers to a set of buried slabs of different thicknesses. It should be noted that in principle any interdiffused interface between two different materials is also a *1d-nanosystem*, since usually the interdiffusion profile extends only over a few monolayers, i.e., is confined to about 10 nm or even less.

Fig. 1.4 shows a sketch of a *2d-nanosystem* in terms of (separated) clusters of atoms on top of or embedded in a substrate. These clusters can be either small islands, (nano-) pillars or (nano-) wires. "Separated" was put cau-

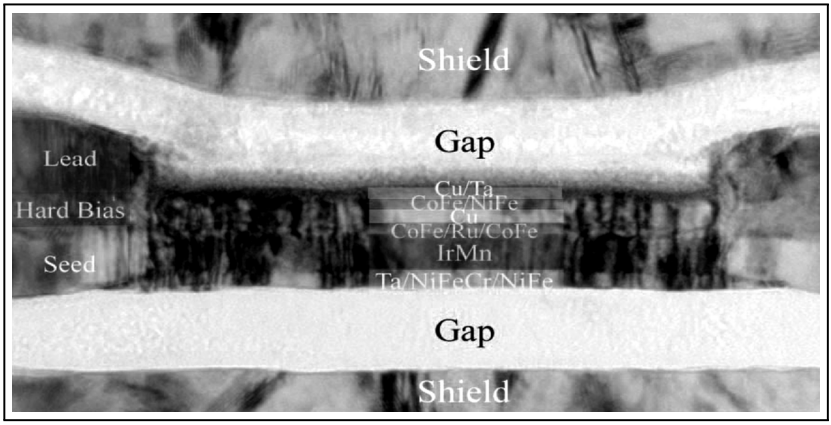

FIGURE 1.3: *Transition electron micrograph of a giant magnetoresistive spin-valve read head. By courtesy of the MRS Bulletin, Ref. [1].*

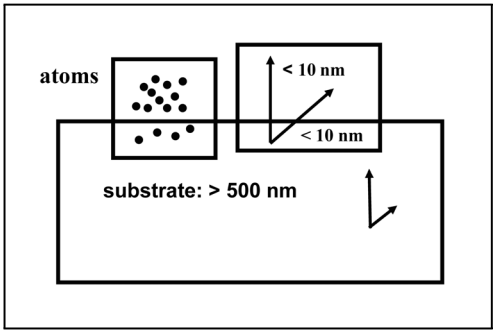

FIGURE 1.4: *Solid system, nanostructured in two dimension.*

tiously in parentheses since although such clusters appear as distinct features in Scanning Tunnelling Microscopy (STM) pictures, see Fig. 1.5, in the case of magnetic atoms forming these clusters they are connected to each other, e.g., by long range magnetic interactions.

It was already said that a classification of nanosystems can be made only in a kind of semi-qualitative manner using typical length scales in one or two dimensions. There are of course cases in which the usual scales seemingly don't apply. Quantum corrals for example, see Fig. 1.5, can have diameters exceeding the usual confinement length of *2d-nanosystems*. Another, very prominent case is that of magnetic domain walls, which usually in bulk systems have a thickness of several hundred nanometers. However, since in nanowires domain walls are thought to be considerably shorter, but also because domain walls

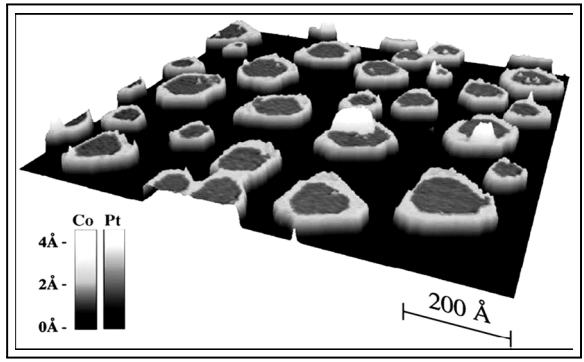

FIGURE 1.5: *Three-dimensional view of a STM image of one-monolayer-high islands with a Pt core and an approximately 3-atom-wide Co shell. By courtesy of the authors of Ref. [2].*

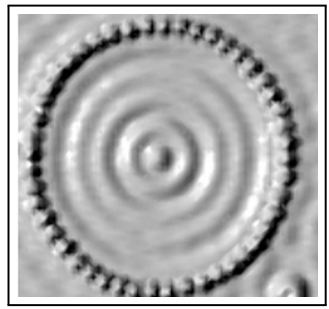

FIGURE 1.6: *Theoretical image of a quantum corral consisting of 48 Fe atoms on top of Cu(111). From Ref. [3].*

are a kind of upper limit for nanostructures, in here they will be considered as such.

Theoretically *1d-* and *2d-nanosystems* require different types of description. While *1d-nanosystems* can be considered as two-dimensional translational invariant layered systems, *2d-nanosystems* have to be viewed in "real space", i.e., with the exception of infinite one-dimensional wires (one dimensional translational invariance) no kind of translational symmetry any longer applies.

It should be very clear right from the beginning that without the concept of nano-sized "functional parts" of a system one cannot speak about nanoscience, since – as the name implies – they are part of a system that of course is not nano-sized. In the case of GMR devices, e.g., there are "macro-sized" leads, while for *2d-nanosystems* the substrate or carrier material is large as compared

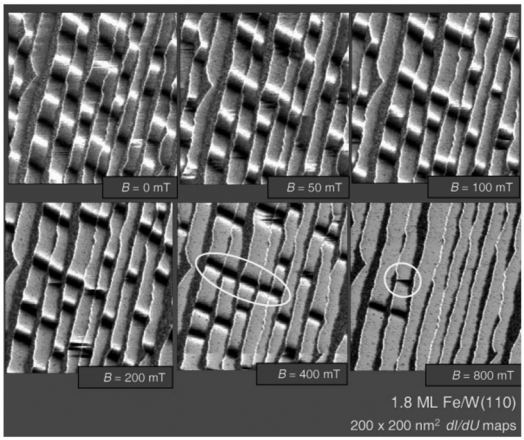

FIGURE 1.7: *Series of SP-STM images showing the response of 180° domain walls in magnetic Fe nanowires to an applied external field. By courtesy of the authors of Ref. [4].*

to the "functional part", see Figs. 1.2 and 1.4. For this reason it is utterly important to state in each single case by what measurements or in terms of which physical property nano-sized "functional parts" are recorded (identified, "seen"). There is perhaps another warning one ought to give right at the beginning of a book dealing with nanostructured matter: nanosystems are not interesting *per se*, but only because of their exceptional physical properties, some of which will be discussed in here.

The other key words in the title of the book, namely *magnetic anisotropies*, also need clarification. Per definition anisotropic physical properties are direction dependent quantities, i.e., are coupled to an intrinsic coordinate system. As probably is well known in the case of the electronic spin (magnetic properties) the directional dependence arises from the famous *spin-orbit* interaction, the coupling to a coordinate system most likely best remembered from the expressions *easy* and *hard* axes.

Unfortunately, the term *spin-orbit interaction* seems to be used very often only in a more or less "colloquial" manner, not to say used as a kind of *deus ex machina*. For this very reason the next chapter provides very preliminary remarks on (a) the concept of *parallel* and *antiparallel*, (b) the distinction between classical spin vectors and spinors, and (c) the actual form of the spin-orbit interaction as derived starting from the Dirac equation [5]. These remarks seem to be absolutely necessary because very often concepts designed for *classical spins* are mixed up with those of *spinors*: only the use of symmetry (Chapter 3) will then provide the formal tools to properly define magnetic structures.

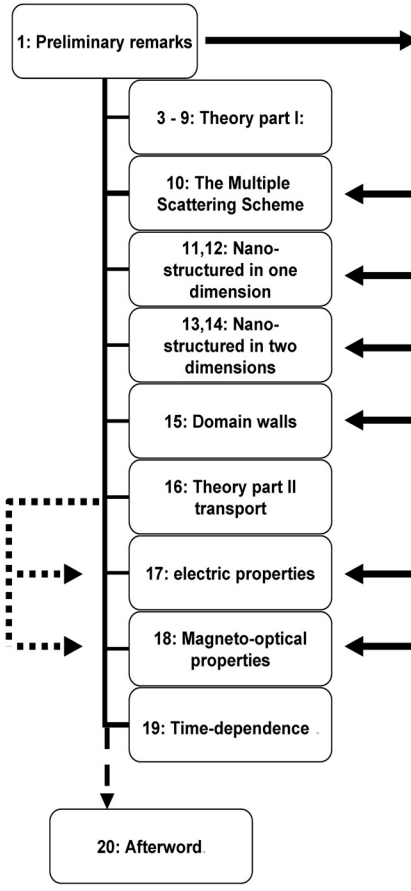

Scheme of chapters

Once this kind of formal stage is set methods suitable to describe (anisotropic) physical properties of magnetic nanostructures are introduced. All these methods will rely on a fully relativistic description by making use of Density Functional Theory, i.e., are based on the Dirac equation corresponding to an effective potential and an effective exchange field (Chapters 4 and 5). From there on the course of this book is directed to the main object promised in the title of this book, namely magnetic anisotropy energies (Chapter 6), exchange and Dzyaloshinskii & Moriya interactions (Chapter 7), temperature dependent effects (Chapter 8), spin dynamics (Chapter 9), and related properties of systems nanostructured in one (Chapters 11, 12) and two (Chapters 13, 14) dimensions.

Not only because magnetic anisotropy energies are not directly measured, but also because of their own enormous importance, methods of describing electric and magneto-optical properties are then shortly discussed (Chapter 16) and applied to magnetic nanostructured matter (Chapters 17 and 18). As a kind of outlook on upcoming magnetic anisotropy effects, concepts of how to deal with time-dependent (anisotropic) magnetic properties will finally be discussed (Chapter 19).

In order to make this book more "handy", the above scheme of chapters is supposed to help to direct the attention either to a particular topic or to leave out theory-only parts.

[1] I. R. McFadyen, E. E. Fullerton, and M. J. Carey, MRS Bulletin **31**, 379 (2006).

[2] S. Rusponi, T. Cren, N. Weiss, M. Epple, P. Buluschek, L. Claude, and H. Brune, Nat. Mat. **2**, 546 (2003).

[3] B. Lazarovits, B. Újfalussy, L. Szunyogh, B. L. Györffy, and P. Weinberger, J. Phys.: Condens. Matter **17**, 1037 (2005).

[4] A. Kubetzka, O. Pietsch, M. Bode, and R. Wiesendanger, Phys. Rev. B **67**, 020401 (R) (2003).

[5] P. A. M. Dirac, Proc. Roy. Soc. **A117**, 610 (1928); Proc. Roy. Soc. **A126**, 360 (1930)

2

Preliminary considerations

In preliminary considerations basic definitions concerning frequently used colloquial terminologies are introduced. In particular the "geometrical" origin of terms like parallel and antiparallel or collinear and non-collinear and the difference between "spin" viewed as a classical vector or as a spinor are emphasized. Also introduced is an explicit formulation for the spin orbit interaction for a central field as derived from the Dirac equation by means of the elimination method.

2.1 Parallel, antiparallel, collinear & non-collinear

Parallel, antiparallel and for that matter *collinear* and *non-collinear* are geometrical terms that have to be "translated" into algebraic expressions in order to become useful "formal" concepts. Consider two vectors $\mathbf{n}_1$ and $\mathbf{n}_2$,

$$\mathbf{n}_1 = \begin{pmatrix} n_{1,x} \\ n_{1,y} \\ n_{1,z} \end{pmatrix} \quad , \quad \mathbf{n}_2 = \begin{pmatrix} n_{2,x} \\ n_{2,y} \\ n_{2,z} \end{pmatrix} \quad , \quad n_{2,z} = n_{1,z} + a \quad , \tag{2.1}$$

and a transformation matrix* $D^{(3)}(R)$ corresponding to a rotation R around the z axis

$$\begin{pmatrix} D_{11}(R) & D_{12}(R) & 0 \\ D_{12}(R) & D_{22}(R) & 0 \\ 0 & 0 & 1 \end{pmatrix} \left\{ \begin{pmatrix} n_{2,x} \\ n_{2,y} \\ n_{2,z} \end{pmatrix} - \begin{pmatrix} 0 \\ 0 \\ a \end{pmatrix} \right\} = \begin{pmatrix} n'_{2,x} \\ n'_{2,y} \\ n_{1,z} \end{pmatrix} \quad . \tag{2.2}$$

If the transformation matrix $D^{(2)}(R)$,

$$D^{(2)}(R) = \begin{pmatrix} D_{11}(R) & D_{12}(R) \\ D_{12}(R) & D_{22}(R) \end{pmatrix} \quad , \quad D^{(3)}(R) = \begin{pmatrix} D^{(2)}(R) & 0 \\ 0 & 1 \end{pmatrix} \quad , \tag{2.3}$$

*The dimensions of rotation matrices are indicated by a superscript.

is the (two-dimensional) unit matrix I_2 then $\mathbf{n}_1$ and $\mathbf{n}_2$ are said to be *parallel* to each other. If on the other hand $D^{(2)}(R) = -I_2$ then these two vectors are oriented *antiparallel*.

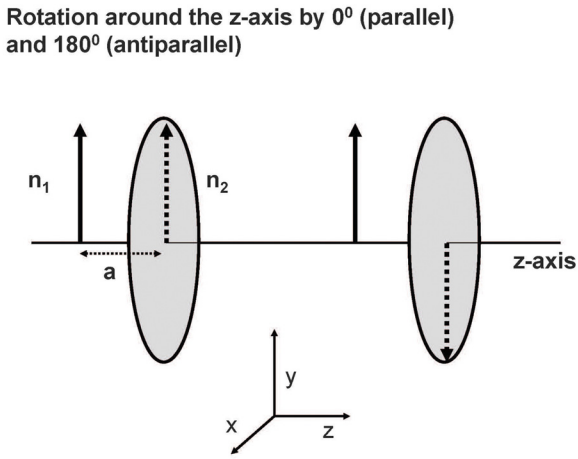

FIGURE 2.1: *The geometrical concept of "parallel" and "antiparallel" expressed in terms of rotations.*

Furthermore, consider a given vector $\mathbf{n}_0 = (n_{0,x}, n_{0,y}, n_{0,z})$ and the following set S of vectors $\mathbf{n}_k = (n_{k,x}, n_{k,y}, n_{k,z})$

$$S = \{\mathbf{n}_k |\ D^{(2)}(R) \begin{pmatrix} n_{k,x} \\ n_{k,y} \end{pmatrix} = \begin{pmatrix} n_{0,x} \\ n_{0,y} \end{pmatrix}, \\ n_{k,z} = n_{0,z} \pm ka, \quad k = 0, 1, 2, ..., K\} \quad . \tag{2.4}$$

This set consists of vectors $\mathbf{n}_k$ that are *collinear* to $\mathbf{n}_0$ (with respect to the z axis, $\mathbf{z} = (0, 0, 1)$), if in Eq. (2.4) $D^{(2)}(R) = \pm I_2$, i.e., if for all k, R is either the identity operation E or the "inversion" i,

$$D^{(n)}(E) = I_n \quad , \quad D^{(n)}(i) = -I_n \quad , \quad n = 2 \quad . \tag{2.5}$$

If this is not the case then S is said to be *non-collinear* to $\mathbf{n}_0$.

Obviously the above description is not restricted to rotations around the z axis. The only requirement is that the three-dimensional rotation matrix can be partitioned into two irreducible parts, namely a one-dimensional and a

two-dimensional one. The one-dimensional part reflects the rotation axis. It should be noted that although these definitions already sound like a description of magnetic structures they are not: what is meant is a simple geometrical construction with no implications for physics.

2.2 Characteristic volumina

Suppose the configurational space is partitioned into space filling cells of volumina Ω_i centered around atomic or fictional sites i. The total volume is then given by the sum over all individual cells N,

$$\Omega = \sum_{i=1}^{N} \Omega_i \quad . \tag{2.6}$$

Suppose further that $\bar{\Omega}(n)$ is the volume of n connected cells,

$$\bar{\Omega}(n) \subset \Omega \quad , \quad \bar{\Omega}(n) = \sum_{i=1}^{n} \Omega_i \quad , \tag{2.7}$$

and F_i represents a physical property corresponding to an operator whose representation is diagonal in configuration space, $F(\mathbf{r}, \mathbf{r})$. The quantity $F(n)$,

$$F(n) = \frac{1}{\bar{\Omega}(n)} \sum_{i=1}^{n} F_i \quad , \quad F_i = \int\limits_{\Omega_i} F(\mathbf{r}, \mathbf{r}) d\mathbf{r} \quad . \tag{2.8}$$

is called *intrinsic* (a materials specific constant) and $\bar{\Omega}(n)$ the *characteristic volume* if

$$F(n+m) - F(n) \leq \delta \quad , \tag{2.9}$$

where m is a positive integer and δ an infinitesimally small number.

The above definition is immediately transparent if in a bulk system Ω_i is identical to the unit cell Ω_0, since the very meaning of a unit cell is that

$$F_i = F_0 \quad , \quad \forall i \quad . \tag{2.10}$$

Quite clearly Eq. (2.10) can easily be achieved in terms of three-dimensional cyclic boundary conditions. If, however, translational invariance applies in less than three dimensions then Eqs. (2.8, 2.9) have to be checked for each physical property in turn. As an example simply consider the magnetic moments in bulk Fe and for Fe(100). In the bulk case (infinite system) in each unit cell the same magnetic moment pertains, while in the semi-infinite system Fe(100) the moment in surface near layers is different from the one deep inside the

system. As is well known, sizeable oscillations of the moment with respect to the distance from the surface can range over quite a few atomic layers. If no translational symmetry is present at all, see Figs. 1.4 and 1.5, characteristic volumes are even more difficult to define, since individual clusters (islands) can interact with each other.

2.3 "Classical" spin vectors and spinors

2.3.1 "Classical vectors" and Heisenberg models

Suppose the "spin" is viewed as a "classical" three-dimensional vector,

$$\mathbf{s}_i = (s_{i,x}, s_{i,y}, s_{i,z}) \quad , \tag{2.11}$$

where i denotes "site-indices", referring to location vectors $\mathbf{R}_i$ in "real space", $i = 1, 2, \ldots, N$. As is well known, very often spin models based on a semi-classical Hamilton (Heisenberg) function such as

$$\mathcal{H} = -\frac{1}{2}J \sum_{i,j=1}^{N} (\mathbf{s}_i \cdot \mathbf{s}_j) + \frac{1}{2}\omega \sum_{i,j=1}^{N} \left[\frac{(\mathbf{s}_i \cdot \mathbf{s}_j)}{R_{ij}^3} - 3\frac{(\mathbf{s}_i \cdot \mathbf{R}_{ij})(\mathbf{s}_j \cdot \mathbf{R}_{ij})}{R_{ij}^5} \right] - \lambda \sum_{i=1}^{N} s_{i,z}^2 \quad , \tag{2.12}$$

are used with considerable success [1]. In Eq. (2.12) $\mathbf{R}_{ij} = \mathbf{R}_i - \mathbf{R}_j$, and J, ω and λ refer in turn to the exchange interaction parameter, the magnetic dipole-dipole parameter and the spin-orbit interaction parameter. Quite clearly by the terms "collinear" or "non-collinear spins" transformation properties of *classical vectors* are implied, however, in a very particular manner.

Consider an arbitrary pair of "spins", $\mathbf{s}_i$ and $\mathbf{s}_j$. In principle, since they refer to different origins (sites $\mathbf{R}_i$) they have to be shifted to one and the same origin in order to check – as shown in Sect. 2.1 – conditions based on rotational properties, i.e.,

$$\mathbf{s}_i = D^{(3)}(R)(\mathbf{s}_j - \mathbf{R}_{ij}) \quad . \tag{2.13}$$

Clearly enough $\mathbf{s}_i$ and $\mathbf{s}_j - \mathbf{R}_{ij}$ are identical only if the rotation R is the identity operation E. If the x- and y-components of $\mathbf{R}_{ij}$ are zero then obviously the same simple case as in Eq. (2.2) applies, namely a rotation around $\mathbf{z}$.

Suppose now $\mathcal{N} = \{\mathbf{n}_i |\ \mathbf{n}_i = \mathbf{n}_0, i = 1, 2, \ldots N\}$ denotes a set of unit vectors in one and the same (chosen) direction $\mathbf{n}_0$ centered in sites $\mathbf{R}_i$ "carrying the spins" in the set $\mathcal{S} = \{\mathbf{s}_i |\ i = 1, 2, \ldots N\}$ such that for an arbitrarily chosen

$\mathbf{s}_k \in S$, $\mathbf{s}_k/|\mathbf{s}_k| = \mathbf{n}_0$. Any given pair of "spins", $\mathbf{s}_i$ and $\mathbf{s}_j \in \mathcal{S}$, is then said to be *parallel to* $\mathbf{n}_0$, if

$$\widehat{\mathbf{s}}_i = I_3\mathbf{n}_i \quad ; \quad \widehat{\mathbf{s}}_j = I_3\mathbf{n}_j \quad , \tag{2.14}$$

antiparallel, if

$$\widehat{\mathbf{s}}_i = I_3\mathbf{n}_i \quad ; \quad \widehat{\mathbf{s}}_j = -I_3\mathbf{n}_j \quad , \tag{2.15}$$

and *collinear*, if

$$\begin{aligned} &\widehat{\mathbf{s}}_i = \pm I_3\mathbf{n}_i \quad ; \quad \widehat{\mathbf{s}}_j = \pm I_3\mathbf{n}_j \quad ; \\ &\widehat{\mathbf{s}}_i = \frac{\mathbf{s}_i}{|\mathbf{s}_i|} \quad , \quad i = 1, \ldots, N \quad . \end{aligned} \tag{2.16}$$

All other cases have to be regarded as a *non-collinear* arrangement.

It is important to note that opposite to quantum mechanical formulations there are no symmetry restrictions connected with Eq. (2.12), since J, ω and λ are scalars, which have to be supplied externally, and of course also the rest in this equation consists of numbers only,

$$(\mathbf{s}_i \cdot \mathbf{s}_j) = |\mathbf{s}_i|\,|\mathbf{s}_j|\,(\widehat{\mathbf{s}}_i \cdot \widehat{\mathbf{s}}_j) \quad ; \quad (\mathbf{s}_i \cdot \mathbf{R}_{ij}) = |\mathbf{s}_i|\,|\mathbf{R}_{ij}|\left(\widehat{\mathbf{s}}_i \cdot \hat{\mathbf{R}}_{ij}\right) \quad . \tag{2.17}$$

Imposing therefore a certain symmetry such as, for example translational invariance, such a restriction has to be regarded as a "variational" constraint.

2.3.2 Spinors and Kohn-Sham Hamiltonians

In an effective one-electron description such as provided by Density Functional Theory [2] with $V^{eff}(\mathbf{r}) = V(\mathbf{r})$ and $\mathbf{B}^{eff}(\mathbf{r}) = \mathbf{B}(\mathbf{r})$ referring to the effective potential and exchange field,

$$V^{\text{eff}}[n, \mathbf{m}] = V^{\text{ext}} + V^{\text{Hartree}} + \frac{\delta E_{\text{xc}}[n, \mathbf{m}]}{\delta n} \quad , \tag{2.18}$$

$$\mathbf{B}^{\text{eff}}[n, \mathbf{m}] = \mathbf{B}^{\text{ext}} + \frac{e\hbar}{2mc}\frac{\delta E_{\text{xc}}[n, \mathbf{m}]}{\delta \mathbf{m}} \quad , \tag{2.19}$$

where $E_{\text{xc}}[n, \mathbf{m}]$ is the exchange-correlation energy, n the particle density, $\mathbf{m}$ the magnetization density, and V^{ext} and $\mathbf{B}^{\text{ext}}$ external fields, the corresponding Hamiltonian is given by

$$H(\mathbf{r}) = (T + V(\mathbf{r}) + \mathbf{S} \cdot \mathbf{B}(\mathbf{r}))I_n \quad , \tag{2.20}$$

$$T = \begin{cases} -\nabla^2 & ; \text{ non-relativistic} \\ c\boldsymbol{\alpha}\cdot\mathbf{p} + \beta mc^2 & ; \text{ relativistic} \end{cases} \quad , \tag{2.21}$$

$$\mathbf{S} = \begin{cases} \boldsymbol{\sigma} & ; \text{non-relativistic} \\ \\ \beta\boldsymbol{\Sigma} & ; \text{relativistic} \end{cases} \quad . \tag{2.22}$$

In Eq. (2.21) $\boldsymbol{\alpha}$ and β are Dirac matrices, $\boldsymbol{\Sigma}$ is the so-called spin operator,

$$\boldsymbol{\alpha} = \begin{pmatrix} 0 & \boldsymbol{\sigma} \\ \boldsymbol{\sigma} & 0 \end{pmatrix} \quad , \quad \beta = \begin{pmatrix} I_2 & 0 \\ 0 & -I_2 \end{pmatrix} \quad , \quad \boldsymbol{\Sigma} = \begin{pmatrix} \boldsymbol{\sigma} & 0 \\ 0 & \boldsymbol{\sigma} \end{pmatrix} \quad , \tag{2.23}$$

and $\boldsymbol{\sigma}$ is a formal vector consisting of Pauli spin matrices:

$$\boldsymbol{\sigma} = (\sigma_x, \sigma_y, \sigma_z) \quad , \tag{2.24}$$

$$\sigma_x = \begin{pmatrix} 0 & 1 \\ 1 & 0 \end{pmatrix} \quad , \quad \sigma_y = \begin{pmatrix} 0 & -i \\ i & 0 \end{pmatrix} \quad , \quad \sigma_z = \begin{pmatrix} 1 & 0 \\ 0 & -1 \end{pmatrix} \quad . \tag{2.25}$$

It should be noted that $\mathbf{S} \cdot \mathbf{B}(\mathbf{r})$ is not a "proper" scalar product, but only an abbreviation, since $\mathbf{B}(\mathbf{r})$ is a classical vector while the components of $\mathbf{S}$ in the simplest case are Pauli spin matrices, i.e.,

$$\boldsymbol{\sigma} \cdot \mathbf{B}(\mathbf{r}) \equiv \sigma_x B_x(\mathbf{r}) + \sigma_y B_y(\mathbf{r}) + \sigma_z B_z(\mathbf{r}) \quad . \tag{2.26}$$

In using the so-called local (spin) DFT (LS-DFT) to obtain computable expressions for the effective potential and the effective exchange field, the latter one is defined only with respect to an artificial z axis; i.e., in using LS-DFT the Hamiltonian in Eq. (2.20) reduces to

$$H(\mathbf{r}) = (T + V(\mathbf{r}) + S_z B_z(\mathbf{r})) I_n \quad . \tag{2.27}$$

One thus is faced with the necessity to eventually transform $H(\mathbf{r})$ such that $\mathbf{B}(\mathbf{r})$ can point also along a direction other than the z axis.

2.4 The famous spin-orbit interaction

Consider for matters of simplicity a Dirac-type Hamiltonian for a non-magnetic system, see Eq. (2.21), in atomic units ($\hbar = m = 1$),

$$\mathcal{H} = c\boldsymbol{\alpha} \cdot \mathbf{p} + (\beta - I_4)\, c^2 + V I_4 \quad , \tag{2.28}$$

where c is the speed of light. In making use of the bi-spinor property of the wavefunction $|\psi\rangle = |\phi, \chi\rangle$, the corresponding eigenvalue equation,

$$\mathcal{H}\,|\psi\rangle = \epsilon\,|\psi\rangle \quad , \tag{2.29}$$

can be split into two equations, namely

$$\begin{aligned} c\boldsymbol{\sigma}\cdot\mathbf{p}\,|\chi\rangle - V\,|\phi\rangle &= \epsilon\,|\phi\rangle \quad , \\ c\boldsymbol{\sigma}\cdot\mathbf{p}\,|\phi\rangle + \left(V - 2c^2\right)|\chi\rangle &= \epsilon\,|\chi\rangle \quad . \end{aligned} \tag{2.30}$$

Clearly, the spinor $|\chi\rangle$ can now be expressed in terms of $|\phi\rangle$:

$$|\chi\rangle = (1/2c)\,B^{-1}\boldsymbol{\sigma}\cdot\mathbf{p}\,|\phi\rangle \quad , \tag{2.31}$$

$$B = 1 + \left(1/2c^2\right)(\epsilon - V) \quad , \tag{2.32}$$

leading thus to only one equation for $|\phi\rangle$:

$$\mathcal{D}\,|\phi\rangle = \varepsilon\,|\phi\rangle \quad , \tag{2.33}$$

$$\mathcal{D} = (1/2)\,\boldsymbol{\sigma}\cdot\mathbf{p}B^{-1}\boldsymbol{\sigma}\cdot\mathbf{p} + V \quad . \tag{2.34}$$

The normalization of the wave function $|\psi\rangle$, by the way, can also be expressed in terms of the spinor $|\phi\rangle$:

$$\begin{aligned} \langle\psi|\,\psi\rangle &= \langle\phi|\,\phi\rangle + \langle\chi|\,\chi\rangle \\ &\langle\phi|\,1 + \left(1/4c^2\right)\boldsymbol{\sigma}\cdot\mathbf{p}B^{-2}\boldsymbol{\sigma}\cdot\mathbf{p}\,|\phi\rangle \quad . \end{aligned} \tag{2.35}$$

2.4.1 The central field formulation

For a *central field* the operator $\mathcal{D}$ in Eq. (2.34) has the same constants of motion [5] as the corresponding Dirac Hamiltonian, namely the angular momentum operators $\mathbf{J}^2$, J_z, and $K = \beta\,(1 + \boldsymbol{\sigma}\cdot\mathbf{L})$. Eq. (2.33) is therefore separable with respect to the radial and angular variables. The differential equation [3], [4] for the radial amplitudes of $|\phi\rangle$, $R_\kappa\,(r)\,/r$, is given by

$$\begin{aligned} &\left[\frac{1}{2}\left(-\frac{d^2}{dr^2} + \frac{\ell\,(\ell+1)}{r^2}\right) + V\,(r) - \epsilon\right] R_\kappa\,(r) = \\ &= \frac{1}{4c^2}\left\{B^{-2}(r)\frac{dV\,(r)}{dr}\frac{\kappa}{r} + \left[\left[\epsilon - V\,(r)\right]B^{-1}(r)\left(-\frac{d^2}{dr^2} + \frac{\ell\,(\ell+1)}{r^2}\right)\right]\right. \\ &\qquad \left. + B^{-2}(r)\frac{dV\,(r)}{dr}\frac{d}{dr}\right\} R_\kappa\,(r) \quad , \end{aligned} \tag{2.36}$$

where ℓ is the "usual" angular momentum quantum number, and κ is the quantum number corresponding to K,

$$\begin{aligned} \kappa &= \ell \quad , \quad j = \ell - 1/2 \\ \kappa &= -\ell - 1 \, , \quad j = \ell + 1/2 \end{aligned} \quad , \tag{2.37}$$

see also Eqs. (4.60) - (4.65) in Chapter 4.

Equation (2.36) shows a remarkably "physical structure" , namely

1. For $c = \infty$ (non-relativistic limit) this equation is reduced to the well-known *radial Schrödinger equation.*

2. By approximating the elimination operator B in Eq. (2.32) by unity ($B = 1$) the so-called (radial) *Pauli-Schrödinger equation* is obtained. The terms on the right-hand side of Eq. (2.36) are then in turn the *spin-orbit coupling*, the *mass velocity term*, and the *Darwin shift.*

3. For $B \neq 1$ relativistic corrections in order higher than c^{-4}, enter the description of the electronic structure via the normalization, Eq. (2.35).

It should be noted that although all three terms on the right-hand side of Eq. (2.36) have a prefactor $1/4c^2$, i.e., are of relativistic origin, the only one which explicitly depends on a relativistic quantum number, namely κ, is spin-orbit coupling. This term, however, because of dV/dr, has the unpleasant property of being singular for $r \to 0$. For this very reason throughout this book a fully relativistic description will be used, namely a description based on the Dirac equation, see Eq. (2.20) or Eq. (2.28), which of course contains all relativistic corrections to all orders of n in an expansion of the solutions of the Dirac equation in c^{-n}.

[1] For an excellent treatment and use of Heisenberg models see E. Y. Vedmedenko, *Competing Interactions and Pattern Formation in Nanoworld*, Wiley-VCH Verlag GmbH & Co.KGaA, Weinheim, Germany, 2007.

[2] See in particular: R. G. Parr and Y. Weitao, *Density-Functional Theory of Atoms and Molecules*, Oxford University Press, 1994; R. M. Dreizler and E. K. U. Gross, *Density Functional Theory. An Approach to the Quantum Many-Body Problem*, Springer, 1996; H. Eschrig, *The Fundamental of Density Functional Theory*, Teubner Verlag, 1997.

[3] P. A. M. Dirac, Proc. Roy. Soc. **A117**, 610 (1928); Proc. Roy. Soc. **A126**, 360 (1930)

[4] F. Rosicky, P. Weinberger, and F. Mark, J. Phys.: Molec. Phys. **9**, 2971 (1976).

[5] M. E. Rose, *Relativistic Electron Theory*, Wiley, New York 1961.

3

Symmetry considerations

Translational and rotational symmetry is used to unambiguously define magnetic configurations. In particular from the translational invariance of the Dirac equation terms such as "parallel" and "antiparallel" finally will become clear and turn into quantum mechanical concepts.

3.1 Translational invariance

A three-dimensional complex lattice is defined quantum mechanically in the following way,

$$\mathcal{L}^{(3)} = \{\mathbf{t}_i \mid H(\mathbf{r}+\mathbf{t}_i+\mathbf{a}_j) = H(\mathbf{r}+\mathbf{a}_j)\ ,\ j=1,N\ \} \quad , \tag{3.1}$$

$$\mathbf{r} = r_x\mathbf{x} + r_y\mathbf{y} + r_z\mathbf{z} \quad , \quad \mathbf{t}_i = t_{i,x}\mathbf{x} + t_{i,y}\mathbf{y} + t_{i,z}\mathbf{z} \quad , \tag{3.2}$$

where $H(\mathbf{r})$ is a Hamiltonian that is diagonal in configuration space (as is the case in DFT, see Eq. 2.20) and the vectors $\mathbf{a}_j$ are the so-called non-primitive lattice vectors, which specify inequivalent sites, i.e., generate sublattices. Simple lattices refer then "simply" to the case

$$N = 1\ ;\ \mathbf{a}_j = 0 \quad , \quad \forall j \quad . \tag{3.3}$$

In the following, for matters of simplicity, only simple lattices shall be dealt with; extensions to complex lattices do not pose further formal difficulties, but they occasionally will be mentioned.

Suppose one defines the following two-dimensional vectors

$$\mathbf{r}_\parallel = r_x\mathbf{x} + r_y\mathbf{y} \quad , \tag{3.4}$$

$$\mathbf{t}_{i,\parallel} = t_{i,x}\mathbf{x} + t_{i,y}\mathbf{y} \quad , \quad \mathbf{t}_i = \mathbf{t}_{i,\parallel} + t_{i,z}\mathbf{z} \quad , \quad t_{i,z} = 0 \quad , \quad \forall i \quad , \tag{3.5}$$

then a difference vector $\mathbf{r} - \mathbf{t}_i$ is given by

$$\mathbf{r} - \mathbf{t}_i = (r_x - t_{i,x})\mathbf{x} + (r_y - t_{i,y})\mathbf{y} + r_z\mathbf{z} = \mathbf{r}_\parallel - \mathbf{t}_{i,\parallel} + r_z\mathbf{z} \quad . \tag{3.6}$$

Consequently a two-dimensional (simple) lattice has then to be defined by

$$\begin{aligned}\mathcal{L}^{(2)}(r_z) &= \{\mathbf{t}_i \mid H(\mathbf{r}+\mathbf{t}_i) = H(\mathbf{r}) \ , \ t_{i,z} = 0\} \\ &\equiv \left\{\mathbf{t}_{i,\parallel} \mid H(\mathbf{r}+\mathbf{t}_{i,\parallel}) = H(\mathbf{r}) \ \right\} \quad . \end{aligned} \tag{3.7}$$

Note that in principle because of Eq. (3.6) r_z appears as an argument in the definition of such a lattice!

3.2 Rotational invariance

Suppose the following group of (rotation) operators leaves the Hamiltonian in Eq. (2.20) invariant,

$$\mathcal{G}^{(3)} = \left\{R \mid H(R^{-1}\mathbf{r}) = H(\mathbf{r}') = H(\mathbf{r})\right\} \quad , \tag{3.8}$$

the representatives of the group elements in $\mathbb{R}^{(3)}$ being three-dimensional matrices,

$$D^{(3)}(R)\mathbf{r} = \mathbf{r}' \quad , \quad R \in \mathcal{G}^{(3)} \quad . \tag{3.9}$$

$\mathcal{G}^{(3)}$ is usually called the three-dimensional point group. Similarly a two-dimensional point group with respect to $\mathbf{z}$ (*rotational invariance group along* $\mathbf{z}$) is defined as

$$\mathcal{G}^{(2)}(r_z) = \left\{R \mid H(R^{-1}\mathbf{r}) = H(\mathbf{r}) \ , R^{-1}\left(r_z\mathbf{z}\right) = r_z\mathbf{z}\right\} \quad . \tag{3.10}$$

From Eq. (3.10) it follows immediately that such a two-dimensional point group with respect to $\mathbf{z}$ can only contain *rotations* around $\mathbf{z}$ and *mirror planes* that include the $\mathbf{z}$-axis, but not, e.g., a mirror plane perpendicular to $\mathbf{z}$.

Consider now the case that translational as well as rotational symmetry applies then – in the case of symmorphic space groups, which was assumed anyhow, see Eq. (3.3) – the corresponding three-dimensional space group is defined by

$$\mathcal{S}^{(3)} = \left\{[R|t] \mid H(R^{-1}\mathbf{r}+\mathbf{t}) = H(\mathbf{r})\right\} \quad , \tag{3.11}$$

and a two-dimensional spacegroup with respect to $\mathbf{z}$ as

$$\mathcal{S}^{(2)}(r_z) = \left\{[R|t] \mid H(R^{-1}\mathbf{r}+\mathbf{t}) = H(\mathbf{r}) \ , R^{-1}\left(r_z\mathbf{z}\right) = r_z\mathbf{z}\right\} \quad . \tag{3.12}$$

3.3 Colloquial or parent lattices

Eq. (3.1) refers to a proper quantum mechanical definition of lattices, namely to the invariance properties of a given Hamilton operator. In principle, how-

ever, lattices can also be constructed as particular subspaces in $\mathbb{R}^{(3)}$,

$$L^{(3)} = \{\mathbf{t}_n \mid \mathbf{A}\ \mathbf{n} + \mathbf{a}_j\ ,\quad j = 1, N\ \} \quad , \tag{3.13}$$
$$\mathbf{n} = (n_1, n_2, n_3), \quad n_1, n_2, n_3 \in \mathbb{Z} \quad ,$$

with $\mathbf{A}$ usually being called the *Bravais matrix*. For example, for simple lattices ($\mathbf{a}_j = 0, \forall j$) $\mathbf{A}$ is of the form

$$\mathbf{A}^{sc} = a \begin{pmatrix} 1 & 0 & 0 \\ 0 & 1 & 0 \\ 0 & 0 & 1 \end{pmatrix} \quad , \quad \mathbf{A}^{fcc} = \frac{a}{2} \begin{pmatrix} 0 & 1 & 1 \\ 1 & 0 & 1 \\ 1 & 1 & 0 \end{pmatrix} \quad , \tag{3.14}$$

$$\mathbf{A}^{bcc} = \frac{a}{2} \begin{pmatrix} -1 & 1 & 1 \\ 1 & -1 & 1 \\ 1 & 1 & -1 \end{pmatrix} \quad , \tag{3.15}$$

where a is a scaling factor ("lattice constant") and *sc*, *fcc* and *bcc* refer in turn to *simple cubic*, *face centred cubic* and *body centred cubic*. It should be noted that Eq. (3.13) is entirely a "formal" construction that *a priori* has nothing in common with a given physical system: $L^{(3)}$ refers to an *icon* of a particular lattice.

Suppose now that according to Eq. (3.12) a given system can be viewed as a stack of translational invariant atomic planes such that

$$\mathcal{L}^{(2)}(r_{n,z}) = \mathcal{L}^{(2)} \quad , \quad \forall r_{n,z} \quad , \tag{3.16}$$

where the $r_{n,z}$ specify the individual atomic layers. Furthermore, suppose that

$$\mathcal{L}^{(2)} \subset L^{(3)} \quad , \tag{3.17}$$

$$(r_{n+m,z} - r_{n,z})\,\mathbf{z} \quad \in L^{(3)} \quad , \quad m \in \mathbb{Z} \quad , \tag{3.18}$$

then $L^{(3)}$ has to be called a *parent* or *underlying three-dimensional lattice*. Such a system very often is colloquially called an *fcc* or *bcc* lattice or what ever the respective Bravais matrix $\mathbf{A}$ corresponds to. It should be noted, however, that $\mathcal{L}^{(3)}$ refers to an infinite system, while a parent three-dimensional lattice $L^{(3)}$ comprises not only the case of a semi-infinite system (solid system with a surface), but also covers the case that the atomic species in different atomic planes can be different. A parent lattice can be viewed as an *icon* of a lattice with – in contradiction to translational invariance – equivalent lattice sites being decorated with atoms of different kind. Consider for example Cu(100): if no relaxation is present then this system may colloquially be referred to as *fcc*, although it is only a semi-infinite system, i.e., a system with a surface. If condition (3.18) is not met then further specifying adjectives are frequently introduced such as, e.g., a *distorted parent lattice* ("distorted fcc lattice").

3.4 Tensorial products of spin and configuration

Although up-to-now quite a few geometrical concepts and general transformation properties were already introduced in order to define magnetic configurations properly, one still has to investigate explicitly the transformation properties of $H(\mathbf{r})$ in Eq. (2.20).

3.4.1 Rotational properties

Consider first the relativistic form of $H(\mathbf{r})$ and a rotation R. Invariance by R implies that

$$S(R)H(R^{-1}\mathbf{r})S^{-1}(R) = H(\mathbf{r}) \quad , \tag{3.19}$$

where $S(R)$ is a 4×4 matrix transforming the Dirac matrices α_i, β, and Σ_i. Since β is a real matrix, see Eq. (2.23), it can be shown [1] that $S(R)$ is of block-diagonal form,

$$S(R) = \begin{pmatrix} U(R) & 0 \\ 0 & \det[\pm]U(R) \end{pmatrix} \quad , \tag{3.20}$$

where $U(R)$ is a (unimodular) 2×2 matrix and $\det[\pm] = \det[D^{(3)}(R)]$ is the determinant of $D^{(3)}(R)$.

Using now the invariance condition in Eq. (3.19) explicitly,

$$\begin{aligned} &S(R)\mathcal{H}(R^{-1}\mathbf{r})S^{-1}(R) = \\ &= S(R)\left[c\boldsymbol{\alpha}\cdot\mathbf{p} + \beta mc^2 + I_4 V(R^{-1}\mathbf{r}) + \beta\boldsymbol{\Sigma}\cdot\mathbf{B}(R^{-1}\mathbf{r})\right]S^{-1}(R) \quad , \end{aligned} \tag{3.21}$$

one can see immediately that the condition

$$S(R)\left[I_4 V(R^{-1}\mathbf{r})\right]S^{-1}(R) = I_4 V(R^{-1}\mathbf{r}) = I_4 V(\mathbf{r}) \tag{3.22}$$

yields the usual *rotational invariance* condition for the potential discussed previously, while the terms $S(R)\left[c\boldsymbol{\alpha}\cdot\mathbf{p}\right]S^{-1}(R)$ and

$$S(R)\left[\beta\boldsymbol{\Sigma}\cdot\mathbf{B}(R^{-1}\mathbf{r})\right]S^{-1}(R) \tag{3.23}$$

have to be examined with more care. Considering the scalar product in (3.23) explicitly term-wise, i.e., inspecting terms such as

$$S(R)\left[\begin{pmatrix} \sigma_i & 0 \\ 0 & -\sigma_i \end{pmatrix} B_i(R^{-1}\mathbf{r})\right]S^{-1}(R) \quad , \quad i = x, y, z \quad , \tag{3.24}$$

it is clear that matrix products of the form

$$\begin{aligned} &S(R)\begin{pmatrix} \sigma_i & 0 \\ 0 & -\sigma_i \end{pmatrix}S^{-1}(R) = \\ &\begin{pmatrix} U(R) & 0 \\ 0 & \det[\pm]U(R) \end{pmatrix}\begin{pmatrix} \sigma_i & 0 \\ 0 & -\sigma_i \end{pmatrix}\begin{pmatrix} U^{-1}(R) & 0 \\ 0 & \det[\pm]U^{-1}(R) \end{pmatrix} \end{aligned} \tag{3.25}$$

are needed, which – as easily can be seen from (3.25) – reduce to matrix products of the following kind:

$$U(R)\sigma_i U^{-1}(R) = \sigma_i' \quad . \tag{3.26}$$

In essence one has to deal therefore with the transformation properties of Pauli spin matrices, which can be either formulated using a quarternion-like description [2] or in a more pedestrian way described, e.g., in [1], which for matters of simplicity is used in the following. If $\mathbf{n} = (n_1, n_2, n_3)$ denotes a unit vector along a rotation axis whose components are the direction cosines of this axis, and φ is the rotation angle in a right-hand screw sense about $\mathbf{n}$, $0 \leq \varphi \leq \pi$, then $\pm U(R)$ is given [1] by*

$$\pm U(R) = \pm U(\mathbf{n}, \varphi) \quad , \tag{3.27}$$

$$U(\mathbf{n}, \varphi) = \begin{pmatrix} C - in_3 S & -(n_2 + in_1)S \\ \\ (n_2 - in_1)S & C + in_3 S \end{pmatrix} \quad , \tag{3.28}$$

$$S = \sin(\varphi/2) \quad , \quad C = \cos(\varphi/2) \quad . \tag{3.29}$$

$U(R)$ is a transformation in spin space only, i.e., $U(R) \in SU2$. Returning now to (3.24) and using the invariance condition in (3.19),

$$\begin{aligned} &S(R)\left[\begin{pmatrix} \sigma_i & 0 \\ 0 & -\sigma_i \end{pmatrix} B_i(R^{-1}\mathbf{r})\right] S^{-1}(R) = \begin{pmatrix} \sigma_i'(R) & 0 \\ 0 & -\sigma_i'(R) \end{pmatrix} B_i(R^{-1}\mathbf{r}) \\ &\equiv \begin{pmatrix} \sigma_i & 0 \\ 0 & -\sigma_i \end{pmatrix} B_i(\mathbf{r}) \quad , \end{aligned} \tag{3.30}$$

one easily can see that this implies that

$$B_i(R^{-1}\mathbf{r}) = B_i(\mathbf{r}) \quad \wedge \quad U(R)\sigma_i U^{-1}(R) = \sigma_i \quad , \quad i = 1, 2, 3 \quad , \tag{3.31}$$

or, writing the second part of this condition in a short-hand notation,

$$U(R)\boldsymbol{\sigma} U^{-1}(R) = \boldsymbol{\sigma} \quad . \tag{3.32}$$

It should be noted that of course also the term $S(R)\,[c\boldsymbol{\alpha}\cdot\mathbf{p}]\,S^{-1}(R)$ has to be inspected,

$$\left(S(R)\begin{pmatrix} 0 & \boldsymbol{\sigma} \\ \boldsymbol{\sigma} & 0 \end{pmatrix} S^{-1}(R)\right) \cdot \mathbf{p} = \begin{pmatrix} 0 & \boldsymbol{\sigma} \\ \boldsymbol{\sigma} & 0 \end{pmatrix} \cdot \mathbf{p} \quad , \tag{3.33}$$

which in turn yields the condition

$$\det[\pm] U(R)\boldsymbol{\sigma} U^{-1}(R) = \boldsymbol{\sigma} \quad . \tag{3.34}$$

Since the *same invariance condition has to apply simultaneously* for both terms, only the positive sign in Eq. (3.20) applies.

*Quaternions are not really avoided here, since $(\mathbf{n}, \varphi)$ is a quaternion, namely an object containing a vector $\mathbf{n}$ and a scalar φ [2].

3.4.2 Local spin density functional approaches

It was already mentioned in Sect. 2.3.2 that in using a local spin density functional (LS-DFT) approach the exchange field is only defined with respect to a fictional z axis,

$$H(\mathbf{r}) = c\boldsymbol{\alpha}\cdot\mathbf{p} + \beta mc^2 + V(\mathbf{r})I_4 + \beta\Sigma_z B_z(\mathbf{r}) \quad , \tag{3.35}$$

$$\beta\Sigma_z B_z(\mathbf{r}) = \begin{pmatrix} I_2 & 0 \\ 0 & -I_2 \end{pmatrix} \begin{pmatrix} \sigma_z & 0 \\ 0 & \sigma_z \end{pmatrix} B_z(\mathbf{r}) \quad , \tag{3.36}$$

Denoting this fictional z axis by say $\mathbf{n} \in \mathbb{R}_3$ such that $\mathbf{B}(\mathbf{r})$ is of the form

$$\mathbf{B}(\mathbf{r}) = B(\mathbf{r})\mathbf{n} \quad , \quad \mathbf{n} = (0,0,1) \quad , \tag{3.37}$$

Eq. (3.35) can formally be rewritten as

$$H(\mathbf{r}) = c\boldsymbol{\alpha}\cdot\mathbf{p} + \beta mc^2 + (\beta\boldsymbol{\Sigma}\cdot B(\mathbf{r})\mathbf{n}) \quad . \tag{3.38}$$

Considering only the last term in Eq. (3.38) an arbitrary rotation T of this particular Hamiltonian can be viewed in the following way

$$\begin{aligned} U(T)\left[\left(\boldsymbol{\sigma}\cdot B(T^{-1}\mathbf{r})\mathbf{n}\right)\right]U^{-1}(T) &= \left[\left(U(T)\boldsymbol{\sigma}U^{-1}(T)\right)\cdot B(T^{-1}\mathbf{r})\mathbf{n}\right] \\ &= (\boldsymbol{\sigma}'\cdot B(T^{-1}\mathbf{r})\mathbf{n}) \\ &= (\boldsymbol{\sigma}\cdot B(\mathbf{r}')\mathbf{n}') \\ &= (\boldsymbol{\sigma}\cdot \mathbf{B}'(\mathbf{r}')) \quad , \end{aligned} \tag{3.39}$$

i.e., such a transformation can be interpreted as a change in the direction of the exchange field. Clearly enough, also the other parts in Eq.(3.35) have to be transformed, i.e., the transformed Hamiltonian is given by:

$$S(T)H(T^{-1}\mathbf{r})S^{-1}(T) = S(T)\left[c\boldsymbol{\alpha}\cdot\mathbf{p} + \beta mc^2\right]S^{-1}(T) + V(\mathbf{r}')I_4 + \beta\boldsymbol{\Sigma}\cdot\mathbf{B}'(\mathbf{r}') \quad . \tag{3.40}$$

If T happens to be a symmetry operator, see Eqs. (3.30) - (3.31), then of course $H(\mathbf{r})$ remains unchanged; i.e., the point group of $H(\mathbf{r})$ is given by the condition

$$\mathcal{G}_H = \left\{ R \middle| \; S(R)H(R^{-1}\mathbf{r})S^{-1}(R) = H(\mathbf{r}) \right\} \quad . \tag{3.41}$$

Furthermore, if $B_z(\mathbf{r})$ is a spherical symmetric function, $B_z(|\mathbf{r}|)$, as is the case whenever the so-called Atomic Sphere Approximation (ASA) is used, then Eq. (3.39) reduces to

$$B(r)(\boldsymbol{\sigma}'\cdot\mathbf{n}) = B(r)(\boldsymbol{\sigma}\cdot\mathbf{n}') \quad . \tag{3.42}$$

From Eq.(3.40) it is obvious that a "change in the direction" of the exchange field is of course also coupled to corresponding changes in configurational space.

3.4.3 Induced transformations

Going back to the *rhs* of Eq. (3.39) one easily can see that for a given transformation

$$U(R)\boldsymbol{\sigma}U^{-1}(R) = \boldsymbol{\sigma}' \quad ,$$

the occurring identities can be rewritten as

$$(\boldsymbol{\sigma}' \cdot B(R^{-1}\mathbf{r})\mathbf{n}) = (\boldsymbol{\sigma}\cdot\ B(\mathbf{r}')\mathbf{n}') = (\boldsymbol{\sigma}\cdot\ B(R^{-1}\mathbf{r})D^{(3)}(R)\mathbf{n}) \quad ,$$

and Eq.(3.42) as

$$B(r)(\boldsymbol{\sigma}' \cdot \mathbf{n}) = B(r)(\boldsymbol{\sigma} \cdot D^{(3)}(R)\mathbf{n}) \quad ,$$

i.e., a rotation in spin space by $U(R)$ *induces* a transformation of the orientation $\mathbf{n}$ of the exchange field by $D^{(3)}(R)$.

For $\mathbf{n} = (0, 0, 1)$, see Eq. (3.37), the identity rotation $D^{(3)}(E)$ for example is *induced* by a transformation in spin space by

$$U(\hat{\mathbf{z}}, 0) = I_2 = \begin{pmatrix} 1 & 0 \\ 0 & 1 \end{pmatrix} \quad , \tag{3.43}$$

while $D^{(3)}(i) = -I_3$ is induced by

$$U(\hat{\mathbf{y}}, 0) = \sigma_y = \begin{pmatrix} 0 & -i \\ i & 0 \end{pmatrix} \quad , \tag{3.44}$$

since

$$U(\hat{\mathbf{y}}, 0)U(\hat{\mathbf{y}}, 0)^{-1} = \sigma_y^2 = I_2 \quad , \tag{3.45}$$

and

$$\sigma_y\sigma_z\sigma_y = -\sigma_z \quad . \tag{3.46}$$

However, since the same arguments apply for

$$U(\zeta, \varphi) \equiv U(\hat{\mathbf{x}}, 0) = \sigma_x = \begin{pmatrix} 0 & 1 \\ 1 & 0 \end{pmatrix} \quad , \tag{3.47}$$

$$\sigma_x^2 = I_2 \quad , \quad \sigma_x\sigma_z\sigma_x = -\sigma_z \quad , \tag{3.48}$$

it is obvious from Eq. (3.42) that an inversion of $\mathbf{n}$ can be obtained either by a rotation around $\hat{\mathbf{x}}$ or around $\hat{\mathbf{y}}$ with a rotation angle of $\varphi = 0$.

3.4.4 Non-relativistic approaches

Within LS-DFT, in the non-relativistic case of Eq. (2.21), an arbitrary rotation R in spin space (no transformations in configurational space!) implies the following invariance properties,

$$\begin{aligned} U(R)H(\mathbf{r})U^{-1}(R) &= U(R)\left[-\nabla^2 + V(\mathbf{r}) + B(\mathbf{r})(\boldsymbol{\sigma}\cdot\mathbf{n})\right]U^{-1}(R) \\ &= -\nabla^2 + V(\mathbf{r}) + B(\mathbf{r})\,(\boldsymbol{\sigma}'\cdot\mathbf{n}) \\ &= -\nabla^2 + V(\mathbf{r}) + B(\mathbf{r})\,(\boldsymbol{\sigma}\cdot\mathbf{n}') \quad . \end{aligned} \tag{3.49}$$

Note that because $U(R)$ is a transformation in spin space, see Eqs. (3.27) - (3.29), such a transformation leaves the configurational part unchanged. Considering therefore all rotational properties discussed up to now – including "classical spins" $\mathbf{s}$ – one arrives at the following compact characterization of the rotational properties of "spins":

level	**"spin"**	**rotation matrices**	**restrictions**
classical	$\mathbf{s}$	$D^{(3)}(R)$,	$R \in SO3$
DFT, non-relativistic	$\boldsymbol{\sigma}$	$U(R) \equiv U(\mathbf{n},\varphi)$,	$R \in SU2$
DFT, relativistic	$\boldsymbol{\Sigma}$	$S(R) = \begin{pmatrix} U(R) & 0 \\ 0 & \det[\pm]U(R) \end{pmatrix}$,	$R \in \mathcal{G}_H$

3.4.5 Translational properties

Recalling that the elements of the translation group can be viewed as space group elements, $[E \mid \mathbf{t}_j]$, where E is the identity rotation, invariance of the relativistic form of $\mathcal{H}(\mathbf{r})$ with respect to $[E \mid \mathbf{t}_j]$ simply reduces to

$$\begin{aligned} &S(E)H([E \mid \mathbf{t}_j]^{-1}\mathbf{r})S^{-1}(E) = \\ &= S(E)\left[c\boldsymbol{\alpha}\cdot\mathbf{p} + \beta mc^2 + I_4 V([E \mid \mathbf{t}_j]^{-1}\mathbf{r}) + \beta\boldsymbol{\Sigma}\cdot\mathbf{B}([E \mid \mathbf{t}_j]^{-1}\mathbf{r})\right]S^{-1}(E) \end{aligned} , \tag{3.50}$$

where $S(E) = I_4$, namely a 4×4 unit matrix.

Eq. (3.50) has considerable consequences for the concepts of *collinear* and *non-collinear* magnetic structures: if translational invariance applies then in all lattice points belonging to one and the same sublattice the exchange field has to point along the same direction; i.e., the orientations of the exchange field in these lattice points have to be *parallel* to each other. If only two-dimensional translational invariance is present, see Eq.(3.12), as, e.g., is the case in layered systems, then the orientation of the exchange field has to be uniform in each particular layer. Spacially different layers can of course have different uniform orientations.

3.5 Cell-dependent potentials and exchange fields

Now we shall return for a moment to the concept of individual volumina discussed in Sect. 2.2. Suppose $V(\mathbf{r})$ is given in terms of a superposition of

individual potentials,

$$V(\mathbf{r}) = \sum_{i=1}^{N} V_i(\mathbf{r}_i) \quad , \quad \mathbf{r} = \mathbf{r}_i + \mathbf{R}_i \quad , \tag{3.51}$$

and $\mathbf{B}(\mathbf{r})$ is of the same form:

$$\mathbf{B}(\mathbf{r}) = \sum_{i=1}^{N} \mathbf{B}_i(\mathbf{r}_i) \quad , \tag{3.52}$$

such that the domains $\Delta_{V_i}, \Delta_{\mathbf{B}_i}$ of the individual operators V and $\mathbf{B}$ are disjoint in the configurational space Δ,

$$\Delta_{V_i} = \Delta_{\mathbf{B}_i} \ , \forall i \quad ; \quad \Delta_{V_i} \cap \Delta_{Vj} \ = 0, \forall i \neq j \quad ; \quad \Delta = \bigcup_i \Delta_{V_i} \quad . \tag{3.53}$$

The Hamiltonian in Eq. (2.20) is therefore of the following form:

$$H(\mathbf{r}) = \begin{cases} -\nabla^2 I_2 + \sum\limits_{i=1}^{N} \{I_2 V_i(\mathbf{r}_i) + \boldsymbol{\sigma} \cdot \mathbf{B}_i(\mathbf{r}_i)\} \\ \\ c\boldsymbol{\alpha} \cdot \mathbf{p} + \beta mc^2 + \sum\limits_{i=1}^{N} \{I_4 V_i(\mathbf{r}_i) + \beta \boldsymbol{\Sigma} \cdot \mathbf{B}_i(\mathbf{r}_i)\} \end{cases} . \tag{3.54}$$

Consequently in the case of two-dimensional translational invariance one gets in the relativistic case the following definition of a (two-dimensional) lattice

$$\begin{aligned} \mathcal{L}^{(2)}(R_{i,z}) = \big\{ \mathbf{R}_{j,\|} \mid V_k(\mathbf{r}_k - \mathbf{R}_{j,\|}; R_{iz}) = V_k(\mathbf{r}_k; R_{iz}) \ , \\ \mathbf{B}_k(\mathbf{r}_k - \mathbf{R}_{j,\|}; R_{iz}) = \mathbf{B}_k(\mathbf{r}_k; R_{iz}) \big\} \quad , \end{aligned} \tag{3.55}$$

whereas the corresponding point group with respect to $\mathbf{z}$ (*rotational invariance along* $\mathbf{z}$) is defined as

$$\begin{aligned} \mathcal{G}^{(2)}(R_{i,z}) = \Big\{ R \mid \widehat{R}(V(\mathbf{r}_k + \mathbf{R}_{k,\|} + R_{i,z}\mathbf{z})) = V_k(\mathbf{r}_k; R_{i,z}) \quad , \\ \widehat{R}\left(\mathbf{B}(\mathbf{r}_k + \mathbf{R}_{k,\|} + R_{i,z}\mathbf{z})\right) = \mathbf{B}_k(\mathbf{r}_k; R_{i,z}) \quad , \\ U(R)\boldsymbol{\sigma}U^{-1}(R) = \boldsymbol{\sigma} \quad , \\ R^{-1}\left(R_{i,z}\mathbf{z}\right) = R_{i,z}\mathbf{z} \Big\} \quad , \end{aligned} \tag{3.56}$$

where an arbitrary index k simply serves to specify the origin.

3.6 Magnetic configurations

Now we are in the proper stage to define magnetic configurations formally correct. Suppose a system consists of N atomic layers, whereby each of the layers is two-dimensionally translational invariant. If the two-dimensional lattice in each layer consists of J sublattices, then the orientation of the exchange fields in each layer i can be specified by a set of directions

$$n_i = \{\mathbf{m}_1, \mathbf{m}_2, \mathbf{m}_3, \ldots, \mathbf{m}_J\} \quad , \tag{3.57}$$

in which the $\mathbf{m}_j$ denote the orientations of the exchange fields in each sublattice j. The magnetic configuration of the whole system is then given by

$$\{n_1, n_2, n_3, \ldots, n_N\} \quad . \tag{3.58}$$

Consider the case of $J = 2$. The orientations $\mathbf{m}_1$ and $\mathbf{m}_2$ can then for example be *parallel* or *antiparallel* to each other. Different planes ($n_i \neq n_j$) can show different sublattice orientations. One thus can have the case of *antiferromagnetism* within the atomic planes and/or *antiferromagnetism* between planes. If $J = 1$ then in each atomic layer only one and the same (uniform) orientation applies. Different planes, however, can have different orientations.

It should be understood by now that because of Eq. (3.50) the term *parallel* can apply only to one particular sublattice. *Antiparallel* arrangements, however, can be present either within the atomic planes (implying more than one sublattice, $J \geq 1$) or between atomic planes.

Rather well-known examples of non-collinear magnetic configurations are, e.g., *domain walls* and *spin spirals*. In both cases the orientation of the exchange field in the various atomic planes can be grouped in various regimes. Suppose that only a simple parent lattice is present and let L be either the domain wall width or the length of a spin spiral (in atomic monolayers); then:

$$\text{domain wall: } \{n_l, n_1, n_2, n_3, \ldots, n_L, n_r\} \quad , \tag{3.59}$$

$$\text{spin spiral: } \left\{ \begin{array}{c} \ldots, \{n_1, n_2, n_3, \ldots, n_L = n_1\}, \ldots, \\ \{n_1, n_2, n_3, \ldots, n_L = n_1\}, \ldots \end{array} \right\} = \{n_1, n_2, n_3, \ldots, n_L = n_1\}_N \quad . \tag{3.60}$$

where in the case of domain walls the orientations in two neighboring domains are denoted by n_l and n_r (l denoting "left" and r "right") and in that of spin spirals the spiral is repeated N times.

If no translational symmetry is present then of course the orientation of the magnetization in each individual site has to be specified. This definitely is the case for magnetic nanostructures on top of suitable substrates (2d-nanosystems). Clearly enough it can turn out that in finite chains of magnetic atoms the orientations of the exchange field are parallel to each other; however, by symmetry restrictions they don't have to.

[1] L. Jansen and M. Boon, *Theory of Finite Groups. Applications in Physics,* pp.314 North-Holland Publ.Co., Amsterdam, 1967

[2] S.L. Altmann, *Rotations, Quaternions and Double Groups*, Clarendon Press, Oxford, 1986

[3] P. Weinberger, Phil. Mag. B**75**, 509 (1997)

4

Green's functions and multiple scattering

The basic concepts of multiple scattering and of the so-called Screened Korringa-Kohn-Rostoker method are shortly reviewed.* These concepts will serve as the theoretical basis for most aspects to be discussed in the context of magnetic anisotropies of nanostructured matter. In particular since a fully relativistic formulation of single-particle Green's functions can be given, related physical quantities such as transport properties of such systems will also be accessible.

4.1 Resolvents and Green's functions

The resolvent of a Hermitian operator (Hamilton operator) is defined as follows

$$\mathcal{G}(z) = (z\mathcal{I} - \mathcal{H})^{-1} \quad , \quad z = \epsilon + i\delta \quad , \quad \mathcal{G}\left(z^*\right) = \mathcal{G}\left(z\right)^\dagger \quad , \tag{4.1}$$

where $\mathcal{I}$ is the unity operator. Any representation of such a resolvent is called a Green's functions, e.g., also the following configuration space representation of $\mathcal{G}(z)$,

$$< \mathbf{r} \left| \mathcal{G}(z) \right| \mathbf{r}' > = G(\mathbf{r}, \mathbf{r}'; z) \quad . \tag{4.2}$$

The so-called side-limits of $\mathcal{G}(z)$ are then defined by

$$\lim_{|\delta| \to 0} \mathcal{G}(z) = \begin{cases} \mathcal{G}^+(\epsilon) \; ; \delta > 0 \\ \\ \mathcal{G}^-(\epsilon) \; ; \delta < 0 \end{cases} \quad , \tag{4.3}$$

$$\mathcal{G}^+(\epsilon) = \mathcal{G}^-(\epsilon)^\dagger \quad , \tag{4.4}$$

and therefore lead to the property,

$$\mathrm{Im}\, \mathcal{G}^+(\epsilon) = \frac{1}{2i} \left(\mathcal{G}^+(\epsilon) - \mathcal{G}^-(\epsilon) \right) \quad , \tag{4.5}$$

*For a more complete discussion, see Refs.[1, 2, 3]

or – assuming for matters of simplicity only a discrete eigenvalue spectrum $\{\epsilon_k\}$ of $\mathcal{H}$,

$$\mathrm{ImTr}\,\mathcal{G}^{\pm}(\epsilon) = \mp\pi^{-1}\sum_k \delta(\epsilon-\epsilon_k) \quad , \tag{4.6}$$

$$n(\epsilon) = \mp\mathrm{ImTr}\,\mathcal{G}^{\pm}(\epsilon) \quad , \tag{4.7}$$

where Tr denotes the trace of an operator and $n(\epsilon)$ is the density of states.

4.2 The Dyson equation

Suppose $\mathcal{H}$ is given in terms of an unperturbed Hamiltonian $\mathcal{H}_0$ and a (Hermitian) perturbation $\mathcal{V}$,

$$\mathcal{H} = \mathcal{H}_0 + \mathcal{V} \quad . \tag{4.8}$$

The resolvents of $\mathcal{H}$ and $\mathcal{H}_0$

$$\mathcal{G}(z) = (z\mathcal{I}-\mathcal{H})^{-1} \quad , \quad \mathcal{G}_0(z) = (z\mathcal{I}-\mathcal{H}_0)^{-1} \quad , \tag{4.9}$$

are then coupled in terms of a Dyson equation,

$$\mathcal{G}(z) = \mathcal{G}_0(z) + \mathcal{G}(z)\,\mathcal{V}\mathcal{G}_0(z) = \mathcal{G}_0(z) + \mathcal{G}_0(z)\,\mathcal{V}\mathcal{G}(z) \quad , \tag{4.10}$$

which can be reformulated as

$$\mathcal{G}(z) = \mathcal{G}_0(z) + \mathcal{G}_0(z)\,(\mathcal{V} + \mathcal{V}\mathcal{G}_0(z)\,\mathcal{V} + \ldots)\,\mathcal{G}_0(z) \quad . \tag{4.11}$$

The so-called *T-operator* is then defined as

$$\mathcal{T}(z) = \mathcal{V} + \mathcal{V}\mathcal{G}_0(z)\,\mathcal{V} + \mathcal{V}\mathcal{G}_0(z)\,\mathcal{V}\mathcal{G}_0(z)\,\mathcal{V} + \ldots \quad , \tag{4.12}$$

such that

$$\mathcal{G}(z) = \mathcal{G}_0(z) + \mathcal{G}_0(z)\,\mathcal{T}(z)\,\mathcal{G}_0(z) \quad , \tag{4.13}$$

or, alternatively, as

$$\mathcal{T}(z) = \mathcal{V} + \mathcal{V}\mathcal{G}_0(z)\,\mathcal{T}(z) = \mathcal{V} + \mathcal{T}(z)\,\mathcal{G}_0(z)\,\mathcal{V} \quad . \tag{4.14}$$

Since $\mathcal{V}$ is assumed to be Hermitian, the T-operator satisfies the relation,

$$\mathcal{T}(z^*) = \mathcal{T}(z)^{\dagger} \quad , \tag{4.15}$$

and, in particular, for the side-limits the below property applies:

$$\mathcal{T}^{+}(\varepsilon)^{\dagger} = \mathcal{T}^{-}(\varepsilon) \quad . \tag{4.16}$$

4.3 Scaling transformations

Clearly enough, by introducing a "scaling potential" $\mathcal{W}$, the Hamilton operator $\mathcal{H}$ in Eq. (4.8) can be rewritten as

$$\mathcal{H} = \mathcal{H}_0 + \mathcal{V} \equiv \mathcal{H}_0 + \mathcal{V} + \mathcal{W} - \mathcal{W} \equiv \mathcal{H}_0' + \mathcal{V}' \quad , \tag{4.17}$$

where

$$\mathcal{H}_0' = \mathcal{H}_0 - \mathcal{W} \quad , \quad \mathcal{V}' = \mathcal{V} + \mathcal{W} \quad . \tag{4.18}$$

From the resolvent of $\mathcal{H}_0'$,

$$\mathcal{G}_0'(z) = (z - \mathcal{H}_0')^{-1} = (z - \mathcal{H}_0 + \mathcal{W})^{-1} \quad , \tag{4.19}$$

written below in terms of a Dyson equation,

$$\mathcal{G}_0'(z) = \mathcal{G}_0(z)[1 - \mathcal{W}\mathcal{G}_0'(z)] \quad , \tag{4.20}$$

then follows directly that the Dyson equation for $\mathcal{G}(z)$ can be expressed either in terms of $\mathcal{G}_0(z)$ or $\mathcal{G}_0'(z)$,

$$\mathcal{G}(z) = \mathcal{G}_0(z)[1 + \mathcal{V}\mathcal{G}(z)] = \mathcal{G}_0'(z)[1 + \mathcal{V}'\mathcal{G}(z)] \quad . \tag{4.21}$$

4.4 Integrated density of states

Rewriting Eq. (4.7) in terms of Eq. (4.13) yields

$$n(\varepsilon) = -\frac{1}{\pi}\mathrm{ImTr}\left(\mathcal{G}_0^+(\varepsilon) + \mathcal{G}_0^+(\varepsilon)\,\mathcal{T}^+(\varepsilon)\,\mathcal{G}_0^+(\varepsilon)\right) \tag{4.22}$$

$$= n_0(\varepsilon) + \delta n(\varepsilon) \quad , \tag{4.23}$$

where

$$n_0(\varepsilon) = -\frac{1}{\pi}\mathrm{ImTr}\left(\mathcal{G}_0^+(\varepsilon)\right) \quad , \tag{4.24}$$

$$\delta n(\varepsilon) = -\frac{1}{\pi}\mathrm{ImTr}\left(\mathcal{G}_0^+(\varepsilon)\,\mathcal{T}^+(\varepsilon)\,\mathcal{G}_0^+(\varepsilon)\right) \tag{4.25}$$

$$= -\frac{1}{\pi}\mathrm{ImTr}\left(\mathcal{G}_0^+(\varepsilon)^2\,\mathcal{T}^+(\varepsilon)\right) \tag{4.26}$$

$$= \frac{1}{\pi}\mathrm{ImTr}\left(\frac{d\mathcal{G}_0^+(\varepsilon)}{d\varepsilon}\mathcal{T}^+(\varepsilon)\right) \quad , \tag{4.27}$$

and use was made of the following identity

$$\frac{d\mathcal{G}(z)}{dz} = -\mathcal{G}(z)^2 \quad . \tag{4.28}$$

Furthermore, it can be shown that

$$\frac{d\mathcal{T}(z)}{dz} = \mathcal{T}(z)\frac{d\mathcal{G}_0(z)}{dz}\mathcal{T}(z) \quad , \tag{4.29}$$

and therefore

$$\mathcal{T}(z)^{-1}\frac{d\mathcal{T}(z)}{dz} = \frac{d\mathcal{G}_0(z)}{dz}\mathcal{T}(z) \quad , \tag{4.30}$$

which substituted into Eq. (4.27) yields

$$\delta n(\varepsilon) = \frac{1}{\pi}\mathrm{ImTr}\left(\mathcal{T}^+(\varepsilon)^{-1}\frac{d\mathcal{T}^+(\varepsilon)}{d\varepsilon}\right) \tag{4.31}$$

$$= \frac{d}{d\varepsilon}\left(\frac{1}{\pi}\mathrm{ImTr}\,\ln\mathcal{T}^+(\varepsilon)\right) \quad . \tag{4.32}$$

The integrated DOS,

$$N(\varepsilon) = \int_{-\infty}^{\varepsilon} d\varepsilon'\, n(\varepsilon') \quad , \tag{4.33}$$

can then be directly expressed as

$$N(\varepsilon) = N_0(\varepsilon) + \delta N(\varepsilon) \quad , \tag{4.34}$$

where

$$N_0(\varepsilon) = \int_{-\infty}^{\varepsilon} d\varepsilon'\, n_0(\varepsilon') \quad , \tag{4.35}$$

and

$$\delta N(\varepsilon) = \frac{1}{\pi}\mathrm{ImTr}\,\ln\mathcal{T}^+(\varepsilon) \quad , \tag{4.36}$$

or, in terms of Eq. (4.12) as

$$\delta N(\varepsilon) = -\frac{1}{\pi}\mathrm{ImTr}\,\ln\left(I - \mathcal{G}_0^+(\varepsilon)\,\mathcal{V}\right) \quad . \tag{4.37}$$

The above expression is usually referred to as the *Lloyd formula* or *Lloyd's formula* [4]. Later on this expression will be of great help in formulating, e.g., exchange and Dzyaloshinskii-Moriya interactions as well as temperature dependent effects for magnetic anisotropy energies.

4.5 Superposition of individual potentials

In general for an ensemble of N scatterers, not necessarily confined to atoms, the Kohn-Sham Hamiltonian is given by an appropriate expression for the kinetic energy operator (K), which can be either non-relativistic or relativistic, and the effective single particle potential $V(\mathbf{r})$,

$$H(\mathbf{r}) = K + V(\mathbf{r}) \quad , \quad V(\mathbf{r}) = \langle \mathbf{r} | \, \mathcal{V} \, | \mathbf{r} \rangle \quad , \tag{4.38}$$

which in turn can be viewed as a sum of individual (effective) potentials measured from particular positions $\mathbf{R}_i$,

$$V(\mathbf{r}) = \sum_{n \, = \, 1}^{N} V_n(\mathbf{r}_n) \quad , \quad \mathbf{r}_n = \mathbf{r} - \mathbf{R}_n \quad , \tag{4.39}$$

such that the domains D_{V_n} of these potentials are disjoint in $\mathbb{R}^3$,

$$D_{V_n} \cap D_{V_m} = \delta_{nm} D_{V_n} \quad . \tag{4.40}$$

4.6 The scattering path operator

4.6.1 The single-site T-operator

If only a single potential, $\mathcal{V}_n$, is present the corresponding T-operator is termed *single-site T-operator*, and, in dropping for a moment the complex energy argument z, is usually denoted by t^n,

$$t^n = \mathcal{V}_n + \mathcal{V}_n \mathcal{G}_0 t^n = \left(\mathcal{I} - \mathcal{V}_n \mathcal{G}_0 \right)^{-1} \mathcal{V}_n \quad . \tag{4.41}$$

4.6.2 The multi-site T-operator

For an ensemble of N "scatterers" the T-operator,

$$\mathcal{T} = \sum_n \mathcal{V}_n + \sum_{n,m} \mathcal{V}_n \mathcal{G}_0 \mathcal{V}_m + \sum_{n,m,k} \mathcal{V}_n \mathcal{G}_0 \mathcal{V}_m \mathcal{G}_0 \mathcal{V}_k + \ldots \quad ; \quad n, m, k, .. \leq N \quad , \tag{4.42}$$

can be rewritten in terms of single-site T-operators, see Eq. (4.41),

$$\begin{aligned} \mathcal{T} = & \sum_n t^n + \sum_{n,m} t^n \mathcal{G}_0 \left(1 - \delta_{nm}\right) t^m + \sum_{n,m,k} t^n \mathcal{G}_0 \left(1 - \delta_{nm}\right) t^m \mathcal{G}_0 \left(1 - \delta_{mk}\right) t^k \\ & + \sum_{n,m,k,j} t^n \mathcal{G}_0 \left(1 - \delta_{nm}\right) t^m \mathcal{G}_0 \left(1 - \delta_{mk}\right) t^k \mathcal{G}_0 \left(1 - \delta_{kj}\right) t^j + \ldots \quad . \end{aligned} \tag{4.43}$$

4.6.3 The scattering path operator

A different kind of summation over sites for $\mathcal{T}$, namely in terms of the so-called *scattering path operators* (SPO),

$$\mathcal{T} = \sum_{nm} \tau^{nm} \quad , \tag{4.44}$$

$$\begin{aligned} \tau^{nm} = {} & t^n \delta_{nm} + t^n \mathcal{G}_0 \left(1 - \delta_{nm}\right) t^m + \sum_k t^n \mathcal{G}_0 \left(1 - \delta_{nk}\right) t^k \mathcal{G}_0 \left(1 - \delta_{km}\right) t^k \\ & + \sum_{k,j} t^n \mathcal{G}_0 \left(1 - \delta_{nk}\right) t^k \mathcal{G}_0 \left(1 - \delta_{kj}\right) t^j \mathcal{G}_0 \left(1 - \delta_{jm}\right) t^m + \ldots \quad , \end{aligned} \tag{4.45}$$

or, equivalently for $\mathcal{G}$,

$$\mathcal{G} = \mathcal{G}_0 + \sum_{n,m} \mathcal{G}_0 \tau^{nm} \mathcal{G}_0 \quad , \tag{4.46}$$

is in particular useful, since the following Dyson equation applies

$$\tau^{nm} = t^n \delta_{nm} + \sum_k t^n \mathcal{G}_0 \left(1 - \delta_{nk}\right) \tau^{km} \tag{4.47}$$

$$= t^n \delta_{nm} + \sum_k \tau^{nk} \mathcal{G}_0 \left(1 - \delta_{km}\right) t^m \quad . \tag{4.48}$$

4.7 Angular momentum and partial wave representations

In order to use the above discussed operator relations in practical terms angular momentum and partial wave representations need to be formed. Consider the following Hamiltonian in atomic Rydberg units: $m = 1/2,\ \hbar = 1,\ e^2 = 2,$ $c \sim 274.072$ (speed of light)

$$\begin{aligned} \mathcal{H}(\mathbf{r})\psi(\epsilon;\mathbf{r}) &= \left(\mathcal{H}_0\ (\mathbf{r}) + U(\mathbf{r})\right)\psi(\epsilon;\mathbf{r}) \\ &= W\psi(\epsilon;\mathbf{r}) \quad , \end{aligned} \tag{4.49}$$

$$\mathcal{H}_0 \ = \begin{cases} -\nabla^2 & ;\ \text{non-relativistic} \\ \\ c\boldsymbol{\alpha}\cdot\mathbf{p} + \beta mc^2 & ;\ \text{relativistic} \end{cases} \quad , \tag{4.50}$$

where $\boldsymbol{\alpha} = (\alpha_x, \alpha_x, \alpha_x)$ and β are Dirac matrices, see Eqs. (2.23) - (2.25).

4.7.1 Solutions of $\mathcal{H}_0$

In the *non-relativistic case* partial waves with respect to a chosen origin $\mathbf{R}_n$, $\mathbf{r} = \mathbf{r}_n + \mathbf{R}_n$, are of the general form

$$f_L(z;\mathbf{r}_n) = f_\ell(zr_n)Y_L(\hat{\mathbf{r}}_n) \quad , \tag{4.51}$$

$$W = \epsilon \quad , \quad p^2 = \epsilon \quad , \quad \mathrm{Im}\, p > 0 \quad , \quad f_\ell(zr_n) = \begin{cases} j_\ell(zr_{n)} \\ n_\ell(zr_{n)} \\ h_\ell^{\pm}(zr) \end{cases} \quad , \tag{4.52}$$

where $j_\ell(pr_{n)}, n_\ell(pr_{n)}$ and $h_\ell^{\pm}(pr_n) = n_\ell(pr_{n)} \pm i j_\ell(pr_{n)}$ are in turn spherical Bessel, Neumann and Hankel functions, the $Y_L(\hat{\mathbf{r}}_n)$ denote (complex) spherical harmonics, $\ell = 0, 1, 2, \ldots,\ m = 0, \pm 1, \pm 2, \ldots$, and

$$L = \ell(\ell+1) + m + 1 \tag{4.53}$$

is a collective index for ℓ and m. At $r_n \to 0$ the Bessel functions are so-called regular functions, while the Neumann functions are irregular.

By using L, see Eq. (4.53), as a counting index the following compact vector notation for partial waves can be introduced

$$\mathsf{f}(z;\mathbf{r}_n) = (\, f_1(z;\mathbf{r}_n),\, f_2(z;\mathbf{r}_n), \ldots) \quad , \quad \mathsf{f}(z;\mathbf{r}_n)^{\times} = \begin{pmatrix} f_1(z;\mathbf{r}_n)^{\times} \\ f_2(z;\mathbf{r}_n)^{\times} \\ \vdots \end{pmatrix} \quad , \tag{4.54}$$

in terms of which the configuration space representation of $\mathcal{G}_0\,(z)$, see Eq. (4.9), can now be written as

$$\begin{aligned} G_0\,(z;\mathbf{r}_n + \mathbf{R}_n, \mathbf{r}'_m + \mathbf{R}_m) = & \\ (1-\delta_{nm})\, \mathsf{j}\,(z;\mathbf{r}_n)\, \underline{G}_0^{nm}\,(z)\, \mathsf{j}\,(z;\mathbf{r}'_m)^{\times} & \\ - ip\delta_{nm} \Big\{ \mathsf{j}\,(z;\mathbf{r}_n)\, \mathsf{h}^{+}\,(z;\mathbf{r}'_n)^{\times}\, \Theta\,(r'_n - r_n) & \\ + \mathsf{h}^{+}\,(z;\mathbf{r}_n)\, \mathsf{j}\,(z;\mathbf{r}'_n)^{\times}\, \Theta\,(r_n - r'_n) \Big\} \quad , & \end{aligned} \tag{4.55}$$

where $\Theta\,(x)$ denotes a Heavyside step-function and $\underline{G}_0^{nm}\,(z) = \{G_{0,LL'}^{nm}\,(z)\}$ is the so-called *structure constants matrix*,

$$G_{0,LL'}^{nm}\,(z) = -4\pi i\, p \sum_{L''} i^{\ell-\ell'-\ell''}\, h_{L''}^{+}(z;\mathbf{R}_{nm})\, C_{LL''}^{L'} \quad . \tag{4.56}$$

In Eq. (4.56) $\mathbf{R}_{nm}$ denotes the difference vector between sites (origins) $\mathbf{R}_m$ and $\mathbf{R}_n$,

$$\mathbf{R}_{nm} = \mathbf{R}_m - \mathbf{R}_n \quad , \tag{4.57}$$

and the $C_{LL'}^{L''}$ refer to the so-called Gaunt coefficients,

$$C_{LL'}^{L''} = \int d\hat{\mathbf{x}}\, Y_L(\hat{\mathbf{x}})^* Y_{L'}(\hat{\mathbf{x}})^* Y_{L''}(\hat{\mathbf{x}}) = \int d\hat{\mathbf{x}}\, Y_L(\hat{\mathbf{x}}) Y_{L'}(\hat{\mathbf{x}}) Y_{L''}(\hat{\mathbf{x}})^* \quad . \tag{4.58}$$

In the *relativistic case*

$$W^2 = c^2p^2 + m^2c^4 \quad , \quad \epsilon = W - mc^2 \quad , \tag{4.59}$$

by using the so-called *weak relativistic limit* ($p \ll mc$), which shall be applied throughout this book, namely $p^2 \approx \epsilon$, partial waves (with respect to $\mathbf{R}_n$) are of the form

$$f_Q(\epsilon;\mathbf{r}_n) = \begin{pmatrix} f_\ell(zr_n)\chi_Q(\hat{\mathbf{r}}_n) \\ \\ (iS_\kappa p/c) f_{\overline{\ell}}(zr_n)\chi_{\overline{Q}}(\hat{\mathbf{r}}_n) \end{pmatrix} \quad , \quad Q = (\kappa\mu) \quad , \quad \overline{Q} = (-\kappa\mu) \quad , \tag{4.60}$$

where the functions f_ℓ can be either spherical Bessel, Neumann or Hankel functions and the $\chi_{\kappa\mu}(\hat{\mathbf{r}}_n)$ refer to so-called spin spherical harmonics

$$\chi_Q(\hat{\mathbf{r}}_n) \equiv \chi_{\kappa\mu}(\hat{\mathbf{r}}_n) = \sum_{s=\pm 1/2} C(\ell,\kappa,\frac{1}{2}|\ \mu - s, s) Y_{\ell,\mu-s}(\hat{\mathbf{r}}_n)\Phi_s \quad . \tag{4.61}$$

In Eq. (4.61) the Φ_s denote the well-known spinor basis functions,

$$\Phi_{1/2} = \begin{pmatrix} 1 \\ 0 \end{pmatrix} \quad , \quad \Phi_{-1/2} = \begin{pmatrix} 1 \\ 0 \end{pmatrix} \quad , \tag{4.62}$$

the $C(\ell,\kappa,\frac{1}{2}|\ \mu - s, s)$ being the famous Clebsch-Gordan coefficients. The various relativistic quantum numbers in Eq. (4.60) are defined as follows

$$\kappa = \begin{cases} \ell \quad , & j = \ell - 1/2 \\ -\ell - 1 \, , & j = \ell + 1/2 \end{cases} \quad , \tag{4.63}$$

$$\mu \in \{-j,\ -j+1, \ldots,\ j-1,\ j\} \quad , \tag{4.64}$$

$$\overline{\ell} = \ell - S_\kappa \quad , \quad S_\kappa = \kappa/|\kappa| \quad . \tag{4.65}$$

By using now Q as a counting index again a compact vector notation for the partial waves,

$$f_Q(z;\mathbf{r}_n) = \left(f_\ell(zr_n)\chi_Q(\hat{\mathbf{r}}_n),\, (iS_\kappa p/c) f_{\overline{\ell}}(zr_n)\chi_{\overline{Q}}(\hat{\mathbf{r}}_n) \right) \quad , \tag{4.66}$$

can be introduced,

$$\mathsf{f}(z;\mathbf{r}_n) = (\, f_1(z;\mathbf{r}_n),\, f_2(z;\mathbf{r}_n), \ldots) \quad , \quad \mathsf{f}(z;\mathbf{r}_n)^\times = \begin{pmatrix} f_1(z;\mathbf{r}_n)^\times \\ f_2(z;\mathbf{r}_n)^\times \\ \vdots \end{pmatrix} \quad , \tag{4.67}$$

that in turn leads to the partial wave representation of $\mathcal{G}_0$ (in the weak relativistic limit, $\left(W + mc^2\right)/2mc^2 \sim 1$), which because of Eq. (4.66) is formally

a 2×2 matrix

$$G_0^D\left(z;\mathbf{r}_n+\mathbf{R}_n,\mathbf{r}'_m+\mathbf{R}_m\right)=\left(1-\delta_{nm}\right)\,\mathsf{j}\left(z;\mathbf{r}_n\right)\underline{G}_0^{D,nm}\left(z\right)\,\mathsf{j}\left(z;\mathbf{r}'_m\right)^{\times}$$
$$-ip\,\delta_{nm}\,\left\{\mathsf{h}^{+}\left(z;\mathbf{r}_n\right)\,\mathsf{j}\left(z;\mathbf{r}'_n\right)^{\times}\,\Theta\left(r_n-r'_n\right)\right.$$
$$\left.+\,\mathsf{j}\left(z;\mathbf{r}_n\right)\,\mathsf{h}^{+}\left(z;\mathbf{r}'_n\right)^{\times}\,\Theta\left(r'_n-r_n\right)\right\}\quad , \tag{4.68}$$

$$\underline{G}_0^{D,nm}\left(z\right)=\left\{G_{0,QQ'}^{D,nm}\left(z\right)\right\}\quad . \tag{4.69}$$

The matrix elements $G_{0,QQ'}^{D,nm}\left(z\right)$ are easily obtained from their non-relativistic counterparts in Eq. (4.56), since only a transformation in terms of Clebsch-Gordan coefficients is required

$$G_{o,QQ'}^{D,nm}\left(z\right)=\sum_{s=\pm 1/2}c\left(\ell j 1/2;\mu-s,s\right)G_{0,LL'}^{nm}\left(z\right)c\left(\ell' j' 1/2;\mu'-s,s\right)\quad , \tag{4.70}$$

$$Q=(\kappa\mu)\quad ,\quad Q'=(\kappa'\mu')\quad ,\quad L=\left(\ell,\mu-s\right),\quad ,\quad L'=\left(\ell',\mu'-s\right)\quad . \tag{4.71}$$

4.7.2 Solutions of $\mathcal{H}$

Going back to Eq. (4.49), in order to proceed first the operator $U(\mathbf{r})$ has to be specified and also possible requirements for $V(\mathbf{r})$ have to be stated. In principle again a non-relativistic or relativistic level can be chosen. Since the topic of this book is devoted to magnetic systems, the presence of an exchange field $\mathbf{B}(\mathbf{r})$ will automatically be assumed. In general $U(\mathbf{r})$ is of the form

$$U(\mathbf{r})=\sum_{n=1}^{N}\left\{V_n(\mathbf{r}_n)+\left\{\begin{array}{l}\boldsymbol{\sigma}\cdot\mathbf{B}_n(\mathbf{r}_n)\ \text{, non-relativistic spin-polarized}\\ \\ \beta\boldsymbol{\Sigma}\cdot\mathbf{B}_n(\mathbf{r}_n)\ \text{, relativistic spin-polarized}\end{array}\right\}\right.\quad , \tag{4.72}$$

$$D_{Vn}\cap D_{Vm}=\delta_{nm}D_{V_n}\quad ,\quad D_{B_n}\cap D_{Bm}=\delta_{nm}D_{B_n}\quad ,\quad \mathbf{r}_n{=}\,\mathbf{r}-\mathbf{R}_n\quad , \tag{4.73}$$

where as before $\boldsymbol{\sigma}$ refers to the vector consisting of Pauli spin matrices and $\boldsymbol{\Sigma}$ is the so-called spin operator

$$\boldsymbol{\Sigma}=(\Sigma_x,\Sigma_y,\Sigma_z)\quad ,\quad \Sigma_\nu=\begin{pmatrix}\sigma_\nu & 0\\ 0 & \sigma_\nu\end{pmatrix}\quad ,\quad \nu=x,y,z\quad . \tag{4.74}$$

As already mentioned in Sections (2.3.2) and (3.4.2) within Local Density Functional Theory (LDFT) the exchange field is provided only with respect to a fictitious z axis; i.e., in Eq. (4.72) *a priori* only terms $\sigma_z B_n(\mathbf{r}_n)$ or $\beta\Sigma_z B_n(\mathbf{r}_n)$ are available.

For the $V_n(\mathbf{r}_n)$ and $\mathbf{B}_n(\mathbf{r}_n)$ different levels of sophistication can be chosen. Suppose the domains D_{V_n} and D_{B_n}correspond to convex polyhedra D_n (regions in configuration space)

$$D_{V_n} = D_{B_n} = D_n \quad ,$$

then $V_n(\mathbf{r}_n)$ and $\mathbf{B}_n(\mathbf{r}_n)$ can be constructed such that

$$V_n(\mathbf{r}_n) = \begin{cases} V_n(\mathbf{r}_n) \ , & \mathbf{r}_n \in D_n \\ \\ 0 \quad , & \mathbf{r}_n \notin D_n \end{cases} \quad , \quad \mathbf{B}_n(\mathbf{r}_n) = \begin{cases} \mathbf{B}_n(\mathbf{r}_n) \ , & \mathbf{r}_n \in D_n \\ \\ 0 \quad , & \mathbf{r}_n \notin D_n \end{cases} \quad .$$

Furthermore, let r_{BS}^n and r_{MT}^n be the circumscribing ("bounding") and inscribed ("muffin tin") sphere, respectively. The potential and the exchange field can either reflect all directional and polarisational effects, or, for matters of computational simplicity, be presented in an approximate form:

$$V_n(\mathbf{r}_n) = \begin{cases} V_n(\mathbf{r}_n) \ \ |\mathbf{r}_n| = r_n \leq r_{BS}^n \ , \textit{ full potential} \\ \\ V_i(|\mathbf{r}_i|) \ |\mathbf{r}_i| = r_n \leq r_{MT}^n \ , \textit{ shape approximated potential} \end{cases} \tag{4.75}$$

$$\mathbf{B}_n(\mathbf{r}_n) = \begin{cases} \mathbf{B}_n(\mathbf{r}_n) \quad |\mathbf{r}_n| = r_n \leq r_{BS}^n \ \ , \textit{ full exchange field} \\ \\ \mathbf{B}_n(|\mathbf{r}_n|) \ |\mathbf{r}_n| = r_n \leq r_{MT}^n \ , \textit{ shape approximated exchange field.} \end{cases} \tag{4.76}$$

It should be noted that the shape approximated functions are in particular easy to deal with, since they are of spherical symmetry. Very often also a further (shape) approximation is applied, namely the so-called Atomic Sphere Approximation (ASA), in which r_{MT}^n is replaced by a radius r_{ASA}^n such that

$$\frac{4\pi}{3}(r_{ASA}^n)^3 = \Omega_n \quad , \tag{4.77}$$

where Ω_n is the volume of the corresponding polyhedron D_n.

In the non-relativistic case for a given $V_n(\mathbf{r}_n)$ and $\mathbf{B}_n(\mathbf{r}_n)$ the regular solutions of Eq. (4.49) are of the general form

$$\psi(z;\mathbf{r}_n) = \sum_L R_L^n((z;r_n)Y_L(\hat{\mathbf{r}}_n) \quad . \tag{4.78}$$

Traditionally instead of the radial amplitudes $\mathsf{R}^n(z;\mathbf{r}_n)$, see also the notation introduced in Eq. (4.54),

$$\mathsf{R}^n(z;\mathbf{r}_n) = \{R_1^n(z;\mathbf{r}_n), R_1^n(z;\mathbf{r}_n), \ldots\} \quad , \tag{4.79}$$

so-called *scattering solutions* are used

$$\mathsf{Z}^n(z;\mathbf{r}_n) = \begin{cases} \mathsf{R}^n(z;\mathbf{r}_n)\,\underline{t}^n(z)^{-1} & , \quad \mathbf{r}_n \in D_{V_n} \\ \\ \mathsf{j}(z;\mathbf{r}_n)\,\underline{t}^n(z)^{-1} - ip\,\mathsf{h}^+(z;\mathbf{r}_n) \ , & \mathbf{r}_n \notin D_{V_n} \end{cases} \tag{4.80}$$

$$\mathsf{Z}^n(z;\mathbf{r}_n) = \{Z_1^n(z;\mathbf{r}_n), Z_1^n(z;\mathbf{r}_n), \ldots\} \tag{4.81}$$

where $\underline{t}^n(\varepsilon)$ is the already mentioned single site t matrix,

$$\underline{t}^n(\varepsilon) \equiv \{t^n_{L'L}(\varepsilon)\} \quad . \tag{4.82}$$

The form of the single site t matrix arises by the way from switching the configuration space representation $t(z;\mathbf{r},\mathbf{r}')$ to a partial wave representation in terms of $\mathsf{j}(z;\mathbf{r}_n)$.

The irregular scattering solutions are usually normalized for $\mathbf{r}_n \notin D_{V_n}$ either as

$$\mathsf{H}^n(z;\mathbf{r}_n) = -ip\,\mathsf{h}^+(z;\mathbf{r}_n) \quad , \tag{4.83}$$

or

$$\mathsf{J}^n(z;\mathbf{r}_n) = \mathsf{j}(z;\mathbf{r}_n) \quad . \tag{4.84}$$

The above two types of irregular scattering functions are related to each other via

$$\mathsf{J}^n(z;\mathbf{r}_n) = \mathsf{R}^n(z;\mathbf{r}_n) - \mathsf{H}^n(z;\mathbf{r}_n)\,\underline{t}^n(z) \quad . \tag{4.85}$$

Relativistically the regular *scattering solutions* of $\mathcal{H}(\mathbf{r})$ in Eq. (4.49) are given by

$$\mathsf{Z}^n(z;\mathbf{r}_n) = \{Z^n_Q(z;\mathbf{r}_n)\} = (Z^n_1(z;\mathbf{r}_n), Z^n_2(z;\mathbf{r}_n), \ldots) \quad , \tag{4.86}$$

where

$$Z^n_Q(z;\mathbf{r}_n) = \sum_{Q'} \begin{cases} \begin{pmatrix} g^{Z,n}_{Q'Q}(z;r_n)\,\chi_{Q'}(\hat{\mathbf{r}}_n) \\ \\ if^{Z,n}_{Q'Q}(z;r_n)\,\chi_{\bar{Q}'}(\hat{\mathbf{r}}_n) \end{pmatrix} & , \quad \mathbf{r}_n \in D_{V_n} \\ \\ j_Q(z;\mathbf{r}_n)\,P^n_{Q'Q}(z) + pn_Q(z;\mathbf{r}_n) \, , & \mathbf{r}_n \notin D_{V_n} \end{cases} , \tag{4.87}$$

$$P^n_{QQ'}(z) = \left(t^n_{QQ'}(z)^{-1} - ip\delta_{QQ'}\right) \quad , \tag{4.88}$$

and where the radial amplitudes $g^{Z,n}_{Q'Q}(z;r_n)$ (*large component*) and $f^{Z,n}_{Q'Q}$ (*small components*) have to be normalized according to the solutions for $\mathbf{r}_n \notin D$, i.e.,

$$g^{Z,n}_{Q'Q}(z;r_n) = j_{\ell'}(pr_n)\,P^n_{Q'Q}(z) + pn_\ell(pr_n)\,\delta_{QQ'} \quad , \tag{4.89}$$

$$f^{Z,n}_{Q'Q}(z;r_n) = \frac{S_\kappa p}{c}\left(j_{\bar{\ell}'}(pr_n)\,P^n_{Q'Q}(\varepsilon) + pn_{\bar{\ell}}(pr_n)\,\delta_{QQ'}\right) \quad . \tag{4.90}$$

With these particular matching conditions, see Eqs. (4.60) and (4.87), the corresponding irregular solutions are simply given by

$$\mathsf{J}^n(z;\mathbf{r}_n) = \{J^n_Q(z;\mathbf{r}_n)\} = (J^n_1(z;\mathbf{r}_n), J^n_2(z;\mathbf{r}_n), \ldots) \quad . \tag{4.91}$$

4.8 Single particle Green's function

Finally, all that is needed now is to go back to the multiple scattering expansion in Eq. (4.46), repeated for convenience below,

$$\mathcal{G} = \mathcal{G}_0 + \sum_{n,m} \mathcal{G}_0 \tau^{nm} \mathcal{G}_0 \quad ,$$

form a configuration space representation and switch on the *rhs* that representation to the one corresponding to scattering solutions

$$\begin{aligned} G\left(z; \mathbf{r}_n + \mathbf{R}_n, \mathbf{r}'_m + \mathbf{R}_m\right) = & \; \mathsf{Z}^n\left(z; \mathbf{r}_n\right) \underline{\tau}^{nm}\left(z\right) \mathsf{Z}^m\left(z; \mathbf{r}'_m\right)^{\times} \\ & - \delta_{nm} \Big\{ \mathsf{J}^n\left(z; \mathbf{r}_n\right) \mathsf{Z}^n\left(z; \mathbf{r}'_n\right)^{\times} \Theta\left(r_n - r'_n\right) \\ & + \mathsf{Z}^n\left(z; \mathbf{r}_n\right) \mathsf{J}^n\left(z; \mathbf{r}'_n\right)^{\times} \Theta\left(r'_n - r_n\right) \Big\} \quad . \end{aligned} \tag{4.92}$$

Here $\Theta\left(r_n - r'_n\right)$ is a Heavyside step function and $\underline{\tau}^{nm}\left(z\right)$ follows directly from expressing Eq. (4.47), repeated for convenience below,

$$\tau^{nm} = t^n \delta_{nm} + \sum_k t^n \mathcal{G}_0 \left(1 - \delta_{nk}\right) \tau^{km}$$

in a partial wave representation in terms of $\mathsf{J}^n\left(z; \mathbf{r}_n\right)$,

$$\underline{\tau}^{nm}\left(z\right) = \delta_{nm} \underline{t}^n\left(z\right) + \sum_k \underline{t}^n\left(z\right) \underline{G}_0^{nk}\left(z\right) \left(1 - \delta_{nk}\right) \underline{\tau}^{km}\left(z\right) \quad , \tag{4.93}$$

$$\underline{\tau}^{nm}\left(z\right) = \left\{\tau^{nm}_{\Lambda\Lambda'}\left(z\right)\right\} \quad , \quad \underline{t}^n\left(z\right) = \left\{t^n_{\Lambda\Lambda'}\left(z\right)\right\} \quad ,$$

$$\underline{G}_0^{nm}\left(z\right) = \left\{G^{nm}_{0,\Lambda\Lambda'}\left(z\right)\right\} \quad . \tag{4.94}$$

It should be noted in particular that formally for the Green's function one and the same equation applies in a non-relativistic ($\Lambda = L$) and in a relativistic approach ($\Lambda = Q$), just as formally it does not matter whether full or shape truncated potentials and exchange fields are used.

Eq. (4.93) can be further compressed by using a supermatrix notation, since then the Dyson equation for the scattering path operators is simply given by

$$\tau\left(z\right) = \Big(\mathbf{t}\left(z\right)^{-1} - \mathbf{G}_0\left(z\right)\Big)^{-1} \quad , \tag{4.95}$$

where

$$\tau\left(z\right) = \left\{\underline{\tau}^{nm}\left(z\right)\right\} \quad , \quad \mathbf{t}\left(z\right) = \left\{\underline{t}^n\left(z\right) \delta_{nm}\right\} \quad ,$$

$$\mathbf{G}_0\left(z\right) = \left\{\underline{G}_0^{nm}\left(z\right) \left(1 - \delta_{nm}\right)\right\} \quad . \tag{4.96}$$

Alternatively, a similar expression can be found for $\mathbf{G}(\varepsilon)$, namely

$$\mathbf{G}(z) = \mathbf{G}_0(z)\left(\mathbf{I} - \mathbf{t}(\varepsilon)\,\mathbf{G}_0(z)\right)^{-1} \quad , \quad \mathbf{G}(\varepsilon) = \{\underline{G}^{nm}(z)\} \quad . \tag{4.97}$$

Eqs. (4.95) or (4.97) are very often called the *fundamental equations of Multiple Scattering Theory*.

4.9 Symmetry aspects

If the set of position vectors $\mathbf{R}_n$ in Eq. (4.39) that identify the position of scattering centers, $\mathbf{r} = \mathbf{r}_n + \mathbf{R}_n$, corresponds to a simple two-dimensional lattice $\mathcal{L}^{(2)}$ (no sublattices), see Section 3.6,

$$\mathbf{R}_n \equiv \mathbf{R}_{pn} = \mathbf{C}_p + \mathbf{R}_{n,\parallel} \quad , \quad \mathbf{C}_p = R_{n,z}\mathbf{z} \quad , \quad \mathbf{R}_{n,\parallel} \in \mathcal{L}^{(2)} \quad , \tag{4.98}$$

then it is implied that for a given "spanning vector" $\mathbf{C}_p$

$$\begin{aligned} t(z;\mathbf{r}_n + \mathbf{C}_p + \mathbf{R}_{n,\parallel}, \mathbf{r}'_n + \mathbf{C}_p + \mathbf{R}_{n,\parallel}) &= t^{pn}(z;\mathbf{r}_n,\mathbf{r}'_n) \\ &\equiv t^{p}(z;\mathbf{r}_n,\mathbf{r}'_n) \quad ,\forall \mathbf{R}_{n,\parallel} \in \mathcal{L}^{(2)} \quad , \end{aligned} \tag{4.99}$$

where the index n now simply defines the origin of $\mathcal{L}^{(2)}$.

Eq. (4.99) states explicitly that all single site t matrices in an atomic layer characterized by $\mathcal{L}^{(2)}$ and specified by a particular $\mathbf{C}_p$ are identical. Furthermore, by recalling that

$$\mathbf{C}_p + \mathbf{R}_{n,\parallel} - \mathbf{C}_q + \mathbf{R}_{m,\parallel} = \mathbf{C}_p - \mathbf{C}_q + \mathbf{R}_{n,\parallel} - \mathbf{R}_{m,\parallel} \quad , \quad \left(\mathbf{R}_{n,\parallel} - \mathbf{R}_{m,\parallel}\right) \in \mathcal{L}^{(2)} \quad ,$$

a so-called lattice Fourier transformation can be applied for the structure constants

$$\underline{G}^{pq}(\mathbf{k}_\parallel; z) = \sum_{\mathbf{R}_\parallel \in \mathcal{L}^{(2)}} \exp\left[i\mathbf{k}_\parallel \cdot \mathbf{R}_\parallel\right] \underline{G}(\mathbf{C}_p + \mathbf{R}_\parallel, \mathbf{C}_q; z) \quad , \quad p,q = 1,\ldots,n \quad , \tag{4.100}$$

where $\mathbf{k}_\parallel$ belongs to the Surface Brillouin zone corresponding to $\mathcal{L}^{(2)}$ and p and q number atomic layers. It should be noted that Eq. (4.100) is nothing but a $\mathbf{k}_\parallel$ projection of the structure constants with respect to the translational group corresponding to $\mathcal{L}^{(2)}$, which of course also applies to the scattering path operator

$$\underline{\tau}^{pq}\left(\mathbf{k}_\parallel, z\right) = \left[\underline{t}^{p}(z)^{-1}\,\delta_{pq} - \underline{G}^{pq}(\mathbf{k}_\parallel; z)\right]^{-1} \quad . \tag{4.101}$$

The so-called "resolution of identity", namely the sum over all $\mathbf{k}_\parallel$-like projections, is then usually expressed as an integral over the Surface Brillouin zone

belonging to $\mathcal{L}^{(2)}$,

$$\underline{\tau}^{pn,qm}(z) = \frac{1}{\Omega_{\rm SBZ}} \int\limits_{\rm SBZ} \exp\left[-i\mathbf{k}_\parallel \cdot (\mathbf{R}_{n,\parallel} - \mathbf{R}_{m,\parallel})\right] \underline{\tau}^{pq}\left(\mathbf{k}_\parallel, z\right) d\mathbf{k}_\parallel \quad . \quad (4.102)$$

4.10 Charge & magnetization densities

The details of how to evaluate t matrices, structure constants for different types of translational symmetry, k space integrations or contour integrations in the complex plane will not be treated here, just as the problem of solving the Poisson equation in order to perform self-consistent calculations is not dealt with. Readers interested in the corresponding numerical aspects are referred to the recent book by J. Zabloudil et al. [3].

It is probably rather well known that from the single-particle Green's function in Eq. (4.92) immediately densities-of-states $n(\varepsilon)$

$$n(\varepsilon) = \sum_{n=1}^{N} n^n(\varepsilon) \ , \ n^n(\varepsilon) = -\frac{2}{\pi} \, {\rm Im} \int\limits_{\Omega_n} d\mathbf{r} \, G^+(\varepsilon; \mathbf{r} + \mathbf{R}_n, \mathbf{r} + \mathbf{R}_n) \quad (4.103)$$

and charge ($\rho(\mathbf{r})$)- and magnetization ($m(\mathbf{r})$) densities can be calculated,

$$\rho(\mathbf{r}) = \sum_{n=1}^{N} \rho^n(\mathbf{r}_n) \ , \ \rho^n(\mathbf{r}_n) = -\frac{2}{\pi} {\rm Im} \int\limits_{\curvearrowright}^{E_F} dz \, G\left(z; \mathbf{r} + \mathbf{R}_n, \mathbf{r} + \mathbf{R}_n\right) \quad , \quad (4.104)$$

$$m(\mathbf{r}) = \sum_{n=1}^{N} m^n(\mathbf{r}) \, , \, m^n(\mathbf{r}) = -\frac{\mu_{\rm B}}{\pi} {\rm Im} \int\limits_{\curvearrowright}^{E_F} dz \, {\rm Tr} \, \left\{\beta \Sigma_z G\left(z; \mathbf{r}_n + \mathbf{R}, \mathbf{r} + \mathbf{R}_n\right)\right\} \quad . \quad (4.105)$$

In Eqs. (4.104) and (4.105) $\curvearrowright$ denotes an integration along a contour in the upper half of the complex plane starting in principle at $-\infty$, which is closed at the Fermi energy E_F. The factor two in these two equations applies only in the non-relativistic case (trivial spin degeneracy). The charge Q_n corresponding to Ω_n is then given by

$$Q_n = \int\limits_{\Omega_n} d\mathbf{r}_n \, \rho^n(\mathbf{r}_n) \quad , \quad (4.106)$$

the corresponding magnetic moment by

$$m_n = \int\limits_{\Omega_n} d\mathbf{r}_n \, m^n(\mathbf{r}_n) \quad . \quad (4.107)$$

The concept of a characteristic volume introduced in Sec. (2.2) now becomes very obvious, since Ω_n in Eqs. (4.106) and (4.107) not necessarily comprises a characteristic volume, and therefore Q_n and m_n not necessarily are "intrinsic" quantities!

4.11 Changing the orientation of the magnetization

It was said already several times that in using the local spin density functional the exchange fields are given only with respect to a fictitious z direction. Suppose $\underline{t}^n(z) \equiv \underline{t}^n_E(z)$, E denoting the identity rotation, is the single site t matrix in site $\mathbf{R}_n$ for the case that at this site the orientation of the magnetization points along $\widehat{\mathbf{z}}$. Furthermore, let $S \in \mathsf{O}(3)$ be a rotation, which transforms $\widehat{\mathbf{z}}$ into $S\,\widehat{\mathbf{z}}$. Recalling now that the basis functions of $t(z;\mathbf{r}_n,\mathbf{r}'_n)$ are of the form $f_\Lambda(z;\mathbf{r}_n)$, see Eqs. (4.51) and (4.60), it is easy to see that a transformation of the single-site t-operator by S simply implies a transformation of the basis,

$$\underline{t}^n_S(z) = \underline{D}^\dagger(S)\underline{t}^n(z)\underline{D}(S) \quad , \tag{4.108}$$

where $\underline{t}^n_S(z)$ refers to a single site t matrix with an orientation of the magnetization pointing along $S\,\widehat{\mathbf{z}}$, and $\underline{D}(S)$ contains blockwise the irreducible (projective irreducible representations in the case of spin spherical harmonics) representations [6] of S.

Clearly enough two-dimensional translational invariance then implies that

$$\underline{t}^{pi}_S(z) = \underline{t}^{p0}_S(z) \quad , \quad \forall i \in I(\mathcal{L}^{(2)}) \quad , \tag{4.109}$$

where $i = 0$ refers to the origin of $\mathcal{L}^{(2)}$.

In a similar manner the structure constants $\underline{G}^{ij}_0(z)$ in Eq. (4.93) can be transformed,

$$G_0(z;S(\mathbf{r}_i+\mathbf{R}_i),S(\mathbf{r}_j+\mathbf{R}_j)) = \mathsf{j}(z;S\mathbf{r}_i)\underline{G}_0(z;S(\mathbf{R}_j-\mathbf{R}_i))\mathsf{j}(z;S\mathbf{r}_j)^\times \quad , \tag{4.110}$$

since a transformation of the basis in Eq. (4.54) implies

$$\begin{aligned} &G_0(z;S\left(\mathbf{r}_i+\mathbf{R}_i\right),S\left(\mathbf{r}_j+\mathbf{R}_j\right)) = \\ &\quad \mathsf{j}(z;\mathbf{r}_i)\underline{D}(S)\underline{G}_0\left(z;S\left(\mathbf{R}_j-\mathbf{R}_i\right)\right)\underline{D}^\dagger(S)\mathsf{j}(z;\mathbf{r}_j)^\times \quad . \end{aligned} \tag{4.111}$$

In the presence of two-dimensional translational symmetry, the free Green's function is invariant under $\forall S \in \mathcal{G}^{(2)}$

$$G_0(z;S(\mathbf{r}_i+\mathbf{R}_i),S(\mathbf{r}_j+\mathbf{R}_j)) = G_0(z;\mathbf{r}_i+\mathbf{R}_i,\mathbf{r}_j+\mathbf{R}_j) \quad , \tag{4.112}$$

where $\mathcal{G}^{(2)}$ is the corresponding point group. Thus one immediately gets

$$\underline{G}_0\left(z;\mathbf{R}_j-\mathbf{R}_i\right)=\underline{D}(S)\underline{G}_0\left(z;S\left(\mathbf{R}_j-\mathbf{R}_i\right)\right)\underline{D}^{\dagger}(S) \quad , \tag{4.113}$$

a fact that can be used to evaluate efficiently Brillouin zone integrals; see Eq. (4.102).

4.12 Screening transformations

Going now back to Section (4.3) use shall be made of scaling transformations. Suppose $\mathcal{W}$ in Eq. (4.18) is a superposition of individual (non-overlapping) potentials,

$$W(\mathbf{r})=\sum_n \begin{cases} W_{\rm r}\ ;|\mathbf{r}_n|\le b \\ \\ 0 \quad ;\text{otherwise} \end{cases} \quad , \tag{4.114}$$

where $W_{\rm r}$ is a suitable constant, b denotes an appropriate radius such as, e.g., the respective inscribed (muffin-tin-) sphere radius r^n_{MT}.

If the single-site t matrices corresponding to $W_{\rm r}$ are denoted by $\underline{t}^{\rm r}(z)$, the respective Green's function matrix, $\mathbf{G}^{\rm r}(z)$,

$$\mathbf{G}^{\rm r}(z)=\{\underline{G}^{{\rm r},ij}(z)\} \quad , \quad \underline{G}^{{\rm r},ij}(z)=\{G^{{\rm r},ij}_{LL'}(z)\} \quad , \tag{4.115}$$

see in particular Eq. (4.97), is given by

$$\mathbf{G}^{\rm r}(z)=\mathbf{G}^0(z)\left[\mathbf{I}-\mathbf{t}^{\rm r}(\epsilon)\mathbf{G}^0(z)\right]^{-1} \ . \tag{4.116}$$

By introducing the following difference,

$$\mathbf{t}_\Delta(z)=\mathbf{t}(z)-\mathbf{t}^{\rm r}(z) \quad , \tag{4.117}$$

a scattering-path operator $\boldsymbol{\tau}_\Delta(z)$,

$$\boldsymbol{\tau}_\Delta(z)=\left[\mathbf{t}_\Delta(z)^{-1}-\mathbf{G}^{\rm r}(z)\right]^{-1} \quad , \tag{4.118}$$

can be defined such that $\mathbf{G}(z)$ can be expressed as

$$\begin{aligned}\mathbf{G}(z)&=\mathbf{G}^{\rm r}(z)+\mathbf{G}^{\rm r}(z)\boldsymbol{\tau}_\Delta(z)\mathbf{G}^{\rm r}(z)\\ &=\mathbf{t}_\Delta(z)^{-1}_\Delta\boldsymbol{\tau}(z)\mathbf{t}_\Delta(z)^{-1}-\mathbf{t}_\Delta(z)^{-1}\ ,\end{aligned} \tag{4.119}$$

and $\boldsymbol{\tau}(\epsilon)$ as

$$\boldsymbol{\tau}(\epsilon)=\mathbf{t}(z)\left[\mathbf{t}_\Delta(z)^{-1}_\Delta\boldsymbol{\tau}(z)\mathbf{t}_\Delta(z)^{-1}+\left(\mathbf{t}(z)^{-1}-\mathbf{t}_\Delta(z)^{-1}\right)\right]\mathbf{t}(z) \quad . \tag{4.120}$$

By choosing a suitable $W_{\rm r}$, Eq. (4.116) can be solved such that

$$\underline{G}^{\mathrm{r},ij}(z) \sim \underline{0} \qquad \text{for :} \qquad \forall \ |\mathbf{R}_i - \mathbf{R}_j| \geq \ d \quad , \tag{4.121}$$

where the distance d has to be viewed as the radius of a sphere that comprises only a few types of "neighboring" sites, such as, e.g., first- and second-nearest neighbors. The matrix $\underline{G}^{\mathrm{r},ij}(z)$ is usually called *screened structure constants*. Assuming for matters of simplicity a semi-infinite system with a simple two-dimensional lattice, then the matrix structure of $\underline{\tau}^{pq}\left(\mathbf{k}_{\parallel}, z\right)^{-1}$ is of tridiagonal form,

$$\begin{pmatrix} \square & \blacksquare & \blacksquare & 0 & 0 & 0 & 0 & 0 & 0 \\ 0 & \blacksquare & \blacksquare & \blacksquare & 0 & 0 & 0 & 0 & 0 \\ 0 & 0 & \blacksquare & \blacksquare & \blacksquare & 0 & 0 & 0 & 0 \\ 0 & 0 & 0 & \blacksquare & \blacksquare & \blacksquare & 0 & 0 & 0 \\ 0 & 0 & 0 & 0 & 0 & \blacksquare & \blacksquare & \blacksquare & 0 \\ 0 & 0 & 0 & 0 & 0 & 0 & \blacksquare & \blacksquare & \bigcirc \end{pmatrix} \tag{4.122}$$

where the so-called missing elements, shown above as an empty square and empty sphere, can be used for matching or continuation purposes [3, 5].

Quite clearly inverting a tri- or pentadiagonal matrix offers an enormous computational advantage. The Screened Korringa-Kohn-Rostoker Method, which is based on Eqs. (4.119) - (4.121), is in essence a so-called "Order N Method".

4.13 The embedded cluster method

Finally, use shall be made of the Dyson equation in Section (4.2). Suppose a semi-infinite system is two-dimensional translationally invariant, i.e., is a system in which the atomic positions $\mathbf{R}_m$ are defined by

$$\mathbf{R}_m = \mathbf{R}_{m,\parallel} + \mathbf{c}_p \quad , \quad \mathbf{R}_{m,\parallel} \in \mathcal{L}^{(2)} \quad , \mathbf{c}_p \notin \mathcal{L}^{(2)} \quad , \tag{4.123}$$

then the elements of the scattering path operator in Eq. (4.95) are given by

$$\underline{\tau}_{\mathrm{h}}^{mn}(z) \equiv \underline{\tau}_{\mathrm{h}}^{pm,qn}(z) = \frac{1}{\Omega_{\mathrm{SBZ}}} \int\limits_{\mathrm{SBZ}} e^{-i\mathbf{k}_{\parallel}\cdot(\mathbf{R}_{m,\parallel}-\mathbf{R}_{n,\parallel})} \underline{\tau}_{\mathrm{h}}^{pq}(\mathbf{k}_{\parallel}, z) d\mathbf{k}_{\parallel} \quad , \tag{4.124}$$

where an index h is augmented in order to indicate that this system serves as host for a collection of impurities.

Let $\mathcal{C}$ be a finite set of sites in this system occupied by either impurities or interacting host atoms, see Fig. 4.1,

$$\mathcal{C} = \{\mathbf{R}_n\} \quad , \tag{4.125}$$

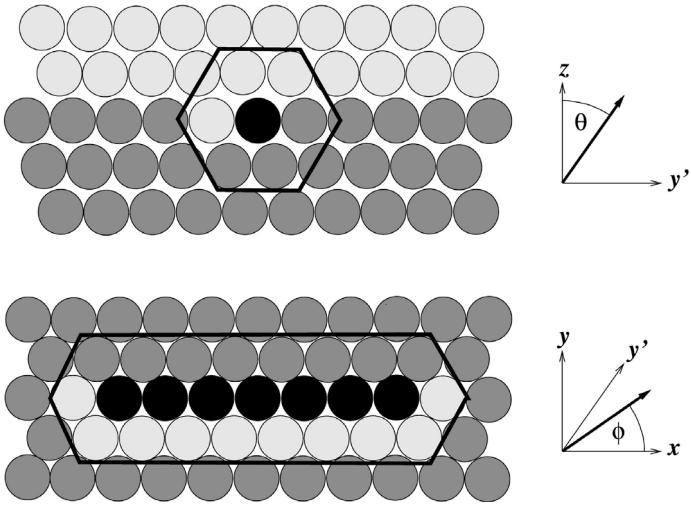

FIGURE 4.1: *Schematic view of the geometry of a seven–atom Co chain along a Pt(111) step edge. Full circles: Co atoms, shaded circles: Pt atoms, open circles: empty spheres. Top: side view, bottom: top view of the surface Pt layer with the Co chain. The embedded cluster is indicated by solid lines. The coordinate systems give reference to the azimuthal and polar angles, θ and ϕ, that characterize the orientation of the magnetization. From Ref. [7].*

such that

$$\underline{t}^n(\epsilon) = \begin{cases} \underline{t}^n(z) \; ; \mathbf{R}_n \in \mathcal{C} \\ \\ \underline{t}_{\rm h}(z) \; ; \mathbf{R}_n \notin \mathcal{C} \end{cases} \quad . \tag{4.126}$$

Furthermore, let $\mathbf{t}_{\rm h}(z)$ denote a diagonal (super-) matrix of single-site t-matrices in the case that only unperturbed host atoms *would* occupy $\mathcal{C}$

$$\mathbf{t}_{\rm h}(z) = \{\underline{t}^n(z)\delta_{nm} \;\; | \;\; \underline{t}^n(z) = \underline{t}_{\rm h}(z) \quad , \quad \forall \mathbf{R}_n \in \mathcal{C} \, \} \quad , \tag{4.127}$$

and let $\mathbf{t}_{\mathcal{C}}(\epsilon)$ be such a matrix referring to the actual occupation of the various sites in $\mathcal{C}$

$$\mathbf{t}_{\mathcal{C}}(z) = \{\underline{t}^n(z)\delta_{nm} \;\; | \;\; \underline{t}^n(z) \neq \underline{t}_{\rm h}(\epsilon) \quad , \quad \forall \mathbf{R}_n \in \mathcal{C} \, \} \quad , \tag{4.128}$$

then the scattering path operator $\boldsymbol{\tau}_{\mathcal{C}}(z)$ comprising all sites in $\mathcal{C}$ is given by the following Dyson like equation [8, 9],

$$\boldsymbol{\tau}_{\mathcal{C}}(z) = \boldsymbol{\tau}_{\rm h}(z) \left[1 - (\mathbf{t}_{\rm h}^{-1}(z) - \mathbf{t}_{\mathcal{C}}^{-1}(\epsilon)) \tau_{\rm h}(z) \right]^{-1} \quad , \tag{4.129}$$

from which in turn all corresponding local quantities, i.e., charge and magnetization densities, spin– and orbital moments, as well as total energies can be calculated.

If N denotes the number of sites in $\mathcal{C}$, then the dimension of the supermatrix $\boldsymbol{\tau}_{\mathcal{C}}(z)$ is N; the actual matrix size is therefore given by $2 \times N \times \ell_{\max}$, where $\ell_{\max}$ refers to the maximal ℓ quantum number used in the angular momentum representations and the factor two applies only in the case of a relativistic description.

[1] P. Weinberger, *Electron Scattering Theory for Ordered and Disordered Matter*, Clarendon Press, Oxford, 1990.

[2] A. Gonis, *Green Functions for Ordered and Disordered Systems*, North-Holland, 1992.

[3] J. Zabloudil, R. Hammerling, L. Szunyogh and P. Weinberger, *Electron Scattering in Solid Matter*, Springer Berlin Heidelber New York, 2005.

[4] P. Lloyd, Proc. Phys. Soc. London **90**, 207 (1967).

[5] I. Turek, V. Drchal, J. Kudrnovský, M. Šob and P. Weinberger, *Electronic Structure of Disordered Alloys, Surfaces and Interfaces,* Kluwer Academic Publishers, 1997.

[6] S.L. Altmann, *Rotations, Quaternions and Double Groups* (Clarendon Press, Oxford, England 1986).

[7] B. Újfalussy, B. Lazarovits, L. Szunyogh, G. M. Stocks, and P. Weinberger, Phys. Rev. B **70**, 100404(R) (2004).

[8] B. Lazarovits, L. Szunyogh, and P. Weinberger, Phys. Rev. B **65**, 104441 (2002).

[9] B. Lazarovits, L. Szunyogh, P. Weinberger, Phys. Rev. B **67**, 024415 (2003).

5

The coherent potential approximation

In this chapter concepts of how to deal with disorder in three- and two-dimensional translationally invariant systems are introduced. These concepts are of great importance in dealing theoretically with alloyed systems such as, for example, permalloy parts of a nano-system or interdiffusion effects at interfaces.

5.1 Configurational averages

Suppose a binary bulk alloy is of composition A_cB_{1-c} with $c_A = c$ being the concentration of species A and $c_B = (1-c)$ the concentration of species B. Assuming that there is no positional disorder and – for matters of simplicity – that $\mathcal{L}$ refers to a simple lattice and $I(\mathcal{L})$ denotes the set of indices i of $\mathcal{L}$, the potential can be written in the same manner as before, namely as

$$V(\mathbf{r}) = \sum_{i \in I(\mathcal{L})} V_i(\mathbf{r}_i) \quad , \tag{5.1}$$

$$V_i(\mathbf{r}_i) = \xi_i V_A(\mathbf{r}_i) + (1-\xi_i) V_B(\mathbf{r}_i) \quad , \tag{5.2}$$

where ξ_i is an occupational variable such that $\xi_i = 1$ if site $\mathbf{R}_i$ is occupied by species A and $\xi_i = 0$ if this site is occupied by species B. For a completely random alloy the probability for ξ_i being 1 is c_A and correspondingly for $\xi_i = 0$ the probability is c_B. In Eq. (5.2) $V_A(\mathbf{r}_i)$ and $V_B(\mathbf{r}_i)$ are the individual (effective) potentials of species A and B at the site $\mathbf{R}_i$, respectively. A particular arrangement of atoms A and B, $\{\xi_i \mid i \in I(\mathcal{L})\}$, on the positions of $\mathcal{L}$ is called a (occupational) *configuration*. Although for a particular configuration the eigenvalue equation for $\mathcal{H}(\{\xi_i\})$ corresponding to $V(\mathbf{r})$ can be solved, it is not possible to average such an equation over all configurations. The configurationally averaged (single particle) Green's function $\langle G^+(\mathbf{r}, \mathbf{r}', \epsilon)\rangle$, however, can be evaluated, since $G^+(\mathbf{r}, \mathbf{r}', \epsilon)$ is a so-called bilinear form.

If N denotes the total number of atoms in a binary bulk system A_cB_{1-c} and N_A and N_B the number of A and B atoms, respectively, $N = N_A + N_B$,

then*

$$N_A = cN \quad , \quad N_B = (1-c)\,N \quad . \tag{5.3}$$

5.2 Restricted ensemble averages

Suppose now that in all cells (domains D_{V_i} of $V_i(\mathbf{r}_i)$) but a particular one (i), an average over occupations is performed such that in the selected cell the occupation is kept fixed first with an A atom and then with a B atom, i.e., that the configurational average is partitioned into two *restricted ensemble averages*.

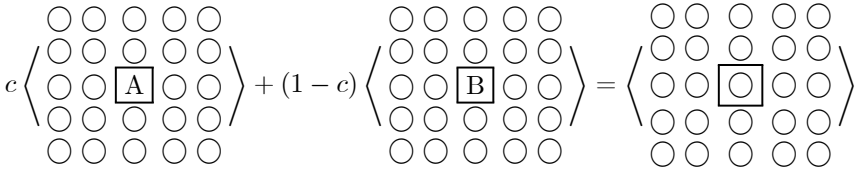

From this partitioning obviously a condition for the averaged Green's function can be generated, namely

$$c\left\langle G^{+}(\mathbf{r}_i,\mathbf{r}_i,\epsilon)\right\rangle_{(i=A)} + (1-c)\left\langle G^{+}(\mathbf{r}_i,\mathbf{r}_i,\epsilon)\right\rangle_{(i=B)} = \left\langle G^{+}(\mathbf{r}_i,\mathbf{r}_i,\epsilon)\right\rangle \quad , \tag{5.4}$$

$$(\mathbf{r}_i \in D_{V_i}) \quad , \quad \forall i \in I(\mathcal{L}) \quad .$$

Since the choice of this particular cell is irrelevant, i.e., since in a simple lattice D_{V_i} is nothing but the unit cell, it is sufficient to restrict Eq. (5.4) to the cell at the origin ($i = 0$) of $\mathcal{L}$.

5.3 The coherent potential approximation

Suppose that in the formal definition of the averaged resolvent $\langle\mathcal{G}(z)\rangle$

$$\langle\mathcal{G}(z)\rangle = \left\langle (z-\mathcal{H})^{-1}\right\rangle = [z-\mathcal{H}_0-\Sigma(z)]^{-1} \quad , \tag{5.5}$$

*Provided that the occupation probabilities for different sites are independent from each other ("statistical disorder").

$\mathcal{H}$ is rewritten as

$$\begin{aligned} \mathcal{H} = \mathcal{H}_0 + \mathcal{V} - \mathcal{W}(z) + \mathcal{W}(z) = \mathfrak{H}(z) + \mathcal{V} - \mathcal{W}(z) \quad , \\ \mathfrak{H}(z) = \mathcal{H}_0 + \mathcal{W}(z) \quad , \end{aligned} \tag{5.6}$$

where $\mathcal{V}$ is given by a superposition of (real) individual site potentials $\mathcal{V}_i$ and $\mathcal{W}(z)$ is a superposition of energy-dependent *translationally invariant* site quantities $\mathcal{W}_i(z)$

$$\mathcal{V} = \sum_i \mathcal{V}_i \quad , \quad \mathcal{W}(z) = \sum_i \mathcal{W}_i(z) \quad , \tag{5.7}$$

$$W(z; \mathbf{r}_i + \mathbf{R}_i + \mathbf{R}_j) = W(z; \mathbf{r}_j + \mathbf{R}_j) \quad , \quad \forall i, j \in I(\mathcal{L}) \quad , \tag{5.8}$$

$$\mathfrak{V}(z) = \sum_i \mathfrak{V}_i(z) = \sum_i (\mathcal{V}_i - \mathcal{W}_i(z)) \quad . \tag{5.9}$$

For a particular configuration $\mathcal{G}(z)$ is therefore given by

$$\mathcal{G}(z) = [z - \mathfrak{H}(z) - \mathfrak{V}(z)]^{-1} \quad . \tag{5.10}$$

Let $\mathfrak{G}(z)$ be the resolvent of $\mathfrak{H}(z)$,

$$\mathfrak{G}(z) = [z - \mathfrak{H}(z)]^{-1} \quad , \tag{5.11}$$

the resolvent $\mathcal{G}(z)$ and the corresponding $\mathcal{T}$ operator, $\mathcal{T}(z)$, are then given by the below Dyson equation,

$$\mathcal{G}(z) = \mathfrak{G}(z) + \mathfrak{G}(z)\,\mathcal{T}(z)\,\mathfrak{G}(z) \quad . \tag{5.12}$$

Since $\mathfrak{G}(z)$ is translationally invariant, see Eq. (5.8), i.e.,

$$\langle \mathfrak{G}(z) \rangle \equiv \mathfrak{G}(z) \quad , \tag{5.13}$$

averaging Eq. (5.9) over all configurations therefore yields

$$\begin{aligned} \langle \mathcal{G}(z) \rangle &= \mathfrak{G}(z) + \mathfrak{G}(z) \langle \mathcal{T}(z) \rangle \mathfrak{G}(z) \\ &\equiv [1 + \mathfrak{G}(z) \langle \mathcal{T}(z) \rangle] \mathfrak{G}(z) \quad . \end{aligned} \tag{5.14}$$

Finally, let $\langle \mathcal{T}(z; \mathcal{W}(z)) \rangle$ denote the averaged $\mathcal{T}$ operator for a particularly chosen medium $\mathcal{W}(z)$and let $\mathfrak{G}(z; \mathcal{W}(z))$ be the corresponding resolvent of $\mathfrak{H}(z) = \mathcal{H}_0 + \mathcal{W}(z)$. Then from Eq. (5.14) one can see immediately that

$$\langle \mathcal{G}(z) \rangle = \mathfrak{G}(z; \mathcal{W}(z)) \quad , \tag{5.15}$$

if and only if

$$\langle \mathcal{T}(z; \mathcal{W}(z)) \rangle = 0 \quad . \tag{5.16}$$

The condition in Eq. (5.16) is usually called the *Coherent Potential Approximation (CPA).*

5.4 The single site coherent potential approximation

From the multiple scattering expansion for the T operator, see Eq. (4.43), it can be seen that within the so-called single-site approximation (explicit exclusion of short-range-order effects) to the CPA condition the above condition is simply reduced to

$$\langle t_i(z; \mathcal{W}(z))\rangle = 0; \qquad \forall i \in I(\mathcal{L}) \quad , \tag{5.17}$$

or, in using the expansion of T in terms of scattering path operators, see Eq. (4.44),

$$\underline{\tau}^{ij}(z) = \underline{t}_i(z)\,\delta_{ij} + \sum_{k\neq i} \underline{t}_i(z)\,\underline{G}^{ik}(z)\,\underline{\tau}^{kj}(z) \quad , \tag{5.18}$$

by

$$\left\langle \underline{\tau}^{ii}(z; W(z))\right\rangle = 0 \quad ; \quad \forall i \in I(\mathcal{L}) \quad . \tag{5.19}$$

From the discussion of restricted averages and the relation of the site-diagonal scattering path operator to the Green's function $G(\mathbf{r}, \mathbf{r}', z)$ with $\mathbf{r}$ and $\mathbf{r}'$ measured from the same origin, it is clear that for a binary system A_cB_{1-c} (simple lattice, one atom per unit cell) the restricted averages $\left\langle \tau^{ii}(z)\right\rangle_{(i=\alpha)}$, $\alpha = A, B$, have to meet the condition

$$c\left\langle \underline{\tau}^{ii}(z)\right\rangle_{(i=A)} + (1-c)\left\langle \underline{\tau}^{ii}(z)\right\rangle_{(i=B)} = \left\langle \underline{\tau}^{ii}(z)\right\rangle \quad ; \quad \forall i \in I(\mathcal{L}) \quad . \tag{5.20}$$

It is therefore sufficient to restrict Eq. (5.20), for example, to $i = 0$, i.e., to the origin of the underlying lattice $\mathcal{L}$. Since Eq. (5.20) can only be solved iteratively, let $\mathbf{t}_c(z)$ be a guess for the single site t matrix for the coherent lattice $\mathcal{L}$:

$$\underline{t}_i(z) = \underline{t}_c(z) \quad ; \quad \forall i \in I(\mathcal{L}) \quad . \tag{5.21}$$

Then the corresponding site-diagonal scattering path operator $\underline{\tau}_c^{00}(\epsilon)$ is given by

$$\underline{\tau}_c^{00}(z) = \Omega_{\mathrm{BZ}}^{-1} \int \left[\underline{t}_c^{-1}(\epsilon) - \underline{G}(\mathbf{k}, z)\right]^{-1} d\mathbf{k} \quad . \tag{5.22}$$

Suppose now that in the unit cell at the origin ($i = 0$) restricted ensemble averages are performed:

$$\left\langle \underline{\tau}_c^{00}(z)\right\rangle_{(0=\alpha)} \equiv \underline{\tau}_\alpha^{00}(z) \quad ; \quad \alpha = A, B \quad , \tag{5.23}$$

where

$$\underline{\tau}_\alpha^{00}(z) = \underline{D}_\alpha^{00}(z)\,\underline{\tau}_c^{00}(z) \quad , \tag{5.24}$$

and

$$\underline{D}_\alpha^{00}(z) = \left[\underline{1} + \underline{\tau}_c^{00}(z)\left(\underline{t}_\alpha^{-1}(z) - \underline{t}_c^{-1}(z)\right)\right]^{-1} \quad . \tag{5.25}$$

Then in the single-site approximation the CPA condition is given by

$$c\underline{\tau}_A^{00}(z) + (1-c)\,\underline{\tau}_B^{00}(z) = \underline{\tau}_c^{00}(z) \quad , \tag{5.26}$$

or,

$$c\underline{D}_A^{00}(\epsilon) + (1-c)\,\underline{D}_B^{00}(\epsilon) = \underline{1} \quad . \tag{5.27}$$

The matrix $\underline{D}_\alpha^{00}(\epsilon)$ is usually called *impurity matrix*, since it is derived from the case that a single impurity occupies a particular cell, namely the one in the origin of the lattice, in an otherwise perfect host. In Eq. (5.24) this host is the coherent lattice and the impurity an A or a B atom. For matters of completeness it shall be mentioned that also a so-called *double impurity* can be described, namely the case that cell i is occupied by species A (B) and cell j by B (A). The corresponding scattering operator is then given by

$$\left\langle \underline{\tau}_c^{ij}(z) \right\rangle_{(i=\alpha, j=\beta)} = \underline{D}_\alpha^{ii}(z)\,\underline{\tau}_c^{ij}(z)\,\widetilde{\underline{D}}_\beta^{jj}(z) \quad , \quad \alpha,\beta = A,B \quad , \tag{5.28}$$

where

$$\underline{D}_\alpha^{ii}(z) = \left[\underline{1} + \underline{\tau}_c^{ii}(z)\left(\underline{t}_\alpha^{-1}(z) - \underline{t}_c^{-1}(z)\right)\right]^{-1} \quad , \tag{5.29}$$

$$\widetilde{\underline{D}}_\alpha^{ii}(z) = \left[\underline{1} + \left(\underline{t}_\alpha^{-1}(z) - \underline{t}_c^{-1}(z)\right)\underline{\tau}_c^{ii}(z)\right]^{-1} \quad . \tag{5.30}$$

Double impurities have to be taken into account whenever physical properties are to be evaluated that are based on products of Green's functions, which is the case, e.g., of electric transport.

5.5 Complex lattices and layered systems

Dealing with (statistically) disordered complex lattices or layered systems is in principle very similar to the description for the single site CPA condition discussed above, if a supermatrix notation is adopted. Suppose P denotes a double index with the following meaning

$$P = ps \quad ,$$

$$p = \begin{cases} \text{unit cells, complex } \mathcal{L}^{(3)} \\ \text{atomic layers, simple } \mathcal{L}^{(2)} \end{cases} \quad ,$$

$$s = \begin{cases} \text{inequivalent position in unit cell } p \\ \text{particular site in layer } p \end{cases}$$

The inverse single site t matrices can now be arranged in terms of a diagonal supermatrix,

$$\mathbf{t}_\alpha(z)^{-1} = \begin{pmatrix} \ddots & 0 & 0 & 0 & 0 \\ 0 & \underline{t}_\alpha^P(z)^{-1} & 0 & 0 & 0 \\ 0 & 0 & \underline{t}_\alpha^Q(z)^{-1} & 0 & 0 \\ 0 & 0 & 0 & \underline{t}_\alpha^R(z)^{-1} & \\ 0 & 0 & 0 & 0 & \ddots \end{pmatrix} \quad , \quad \alpha = A, B, c \quad , \tag{5.31}$$

where because of translational symmetry

$$\underline{t}_\alpha^P(z)^{-1} \equiv \underline{t}_\alpha^{PP}(z)^{-1} = \begin{cases} \underline{t}_\alpha^{ps,ps}(z)^{-1} \equiv \underline{t}_\alpha^{0s}(z)^{-1} \equiv \underline{t}_\alpha^{s}(z)^{-1} & , \text{ complex } \mathcal{L}^{(3)} \\ \underline{t}_\alpha^{ps,ps}(z)^{-1} \equiv \underline{t}_\alpha^{p0}(z)^{-1} \equiv \underline{t}_\alpha^{p}(z)^{-1} & , \text{ simple } \mathcal{L}^{(2)} \end{cases} \tag{5.32}$$

and A, B and c refer in turn to the constituents A and B and "coherent".

In a similar way the impurity matrices form a diagonal supermatrix,

$$\mathbf{D}_\alpha(z) = \begin{pmatrix} \ddots & 0 & 0 & 0 & 0 \\ 0 & \underline{D}_\alpha^{PP}(z) & 0 & 0 & 0 \\ 0 & 0 & \underline{D}_\alpha^{QQ}(z) & 0 & 0 \\ 0 & 0 & 0 & \underline{D}_\alpha^{RR}(z) & \\ 0 & 0 & 0 & 0 & \ddots \end{pmatrix} \quad , \quad \alpha = A, B \quad , \tag{5.33}$$

with

$$\underline{D}_\alpha^{PP}(z) \equiv \underline{D}_\alpha^{P}(z) \equiv \underline{D}_\alpha^{0s}(z) = \left[\underline{1} - \underline{\tau}_c^{0s,0s}(z)(t_c^s(z)^{-1} - t_\alpha^s(z)^{-1}\right] \tag{5.34}$$

in the complex lattice case and

$$\underline{D}_\alpha^{PP}(z) \equiv \underline{D}_\alpha^{P}(z) \equiv \underline{D}_\alpha^{p0}(z) = \left[\underline{1} - \underline{\tau}_c^{p0,p0}(z)(t_c^p(z)^{-1} - t_\alpha^p(z)^{-1}\right] \tag{5.35}$$

in the case of a layered system characterized by a simple two-dimensional lattice.

The coherent scattering path operator, however, is a full supermatrix

$$\boldsymbol{\tau}_c(z) = \begin{pmatrix} \ddots & \vdots & \vdots & \vdots & \\ \cdots & \underline{\tau}_c^{PP}(z) & \underline{\tau}_c^{PQ}(z) & \underline{\tau}_c^{PR}(z) & \cdots \\ \cdots & \underline{\tau}_c^{QP}(z) & \underline{\tau}_c^{QQ}(z) & \underline{\tau}_c^{QR}(z) & \cdots \\ \cdots & \underline{\tau}_c^{RP}(z) & \underline{\tau}_c^{RQ}(z) & \underline{\tau}_c^{RR}(z) & \cdots \\ & \vdots & \vdots & \vdots & \ddots \end{pmatrix} \quad , \tag{5.36}$$

with elements

$$\underline{\tau}_c^{PQ}(z) = \begin{pmatrix} \ddots & \vdots & \vdots & \\ \cdots & \underline{\tau}_c^{ps,qs}(z) & \underline{\tau}_c^{ps,qs'}(z) & \cdots \\ \cdots & \underline{\tau}_c^{ps'qs}(z) & \underline{\tau}_c^{ps',qs'}(z) & \cdots \\ & \vdots & \vdots & \ddots \end{pmatrix} \quad , \tag{5.37}$$

that have to be evaluated using appropriate inverse lattice Fourier transformations; see e.g. Eq. (5.22). Finally by arranging the concentrations of A and B in a diagonal matrix, e.g.,

$$\mathbf{c}^{\alpha} = \begin{pmatrix} \ddots & 0 & 0 & 0 \\ 0 & c_P^{\alpha} & 0 & 0 \\ 0 & 0 & c_Q^{\alpha} & 0 \\ 0 & 0 & 0 & \ddots \end{pmatrix} \quad , \quad \alpha = A, B \quad , \tag{5.38}$$

one gets the following compact inhomogeneous (single site) CPA condition,

$$\underline{\tau}_c^{PP}(z) = \sum_{\alpha=A,B} c_P^{\alpha} \underline{D}_{\alpha}^{PP}(z) \quad , \tag{5.39}$$

which reads in the case of a complex $\mathcal{L}^{(3)}$ as

$$\underline{\tau}_c^{0s,0s}(z) = \sum_{\alpha=A,B} c_p^{\alpha} \underline{D}_{\alpha}^{0s}(z) \underline{\tau}_c^{0s,0s}(z) \quad , \tag{5.40}$$

$$s = 1, \ldots, N \text{ (number of sublattices)} \quad ,$$

and

$$\underline{\tau}_c^{p0,p0}(z) = \sum_{\alpha=A,B} c_p^{\alpha} \underline{D}_{\alpha}^{p0}(z) \underline{\tau}_c^{p0,p0}(z) \quad , \tag{5.41}$$

$$s = 1, \ldots, N \text{ (number of atomic layers)} \quad ,$$

for a layered system with a simple $\mathcal{L}^{(2)}$. This condition is now *inhomogeneous*, since a CPA condition has to be fulfilled simultaneously for all sublattices or atomic layers.

It should be noted that the formulations in this subsection were chosen such that more or less immediately the reader can guess how the case of a layered system with a complex two-dimensional lattice has to be treated. In particular Eq. (5.41) is of quite some importance, since in terms of that condition, e.g., interdiffusion of interfaces or 1d-nanosystems consisting of more than one type of a magnetic alloy, see Fig. 1.3, can be described theoretically even on a fully relativistic level.

Double impurities can now refer to different types of sites, namely in the case of a complex $\mathcal{L}^{(3)}$ they can occupy sites in different sublattices or different sites in one and the same sublattice:

$$\left\langle \underline{\tau}_c^{pi,qj}(z) \right\rangle_{(pi=\alpha,qj=\beta)} = \begin{cases} \underline{D}_\alpha^{0s}(z)\,\underline{\tau}_c^{pi,qj}(z)\,\widetilde{\underline{D}}_\beta^{0q}(z) & ,\forall i,j \\ \underline{D}_\alpha^{0s}(z)\,\underline{\tau}_c^{pi,qj}(z)\,\widetilde{\underline{D}}_\beta^{0s}(z) & ,i \neq j \end{cases} . \qquad (5.42)$$

In layered systems (simple $\mathcal{L}^{(2)}$) the two impurities can occur either in different atomic layers or in different sites of one and the same layer:

$$\left\langle \underline{\tau}_c^{pi,qj}(z) \right\rangle_{(pi=\alpha,qj=\beta)} = \begin{cases} \underline{D}_\alpha^{p0}(z)\,\underline{\tau}_c^{pi,qj}(z)\,\widetilde{\underline{D}}_\beta^{q0}(z) & ,\forall i,j \\ \underline{D}_\alpha^{p0}(z)\,\underline{\tau}_c^{pi,qj}(z)\,\widetilde{\underline{D}}_\beta^{p0}(z) & ,i \neq j \end{cases} . \qquad (5.43)$$

5.6 Remark with respect to systems nanostructured in two dimensions

It should be noted in particular that the CPA condition in Eq. (5.16) requires translational symmetry at least in one direction. If therefore averaging over configurations in solid systems nanostructured in two dimensions, see for example Fig. 1.4, is required for certain purposes, one actually has to evaluate first all possible configurations of the required cluster consisting of A and B atoms, embedded into the substrate. Only then an average over all configurations can be performed. Such a system can for example be present when co-evaporating species A and B onto a suitable substrate.

[1] P. Weinberger, *Electron Scattering Theory for Ordered and Disordered Matter*, Clarendon Press, Oxford, 1990.

[2] A. Gonis, *Green Functions for Ordered and Disordered Systems*, North-Holland, 1992.

[3] J. Zabloudil, R. Hammerling, L. Szunyogh and P. Weinberger, *Electron Scattering in Solid Matter*, Springer Berlin Heidelber New York, 2005.

6

Calculating magnetic anisotropy energies

In this chapter the theoretical concept of magnetic anisotropy energies is introduced. Furthermore, the so-called magnetic Force Theorem, which most frequently is applied to evaluate the difference in total energy between two magnetic configurations, is discussed making use of the stationary properties of the Density Functional Theory. Since the magnetic dipole-dipole interaction, responsible for the so-called shape anisotropy, is not contained in DFT a magnetostatic version thereof is given.

In principle the magnetic anisotropy energy is determined by two kinds of differences in energy, namely the difference in total energy, ΔE_{tot}, with respect to two given (uniform) directions $\mathbf{n}_1$ and $\mathbf{n}_2$ of the magnetization and the corresponding difference in the magnetic dipole-dipole interaction energy, ΔE_{dd},

$$\begin{aligned} E_a &= \Delta E_{tot} + \Delta E_{dd} \quad , \\ \Delta E_{tot} &= E_{tot}[\mathbf{n}_1] - E_{tot}[\mathbf{n}_2] \quad , \\ \Delta E_{dd} &= E_{dd}[\mathbf{n}_1] - E_{dd}[\mathbf{n}_2] \quad , \end{aligned} \tag{6.1}$$

since the latter one is not provided by the Density Functional Theory, and usually is expressed classically.

6.1 Total energies

For a given orientation $\mathbf{n}$ of the magnetization the total energy per cell Ω_i is the sum of the kinetic, the Coulomb, and of the exchange-correlation terms, see the detailed discussion in Chapter 22 of Ref. [1],

$$\begin{aligned} E_{tot}(i) = E_c(i) + E_v(i) - \frac{1}{2} \int\limits_{\Omega_i} d\mathbf{r}_i \, \rho(\mathbf{r}_i) \, \left(V^c(\mathbf{r}_i) + \frac{2Z_i}{|\mathbf{r}_i|} \right) \\ - \frac{1}{2} \, Z_i \, V^{inter}(i) + \int\limits_{\Omega_i} d\mathbf{r}_i \, \rho(\mathbf{r}_i) \left(\epsilon_{xc} \left[\rho(\mathbf{r}_i) \right] - V^{xc}(\mathbf{r}_i) \right) \quad . \end{aligned} \tag{6.2}$$

In here Z_i is the atomic number, $\rho(\mathbf{r}_i)$ the charge density,

$$E_c(i) = \sum_j \epsilon_j^c(i) \quad , \tag{6.3}$$

$$E_v(i) = \int_{\curvearrowright}^{E_F} n_i(z)\epsilon dz \quad , \tag{6.4}$$

$$V^c(\mathbf{r}_i) = -\frac{2Z_i}{|\mathbf{r}_i|} + 2\int \frac{\rho(\mathbf{r}_i')}{|\mathbf{r}_i - \mathbf{r}_i'|} d\mathbf{r}_i' \quad , \tag{6.5}$$

$$V^{inter}(i) = 2\sum_{\substack{j \\ j\neq i}} \left[\int_{\Omega_j} d\mathbf{r}_j' \, \frac{\rho(\mathbf{r}_j')}{|\mathbf{r}_j - \mathbf{r}_j'|} - \frac{Z_j}{|\mathbf{r}_j|} \right] \quad , \tag{6.6}$$

and $\varepsilon_{xc}[\rho(\mathbf{r}_i)]$ and $V^{xc}(\mathbf{r}_i)$ are determined by the choice of a particular local spin density functional. In Eqs. (6.3) - (6.6) the $\epsilon_j^c(i)$ denote the core one-electron energies corresponding to Ω_i, and $n_i(z)$ is the density of states. The starting point of the contour integral in Eq. (6.4) refers to the bottom of the valence energy regime E_b. The term $E_c(i)$ is usually called the core energy, $E_v(i)$ the band energy, $V^c(\mathbf{r}_i)$ is the Coulomb potential, and $V^{inter}(i)$ reflects the contribution of the intercell potential to the total energy.

If N denotes the number of cells Ω_i that constitute the characteristic volume $\bar{\Omega}$, then the total energy per $\bar{\Omega}$ is given by

$$E_{tot}(\mathbf{n}) = \sum_{i=1}^{N} E_{tot}(i) \quad , \tag{6.7}$$

i.e., depending on N the total energy with respect to $\bar{\Omega}$ can be very large indeed. Typically per cell Ω_i the total energy $E_{tot}(i)$ is of the order of 10^3 - 10^4 Ryd. Considering only 10 layers (two-dimensional translational symmetry) E_{tot} is at least of the order of 10^5 Ryd. The total energy of a domain wall (several hundred atomic layers) can be up to 10^7 Ryd. Since magnetic anisotropy energies are of the order of 10^{-7} to 10^{-4} Ryd it would be extremely unwise to evaluate such tiny quantities in terms of differences in total energies.

6.2 The magnetic force theorem

According to Eq. (6.2) the difference in total energies between orientations $\mathbf{n}_1$ and $\mathbf{n}_2$ in cell Ω_i is given explicitly as

$$\begin{aligned} E_{tot}[\mathbf{n}_2] - E_{tot}[\mathbf{n}_1] = & \underbrace{E_c[\mathbf{n}_2] - E_c[\mathbf{n}_1]}_{1} + \underbrace{E_v[\mathbf{n}_2] - E_v[\mathbf{n}_1]}_{2} \\ & \underbrace{- \frac{1}{2} \int\limits_{\Omega_i} d\mathbf{r}_i \, \{\rho(\mathbf{r}_i;[\mathbf{n}_2] - \rho(\mathbf{r}_i;[\mathbf{n}_1])\} \left(V^c(\mathbf{r}_i) + \frac{2Z_i}{|\mathbf{r}_i|} \right)}_{3} \\ & \underbrace{- \frac{1}{2} Z_i \, \left\{ V^{inter}(0;[\mathbf{n}_2]) - V^{inter}(0;[\mathbf{n}_1]) \right\}}_{4} \\ & \underbrace{+ \int\limits_{\Omega_i} d\mathbf{r}_i \, \rho(\mathbf{r}_i;[\mathbf{n}_2]) \left(\epsilon_{xc} \left[\rho(\mathbf{r}_i;[\mathbf{n}_2]) \right] - V^{xc}(\mathbf{r}_i;[\mathbf{n}_2]) \right.}_{5} \\ & \underbrace{- \int\limits_{\Omega_i} d\mathbf{r}_i \, \rho(\mathbf{r}_i;[\mathbf{n}_1]) \left(\epsilon_{xc} \left[\rho(\mathbf{r}_i;[\mathbf{n}_1]) \right] - V^{xc}(\mathbf{r}_i;[\mathbf{n}_1]) \right.}_{6} \quad . \end{aligned} \tag{6.8}$$

Suppose now that the densities for these two different orientations of the exchange field are defined in the neighborhood of some density $\rho[\mathbf{r}_i]$, e.g., $\rho[\mathbf{r}_i;\mathbf{n}_1]$,

$$\rho[\mathbf{r}_i;\mathbf{n}_1] = \rho[\mathbf{r}_i] + \delta\rho[\mathbf{r}_i;\mathbf{n}_1] \quad , \tag{6.9}$$

$$\rho[\mathbf{r}_i;\mathbf{n}_2] = \rho[\mathbf{r}_i] + \delta\rho[\mathbf{r}_i;\mathbf{n}_2] \quad , \tag{6.10}$$

$$\rho[r;\mathbf{n}_2] - \rho[r;\mathbf{n}_1] = \delta\rho[r;\mathbf{n}_2] - \delta\rho[r;\mathbf{n}_1] \simeq 0 \quad , \tag{6.11}$$

then obviously the third and the fourth term in Eq.(6.8) vanish nearly exactly. The last two terms vanish indirectly, since

$$\epsilon_{xc} \left[\rho(\mathbf{r}_i;[\mathbf{n}_1]) \right] - V^{xc}(\mathbf{r}_i;[\mathbf{n}_1] \simeq \epsilon_{xc} \left[\rho(\mathbf{r}_i;[\mathbf{n}_2]) \right] - V^{xc}(\mathbf{r}_i;[\mathbf{n}_2] \quad . \tag{6.12}$$

Furthermore, since the difference in the sum over the eigenvalues of the core one-electron states does not matter – the Zeeman splitting for spherical symmetric potentials depends only on the magnitude of the magnetic field – one is left with a computationally easy expression, namely the difference in the

band energies,

$$E_{tot}[\mathbf{n}_2] - E_{tot}[\mathbf{n}_1] \simeq E_v[\mathbf{n}_2] - E_v[\mathbf{n}_1] = \sum_{i=1}^{N} \left(\int_{\curvearrowright}^{E_F(\mathbf{n}_2)} n_i(\mathbf{n}_2, z) z dz - \int_{\curvearrowright}^{E_F(\mathbf{n}_1)} n_i(\mathbf{n}_1, z) z dz \right) \quad , \tag{6.13}$$

since band energies differences are of the order of only a few mRyd. Furthermore, in the case of a semi-infinite metallic substrate the Fermi energy is determined by the substrate; i.e., Eq. (6.13) reduces to

$$E_{tot}[\mathbf{n}_2] - E_{tot}[\mathbf{n}_1] \simeq \sum_{i=1}^{N} \int_{\curvearrowright}^{E_F} \left(n_i(\mathbf{n}_2, z) - n_i(\mathbf{n}_1, z) \right) z dz \quad , \tag{6.14}$$

where, as should be recalled, N refers to the number of cells Ω_i that have to be considered. It should be noted that even in a bulk system the difference $E_F(\mathbf{n}_2) - E_F(\mathbf{n}_1)$ can safely be neglected. Relation (6.13) is usually termed *magnetic force theorem* [2]. Clearly, by keeping the particle density unchanged (restricted to one given reference orientation),

$$\rho[\mathbf{r}_i; \mathbf{n}_2] = \rho[\mathbf{r}_i; \mathbf{n}_1] + \delta\rho[\mathbf{r}_i; \mathbf{n}_2] \quad , \quad \delta\rho[\mathbf{r}_i; \mathbf{n}_2] = 0 \quad , \tag{6.15}$$

see Eq. (6.11), $E_{tot}[\mathbf{n}_2] - E_{tot}[\mathbf{n}_1]$ can be evaluated very efficiently. The error caused by using the magnetic force theorem is usually around 5% or even less.

6.3 Magnetic dipole-dipole interactions

6.3.1 No translational symmetry

If one partitions the configurational space into cells centered around atomic positions $\mathbf{R}_m$, then within the dipole approximation the relativistic current–current interaction energy is reduced to the magnetostatic dipole–dipole interaction energy, which can be expressed in atomic Rydberg units as

$$E_{dd} = \frac{1}{c^2} \sum_{\substack{\mathbf{R}_m, \mathbf{R}_n \\ (\mathbf{R}_m \neq \mathbf{R}_n)}} \left\{ \frac{\mathbf{m}_m \cdot \mathbf{m}_n}{|\mathbf{R}_m - \mathbf{R}_n|^3} - 3 \frac{[\mathbf{m}_m \cdot (\mathbf{R}_m - \mathbf{R}_n)][\mathbf{m}_n \cdot (\mathbf{R}_m - \mathbf{R}_n)]}{|\mathbf{R}_m - \mathbf{R}_n|^5} \right\} \quad , \tag{6.16}$$

where $\mathbf{m}_m$ is the magnetic moment at site $\mathbf{R}_m$; see (4.107).

6.3.2 Two-dimensional translational symmetry

In a ferromagnetic system the magnetic moments are aligned uniformly along a particular direction $\widehat{\mathbf{n}}$, i.e.

$$\mathbf{m}_{_m} = m_{_m}\ \widehat{\mathbf{n}} \quad .$$

If two–dimensional translational invariance applies, see also Eq. (4.99), which is the case for 1d-nanosystems, the location vectors $\mathbf{R}_m$ are defined by

$$\mathbf{R}_m = \mathbf{R}_{p\alpha} + \mathbf{R}_{m,\|} \quad , \quad \mathbf{R}_{p\alpha} = \mathbf{c}_p + \mathbf{a}_{\alpha,\|} \quad ,$$

$$\mathbf{R}_{m,\|} \in \mathcal{L}^{(2)} \quad , \quad \mathbf{c}_p \notin \mathcal{L}^{(2)} \quad , \quad \mathbf{a}_{\alpha,\|} \notin \mathcal{L}^{(2)} \quad ,$$

where $\mathbf{R}_{p\alpha}$ specifies a site in the unit cell of the system in layer p and sublattice α, generated by the non-primitive translation $\mathbf{a}_{\alpha,\|}$. Eq. (6.16) can then be rewritten [3] as

$$E_{dd} = \sum_{p\alpha,q\beta} \frac{m_{p\alpha} m_{q\beta}}{c^2}\ \widehat{\mathbf{n}}\ \underline{M}^{dd}_{p\alpha,q\beta}\ \widehat{\mathbf{n}}\ . \tag{6.17}$$

In Eq. (6.17) the so–called 2D (ferromagnetic) dipole–dipole Madelung constant matrix is defined by [3]

$$\underline{M}^{dd}_{p\alpha,q\beta} = \sum_{\substack{\mathbf{R}_{m,\|} \\ (\mathbf{R}_{m,\|} \neq 0)}} \frac{1}{|\mathbf{R}_{p\alpha} - \mathbf{R}_{q\beta} - \mathbf{R}_{m,\|}|^3} \times \left\{ I_3 - \frac{(\mathbf{R}_{p\alpha} - \mathbf{R}_{q\beta} - \mathbf{R}_{\|}) \bigotimes (\mathbf{R}_{p\alpha} - \mathbf{R}_{q\beta} - \mathbf{R}_{m,\|})}{|\mathbf{R}_{p\alpha} - \mathbf{R}_{q\beta} - \mathbf{R}_{m,\|}|^2} \right\} \quad , \tag{6.18}$$

where I_3 is a 3×3 unit matrix and $\bigotimes$ denotes a tensorial product of vectors and where for $\mathbf{R}_{p\alpha} = \mathbf{R}_{q\beta}$ the singular term corresponding to $\mathbf{R}_{\|} = 0$ is excluded from the summation.

Reformulating $\mathbf{R}_{p\alpha}$ in the following manner as

$$\mathbf{R}_{p\alpha} = (R_{p\alpha;\perp}, \mathbf{R}_{p\alpha;\|}) \quad , \tag{6.19}$$

the magnetostatic Poisson equation can be solved for $|R_{p\alpha;\perp} - R_{q\beta;\perp}| \neq 0$ in terms of a Fourier expansion that results into a fast convergent series

$$\underline{M}^{dd}_{p\alpha,q\beta} = -\frac{2\pi}{A} \sum_{\substack{G_{\|} \\ (G_{\|} \neq 0)}} \left|\mathbf{G}_{\|}\right| \exp\left(-\left|\mathbf{G}_{\|}\right| |\Delta R_{p\alpha,q\beta;\perp}|\right) \exp\left(i\, \mathbf{G}_{\|} \cdot (\Delta \mathbf{R}_{p\alpha,q\beta;\|})\right)$$

$$\times \begin{pmatrix} -(\mathbf{G}_{\|} \otimes \mathbf{G}_{\|}) / \left|\mathbf{G}_{\|}\right|^2 & -i\, \mathrm{sgn}\left(\Delta R_{p\alpha,q\beta;\perp}\right) \left(\mathbf{G}_{\|} \otimes 1\right) / \left|\mathbf{G}_{\|}\right| \\ -i\, \mathrm{sgn}\left(\Delta R_{p\alpha,q\beta;\perp}\right) 1 \otimes \mathbf{G}_{\|} / \left|\mathbf{G}_{\|}\right| & 1 \end{pmatrix} , \tag{6.20}$$

where A is the 2D unit cell area, $\mathbf{G}_{\parallel}$ is a two-dimensional reciprocal space vector and

$$\Delta R_{p\alpha,q\beta;\perp} = (R_{p\alpha;\perp} - R_{q\beta;\perp}) \quad , \quad \Delta \mathbf{R}_{p\alpha,q\beta;\parallel} = \left(\mathbf{R}_{p\alpha;\parallel} - \mathbf{R}_{q\beta;\parallel}\right) \quad . \tag{6.21}$$

It should be noted that the $\mathbf{G}_{\parallel} = 0$ component does not contribute to *off–plane* terms.

For the (001) and (111) surface orientations of simple cubic lattices (sc, bcc or fcc) Eq. (6.20) can be further reduced to

$$\underline{M}^{dd}_{pq} = M^{dd}_{pq} \begin{pmatrix} -\frac{1}{2} & 0 & 0 \\ 0 & -\frac{1}{2} & 0 \\ 0 & 0 & 1 \end{pmatrix} \quad , \tag{6.22}$$

where

$$M^{dd}_{pq} = -\frac{2\pi}{A} \sum_{\substack{G_{\parallel} \\ (G_{\parallel} \neq 0)}} |\mathbf{G}_{\parallel}| \exp\left(-|\mathbf{G}_{\parallel}| \; |R_{p;\perp} - R_{q;\perp}|\right) \cos\left(\mathbf{G}_{\parallel} \cdot (\mathbf{R}_{p;\parallel} - \mathbf{R}_{q;\parallel})\right) \quad . \tag{6.23}$$

In this special case, the 2D (ferromagnetic) dipole–dipole Madelung constants for $p = q$ can be evaluated by using a standard Ewald summation technique, namely

$$\begin{aligned} M^{dd}_{pp} = & \sum_{\substack{\mathbf{R}_{\parallel} \\ (\mathbf{R}_{\parallel} \neq 0)}} \left\{ \frac{\mathrm{erfc}\left(|\mathbf{R}_{\parallel}|/2\sigma\right)}{|\mathbf{R}_{\parallel}|^3} + \frac{\exp\left(-|\mathbf{R}_{\parallel}|^2/4\sigma^2\right)}{\sigma\sqrt{\pi}\,|\mathbf{R}_{\parallel}|^2} \right\} - \\ & - \frac{2\pi}{A} \sum_{\substack{\mathbf{G}_{\parallel} \\ (\mathbf{G}_{\parallel} \neq 0)}} \left\{ |\mathbf{G}_{\parallel}| \; \mathrm{erfc}\left(|\mathbf{G}_{\parallel}|\sigma\right) - \frac{1}{\sigma\sqrt{\pi}} \exp\left(-|\mathbf{G}_{\parallel}|^2\sigma^2\right) \right\} \\ & - \frac{1}{6\sigma^3\sqrt{\pi}} + \frac{2\sqrt{\pi}}{A\sigma} \quad , \end{aligned} \tag{6.24}$$

where σ is the well-known Ewald parameter and $\mathrm{erfc}(x) = 1 - \mathrm{erf}(x)$.

Finally, the orientational dependence of the magnetostatic dipole–dipole energy shall be discussed. By using polar coordinates for the unit vector $\widehat{\mathbf{n}}$, $\widehat{\mathbf{n}} = (\sin(\Theta)\cos(\phi), \sin(\Theta)\sin(\phi), \cos(\Theta))$, one immediately obtains that

$$\widehat{\mathbf{n}} \begin{pmatrix} -\frac{1}{2} & 0 & 0 \\ 0 & -\frac{1}{2} & 0 \\ 0 & 0 & 1 \end{pmatrix} \widehat{\mathbf{n}} = \frac{3}{2}\cos^2(\Theta) - \frac{1}{2} \quad , \tag{6.25}$$

which implies that the orientational dependence of the magnetostatic dipole–dipole anisotropy energy, ΔE_{dd}, can simply be written as [4]

$$\Delta E_{dd}(\Theta) = (E^{\parallel}_{dd} - E^{\perp}_{dd}) \sin^2(\Theta) \quad . \tag{6.26}$$

[1] J. Zabloudil. R. Hammerling, L. Szunyogh and P. Weinberger, *Electron Scattering Theory in Solid Matter*, Springer-Verlag, Berlin Heidelberg, 2005.

[2] H. J. Jansen, Phys. Rev. B **59**, 4699 (1999).

[3] L. Szunyogh, B. Újfalussy and P. Weinberger, Phys. Rev. **B51**, 9552 (1995).

[4] E. Tsymbal, J. Magn. Magn. Mater. **130**, L6 (1994).

7

Exchange & Dzyaloshinskii-Moriya interactions

In this chapter first and second order derivatives of the grand canonical potential (free energy at zero temperature) will be formed which in turn can be related to (a) anisotropy constants and (b) the famous Dzyaloshinskii-Moriya interactions appearing in classical spin Hamiltonians. The concepts introduced here are essential for discussing, for example, chirality aspects of magnetic nanostructured matter.

7.1 The free energy and its angular derivatives

In using the magnetic force theorem, see Section 6.2, the free–energy (grand potential) at zero temperature can be approximated by

$$\mathcal{F} = \int_{\curvearrowright}^{E_F} dz(z - E_F)n(z) = -\int_{\curvearrowright}^{E_F} dzN(z) \quad , \tag{7.1}$$

where $n(z)$ is the density of states (DOS) and $N(z)$ is the integrated DOS, $z = \epsilon + i\delta$, $\delta > 0$.

In terms of Lloyd's formula, see Eqs. (4.34) - (4.37) in Section 4.4, by discarding there the constant term $N_0(\epsilon)$, the free–energy can be rewritten as

$$\mathcal{F} = -\frac{1}{\pi} Im \int_{\curvearrowright}^{E_F} dz Tr \ln \boldsymbol{\tau}(z) \quad , \tag{7.2}$$

$$\boldsymbol{\tau}(z) = \left(\mathbf{t}^{-1}(z) - \mathbf{G}_0(z)\right)^{-1} \quad ,$$

where as before

$$\boldsymbol{\tau}(z) = \left\{\underline{\tau}_{ij}(z)\right\} \quad , \quad \mathbf{t}(z) = \left\{\underline{t}_i(z)\,\delta_{ij}\right\} \quad , \quad \mathbf{G}_0(z) = \left\{\underline{G}_{0,ij}(z)\,(1 - \delta_{ij})\right\} \quad .$$

7.1.1 First and second order derivatives of the inverse single site t matrices

In order to evaluate changes of $\mathcal{F}$ up to second order with respect to small deviations from the orientations of the magnetization at sites i and j relative to the (ferromagnetic) ground–state orientation (given with respect to a chosen uniform direction), one has to remember that according to Eq. (4.108) the orientational dependence of the single–site t matrix corresponds to a similarity transformation that rotates the z axis of the reference system (the artificial z axis inherent to LDFT),

$$\underline{t}_i(z)^{-1} \equiv \underline{m}_i(z) = R_i \, \underline{m}_i^0(z) \, R_i^+ \quad , \quad R_i \equiv R(\vartheta_i, \varphi_i) \quad . \tag{7.3}$$

Changes of $\underline{m}_i(z)$ up to second order in ϑ_i and φ_i,

$$\Delta\underline{m}_i^{(1)}(z) = \underline{m}_i^{\vartheta}(z) d\vartheta_i + \underline{m}_i^{\varphi}(z) d\varphi_i \quad , \tag{7.4}$$

$$\Delta\underline{m}_i^{(2)}(z) = \frac{1}{2}\underline{m}_i^{\vartheta\vartheta}(z) d\vartheta_i d\vartheta_i + \underline{m}_i^{\varphi\vartheta}(z) d\varphi_i d\vartheta_i + \frac{1}{2}\underline{m}_i^{\varphi\varphi}(z) d\varphi_i d\varphi_i \quad , \tag{7.5}$$

can therefore easily be expressed by means of the below derivatives of the rotation matrices R_i,

$$\underline{m}_i^{\vartheta}(z) \equiv \frac{\partial \underline{m}_i(z)}{\partial \vartheta_i} = \frac{\partial R_i}{\partial \vartheta_i}\underline{m}_i^0(z) R_i^+ + R_i \underline{m}_i^0(z) \frac{\partial R_i^+}{\partial \vartheta_i} \quad , \tag{7.6}$$

$$\underline{m}_i^{\varphi}(z) \equiv \frac{\partial \underline{m}_i(z)}{\partial \varphi_i} = \frac{\partial R_i}{\partial \varphi_i}\underline{m}_i^0(z) R_i^+ + R_i \underline{m}_i^0(z) \frac{\partial R_i^+}{\partial \varphi_i} \quad , \tag{7.7}$$

$$\underline{m}_i^{\vartheta\vartheta}(z) \equiv \frac{\partial^2 \underline{m}_i(z)}{\partial \vartheta_i \partial \vartheta_i} = \frac{\partial^2 R_i}{\partial \vartheta_i^2}\underline{m}_i^0(z) R_i^+ + R_i \underline{m}_i^0(z) \frac{\partial^2 R_i^+}{\partial \vartheta_i^2} + 2\frac{\partial R_i}{\partial \vartheta_i}\underline{m}_i^0(z) \frac{\partial R_i^+}{\partial \vartheta_i} \quad , \tag{7.8}$$

$$\underline{m}_i^{\varphi\vartheta}(z) \equiv \frac{\partial^2 \underline{m}_i(z)}{\partial \varphi_i \partial \vartheta_i} = \frac{\partial^2 R_i}{\partial \varphi_i \partial \vartheta_i}\underline{m}_i^0(z) R_i^+ + \frac{\partial R_i}{\partial \varphi_i}\underline{m}_i^0(z) \frac{\partial R_i^+}{\partial \vartheta_i} + \frac{\partial R_i}{\partial \vartheta_i}\underline{m}_i^0(z) \frac{\partial R_i^+}{\partial \varphi_i} + R_i \underline{m}_i^0(z) \frac{\partial^2 R_i^+}{\partial \varphi_i \partial \vartheta_i} \quad , \tag{7.9}$$

$$\underline{m}_i^{\varphi\varphi}(z) \equiv \frac{\partial^2 \underline{m}_i(z)}{\partial \varphi_i \partial \varphi_i} = \frac{\partial^2 R_i}{\partial \varphi_i^2}\underline{m}_i^0(z) R_i^+ + R_i \underline{m}_i^0(z) \frac{\partial^2 R_i^+}{\partial \varphi_i^2} + 2\frac{\partial R_i}{\partial \varphi_i}\underline{m}_i^0(z) \frac{\partial R_i^+}{\partial \varphi_i} \quad . \tag{7.10}$$

7.1.2 Diagonal terms

In order to evaluate the *diagonal terms* of the second derivative tensor of $\mathcal{F}$ only an infinitesimal change of the orientation of the magnetization at a

particular site i has to be considered such that by using the identity

$$\begin{aligned}\mathbf{m}(z) - \mathbf{G}_0(z) + \Delta\mathbf{m}_i(z) &= \tau(z)^{-1} + \Delta\mathbf{m}_i(z) \\ &= \tau(z)^{-1}(1 + \tau(z)\Delta\mathbf{m}_i(z)) \quad ,\end{aligned} \tag{7.11}$$

$\ln \boldsymbol{\tau}(z)$ in Eq. (7.2) can be written as

$$\begin{aligned}\ln \boldsymbol{\tau}'(z) &= \ln(\mathbf{m}(z) + \Delta\mathbf{m}_i(z) - \mathbf{G}_0(z))^{-1} \\ &= \ln \boldsymbol{\tau}(z) - \ln(\mathbf{1} + \boldsymbol{\tau}(z)\Delta\mathbf{m}_i(z)) \quad ,\end{aligned} \tag{7.12}$$

where $\mathbf{m}(z)$ is a site-diagonal matrix,

$$\mathbf{m}(z) = \{\underline{m}_i\,(z)\,\delta_{ij}\} \quad ,$$

and – quite clearly – the site-diagonal matrix $\Delta\mathbf{m}_i(z)$ has only one non-vanishing block, namely $\underline{\Delta m}_i\,(z)$ corresponding to site i. Expanding the second logarithm on the *rhs* of Eq. (7.12) and keeping only terms up to second order one obtains,

$$\begin{aligned}\ln \boldsymbol{\tau}'(z) - \ln \boldsymbol{\tau}(z) = &-\boldsymbol{\tau}(z)\Delta\mathbf{m}_i^{(1)}(z) - \boldsymbol{\tau}(z)\Delta\mathbf{m}_i^{(2)}(z) \\ &+ \frac{1}{2}\boldsymbol{\tau}(z)\Delta\mathbf{m}_i^{(1)}(z)\boldsymbol{\tau}(z)\Delta\mathbf{m}_i^{(1)}(z) \quad ,\end{aligned} \tag{7.13}$$

where the first term on the *rhs* contributes to the gradient of $\mathcal{F}$, the second and the third term are related to the site–diagonal elements of the second derivative tensor of $\mathcal{F}$.

7.1.3 Off-diagonal terms

The *site–off–diagonal* part of the second derivative of $\mathcal{F}$ can be obtained in a similar manner by (simultaneous) infinitesimal changes of the orientations of the magnetization in two different sites, i and j $(i \neq j)$, i.e.,

$$\begin{aligned}\ln \boldsymbol{\tau}'(z) &= \ln(\mathbf{m}(z) + \Delta\mathbf{m}_i(z) + \Delta\mathbf{m}_j(z) - \mathbf{G}_0(z))^{-1} \\ &= \ln \boldsymbol{\tau}(z) - (\mathbf{1} + \boldsymbol{\tau}(z)(\Delta\mathbf{m}_i(z) + \Delta\mathbf{m}_j(z))) \quad ,\end{aligned} \tag{7.14}$$

or, rewritten as,

$$\begin{aligned}\ln \boldsymbol{\tau}'(z) - \ln \boldsymbol{\tau}(z) = &-\ln(\mathbf{1} + \boldsymbol{\tau}(z)\Delta\mathbf{m}_i(z)) \\ &- \ln(\mathbf{1} + \boldsymbol{\tau}(z)\Delta\mathbf{m}_j(z)) - \ln(\mathbf{1} - \boldsymbol{\tau}(z)\boldsymbol{\Delta}_i(z)\boldsymbol{\tau}(z)\boldsymbol{\Delta}_j(z)) \quad ,\end{aligned} \tag{7.15}$$

where

$$\boldsymbol{\Delta}_i(z) \equiv \Delta\mathbf{m}_i(z)(\mathbf{1} + \boldsymbol{\tau}(z)\Delta\mathbf{m}_i(z))^{-1} \quad .$$

Expanding again the logarithms on the *rhs* of Eq. (7.15) up to second order yields

$$\ln \boldsymbol{\tau}'(z) - \ln \boldsymbol{\tau}(z) = -\boldsymbol{\tau}(z)(\Delta \mathbf{m}_i^{(1)}(z) + \Delta \mathbf{m}_j^{(1)}(z)) + \boldsymbol{\tau}(z)\Delta \mathbf{m}_i^{(1)}(z)\boldsymbol{\tau}(z)\Delta \mathbf{m}_j^{(1)}(z) \quad . \tag{7.16}$$

The second derivatives of $\mathcal{F}$ can now be related to the second term of the *rhs* of Eq. (7.16); see Eq. (7.2).

7.1.4 An example: a layered system corresponding to a simple two-dimensional lattice

Since according to Eq. (4.109) two-dimensional translational invariance implies that

$$\underline{t}_R^{pi}(z) = \underline{t}_R^{p0}(z) \quad , \quad \forall i \in I(\mathcal{L}^{(2)}) \quad ,$$

where $i = 0$ refers to the origin of $\mathcal{L}^{(2)}$ and R to the rotation matrix in Eq. (7.3), explicit use of Eqs. (7.6) – (7.10) in Eq. (7.13) and Eq. (7.16) then directly yields the second derivative tensor of $\mathcal{F}$ with respect to the site–dependent orientations of the magnetization.

7.1.4.1 *Diagonal terms:*

$$\frac{\partial^2 \mathcal{F}}{\partial \varphi_{ri} \partial \varphi_{ri}} = -\frac{1}{\pi} Im \int_{\curvearrowright}^{E_F} dz Tr \left[-\tau_{r0,r0}(z) m_r^{\varphi\varphi}(z) + \tau_{r0,r0}(z) m_r^{\varphi}(z) \tau_{r0,r0}(z) m_r^{\varphi}(z) \right] \quad , \tag{7.17}$$

$$\frac{\partial^2 \mathcal{F}}{\partial \varphi_{ri} \partial \vartheta_{ri}} = -\frac{1}{\pi} Im \int_{\curvearrowright}^{E_F} dz Tr \left[-\tau_{r0,r0}(z) m_r^{\varphi\vartheta}(z) + \tau_{r0,r0}(z) m_r^{\varphi}(\varepsilon) \tau_{r0,r0}(z) m_r^{\vartheta}(z) \right] \quad , \tag{7.18}$$

$$\frac{\partial^2 \mathcal{F}}{\partial \vartheta_{ri} \partial \vartheta_{ri}} = -\frac{1}{\pi} Im \int_{\curvearrowright}^{E_F} dz Tr \left[-\tau_{r0,r0}(z) m_r^{\vartheta\vartheta}(\varepsilon) + \tau_{r0,r0}(z) m_r^{\vartheta}(\varepsilon) \tau_{r0,r0}(z) m_r^{\vartheta}(\varepsilon) \right] \quad . \tag{7.19}$$

7.1.4.2 *Off–diagonal terms:*

$$\frac{\partial^2 \mathcal{F}}{\partial \varphi_{ri} \partial \varphi_{sj}} = -\frac{1}{\pi} Im \int_{\curvearrowright}^{E_F} dz Tr \left[\tau_{sj,ri}(z) m_r^{\varphi}(\varepsilon) \tau_{ri,sj}(z) m_s^{\varphi}(\varepsilon) \right] \quad , \tag{7.20}$$

$$\frac{\partial^2 \mathcal{F}}{\partial \varphi_{ri} \partial \vartheta_{sj}} = -\frac{1}{\pi} Im \int_{\curvearrowright}^{E_F} dz Tr \left[\tau_{sj,ri}(z) m_r^{\varphi}(\varepsilon) \tau_{ri,sj}(z) m_s^{\vartheta}(z) \right] \quad , \tag{7.21}$$

$$\frac{\partial^2 \mathcal{F}}{\partial \vartheta_{ri} \partial \vartheta_{sj}} = -\frac{1}{\pi} Im \int_{\curvearrowright}^{E_F} dz Tr \left[\tau_{sj,ri}(z) m_r^{\vartheta}(z) \tau_{ri,sj}(z) m_s^{\vartheta}(\varepsilon) \right] \quad . \tag{7.22}$$

In Eqs. (7.17) – (7.22) the trace has to be performed in angular momentum space.

It should be appreciated that the approach discussed in Chapter 4, namely the Screened Korringa-Kohn-Rostoker method, immediately yields also the second derivative tensor of the free energy. Since $\boldsymbol{\tau}(z)$ is known from multiple scattering theory, all that is needed is to evaluate derivatives of rotation matrices, which then have to be combined with the already known inverse single site t matrices: although the above expressions look "heavy" in terms of computational efforts they are not!

7.2 An intermezzo: classical spin Hamiltonians

In order to make contact with well-known classical formulations such as Heisenberg-like spin Hamiltonians, first their meaning has to be discussed. Only then a mapping between the derivatives of the free energy obtained via multiple scattering theory and the various terms in a classical formulation can be established.

7.2.1 "Classical" definitions of exchange and Dzyaloshinskii–Moriya interactions

In a quadratic approximation of (effective) spin–spin interactions, a (classical) spin Hamilton function can be written as

$$\mathcal{H} = \sum_i K(\mathbf{s}_i) + \frac{1}{2} \sum_{ij} \mathbf{s}_i \mathcal{J}_{ij} \mathbf{s}_j \quad , \tag{7.23}$$

where the $\mathbf{s}_i$ are classical spins, the parameters $K(\mathbf{s}_i)$ refer to on–site anisotropy energies and the $\mathcal{J}_{ij}$ are 3×3 matrices, which in turn can be decomposed in

three terms,

$$\mathcal{J}_{ij} = J_{ij} I_3 + \mathcal{J}^S_{ij} + \mathcal{J}^A_{ij} \quad , \tag{7.24}$$

where I_3 is the unit matrix and

$$J_{ij} = \frac{1}{3} Tr\left(\mathcal{J}_{ij}\right) \quad . \tag{7.25}$$

The symmetric, traceless part of $\mathcal{J}_{ij}$, denoted in Eq. (7.24) by $\mathcal{J}^S_{ij}$, is defined by

$$\mathcal{J}^S_{ij} = \frac{1}{2}\left(\mathcal{J}_{ij} + \mathcal{J}^t_{ij}\right) - J_{ij} I_3 \quad , \tag{7.26}$$

its antisymmetric part, $\mathcal{J}^A_{ij}$, by

$$\mathcal{J}^A_{ij} = \frac{1}{2}\left(\mathcal{J}_{ij} - \mathcal{J}^t_{ij}\right) \quad , \tag{7.27}$$

where t denotes transposed matrices.

According to Moriya [1] a typical intersite interaction consists of the following three terms,

$$\mathbf{s}_i \mathcal{J}_{ij} \mathbf{s}_j = \underbrace{J_{ij} \mathbf{s}_i \cdot \mathbf{s}_j}_{1} + \underbrace{\mathbf{s}_i \mathcal{J}^S_{ij} \mathbf{s}_j}_{2} + \underbrace{\mathbf{D}_{ij}\left(\mathbf{s}_i \times \mathbf{s}_j\right)}_{3} \quad , \tag{7.28}$$

where the first and second terms on the *rhs* are the *isotropic* and the *symmetric anisotropic exchange interactions*, respectively, while the third term represents the *Dzyaloshinskii–Moriya* (DM) interactions [1, 2] with the DM-vectors $\mathbf{D}_{ij}$ being defined as

$$D^x_{ij} = \frac{1}{2}\left(J^{yz}_{ij} - J^{zy}_{ij}\right) \quad , \quad D^y_{ij} = \frac{1}{2}\left(J^{xz}_{ij} - J^{zx}_{ij}\right) \quad , \quad D^z_{ij} = \frac{1}{2}\left(J^{xy}_{ij} - J^{yx}_{ij}\right) \quad . \tag{7.29}$$

7.2.2 Second order derivatives of $\mathcal{H}$

By taking now the second derivatives of the Hamiltonian in Eq. (7.23) with respect to the polar and azimuthal angles one gets,

$$\frac{\partial^2 \mathcal{H}}{\partial \alpha_i \partial \beta_k} = \delta_{ik} K^{\alpha\beta}(\mathbf{s}_i) + \delta_{ik} \sum_{j(\neq i)} \mathbf{s}^{\alpha\beta}_i \mathcal{J}_{ij} \mathbf{s}_j + (1 - \delta_{ik})\, \mathbf{s}^{\alpha}_i \mathcal{J}_{ik} \mathbf{s}^{\beta}_k \quad , \tag{7.30}$$

where α and β can be either ϑ or φ, and

$$K^{\alpha\beta}(\mathbf{s}_i) = \frac{\partial^2 K(\mathbf{s}_i)}{\partial \alpha_i \partial \beta_i} \quad , \quad \mathbf{s}^{\alpha}_i = \frac{\partial \mathbf{s}_i}{\partial \alpha_i} \quad , \quad \mathbf{s}^{\alpha\beta}_i = \frac{\partial^2 \mathbf{s}_i}{\partial \alpha_i \partial \beta_i} \quad . \tag{7.31}$$

It should be noted that all the derivatives have to be taken [3] at $\vartheta_i = \frac{\pi}{2}$ and $\varphi_i = 0$ in a coordinate system with the z axis normal to the reference orientation of the magnetization.

7.2.2.1 Magnetization along x

Assuming for matters of simplicity a second order uniaxial magnetic anisotropy,

$$K(\mathbf{s}_i) = -K_{2,i}\sin^2(\vartheta_i) \quad , \tag{7.32}$$

the constants $J_{ik}^{\mu\nu}, \mu, \nu \in (x, y, z)$ in Eq. (7.29) can easily be derived:

$$\begin{aligned} \frac{\partial^2\mathcal{H}}{\partial\varphi_i\partial\varphi_i} &= -\sum_{j(\neq i)} J_{ij}^{xx} \quad , \quad \frac{\partial^2\mathcal{H}}{\partial\vartheta_i\partial\vartheta_i} = 2K_{2,i} - \sum_{j(\neq i)} J_{ij}^{xx} \quad , \\ \frac{\partial^2\mathcal{H}}{\partial\vartheta_i\partial\varphi_i} &= \frac{\partial^2\mathcal{H}}{\partial\varphi_i\partial\vartheta_i} = 0 \quad , \end{aligned} \tag{7.33}$$

$$\begin{aligned} \frac{\partial^2\mathcal{H}}{\partial\varphi_i\partial\varphi_k} &= J_{ik}^{yy} \quad , \quad \frac{\partial^2\mathcal{H}}{\partial\vartheta_i\partial\vartheta_k} = J_{ik}^{zz} \quad , \quad \frac{\partial^2\mathcal{H}}{\partial\varphi_i\partial\vartheta_k} = -J_{ik}^{yz} \quad , \\ \frac{\partial^2\mathcal{H}}{\partial\vartheta_i\partial\varphi_k} &= -J_{ik}^{zy} \quad . \end{aligned} \tag{7.34}$$

7.2.2.2 Magnetization along z

If the magnetization points along z, the uniaxial magnetic anisotropy is of the form

$$K(\mathbf{s}_i) = -K_{2,i}\sin^2(\vartheta_i)\cos^2(\varphi_i) \quad , \tag{7.35}$$

and thus again the $J_{ik}^{\mu\nu}$ can be directly obtained:

$$\frac{\partial^2\mathcal{H}}{\partial\varphi_i\partial\varphi_i} = \frac{\partial^2\mathcal{H}}{\partial\vartheta_i\partial\vartheta_i} = 2K_{2,i} - \sum_{j(\neq i)} J_{ij}^{zz} \quad , \quad \frac{\partial^2\mathcal{H}}{\partial\vartheta_i\partial\varphi_i} = \frac{\partial^2\mathcal{H}}{\partial\varphi_i\partial\vartheta_i} = 0 \quad , \tag{7.36}$$

$$\begin{aligned} \frac{\partial^2\mathcal{H}}{\partial\varphi_i\partial\varphi_k} &= J_{ik}^{yy} \quad , \quad \frac{\partial^2\mathcal{H}}{\partial\vartheta_i\partial\vartheta_k} = J_{ik}^{xx} \quad , \\ \frac{\partial^2\mathcal{H}}{\partial\varphi_i\partial\vartheta_k} &= J_{ik}^{yx} \quad , \quad \frac{\partial^2\mathcal{H}}{\partial\vartheta_i\partial\varphi_k} = J_{ik}^{xy} \quad , \quad i \neq k \quad . \end{aligned} \tag{7.37}$$

7.2.3 Non-relativistic description

Since in a non–relativistic description (absence of spin–orbit coupling) there is no preferred orientation of the magnetization, see, e.g., Eq. (3.49), all off–diagonal elements vanish and the diagonal elements are identical in value, i.e.,

$$\frac{\partial^2\mathcal{H}}{\partial\alpha_i\partial\alpha_i} + \sum_{j(\neq i)} \frac{\partial^2\mathcal{H}}{\partial\alpha_i\partial\alpha_j} = 0 \quad (\alpha = \vartheta \text{ or } \varphi) \quad , \tag{7.38}$$

$$J_i = \sum_{j(\neq i)} J_{ij} \quad . \tag{7.39}$$

This clearly corresponds to an *isotropic exchange coupling*.

7.2.4 Relativistic description

In the relativistic case this sum rule does no longer apply. The *lhs* of Eq. (7.38), however, can be used to define an effective *second order magnetic anisotropy constant* λ_i. For example, for the case of the magnetization pointing parallel to the z axis of the global coordination frame, one obtains

$$\lambda_i \equiv \frac{1}{2}\left(\frac{\partial^2 \mathcal{H}}{\partial\vartheta_i\partial\vartheta_i} + \sum_{j(\neq i)} \frac{\partial^2 \mathcal{H}}{\partial\vartheta_i\partial\vartheta_j}\right) = K_{2,i} - \frac{1}{2}\sum_{j(\neq i)} \left(\mathcal{J}_{ij}^{zz} - \mathcal{J}_{ij}^{xx}\right) \quad . \tag{7.40}$$

The physical meaning of the above equation is immediately transparent: beyond the on–site anisotropy term (first term, *rhs*) the magneto–crystalline anisotropy energy of the system contains contributions that arise from the anisotropy of the intersite exchange interactions (second term, *rhs*).

7.3 Relations to relativistic multiple scattering theory

By mapping the free energy $\mathcal{F}$ onto the classical spin Hamiltonian in Eq. (7.23),

$$f : \mathcal{F} \rightarrow \mathcal{H} \quad , \tag{7.41}$$

in terms of multiple scattering theory, see Eq. (7.19) in Section 7.1.4, the layer–resolved anisotropies constants in Eq. (7.40) are simply given for the case of the magnetization pointing along z by

$$\begin{aligned}\lambda_r = &-\frac{1}{2\pi} Im \int_{-\infty}^{E_F} d\varepsilon Tr\left[-\tau_{r0,r0}(\varepsilon) m_r^{\vartheta\vartheta}(\varepsilon) + \tau_{r0,r0}(\varepsilon) m_r^{\vartheta}(\varepsilon) \tau_{r0,r0}(\varepsilon) m_r^{\vartheta}(\varepsilon)\right] \\ &- \sum_{sj} \frac{1}{2\pi} Im \int_{-\infty}^{E_F} d\varepsilon Tr\left[\tau_{sj,r0}(\varepsilon) m_r^{\vartheta}(\varepsilon) \tau_{r0,sj}(\varepsilon) m_s^{\vartheta}(\varepsilon)\right] \quad ,\end{aligned} \tag{7.42}$$

where for practical purposes the sum over sites sj can be rewritten in terms of a lattice Fourier transformation [3], provided that one and the same two-dimensional translational symmetry applies in all atomic layers.

Very clearly, the *Dzyaloshinskii–Moriya (DM) interaction vectors*,

$$\mathbf{D}_{ij} = \frac{1}{2}\left(\left(J_{ij}^{yz} - J_{ij}^{zy}\right), \left(J_{ij}^{xz} - J_{ij}^{zx}\right), \left(J_{ij}^{xy} - J_{ij}^{yx}\right)\right) \quad , \tag{7.43}$$

can be evaluated only using a relativistic approach, since off-diagonal second order derivatives of $\mathcal{H}$ in Eq. (7.30) are required, which in turn can be obtained

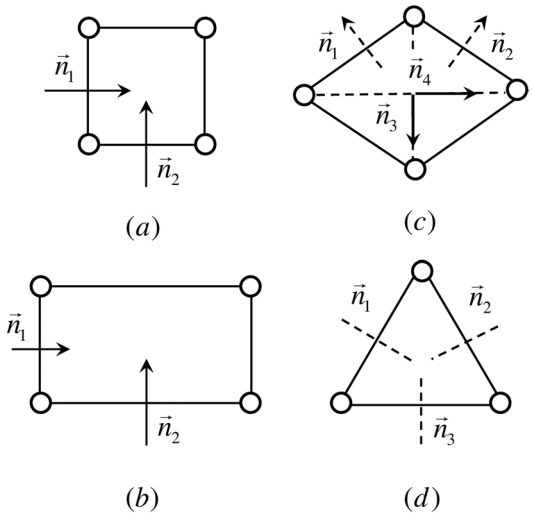

FIGURE 7.1: *Orientations* $\mathbf{n}$ *of non-zero Dzyaloshinskii-Moriya vectors* $\mathbf{D}^{\mathbf{n}}_{\mathbf{R}_{ij}}$ *for (a) a bcc(001) (square lattice), (b) a sc(110) (rectangular lattice), (c) a bcc(110) (lozenge lattice), and (d) an fcc(111) (triangular lattice) surfaces. Panels (a) and (b): the* $\mathbf{n}$ *are from the Refs. [1, 2, 4, 5, 6, 7], the moduli of the vectors can be different for different systems. Panel (c): the* $\mathbf{n}$ *are lying in the lattice plane but the angle between* $\mathbf{n}$ *and* $\overline{\mathbf{R}_{ij} = \mathbf{R}_i - \mathbf{R}_j}$ *cannot be determined [1, 2, 4, 5, 6, 7]. Panel (d): the* $\mathbf{n}$ *are in a plane perpendicular to* $\mathbf{R}_{ij}$*, but their orientation cannot be determined. From Ref.* [8].

from the second derivative tensor of $\mathcal{F}$ using a formulation shown for a simple two-dimensional lattice in Eqs. (7.17) – (7.22).

As an illustration for Dzyaloshinskii-Moriya vectors the orientations of such vectors are sketched in Fig. 7.1 for a few lattice types. In using a Hamiltonian of the type given in Eq. (7.23) with *ab-initio* determined parameters including Dzyaloshinskii-Moriya terms, it was shown for example that for a Cr trimer on Au(111) actually configuration (a) in the top part of Fig. (7.2) is the magnetic ground state. In this figure also the Dzyaloshinskii-Moriya vectors are displayed (bottom part) that correspond to the ground state and to the excited ferromagnetic configuration (perpendicular orientation of the magnetization). The anisotropy energy for the ground state configuration of a Cr trimer on Au(111), by the way, is rather very small, namely only 0.03 meV.

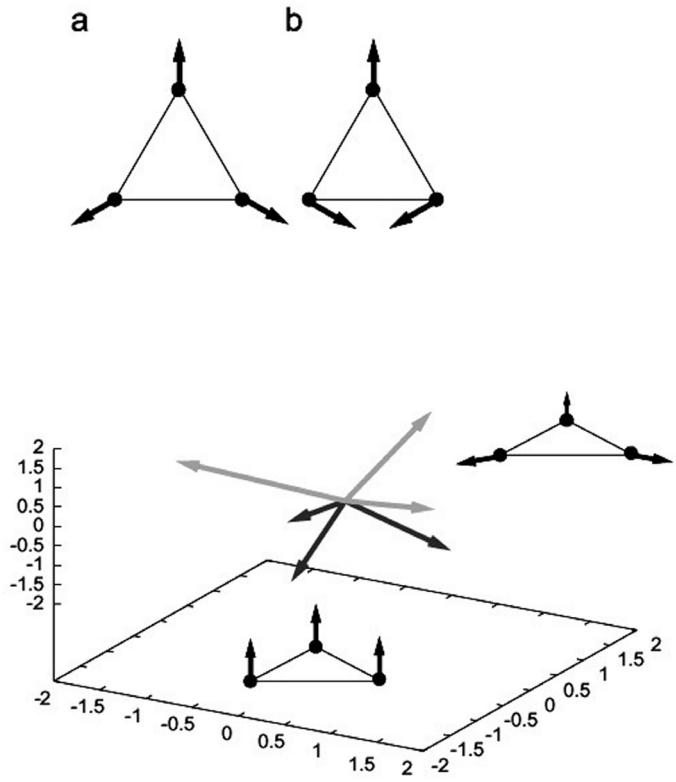

FIGURE 7.2: *Top: Possible magnetic ground state configurations of a Cr trimer on Au(111). Bottom: Dzyaloshinskii-Moriya vectors for a Cr trimer on Au(111). The dark grey arrows correspond to the self-consistent calculation for the ferromagnetic configuration, and the light gray arrows to that for an in-plane configuration of the magnetization. From Ref. [9].*

[1] T. Moriya, Physical Review **120**, 91 (1960).

[2] I. Dzyaloshinskii, J. Phys. Chem. Solids **4**, 241 (1958).

[3] L. Udvardi, L. Szunyogh, K. Palotas, and P. Weinberger, Phys. Rev. B **68**, 104436 (2003).

[4] I. Dzyaloshinskii, Sov. Phys. JETP **5**, 1259 (1957).

[5] T. Moryia, Phys. Rev. Lett. **4**, 228 (1960).

[6] A. Fert, In *Materials Science Forum*, edited by A. Chamberod and J. Hillairat (Transtech Publications, Aedermannsdorf, 1990), Vol. 59-60, p.439.

[7] A. Crépieux and C. Lacroix, J. Magn. Magn. Mater **182**, 341 (1998).

[8] E. Y. Vedmedenko, L. Udvardi, P. Weinberger, and R. Wiesendanger, Phys. Rev. B **75**, 104431 (2007).

[9] A. Antal, L. Udvardi, B. Újfalussy, B. Lazarovits, L. Szunyogh, and P. Weinberger, J. Magn. Magn. Mater **316**, 118 (2007).

8

The Disordered Local Moment Method (DLM)

In this chapter the so-called Disordered Local Moment Method is shortly summarized which can be used to evaluate temperature effects for anisotropy energies and related quantities.

The Disordered Local Moment Method (DLM) is based on the idea that in itinerant metallic magnets, on a certain time scale ζ, which is small as compared to the characteristic time of spin fluctuations, but longer than the electron hopping times, the spin orientations of the electrons leaving an atomic site are sufficiently correlated with those arriving such that a nonzero magnetization exists when the appropriate quantity is averaged over ζ. In this scheme the magnetic excitations are modeled [1] - [4] by associating local spin-polarization axes with all lattice sites and the orientations $\{\hat{e}_i\}$ vary very slowly on the time-scale of the electronic motions. The approach given below is again fully relativistic.

8.1 The relativistic DLM method for layered systems

As in Chapters 5 and 7 the key quantity of the DLM scheme is once again the electronic grand potential of a ferromagnetic system (with at least two-dimensional translational symmetry) corresponding to a given (uniform) direction $\hat{n}$ of the magnetization, this time, however, as a function of the orientations $\hat{e}_i$ of the local spins located at positions $\mathbf{R}_i$.

In the case of a simple two-dimensional lattice $\mathcal{L}^{(2)}$, $\mathbf{R}_i = \mathbf{c}_p + \mathbf{R}_{i,\parallel}$ the so-called Weiss fields in a given layer p,

$$\vec{h}_p^{(\hat{n})} = h_p^{(\hat{n})}\hat{n} \quad , \quad \vec{h}_p^{(\hat{n})} = \vec{h}_{pi}^{(\hat{n})} \quad , \quad \forall i \in I(\mathcal{L}^{(2)}) \quad , \tag{8.1}$$

$$\hat{e}_p = \hat{e}_{pi} \quad , \quad \forall i \in I(\mathcal{L}^{(2)}) \quad , \tag{8.2}$$

$$\widehat{e}_0 = \hat{\mathbf{z}} \quad , \quad \forall p, \forall i \in I(\mathcal{L}^{(2)}) \quad , \tag{8.3}$$

are defined by [4]

$$h_p^{(\hat{n})} = \frac{3}{4\pi} \int d\hat{e}_{pi} \, (\hat{e}_{pi} \cdot \hat{n}) \left\langle \Omega^{(\hat{n})} \right\rangle_{\hat{e}_{pi}} \quad , \tag{8.4}$$

where $\left\langle \Omega^{(\hat{n})} \right\rangle_{\hat{e}_{pi}}$ denotes the thermodynamical average over the orientations of the spins centered in all sites of the system with the exception of a particular site i in layer p for which

$$\hat{e}_{pi} = (\sin\vartheta_{pi}\cos\varphi_{pi}, \sin\vartheta_{pi}\sin\varphi_{pi}, \cos\vartheta_{pi}) \quad . \tag{8.5}$$

It should be noted that this is exactly the same formal construction in terms of restricted averages as before in the case of chemical disorder; see Chapter 5. Furthermore, as before the site index i serves to denote the origin of $\mathcal{L}^{(2)}$; Eq. (8.3) defines the reference configuration. The layer-resolved probabilities in Eq. (8.4) are given by [4]

$$P_p^{(\hat{n})}\left(\widehat{e}_{pi}\right) = \frac{\beta h_p^{(\widehat{n})}}{4\pi \sinh(\beta h_p^{(\widehat{n})})} \exp\left(-\beta h_p^{(\widehat{n})}\left(\widehat{e}_{pi}\cdot\widehat{n}\right)\right) \quad , \tag{8.6}$$

where $\beta = 1/k_B T$.

As in the previous chapter, in using the magnetic force theorem, the free energy can be approximated by the single–particle grand potential (band energy),

$$\Omega^{(\hat{n})}\left(\{\widehat{e}_{pi}\}\right) \simeq -\int_{\curvearrowright} dz\; f\left(z;\mu\right)\; N^{(\hat{n})}\left(z;\{\widehat{e}_{pi}\}\right) \quad , \tag{8.7}$$

where μ is the chemical potential, $z = \epsilon + i\delta$, $f\left(z;\mu\right)$ is the Fermi-Dirac distribution, and $N^{(\hat{n})}\left(z;\{\widehat{e}_{pi}\}\right)$ denotes the integrated density of states expressed in terms of Lloyd's formula; see Eq. (4.37). The Weiss field can now be evaluated in terms of multiple scattering theory as

$$h_p^{(\hat{n})} = \frac{3}{4\pi^2}\mathrm{Im}\int dz\; f\left(z;\mu\right)\left[\int d\hat{e}_{pi}\;\left(\hat{e}_{pi}\cdot\hat{n}\right)\ln\det \underline{M}_p^{(\hat{n})}\left(z;\hat{e}_{pi}\right)\right] \quad , \tag{8.8}$$

where $\underline{M}_p^{(\hat{n})}\left(z;\hat{e}_{pi}\right)$ is the inverse *impurity matrix*, see, e.g., Eq. (5.25),

$$\underline{M}_p^{(\hat{n})}\left(z;\hat{e}_{pi}\right) = \underline{D}_p^{(\hat{n})}\left(z;\hat{e}_{pi}\right)^{-1} \quad , \tag{8.9}$$

$$\underline{M}_p^{(\hat{n})}\left(z;\hat{e}_{pi}\right) = \underline{1} + \left(\underline{t}_p\left(z;\hat{e}_{pi}\right)^{-1} - \underline{t}_p^{c(\hat{n})}\left(z\right)^{-1}\right)\underline{\tau}_{pi,pi}^{c(\hat{n})}\left(z\right) \quad . \tag{8.10}$$

In Eq. (8.10) $\underline{\tau}_{pi,pi}^{c(\hat{n})}\left(z\right)$ is that layer- and site-diagonal scattering path operator, which satisfies the following inhomogeneous Coherent Potential Approximation

$$\underline{\tau}_{pi,pi}^{c(\hat{n})}\left(z\right) = \int d\hat{e}_{pi}\; P_p^{(\widehat{n})}\left(\widehat{e}_{pi}\right)\left\langle \underline{\tau}_{pi,pi}^{(\hat{n})}\left(z\right)\right\rangle_{\widehat{e}_{pi}} \quad , \quad \forall p \quad , \tag{8.11}$$

with $\left\langle \underline{\tau}_{pi,pi}^{(\hat{n})}\left(z\right)\right\rangle_{\widehat{e}_{pi}}$ referring to the case that in site pi the orientation of the magnetization is $\widehat{e}_{pi}$,

$$\left\langle \underline{\tau}_{pi,pi}^{(\hat{n})}\left(z\right)\right\rangle_{\widehat{e}_{pi}} = \underline{\tau}_{pi,pi}^{c(\hat{n})}\left(z\right)\underline{D}_p^{(\hat{n})}\left(z;\hat{e}_{pi}\right) \quad . \tag{8.12}$$

In comparing Eq. (8.9) with Eq. (5.29) and Eq. (5.30) the formal analogy between statistical disorder of spins and statistical chemical disorder becomes obvious; however, the CPA condition is now much more complicated and – in addition – for a layered system has to be solved simultaneously for all layers p. In the case of spherically symmetric effective potentials and exchange fields (Atomic Sphere Approximation, ASA) $\underline{t}_p\left(\varepsilon;\widehat{e}_{pi}\right)$ can easily be calculated by means of the following, by now familiar similarity transformation,

$$\underline{t}_p\left(z;\widehat{e}_{pi}\right)=\underline{R}\left(\widehat{e}_{pi}\right)\underline{t}_p\left(z;\widehat{e}_0\right)\underline{R}\left(\widehat{e}_{pi}\right)^{+} \quad , \tag{8.13}$$

where $\underline{t}_p\left(z;\widehat{e}_0\right)$ refers to the case of an effective field pointing along $\widehat{e}_0$ (z axis, reference configuration) and $\underline{R}\left(\widehat{e}_{pi}\right)$ contains block-wise the (projective) irreducible representations of that element $\in O(3)$ that rotates the z axis into $\widehat{e}_{pi}$; see also Section 4.11.

Since the Weiss fields $h_p^{(\hat{n})}$ are coupled to the grand canonical potential $\Omega^{(\hat{n})}\left(\{\widehat{e}_{pi}\}\right)$ via Eq. (8.4), which in turn is determined by the CPA condition in Eq. (8.11), use of the DLM scheme requires a particular self-consistent treatment. First an initial (usually uniform) set of $h_p^{(\widehat{n})}$ has to be chosen. In using as a start, e.g., $\hat{e}_p=\hat{e}_o,\forall p$, the layer-resolved probabilities $P_p^{(\widehat{n})}\left(\widehat{e}_{pi}\right)$ in Eq. (8.6) can be evaluated and thus also the CPA condition in Eq. (8.11), from which in turn a new set of Weiss fields, see Eq. (8.8), can be obtained. Equations Eq. (8.8) and Eq. (8.11) have to be varied until in all atomic layers the Weiss fields $h_p^{(\widehat{n})}$ no longer change.

8.2 Approximate DLM approaches

Since the above scheme is computationally rather demanding, an approximation for calculating the Weiss fields was suggested [5]. Suppose that in Eq. (8.4) $\left\langle\Omega^{(\hat{n})}\right\rangle_{\hat{e}_{pi}}$ is approximated by

$$\left\langle\Omega^{(\hat{n})}\right\rangle_{\hat{e}_{pi}}=\Omega^{c(\hat{n})}+h_p^{(\hat{n})}\left(\hat{e}_{pi}\cdot\hat{n}\right)+K_p\sin^2\vartheta_{pi} \quad , \tag{8.14}$$

where $\Omega^{c(\hat{n})}$ is the grand canonical potential of the completely disordered effective medium and K_p is a (microscopic) uniaxial anisotropy constant; then the Weiss field can be obtained from the derivative of $\left\langle\Omega^{(\hat{n})}\right\rangle_{\hat{e}_{pi}}$ with respect to the average magnetization direction $\hat{n}$.

For example, for $\hat{n}=\hat{z}$ the corresponding Weiss fields are given by

$$h_p^{(\hat{z})}=-\frac{1}{\pi}\mathrm{Im}\int d\varepsilon\, f\left(\varepsilon;\mu\right)tr\left[\frac{\partial\underline{t}_p\left(\varepsilon;\hat{e}_{pi}\right)^{-1}}{\partial\vartheta_{pi}}\underline{\tau}_{pi,pi}^{c(\hat{z})}(\varepsilon)\underline{D}_p^{(\hat{z})}\left(\varepsilon;\hat{e}_{pi}\right)\right]_{\hat{e}_{pi}=\hat{z}} \quad , \tag{8.15}$$

with

$$\underline{D}_p^{(\hat{z})}\left(\varepsilon;\hat{e}_{pi}\right) \equiv \underline{M}_p^{(\hat{z})}\left(\varepsilon;\hat{e}_{pi}\right)^{-1} \quad . \tag{8.16}$$

It was found [5] that Eq. (8.8) and Eq. (8.15) resulted in Weiss fields that differed only by about 1% .

In order to evaluate K_p again the magnetic force theorem and Lloyd's formula in the context of infinitesimal rotations as discussed in Chapter 7 can be used. For a system characterized by a simple two-dimensional lattice the layer-dependent uniaxial anisotropy constants K_p are defined by

$$K_b = \sum_p K_{b,p} \quad , \tag{8.17}$$

where

$$\begin{aligned} K_{b,p} = \frac{1}{\pi}\,\mathrm{Im} \int d\varepsilon\, f\left(\varepsilon;\mu\right) \int d\widehat{e}_{pi} P_p^{(z)}\left(\widehat{e}_{pi}\right) \\ \times \mathrm{Tr}\left[\frac{\partial \underline{m}_p\left(z;\widehat{e}_{pi}\right)}{\partial \vartheta_p}\left\langle \underline{\tau}_{pi,pi}^{(\hat{n})}\left(z\right)\right\rangle_{\widehat{e}_{pi}}\right]_{\vartheta_p=\frac{\pi}{4},\varphi_p=0} \quad , \end{aligned} \tag{8.18}$$

and according to Eq. (7.6)

$$\begin{aligned} \frac{\partial \underline{m}_p\left(z;\widehat{e}_{pi}\right)}{\partial \vartheta_p} = \left(\frac{\partial \underline{R}_p\left(\widehat{n}\right)}{\partial \vartheta_p}\underline{t}_p\left(z;\widehat{e}_{pi}\right)^{-1}\underline{R}_p\left(\widehat{n}\right)^{+}\right. \\ \left. +\underline{R}_p\left(\widehat{n}\right)\underline{t}_p\left(z;\widehat{e}_{pi}\right)^{-1}\frac{\partial \underline{R}_p^{+}\left(\widehat{n}\right)}{\partial \vartheta_p}\right) \quad . \end{aligned} \tag{8.19}$$

It should be noted that in Eq. (8.18) use was made of the fact that in this particular case Eq. (7.13) reduces to

$$\ln \boldsymbol{\tau}'(z) - \ln \boldsymbol{\tau}(z) = -\boldsymbol{\tau}(z)\Delta\mathbf{m}_i^{(1)}(z) \quad , \tag{8.20}$$

where $\Delta\mathbf{m}_i^{(1)}(z)$ simply is given by Eq. (8.19) at $\vartheta_p = \pi/4, \forall p$; see also the discussion in the previous Chapter.

Unfortunately, up to now there are only very few publications using the relativistic DLM scheme. The probably only one dealing with the magnetic anisotropy energy of solid systems nanostructured in one dimension will be discussed in Chapter 11.

[1] B. L. Györffy, A. J. Pindor, J. B. Staunton, G. M. Stocks, and H. Winter, J. Phys. F **15**, 1337 (1985).

[2] J. B. Staunton, S. Ostanin, S. S. A. Razee, B. L. Györffy, L. Szunyogh, B. Ginatempo, and E. Bruno, Phys. Rev. Lett. **93**, 257204 (2004).

[3] S. S. A. Razee, J. B. Staunton, L. Szunyogh, and B. L. Györffy, Phys. Rev. B **66**, 094415 (2002).

[4] J. B. Staunton, L. Szunyogh, Á. Buruzs, B. L. Györffy, S. Ostanin, and L. Udvardi, Phys. Rev. B **74,** 144411 (2006).

[5] Á. Buruzs, P. Weinberger, L. Szunyogh, L. Udvardi, P.I. Chleboun, A. M. Fischer, and J.B. Staunton, Phys. Rev. B **76**, 064417 (2007).

9

Spin dynamics

In this chapter an iterative multi-scale approach is introduced by combining a semi-classical Landau-Lifshitz-Gilbert equation with multiple scattering theory. This scheme is in particular useful in determining the magnetic ground state of magnetic systems nanostructured in two dimensions.

9.1 The phenomenological Landau-Lifshitz-Gilbert equation

Magnetization or spin dynamics is usually described phenomenologically by means of the well-known Landau-Lifshitz-Gilbert (LLG) equation [1] - [4]:

$$\frac{\delta}{\delta t}\mathbf{M}(\mathbf{r},t) = -\gamma \mathbf{M}(\mathbf{r},t) \times \mathbf{H}^{eff}(\mathbf{r}) + \frac{\lambda}{m}\mathbf{M}(\mathbf{r},t) \times \{\mathbf{M}(\mathbf{r},t) \times \mathbf{H}^{eff}(\mathbf{r})\} \quad , \quad (9.1)$$

where γ is the gyromagnetic ratio, λ the Gilbert damping factor, and the effective forcing field is given by the derivative of the internal energy $E(\mathbf{M}(\mathbf{r},t))$ with respect to $\mathbf{M}(\mathbf{r},t)$,

$$\mathbf{H}^{eff}(\mathbf{r}) = \delta E(\mathbf{M}(\mathbf{r},t))/\delta \mathbf{M}(\mathbf{r},t) \quad . \quad (9.2)$$

For simulation purposes very often $\mathbf{H}^{eff}(\mathbf{r})$ is decomposed into various terms,

$$\mathbf{H}^{eff}(\mathbf{r}) = \mathbf{H}^{extern}(\mathbf{r}) + \mathbf{H}^{exch}(\mathbf{r}) + \mathbf{H}^{anis}(\mathbf{r}) + \mathbf{H}^{dipole}(\mathbf{r}) + \mathbf{H}^{elast}(\mathbf{r}) \quad , \quad (9.3)$$

corresponding in turn to contributions from applied external fields, intrinsic exchange interactions, the magneto crystalline anisotropy, magnetic dipole-dipole interactions, and magneto-elastic effects.

For practical purposes the individual terms in Eq. (9.3) are then taken either from experiment or by adopting parameters listed in the literature.

9.2 The semi-classical Landau-Lifshitz equation

For a set of time-dependent magnetic moments,

$$\{\mathbf{m}_i(t)\} \quad , \quad \mathbf{m}_i(t) = m_i(t)\hat{e}_i(t) \quad , \quad m_i(t) = |\mathbf{m}_i(t)| \quad , \tag{9.4}$$

$$\hat{e}_i(t) = \mathbf{m}_i(t)/m_i(t) \quad , \tag{9.5}$$

the precessional component of their motions is described by a microscopic, quasi-classical equation of motion which is of the same form as the classical Landau-Lifshitz equation

$$\frac{\delta \mathbf{M}(\mathbf{r},t)}{\delta t} = -\gamma \mathbf{M}(\mathbf{r},t) \times \mathbf{H}^{eff}(\mathbf{r}) \quad , \tag{9.6}$$

(Eq. (9.1) without the second term on the *rhs*), however, now with an effective field, $\mathbf{B}_i^{eff}(\mathbf{r})$, that is based on first principles theory:

$$\frac{\delta}{\delta t}\mathbf{m}_i(t) = -\gamma \mathbf{m}_i(t) \times \mathbf{B}_i^{eff}(\mathbf{r}) \quad , \tag{9.7}$$

$$\mathbf{B}_i^{eff}(\mathbf{r}) \equiv \mathbf{B}_i^{eff}(\mathbf{r};\{\mathbf{m}_i(t)\}) = \frac{\delta E^{LSDA}(\{\mathbf{m}_i(t)\})}{\delta \mathbf{m}_i(t)} \quad , \tag{9.8}$$

where $E^{LSDA}(\{\mathbf{m}_i(t)\})$ is the energy obtained by solving the LSDF (Local Spin Density Functional) equations for the instantaneous state corresponding to a given set of moments $\{\mathbf{m}_i(t)\}$.

9.3 Constrained density functional theory

Ordinary Density Functional Theory, however, does not support such general states [5, 6]. In order to overcome this difficulty a so-called Constrained Density Functional Theory (CDFT) was developed [7], in which the LSDA equations are solved subject to the following constraint,

$$\int_{\Omega_i} (\mathbf{m}_i(\mathbf{r}) \times \hat{e}_i)\, d\mathbf{r} = 0 \quad , \tag{9.9}$$

where, as should be recalled,

$$\hat{e}_i = (\sin\vartheta_i \cos\varphi_i,\ \sin\vartheta_i \sin\varphi_i,\ \cos\vartheta_i) \quad . \tag{9.10}$$

This condition ensures that the local magnetizations are aligned with the directions specified by a given set $\{\hat{e}_i\}$. In order to maintain this specific orientational configuration, however, a local transverse constraining field must

be applied at each site in order to extinguish the components of the magnetization transverse to $\hat{e}_i$. The constraining field is then obtained from the condition

$$\frac{\delta E^{con}[\{\hat{e}_i\},\{\mathbf{B}_i^{con}\}]}{\delta \hat{e}_i} = 0 \quad , \quad \forall i \quad . \tag{9.11}$$

The energy $E^{con}[\{\hat{e}_i\},\{\mathbf{B}_i^{con}\}]$ in the presence of the constraining field is given by

$$E^{con}[\{\hat{e}_i\},\{\mathbf{B}_i^{con}\}] = E^{int}[\{\hat{e}_i\},\{\mathbf{B}_i^{con}\}] + \int d\mathbf{r}\ \mathbf{M}(\mathbf{r})\cdot\mathbf{B}(\mathbf{r}) \quad , \tag{9.12}$$

where $\mathbf{M}(\mathbf{r})$ and $\mathbf{B}(\mathbf{r})$ is the total magnetization and exchange field, respectively. This formalism can be made into a practical computational scheme by choosing $B_i^{con}(\mathbf{r})$ to be of the functional form

$$B_i^{con}(\mathbf{r}) = B_{xc}^{i}(\mathbf{r})\mathbf{c}_i \quad , \tag{9.13}$$

with $B_{xc}^{i}(\mathbf{r})$ being the local (longitudinal) exchange correlation potential at the site i and $\mathbf{c}_i$ a unit vector normal to the local orientation $\hat{e}_i$.

The fact that Eq. (9.13) is a good approximation for the constraining field can be monitored *a posteriori* by checking the extent to which the transverse components of $m_i(\mathbf{r})$ are quenched. It should be noted, by the way, that "standard" LSDA ground states are simply constrained local moment (CLM) states for which $B_i^{con} = 0$ in all sites.

In order to make use of the CLM model and a first principles spin dynamics (FP-SD) scheme it is sufficient to note that the internal effective field that rotates the spins is just the opposite of the constraining field, i.e., $\mathbf{B}_i^{eff} = -\mathbf{B}_i^{con}$ in Eq. (9.8). Furthermore, as obviously implied by the use of Eq. (9.8), Eq. (9.7) does not include a torque term coupling the spin with the orbital degrees of freedom [8]; see also Section 19.4.

9.4 The semi-classical Landau-Lifshitz-Gilbert equation

As easily seen, Eq. (9.7) only takes care of the precessional motion of the moments: an equivalent expression for the Gilbert term does not occur. Since up-to-now no quantum mechanical description of the Gilbert damping parameter λ is available and since FP-SD serves the sole purpose of finding the (magnetic) ground state, it is sufficient to add a Gilbert damping term phenomenologically as

$$\frac{\delta}{\delta t}\mathbf{m}_i(t) = -\gamma\mathbf{m}_i(t)\times\mathbf{B}_i^{eff}(\mathbf{r}_i) + \lambda\mathbf{m}_i(t)\times[\mathbf{m}_i(t)\times\mathbf{B}_i^{eff}(\mathbf{r}_i)] \quad , \tag{9.14}$$

where α is now a constant that can be adjusted to ensure rapid convergence to the ground state (or, at least, the nearest local minimum). Dividing Eq. (9.14) by $m_i(t)$ immediately leads to an equation of motion for the time-dependent orientations $\hat{e}_i(t)$,

$$\frac{d\hat{e}_i(t)}{dt} = \gamma \hat{e}_i(t) \times \mathbf{B}_i^{eff}(\mathbf{r}_i) + \lambda \left[\hat{e}_i(t) \times \left[\hat{e}_i(t) \times \mathbf{B}_i^{eff}(\mathbf{r}_i) \right] \right] \quad , \tag{9.15}$$

with $\mathbf{B}_i^{eff}(\mathbf{r}_i)$ being an effective magnetic field averaged over the cell centered at $\mathbf{R}_i$.

9.5 First principles spin dynamics for magnetic systems nanostructured in two dimensions

Suppose that in Eq. (2.20) the Kohn–Sham–Dirac Hamiltonian is of the following form

$$H(\mathbf{r}) = c\,\boldsymbol{\alpha}\cdot\mathbf{p} + \beta mc^2 + V(\mathbf{r}) + \beta\,\boldsymbol{\sigma}\cdot(\mathbf{B}(\mathbf{r}) + \mathbf{B}^{con}(\mathbf{r})) \quad , \tag{9.16}$$

where according to the requirements of multiple scattering

$$V(\mathbf{r}) = \sum_{n=1}^{N} V_n(\mathbf{r}_n) \quad , \quad \mathbf{B}(\mathbf{r}) = \sum_{n=1}^{N} \mathbf{B}_n(\mathbf{r}_n) \quad , \quad \mathbf{B}^{con}(\mathbf{r}) = \sum_{n=1}^{N} \mathbf{B}_n^{con}(\mathbf{r}_n) \quad ,$$
$$D_{V_n} = D_{\mathbf{B}_n} = D_{\mathbf{B}_n^{con}} \quad , \quad D_{V_n} \cap D_{V_m} = D_{V_n}\delta_{nm} \quad ,$$

and the $\mathbf{B}_n^{con}(\mathbf{r})$ are constraining fields,

$$\mathbf{B}_n^{con}(\mathbf{r}_n) = -\mathbf{B}_n^{eff}(\mathbf{r}_n) \quad . \tag{9.17}$$

9.5.1 FP-SD & ECM

Going back now to Section 4.13 dealing with the Embedded Cluster Method, let $\mathbf{t}_{\rm h}(z;\hat{e}_h(t))$ denote a diagonal (super-) matrix of single-site t-matrices in the case that only unperturbed host atoms *would* occupy a particular cluster $\mathcal{C}$ comprising N sites of a system characterized by a simple lattice $\mathcal{L}^{(2)}$,

$$\mathbf{t}_{\rm h}(z;\hat{e}_h(t)) = \{\underline{t}^n(z;\hat{e}_h(t))\delta_{nm} \mid \underline{t}^n(z;\hat{e}_h(t)) = \underline{t}_{\rm h}(z;\hat{e}_h(t)) \quad , \quad \forall \mathbf{R}_n \in \mathcal{C}\} \quad , \tag{9.18}$$

where $\hat{e}_h(t)$ refers to the uniform direction of the magnetization in all sites of the host.

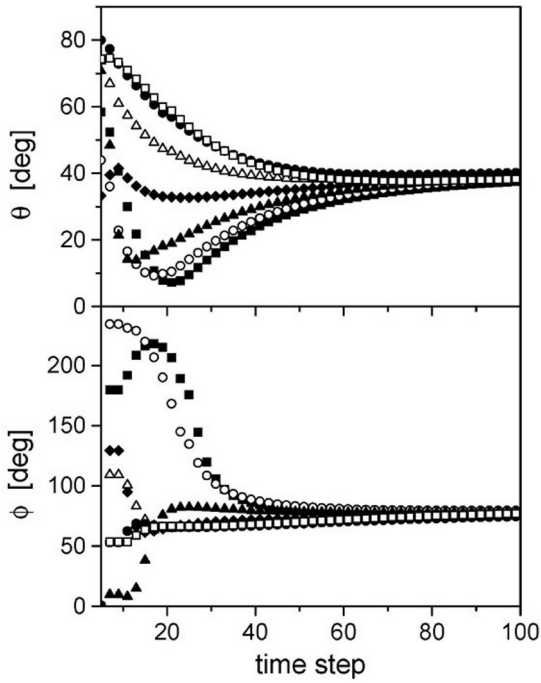

FIGURE 9.1: *Artificial time evolution of the angles θ (top) and the ϕ (bottom) angles defining the orientation of the spin moments for the seven Co atoms in the finite chain depicted in Fig. 4.1. The symbols refer to the following Co atoms numbered from the left to the right in the bottom part of Fig. 4.1: 1: full squares, 2: open circles, 3: full triangles, 4: full diamonds, 5: open triangles, 6: full circles and 7: open squares. Shown are the results for only the first 100 time steps. During the next 900 time steps the angles converge very smoothly. From Ref. [9].*

Furthermore, let $\mathbf{t}_{\mathcal{C}}(z;\{\hat{e}_n(t)\})$ be that matrix that refers to the actual occupation *and* orientation $\hat{e}_n(t)$ of the various sites in $\mathcal{C}$,

$$\mathbf{t}_{\mathcal{C}}(z;\{\hat{e}_n(t)\}) = \{\underline{t}^n(z;\hat{e}_n)\delta_{nm} \mid \underline{t}^n(z;\hat{e}_n) \neq \underline{t}_{\rm h}(\epsilon;\hat{e}_h(t)) \quad , \quad \forall \mathbf{R}_n \in \mathcal{C}\} \quad ; \tag{9.19}$$

then the scattering path operator $\boldsymbol{\tau}_{\mathcal{C}}(z;\{\hat{e}_n(t)\})$ comprising all sites in $\mathcal{C}$ is given by the following Dyson-like equation,

$$\begin{aligned}\boldsymbol{\tau}_{\mathcal{C}}(z;\{\hat{e}_n(t)) &= \boldsymbol{\tau}_{\rm h}(z;\{\hat{e}_n(t)) \\ &\times \left[1 - (\mathbf{t}_{\rm h}^{-1}(z;\hat{e}_h(t)) - \mathbf{t}_{\mathcal{C}}^{-1}(\epsilon;\{\hat{e}_n(t)))\tau_{\rm h}(z;\{\hat{e}_n(t))\right]^{-1} \quad ,\end{aligned} \tag{9.20}$$

from which in turn iteratively all corresponding local quantities, i.e., charge

$\rho_n(z;\hat{e}_n(t))$ and magnetization densities $\mathbf{m}_n(z;\hat{e}_n(t))$, see Eqs. (4.17) - (4.21), can be calculated and thus self-consistently also a new set of potentials and exchange fields. For an extended review article concerning first principles spin dynamics in the context of the embedded cluster method, see Ref. [10].

From the point of view of searching for the magnetic ground state of a system it is sufficient to consider only the second (damping) term on the *rhs* of Eq. (9.15). The evolution of the orientations is then measured on a time scale with a unit (time step) of the inverse Gilbert damping constant in Eq. (9.14), $1/\lambda$. A stable ground state is achieved by a concomitant convergence of all θ_i and ϕ_i to intrinsic constants and (additionally) of the constraining fields to zero.

In Fig. 9.1 the evolution of the θ_i and ϕ_i is plotted for the first 100 steps in this artificial time scale for each Co atom in a chain of seven Co atoms along a Pt(111) edge; see also Fig. 4.1 in Chapter 4. In this calculation the initial directions of the atomic magnetic moments were set by a random number generator. It can be seen that after some oscillations both the θ and ϕ angles approach a very similar value for all the Co atoms. Further details of this study are discussed in Chapter 13, dealing with the properties of the anisotropy energy in solid systems nanostructured in two dimensions.

[1] W. F. Brown, *Micromagnetics*, (Interscience, New York, 1963)

[2] T. Gilbert, Armour Research Foundation, Report No. 11, (Illinois Institute of Technology, 1955).

[3] T. L. Gilbert, Phys. Rev. **100** 1243, (1955).

[4] A. Aharoni, *Introduction to the Theory of Magnetism*, Oxford Science Publications (Oxford, 2000).

[5] G. M. Stocks, B. Újfalussy, Xindong Wang, D. M. C. Nicholson, W. A. Shelton, Yang Wang, A. Canning and B. L. Györffy, Philos. Mag. B **78**, 665 (1998).

[6] Újfalussy, B., X. Wang, D. M. C. Nicholson, W. A. Shelton, G. M. Stocks, Y. Wang, and B. L. Györffy, J. Appl. Phys. **85**, 4824 (1999).

[7] P. H. Dederichs, S. Blügel, R. Zeller and H. Akai, Phys. Rev. Lett. **53**, 2512, (1984).

[8] V. P. Antropov, M. I. Katsnelson, B. N. Harmon, M. van Schilfgaarde, and D. Kusnezov, Phys. Rev. B **54**, 1019 (1996).

[9] B. Újfalussy, B. Lazarovits, L. Szunyogh, G. M. Stocks, and P. Weinberger, Phys. Rev. B **70**, 100404(R) (2004).

[10] G. M. Stocks, M. Eisenbach, B. Újfalussy, B. Lazarovits, L. Szunyogh, and P. Weinberger, Prog. Mat. Sci. **52**, 371 (2007).

10

The multiple scattering scheme

This chapter essentially is intended to give an overview over all those concepts that were introduced up-to-now. It is also meant for all those readers that are not interested in formal details.

Multiple scattering can in principle be expressed in terms of the so-called scattering path operator $\boldsymbol{\tau}(z)$, which in turn is defined by two kinds of quantities, namely single site t matrices $\mathbf{t}(z)$ and so-called structure constants $\mathbf{G}_0(z)$:

$$\boxed{\boldsymbol{\tau}(z) = \left(\mathbf{t}(z)^{-1} - \mathbf{G}_0(z)\right)^{-1}}$$

The quantities $\boldsymbol{\tau}(z)$, $\mathbf{t}(z)$ and $\mathbf{G}_0(z)$ are matrices with rows and columns labelled by sites defined by location vectors $\mathbf{R}_n$,

$$\boxed{\boldsymbol{\tau}(z) = \{\underline{\tau}^{nm}(z)\} \quad , \quad \mathbf{t}(z) = \{\underline{t}^{n}(z)\,\delta_{nm}\} \quad , \quad \underline{t}^{n}(z) = \{t^{n}_{\Lambda\Lambda'}(z)\}}$$

$$\boxed{\mathbf{G}_0(z) = \{\underline{G}_0^{nm}(z)\,(1-\delta_{nm})\} \quad , \quad \underline{G}_0^{nm}(z) = \left\{G^{nm}_{0,\Lambda\Lambda'}(z)\right\}}$$

each matrix element being itself a matrix labelled by angular momentum quantum numbers, namely

$$\boxed{\Lambda = \begin{cases} L = (\ell m)\ , \text{ non-relativistic} \\ Q = (\kappa\mu)\ , \text{ relativistic} \end{cases}}$$

The location vectors $\mathbf{R}_n$ can refer to atomic positions in an infinite (bulk), semi-infinite (bulk with surface) or finite solid (cluster) system, or specify positions in the vacuum. From the scattering path operator the single particle Green's function can directly be obtained and therefore all related physical properties. In the presence of three- or two-dimensional translational symmetry use can be made of lattice Fourier transformations.

In Fig. 10.1 all the options available in using a multiple scattering scheme are compiled.

10.1 The quantum mechanical approach

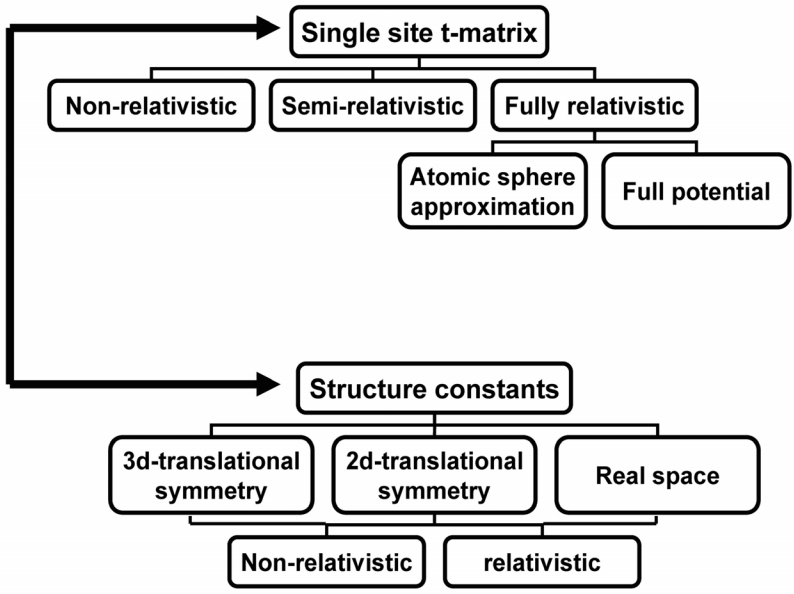

FIGURE 10.1: *The various options to use a Korringa-Kohn-Rostoker (KRR) type multiple scattering approach self-consistently within the framework of local Density Functional Theory. For matters of magnetic anisotropy effects only the (fully relativistic) options apply.*

10.2 Methodological aspects in relation to magnetic anisotropies

The very reason for using a Green's function approach of this type is quite obvious from Fig. 10.2, since very important features not accessible in so-called "wave function approaches" to the Density Functional Theory can be included even on a fully relativistic level, namely disorder, temperature effects and even time dependence. Disorder, for example, appears at a first glance as an academic issue. However, since, e.g., permalloy, Ni_cFe_{1-c}, most likely is the most prominent magnetic system used in spintronics, the possibility to treat statistically disordered semi-infinite systems is of utter importance. Similar arguments pertain for temperature effects.

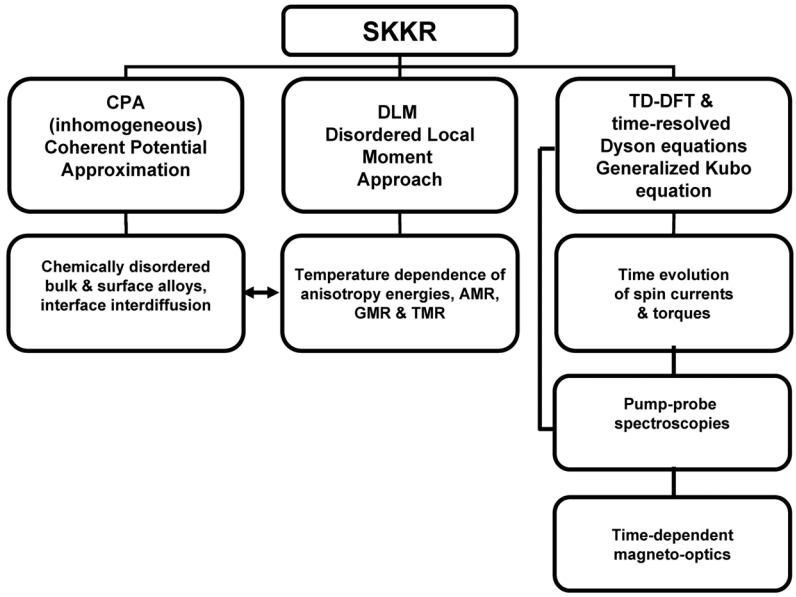

FIGURE 10.2: *Additional features of the multiple scattering scheme.*

10.3 Physical properties related to magnetic anisotropies

As already said at the very beginning of this book: magnetic nanostructured systems are not interesting *per se*, but because of their extraordinary physical properties. Additional concepts are therefore needed not only to describe electric and magneto-optical properties, but also to provide suitable parameters for structural simulations.

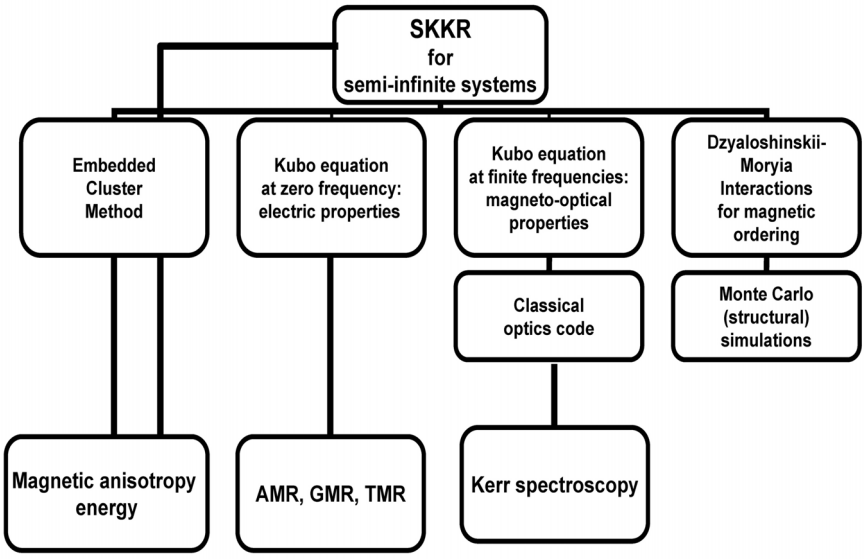

FIGURE 10.3: *Additional approaches based on the multiple scattering scheme.*

In the following chapters particular aspects depicted either in Fig. 10.2 or Fig. 10.3 are discussed, dealing, however, with transport properties in separate chapters.

11

Nanostructured in one dimension: free and capped magnetic surfaces

Although a distinction between capped magnetic surfaces and spin valves is a bit artificial, in terms of devices such a separation does make sense. Here mainly properties of the magnetic anisotropy energy in free and capped magnetic surfaces such as reorientation transitions, influence of the orientation of the substrate or effects of alloying are discussed. Furthermore, as a special case of an anisotropic behavior the so-called interlayer exchange coupling is introduced.

11.1 Reorientation transitions

In search of systems that show perpendicular magnetism in the last two decades a large number of experimental studies was published in which the magnetic properties of finite films of Fe, Co or Ni on noble metal substrates were investigated. It turned out that in quite a few cases the experimental set-ups had to be improved considerably in order to produce laboratory-independent results. There were (are) even a few systems that gave rise to heated discussions concerning the reported findings. Most prominently in this respect were (are?) the systems Ni and Fe on Cu(100), since not only the kind of deposition mattered, but also the concentration of remaining gases in the high vacuum chamber was (is) of crucial importance. In particular layer relaxation at and in surface near regions seemed to dependent strongly on growth and vacuum conditions.

In the following, first two kinds of systems, namely Fe_n/Au(100) and Co_m/Ni_n/Cu(100), are chosen in order to illustrate a very important property of magnetically coated surface, the so-called reorientation transition, which occurs at some materials-dependent critical thickness. The first example is shown because later in Chapter 18 this system will be discussed again in terms of *ab-initio* magneto-optics, i.e., in terms of theoretical concepts describing the actually measured quantities. The second system, which in fact shows

two reorientation transitions, serves to introduce the concept of layer-resolved quantities, which turned out to be extremely useful not only for the interpretation of experimentally determined magnetic anisotropy constants but also for related properties such as electric transport.

Further on additional aspects like alloying effects or the use of "superstructures" will be discussed in order to characterize the diversity of phenomena to be encountered in dealing with the magnetic anisotropy energy of free or capped surfaces, i.e., in the search of perpendicularly magnetized systems.

11.1.1 The Fe_n/Au(100) system

In 1990 Liu and Bader communicated [1] that when grown at 100 K Fe films on Au(100) have a magnetization perpendicular to the surface for thicknesses of less then 2.8 monolayers (ML) and an in–plane magnetization beyond that.

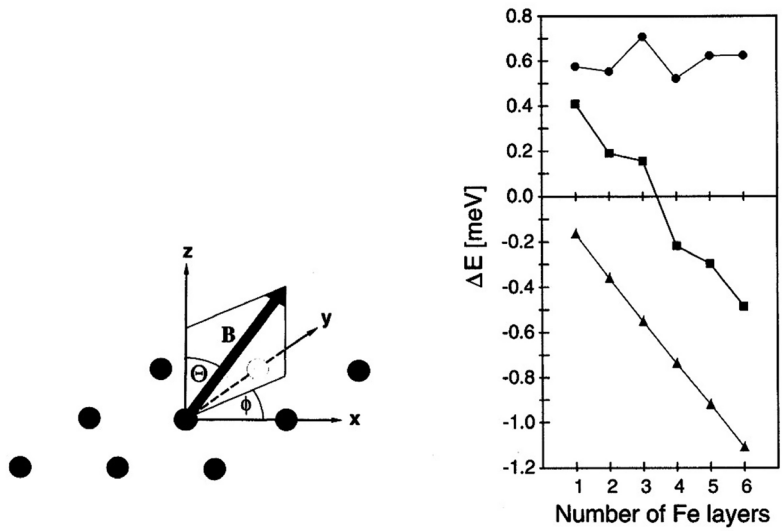

FIGURE 11.1: *Left: Magnetic field pointing into a general direction characterized by angles Θ and ϕ, relative to a two–dimensional square lattice. Right: Calculated magnetic anisotropy energies for Fe multilayers on Au(001). $\Delta E_{\rm b}$: circles, $\Delta E_{\rm dd}$: triangles, $\Delta E = \Delta E_{\rm b} + \Delta E_{\rm dd}$: squares. Solid lines serve as a guide for eye. From Ref. [2].*

Using the magnetic force theorem (Section 6.2) Szunyogh *et al.* [2] for the first time applied the fully relativistic approach in terms of the Atomic Sphere

Approximation in order to evaluate the difference $\Delta E_b(n)$ of the band energies,

$$\Delta E_b(n) = E_b(n; \|) - E_b(n; \perp) \quad , \tag{11.1}$$

where n denotes the number of Fe monolayers on Au(100), with the magnetic field pointing (a) perpendicular to the surface ($\perp$) and (b) along the x axis of the 2D square lattice ($\|$); see the left part of Fig. 11.1. Taking also into account the corresponding difference in the magnetic dipole-dipole energy $\Delta E_{dd}(n)$ (Section 6.3), the resulting magnetic anisotropy,

$$\Delta E(n) = \Delta E_b(n) + \Delta E_{dd}(n) \quad , \tag{11.2}$$

displayed in Fig. 11.1 as a function of n, was found to reproduce the experimentally observed reorientation transition rather well. This particular figure confirmed the view that a reorientation of the magnetization from perpendicular to in-plane is essentially caused by an increase in the shape anisotropy $\Delta E_{dd}(n)$ with increasing thickness of the magnetic overlayer. The critical thickness, however, at which this transition occurs is governed by $\Delta E_b(n)$. The band energy contribution to the magnetic anisotropy energy has to be positive and large enough in order to give rise to a reorientation transition. Both $\Delta E_b(n)$ and $\Delta E_{dd}(n)$ are materials-specific quantities. While $\Delta E_{dd}(n)$ is always negative and increasing with n, no *a priori* rules for $\Delta E_b(n)$ can be given. In some systems $\Delta E_b(n)$ is positive, in others negative. The search for suitable systems showing perpendicular magnetism is therefore a search for systems with a large enough $\Delta E_b(n)$.

11.1.2 The system $Co_m/Ni_n/Cu(100)$

11.1.2.1 The first reorientation transition

Thin films of Ni on Cu(100) show an unexpected behavior of magnetic (reorientation) phase transitions, since in contrast to quite a few other magnetic thin films on noble metal surfaces the moments first line up in-plane and then reorient to an out-of-plane (perpendicular) direction. For free surfaces of Ni on Cu(100) this reorientation occurs between $n = 7$ [3, 4] and $n = 10 - 11$ [5, 6]. For $n > 37$ [7] the magnetization eventually switches back to in-plane. Experimentally it was found that adsorbates strongly influence the critical thickness. In particular it was found that at 170 K the adsorption of about 2 Langmuir H_2 reduces the critical thickness for the first reorientation from about 10 to 7 ML.

In theoretical investigations it turned out [8, 9] that the magnetic anisotropy energy as a function of the number of Ni layers is extremely sensitive to layer relaxation. The left half of Fig. 11.2 shows these effects considering three different uniform relaxations with respect to the interlayer distance of the Cu(100) substrate, referred to in this figure as the unrelaxed case.

The reason for this behavior can easily be seen by considering layer-resolved band energies. Since in Eq. (6.14) a sum over sites has to be performed, by

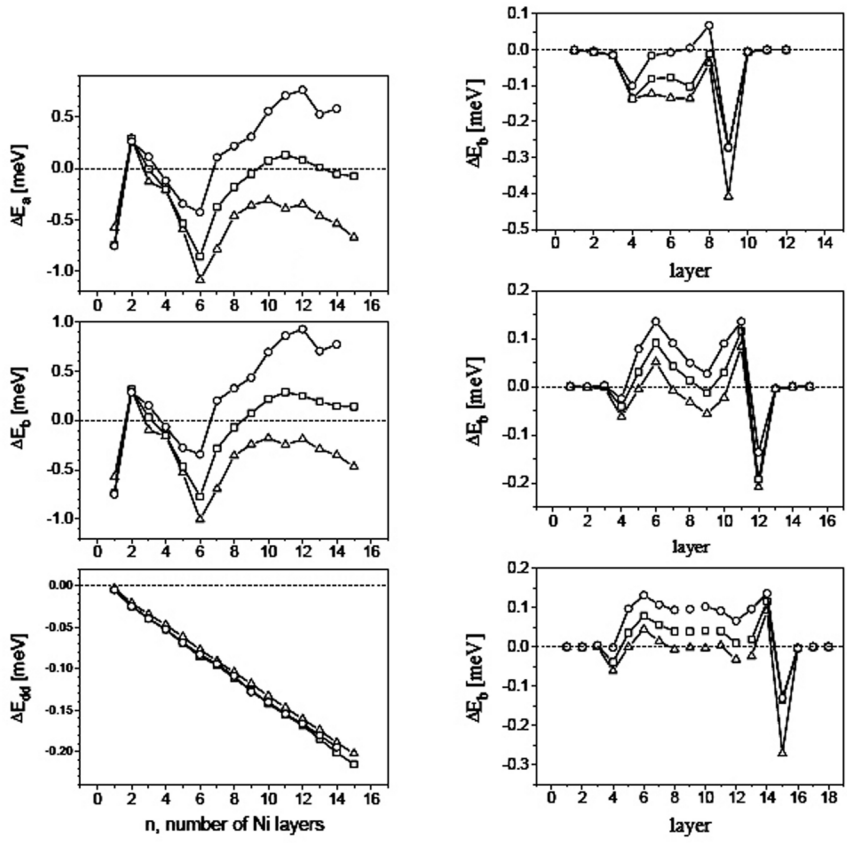

FIGURE 11.2: *Left: Magnetic anisotropy energy ΔE_a (top), band energy difference ΔE_b (middle) and magnetic dipole-dipole energy difference ΔE_{dd} (bottom) versus the number of Ni layers on Cu(100). Triangles, squares and circles refer in turn to a uniform relaxation by 0, -2.5 and -5.5%, i.e., to a c/a ratio of 1, 0.975 and 0.945 with respect to the interlayer spacing in bulk Cu. Right: Layer resolved band energy differences ΔE_b^n for 6 (top), 9 (middle) and 12 (bottom) Ni-layers on Cu(100). Triangles, squares and circles refer in turn to a uniform relaxation by 0, -2.5 and -5.5%. From Ref. [8].*

using an appropriate lattice Fourier transformation for a layered system this sum reduces to a sum over layers. For a system with m magnetic layers on top of a suitable substrate, the band energy part $\Delta E_b(m, N)$ of the anisotropy energy can therefore be split into contributions arising from the individual atomic layers. The summation extends over all contributing atomic layers, i.e., includes also a sufficient number m_S of the substrate and vacuum layers m_V; see, e.g., Eq. (2.9) in section 2.2,

$$\Delta E_b(m;N) = \sum_{i=1}^{N} \Delta E_b^i(m) = \sum_{i=1}^{N} E_b^i(m;\|) - E_b^i(m;\perp) \quad , \tag{11.3}$$

$$N = m + m_S + m_V \quad , \tag{11.4}$$

$$\Delta E_b^i(m) = \int_{\curvearrowright}^{E_F} (n_i(m;\|,z) - n_i(m;\perp,z))\, z dz \quad . \tag{11.5}$$

In Eq. (11.5) the $n_i(m;\xi,z)$ are layer-dependent densities of states corresponding to ξ being either $\|$ or $\perp$. These quantities can directly be evaluated using Eq. (4.103).

In the following, mostly the below-short-term notation for the quantities in Eqs. (11.2) and (11.5) will be used. Only in very particular cases necessary specifications with respect to the number of certain atomic layers shall be made.

ΔE_a :	anisotropy energy
ΔE_b :	band energy
ΔE_b^i :	layer-resolved band energy
ΔE_{dd} :	magnetic dipole-dipole energy

In the right part of Fig. 11.2 the layer resolved band energy differences ΔE_b^i are shown for 6, 9 and 12 Ni-layers on Cu(100). One can see that the surface and interface contributions are negative, the surface giving the larger contribution, and that relaxation predominantly increases the contribution from interior layers in the Ni films.

The anisotropic part of the free energy for magnetic multilayer systems, see, e.g., Ref. [10] and references therein, is phenomenologically very often described by

$$E = 2\pi M^2 \cos^2\theta + K_2 \cos^2\theta \quad , \tag{11.6}$$

$$K_2 = K_2^v + K_2^s/d \quad , \tag{11.7}$$

where K_2 refers to the second order term of the magnetic anisotropy energy and θ denotes the angles of the magnetization $\mathbf{M}$ with respect to the surface normal. As indicated in Eq. (11.7), where d refers to the film thickness, K_2 is thought to consist of two parts, namely a thickness-independent, "volume"-like contribution K_2^v and a thickness-dependent "interface-surface"-like contribution K_2^s.

By picking up in Eq. (11.3) the individual contributions from (1) the Cu/Ni interface ($K_2^{S_1}$), (2) the Ni/Vacuum interface ($K_2^{S_2}$), and (3) a layer averaged contribution from the interior (K_2^I, remainder divided by the number of interior Ni layers), one easily can identify these quantities with the second order constants in Eq. (11.6):

$$K_2^v = K_2^I, \quad K_2^s = K_2^{S_1} + K_2^{S_2} \quad . \tag{11.8}$$

Although such an identification seems to be quite intriguing, one has to keep in mind that the only well-defined quantity is ΔE_b. The grouping of terms in the sum in Eq. (11.3) over layer dependent contributions merely serves purposes of interpretation.

11.1.2.2 The second reorientation transition

By capping the Ni films with Co, measurements revealed that the orientation of the magnetization switches to in-plane with an increasing number of Co layers. Epitaxial Cu(100)/Ni(8 Å)/Co(2-10 Å)/Ni(17 Å)/Cu structures, e.g., did not show a perpendicular magnetic anisotropy; in fact, 2 Å Co turned out to be the critical thickness for a perpendicular magnetization. Furthermore, the system Si(100)/Cu(1000 Å)/Ni(60 Å)/Co(step-wedge)/Cu(30 Å) was studied [11] in an attempt to control the critical thickness for the perpendicular magnetization: it was found that the magnetization turns in-plane at a critical Co thickness of 6.15±1.25 Å. As reported by O'Brien *et al.* [7] strain relaxations in the Ni layers set in beyond about 13 of (-5.5%) uniformly relaxed Ni layers.

In order to deal with this rather complex situation the concept of layer-resolved contributions to the anisotropy energy is again of great help. Considering the following obviously quite different systems (Table 11.1), it turned out that in fact, in terms of a simulation model, they can be stacked together.

Table 11.1: *Second reorientation transition in Ni_n/Cu(100): stacking of different systems.*

system A	fcc Cu(100)/Ni_{15}(-5.5%)/Ni_{12}(0%)/Vac
system B	fcc Cu(100)/Ni_{21}(-5.5%)/Vac
system C	fcc Ni(100)/Ni_{18}(0%)/Vac
system D	fcc Ni(100)/Ni_{12}(0%)/Co_m/Vac
system E	fcc Cu(100)/Ni_{n_1}(-5.5%)/Ni_{n_2}(0%)/Co_m

In the left part of Fig. 11.3 the layer-resolved band energies are displayed for the uncapped systems. In the top part of this figure *system A* and *B* are

compared with each other by viewing both systems from the side of the Cu substrate (left-hand-side). Evidently, the layer-resolved band energies of the first 13 Ni layers from the left (Cu/Ni interface) in *system A* hardly differ from those of *system B*. In the bottom part of Fig. 11.3 *system A* is compared with *system C* by viewing both from the vacuum (right-hand) side. Apparently again, the first 12 layer-resolved contributions from the right in *system A* are very close in value to those in *system C*.

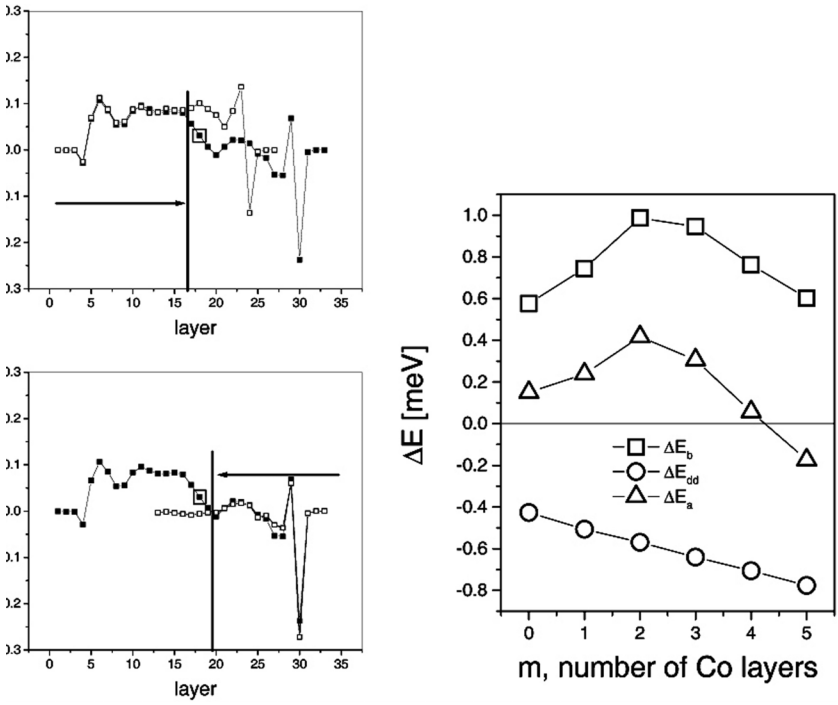

FIGURE 11.3: *Left: Comparison of the layer-resolved band energy contributions* ΔE_b^n *of* $\overline{Cu(100)}/Ni_{15}$*(-5.5%)/*$Ni_{12}$*(0.0%) (system A, squares) with* $Cu(100)/Ni_{21}$*(-5.5%) (system B, open squares, top), and in* $Ni(100)/Ni_{18}$ *(system C, open squares, bottom). In all cases the first layers to the right denote vacuum layers. In the case of system A the first three layers to left refer to Cu layers. The view from the Cu/Ni and from the Ni/Vac interface is indicated by arrows. The small boxes denote the last relaxed Ni layer in system A. Right: Calculated band energy,* ΔE_b *and magnetic dipole-dipole energy contributions,* ΔE_{dd} *to the total magnetic anisotropy energy,* ΔE_a *in* $Cu(100)/Ni_{13}$*(-5.5%)/*Ni_{17}*(0%)/*Co_m*. From Ref. [12].*

From Fig. 11.3 it is obvious that in *system A* a transition region of about three layers can be identified (see thick vertical lines) situated between a regime of layers corresponding to an in-plane lattice constant of fcc Cu and a 5.5%-contracted interlayer spacing (*regime 1*) and a regime of layers corresponding to a parent fcc Ni lattice (*regime 2*), since outside of this transition region the layer-resolved contributions seem to be unaffected by the interface between *regime 1* and *regime 2*.

If therefore n_1 denotes the number of tetragonally relaxed Ni layers on fcc Cu(100) and n_2 the number of unrelaxed Ni layers on top of fcc Ni(100) the total band energy contribution to the magnetic anisotropy energy can be estimated by adding up the corresponding contributions from both systems. Since for ΔE_{dd} similar arguments apply, an estimate of ΔE_a for *system E* ($m = 0$) as a function of $n_1 (> 8)$ and $n_2 (> 10)$, $n_1 + n_2 = n$, can be given.

Experimental studies showed that the critical thickness for a reorientation transition from perpendicular to in-plane in $Cu(100)/Ni_n$ is between $n = 37$ [3] and $n = 41$ [7]. Furthermore, from these and related studies it seems that about 13 ML of Ni on Cu(100) is the critical thickness for the pseudomorphic region. Using this value for n_1, for free surfaces of Ni on Cu(100) the above model predicted [12] the (second) reorientation transition to occur at 38 Ni layers which clearly enough is in good agreement with the experimental findings.

For $n_1 = 13$ and $n_2 = 17$ the calculated results for ΔE_b, ΔE_{dd} and ΔE_a are displayed in Fig. 11.3 as a function of the number of capping Co layers, m. Although, as to be expected, ΔE_{dd} decays monotonously, the magnitude of ΔE_a with respect to m is clearly governed by ΔE_b leading to a maximum at $m = 2$ and a reorientation transition at about $m = 4$.

11.1.3 Influence of the substrate, repetitions

As can be imagined the orientation of the substrate is of quite some importance for the size and the sign of the anisotropy energy, just as well as preparing repetitions of overlayer structures ("*superstructures*") is an excellent tool to design systems with a perpendicular orientation of the magnetization.

An example of this particular feature of the anisotropy energy is to be found in Fig. 11.4. This figure shows in particular that independent of the surface orientation free surfaces of Co on Pt are oriented always in-plane, the actual anisotropy, however, being almost twice as large in value for Pt(111) than for Pt(100).

Rather spectacular are the consequences when repeating double layers of CoPt on top of Pt(100) and Pt(111). As can be seen from the right part of Fig. 11.4 not only is the orientation of the magnetization now parallel to the surface normal, but the differences between a Pt(111) and a Pt(100) substrate are indeed striking. For both types of substrates, the anisotropy energy is increasing nearly linearly with the number of repetitions; in the case of a Pt(111) substrate it is by a factor of about 5 bigger than for Pt(100).

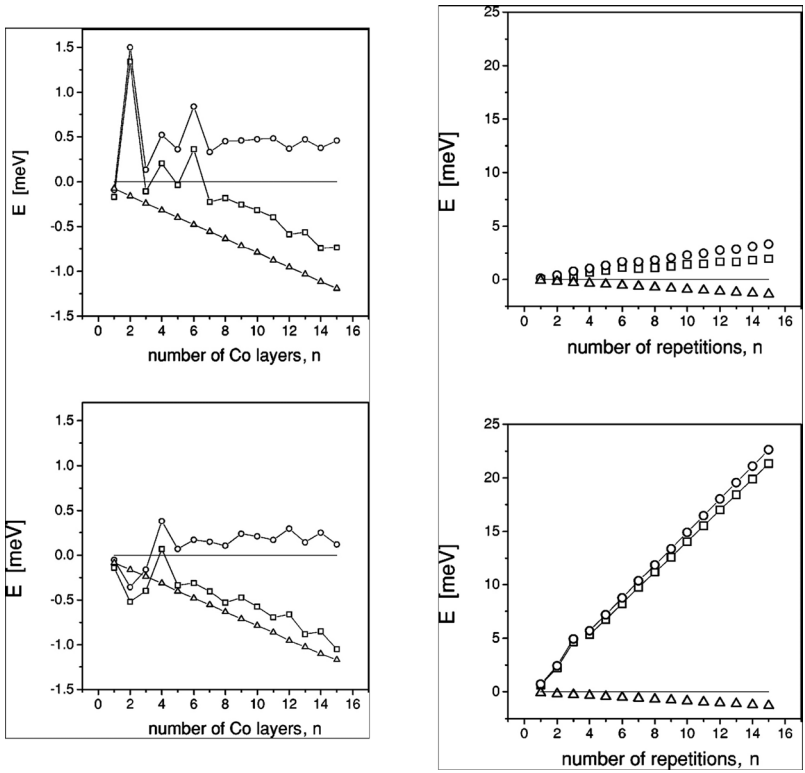

FIGURE 11.4: *Left: Magnetic anisotropy energy and its contributions for free surfaces of Co_n on Pt(100) (top) and Pt(111) (bottom). Right: Magnetic anisotropy energy and its contributions for free surfaces of the superstructure $(CoPt)_n$ on Pt(100) (top) and Pt(111) (bottom). E_a, E_b and E_{dd} are denoted in turn by squares, circles and triangles. From Ref. [13].*

This feature of "superstructures" was exploited in quite a few experimental studies by generating $(\mathrm{Co}_n\mathrm{Pt}_m)$ slabs r times repeated.

An interesting question is that of what happens if alloying between Co and Pt occurs. In using the Coherent Potential Approximation, see Chapter 5, a layer-resolved band energy contribution $\Delta E_b^i(m)$ in Eq. (11.3) is then of the form

$$\Delta E_b^i(m) = \sum_{\alpha=A,B} c_\alpha^i \Delta E_b^{i,\alpha}(m) = \sum_{\alpha=A,B} c_\alpha^i \left(E_b^{i,\alpha}(m;\|) - E_b^{i,\alpha}(m;\perp) \right) \quad , \tag{11.9}$$

where c_α^i is the concentration of constituent α = Co, Pt in the i-th atomic layer. In the averaging of the magnetic dipole-dipole interaction, see Eq. (6.16),

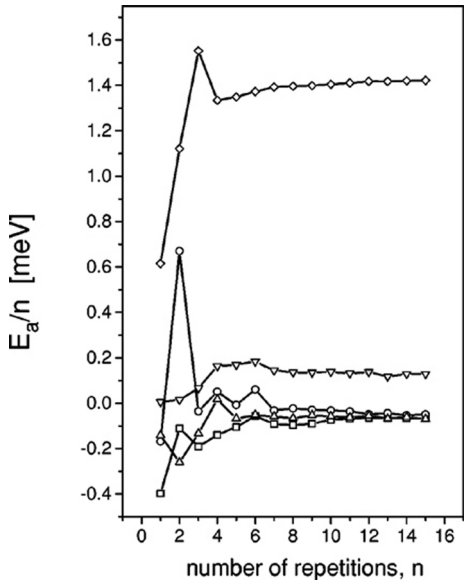

FIGURE 11.5: *Magnetic anisotropy energy per repetition n for Pt(100)/Co_n (circles), Pt(111)/Co_n (up triangles), Pt(100)/$(CoPt)_n$ (down triangles), Pt(111)/$(CoPt)_n$ (diamonds) and $(Co_{0.5}Pt_{0.5})_n$ (squares). From Ref. [13].*

possible vertex corrections are usually neglected [14],

$$\langle \mathbf{m}_i \cdot \mathbf{m}_i \rangle \simeq \langle \mathbf{m}_i \rangle \cdot \langle \mathbf{m}_j \rangle \quad , \tag{11.10}$$

$$\langle \mathbf{m}_i \rangle = \sum_{\alpha=A,B} c_i^\alpha \mathbf{m}_i^\alpha \quad . \tag{11.11}$$

In all above-mentioned Co/Pt systems the magnetic anisotropy energy per number of repetition n, E_a/n, see Fig. 11.5, tends to a constant for a sufficiently large n, which in the case of the superstructure (CoPt) on Pt(111) is surprisingly large, namely about 1.4 meV.

It is by now a rather well-known fact that in semi-infinite systems the magnetic anisotropy energy is by orders of magnitude larger than comparable bulk-values. For example, in an evaluation [16] of the magnetic anisotropy energy of bulk Co_cPt_{1-c} alloys the largest value was found for $c = 0.50$, which, however, amounted to only 3 μeV.

11.1.4 Alloying, co-evaporation

Thin films of Fe and Co have different orientations of the easy axis on Cu(001): Fe films up to a thickness of at least ten ML's show experimentally an out-of-plane magnetization [17], while thin Co films are magnetized in-plane [18].

Thus, an interesting behavior is to be expected when alloying Fe with Co, i.e., to address the question, whether regions of different preferred orientations of the magnetization can be identified as a function of the number of magnetic layers and of the alloy composition.

Table 11.2: *Calculated spin–only magnetic moments [μ_B] of Fe in $Cu_mFe_n/Cu(001)$ multilayers, $n = 1, 2, \ldots, 7$, corresponding to the antiferromagnetic ground state. The numbering of the Fe layers increases from the vacuum (or capped) side towards the bulk. For comparison the case of $n = 2$ is included here although the ground state refers to the ferromagnetic configuration. A parallel or antiparallel orientation of the magnetization along the surface normal is indicated by a plus and minus sign, respectively. From Ref. [21].*

n	m	Fe(7)	Fe(6)	Fe(5)	Fe(4)	Fe(3)	Fe(2)	Fe(1)
2	0						-2.340	2.355
	∞						-2.207	2.207
3	0					-2.121	2.297	2.820
	∞					2.232	-1.428	2.232
4	0				2.262	-1.430	2.259	2.788
	∞				-2.130	-2.094	2.094	2.130
5	0			-2.224	1.453	-1.506	2.245	2.793
	∞			2.507	2.147	-1.609	2.147	2.507
6	0		2.523	2.089	-2.029	-2.022	2.162	2.789
	∞		2.509	2.069	-2.029	-2.029	2.069	2.509
7	0	-2.232	1.534	-1.450	1.779	-1.457	2.264	2.802
	∞	2.520	2.264	-1.939	-1.753	-1.939	2.264	2.520

Since only antiferromagnetically coupled Fe-layers on Cu(001) exhibited perpendicular magnetism up to a film thickness of at least seven atomic layers, see Table 11.2, while when ferromagnetically arranged the moments were oriented in-plane [19], also for Fe-rich Fe/Co thin films the type of the magnetic interlayer coupling proved to be of crucial importance. Only after having determined the correct magnetic ground state configuration this configuration can be used for the determination of the magnetic anisotropy energy.

In Fig. 11.6 a "phase diagram" of reorientations in $(Fe_xCo_{1-c})_n/Cu(100)$ is shown with respect to the number of layers n and x, the concentration of Fe. The corresponding experimental data [22], generated by co-evaporation of Fe and Co in a temperature range between 120 and 300 K suggested, however, that the reorientation transition occurs already at a film thickness of two monolayers, and that above four monolayers, only an in–plane magneti-

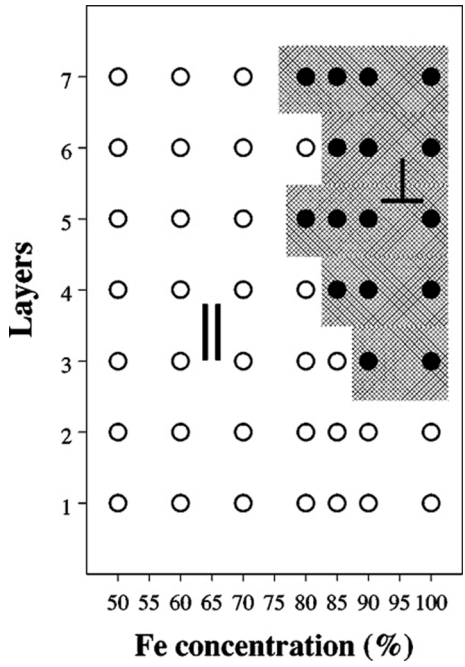

FIGURE 11.6: "*Phase diagram*" *of the reorientation transition in terms of regions of perpendicular and in-plane magnetization. Solid circles in the shaded region correspond to a positive magnetic anisotropy energy and therefore to a perpendicular magnetization. Open circles indicate a negative magnetic anisotropy energy and an in-plane orientation of the magnetic moments. From Ref. [14].*

zation is present (except for Fe concentrations close to one). Since at a given composition finite temperatures most likely decrease the critical thickness of the film at which the reorientation occurs, the "phase field" of perpendicular orientation in the phase diagram of Ref. [22] is expected to move also in the experiment to larger film thicknesses as the temperature approaches $T = 0$ K.

11.1.5 Oscillatory behavior of the magnetic anisotropy energy

Very often for matters of protection in experimental studies magnetic overlayers (free surfaces) were covered by more or less thin caps of a suitable chemically inert metal such as Cu or Au. However, this procedure caused additional effects, since the magnetic anisotropy energy proved to depend

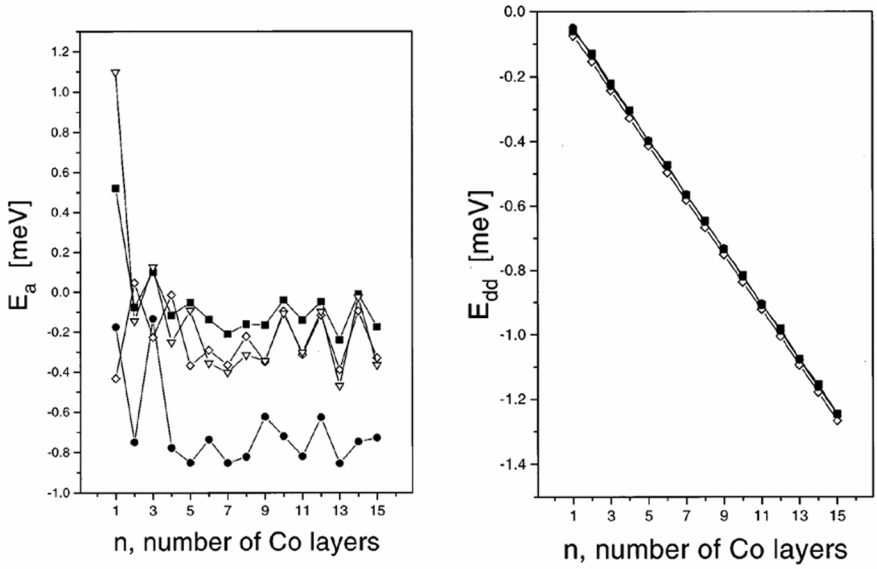

FIGURE 11.7: *Left: Band energy contribution to the magnetic anisotropy energy as a function of the number of Co layers in Cu(100)/Co_n (diamonds), Cu(100)/Co_n/Cu(100) (squares), Cu(100)/$AuCo_nAu$/Cu(100) (circles) and Cu(100)/$Co_nCu_3Co_n$/Cu(100) (triangles). Right: Magnetic dipole-dipole energy contribution to the magnetic anisotropy energy as a function of the number of Co layers in Cu(100)/Co_n (diamonds), Cu(100)/Co_n/Cu(100) (squares), and Cu(100)/$AuCo_nAu$/Cu(100) (circles). From Ref. [20].*

characteristically on the thickness of such a cap. It turned out that in fact E_a oscillates with respect to the number of cap layers.

In the left part of Fig. 11.7 the oscillations of the band energy contribution to the magnetic anisotropy energy with respect to the number of Co layers are shown for free surfaces of Co_n on Cu(100), capped surfaces, and one particular spacer system (Table 11.3). As one immediately can see from this figure, there seem to be three different regimes of oscillations, namely for (I) very thin films ($n \leq 4$), (II) moderately thin films ($4 < n < 10$), and (III) medium thick to thick films ($n \geq 10$). Also obvious is that in regime III the oscillations for free surfaces of Co_n on Cu(100) and for the systems with three Cu-spacer layers are indeed very similar in shape and are closely related to the oscillations for the capped surfaces. Set off in scale and also less pronounced are the oscillations for the systems with Co/Au interfaces.

In the right part of Fig. 11.7 the magnetic dipole-dipole contribution to the magnetic anisotropy energy for free and capped surfaces of Co_n on Cu(100) is displayed versus the number of Co layers. From this figure it is evident

Table 11.3: *Free and capped surfaces of $Co_n/Cu100)$.*

system	n, number of Co layers	m, number of Cu spacer layers
$Cu(100)/Co_n$	$1 \leq n \leq 15$	0
$Cu(100)/Co_n/Cu(100)$	$1 \leq n \leq 15$	0
$Cu(100)/AuCo_nAu/Cu(100)$	$1 \leq n \leq 15$	0
$Cu(100)/Co_nCu_mCo_n/Cu(100)$	$1 \leq n \leq 15$	$1 \leq m \leq 15$

that very little variation with respect to the actual system – even in the case of Co/Au interfaces – pertains to this quantity: E_{dd} decreases nearly linearly with the number of Co layers.

Keeping in mind that the anisotropy energy is the sum of $E_a(n, m)$ and $E_{dd}(n, m)$, it follows from Fig. 11.7 that only in the $Cu(100)/Co_n/Cu(100)$ sandwich and in the Cu-spacer system with three spacer layers and $n = 1$, i.e., for Co monolayers, the magnetization is perpendicular to the surface, while in all other cases ($n \geq 2$) the orientation of the magnetization is in-plane.

11.2 Trilayers, interlayer exchange coupling

As documented in many publications in the last 20 years, Fe/Cr multilayer systems raised a lot of experimental and theoretical interest. There were essentially Fe/Cr/Fe trilayers or Fe/Cr multilayers that produced a first sizeable giant magnetoresistance (GMR) [24, 25], a discovery that in 2007 led to the award of the Nobel prize in physics to Peter Grünberg and Albert Fert. All Fe/Cr systems showed oscillations in the so-called interlayer exchange coupling (IEC) [23]. Quite clearly since their discovery the experimental techniques became much more sophisticated: variations of system parameters (thickness studies etc.) and an increasingly careful recording of the growth conditions gave quite some insight into the conditions causing a giant magnetoresistance (GMR) effect and led to a flood of technological applications, which revolutionized for example the efficiency of hard disks drives. Since some experimental measurements of interlayer coupling showed oscillations that coincided with the peaks in the GMR both effects were assumed to be of the same physical origin. The discovery [26] of the so-called long periods in the IEC with respect to the number of Cr layers invoked further speculations and interpretations, even in terms of related properties of bulk Cr.

Going back for a moment to Section 3.6 dealing with magnetic configurations in magnetic multilayer systems, in the following a more general definition shall be given of the band energy contribution to the anisotropy energy and of the interlayer exchange energy, namely one that can be used also in the

case of non-collinear magnetic configurations.

Suppose that in a particular magnetic configuration $\mathcal{C}_k$ the orientation of the magnetization (unit vector) in each layer i of a layered system corresponding to a simple parent lattice is denoted by n_i^k,

$$\mathcal{C}_k = \{ \underbrace{n_l^k}_{\substack{\text{left semi-}\\ \text{infinite}\\ \text{system}}} , \underbrace{n_1^k, n_2^k, \ldots, n_{L-1}^k, n_L^k}_{\substack{\text{functional}\\ \text{multilayer}\\ \text{system}}}, \underbrace{n_r^k}_{\substack{\text{right semi-}\\ \text{infinite}\\ \text{system}}} \} \quad . \tag{11.12}$$

Here n_l^k and n_r^k refer to the orientation of the magnetization in the left and right semi-infinite system. The meaning of – for example – n_l^k is that in the left semi-infinite system in each atomic layer one and the same orientation of the magnetization applies, namely n_l^k:

$$\begin{array}{l} n_l^k : \text{substrate or lead} \\ \\ n_r^k : \text{substrate, lead or vacuum} \end{array} \quad . \tag{11.13}$$

Suppose now that $\widehat{x}$ and $\widehat{y}$ refer to the in-plane unit vectors and $\widehat{z}$ is parallel to the surface normal; then Eq. (11.1), used before to discuss various features of the magnetic anisotropy energy in magnetically coated surfaces, can be rewritten as

$$\Delta E_b = E(\mathcal{C}_1) - E(\mathcal{C}_2) \quad , \tag{11.14}$$

with

$$\begin{array}{l} \mathcal{C}_1 : n_l^k = n_r^k = \widehat{x} \quad ; \quad n_i^k = \widehat{x} \quad , \forall i \quad , \\ \mathcal{C}_2 : n_l^k = n_r^k = \widehat{z} \quad ; \quad n_i^k = \widehat{z} \quad , \forall i \quad , \end{array} \tag{11.15}$$

meaning that in $\mathcal{C}_1$ the magnetization is pointing uniformly along $\widehat{x}$ ("in-plane"), while in $\mathcal{C}_2$ it is oriented uniformly along the surface normal ("perpendicular").

In trilayer systems which consist of a substrate and two magnetic slabs separated by a non-magnetic spacer (metallic or non-metallic) the exact magnetic configurations start to matter, because of induced magnetic moments in atomic spacer layers neighboring a magnetic slab. A typical magnetic configuration in a trilayer is of the form

$$\begin{array}{l} \mathcal{C}_k = \{ \underbrace{n_s^k}_{\text{substrate}} , \underbrace{n_1^k, n_1^k, \ldots, n_{K-1}^k, n_K^k}_{\text{magnetic slab}} , \underbrace{n_1^k, n_2^k, \ldots, n_{L-1}^k, n_L^k}_{\textbf{spacer}}, \\ \underbrace{n_1^k, n_2^k, \ldots, n_{M-1}^k, n_M^k}_{\text{magnetic slab}}, \underbrace{n_1^k, n_2^k, \ldots, n_{N-1}^k, n_N^k}_{\text{cap}}, \underbrace{n_v^k}_{\text{vacuum}} \} \quad , \end{array} \tag{11.16}$$

where n_s^k contains also a sufficient number of buffer layers in order to guarantee a smooth transition from the left magnetic slab to the bulk-like property of the left semi-infinite system

$$n_s^k = \{n_l^k, \underbrace{n_1^k, n_2^k, \ldots, n_{B-1}^k, n_B^k}_{\text{buffer}}\} \quad . \tag{11.17}$$

The interlayer exchange energy is then the difference in band energy between two magnetic configurations, in one of which the orientation of the second magnetic slab (better: half of all layers considered) points in the opposite direction.

11.2.1 The system Fe/Cr$_n$/Fe

The Fe/Cr$_n$/Fe trilayer system is already a very good example that even in the case of collinear magnetic configurations the magnetic ground state has to be obtained by minimizing the total energy (or the equivalent band energy) with respect to all possible configurations, since Cr carries a magnetic moment. Table 11.4 contains 5 different types of magnetic configurations. If the trilayer system contains n layers of Cr then in these configurations

$$n = l_1 + l_2 \quad . \tag{11.18}$$

In the left half of Fig. 11.8 the following energy differences

$$\Delta E_b(r,n,m) = \begin{cases} E_b(C_1;r,n,m) - E_b(C_0,r,n,m) & \text{"interlayer exchange coupling energy"} \\ E_b(C_4;r,n,m) - E_b(C_3;r,n,m) & \text{"perpendicular coupling energy"} \end{cases} \tag{11.19}$$

Table 11.4: *Magnetic configurations of bcc Fe(100)/Fe$_r$Cr$_n$/Fe$_m$/Vac trilayers: $\widehat{x}, \widehat{y}$ are unit vectors in the planes of atoms, $\widehat{z}$ is a unit vector along the surface. The index r refers to the number of Fe "buffer" layers, m denotes the number of Fe cap layers.*

	C_0	C_1	C_2	C_3	C_4	$C_{(k)}$
$Fe(100)$	$\widehat{z}$	$\widehat{z}$	$\widehat{z}$	$\widehat{x}$	$\widehat{x}$	$\widehat{z}$
$[Fe]_r$	$\widehat{z}$	$\widehat{z}$	$\widehat{z}$	$\widehat{x}$	$\widehat{x}$	$\widehat{z}$
$[Cr]_{l_1}$	$\widehat{z}$	$\widehat{z}$	$\widehat{z}$	$\widehat{x}$	$\widehat{x}$	$\widehat{z}$
$[Cr]_{l_2}$	$\widehat{z}$	$\widehat{z}$	$\widehat{z}$	$\widehat{x}$	$\widehat{x}$	$-\widehat{z}$
$[Fe]_m$	$\widehat{z}$	$-\widehat{z}$	$\widehat{x}$	$\widehat{x}$	$-\widehat{x}$	$-\widehat{z}$
Vac						

are displayed. As can be seen there are two oscillation periods, a short one of periodicity 2 ML's (monolayers) and a long one with about 15 - 16 ML's. Furthermore, a kind of phase slip at the beginning of each long period seems to occur. However, from this figure one also can see that there is a ferromagnetic bias of about 11 meV for the IEC and about 5.5 meV for the perpendicular coupling.

In the right half of Fig. 11.8 the energy difference

$$\Delta E_b(\Theta; r, n, m) = E_b(\Theta; r, n, m) - E_b(C_0, r, n, m) \quad ,$$

where Θ refers to a rotation of the orientation of the magnetization in the second Fe slab (cap layer) by an angle Θ around the y-axis, is shown for $n = 17$. Clearly enough a value of $\Theta = 90°$ implies a perpendicular alignment; $\Theta = 180°$ an antiparallel alignment. As can be seen the calculated values follow closely a $(1 - \cos\Theta)$ behavior, i.e.,

$$\Delta E_b(\Theta; r, n, m) \sim \frac{1}{2}\left[E_b(C_1; r, n, m) - E_b(C_0, r, n, m)\right](1 - \cos\Theta) \quad , \tag{11.20}$$

the deviations from this functional form being only marginal. Also marked in this figure is the result when for $\Theta = 180°$ the magnetic force theorem is *not* used, i.e., when for both configurations, C_0 and C_1, self-consistency was required. The computational error of using the magnetic force theorem amounts therefore to about 3 - 5%. This confirms the statement about the validity of the magnetic force theorem made in Chapter 6.

In order to interpret the bias mentioned above let $\Delta E_b(r; n; m)$ denote the IEC for systems of the type $\mathrm{Fe(100)/Fe}_r\mathrm{Cr}_n\mathrm{Fe}_m\mathrm{/Vac}$. In principle this quantity depends weakly on the number r of buffer layers considered. For a large enough r, however, $\Delta E_b(r; n; m)$ becomes independent of r; i.e., r is only a "technical" parameter. Suppose now that for a particular cap thickness m, the number of Cr layers, becomes very large,

$$\lim_{n \to N} \Delta E_b(r, n, m) = \Delta E_b(r, N, m) \quad , \tag{11.21}$$

then for $\Delta E_b(r, N, m) > 0$ the ferromagnetic configuration is the ground state and consequently the anti-ferromagnetic configuration an excited state. It is important to note that independent of the sign of $\Delta E_b(r, N, m)$ this quantity always describes the energy difference between the ground state and an excited state. In the limit of $n \to N$, N denoting a sufficiently large number, the bias is defined in terms of the following arithmetic mean,

$$B(m) \sim \frac{1}{2}\left[\Delta E_b(r, N, m) + \Delta E_b(r, N + 1, m)\right] \quad . \tag{11.22}$$

$B(m) > 0$ refers to oscillations around a ferromagnetic ground state, $B(m) < 0$ to oscillations around an antiferromagnetic ground state, and $B(m) = 0$ to alternating ground states. For $n > 7$ the oscillations in Fig. 11.8 are

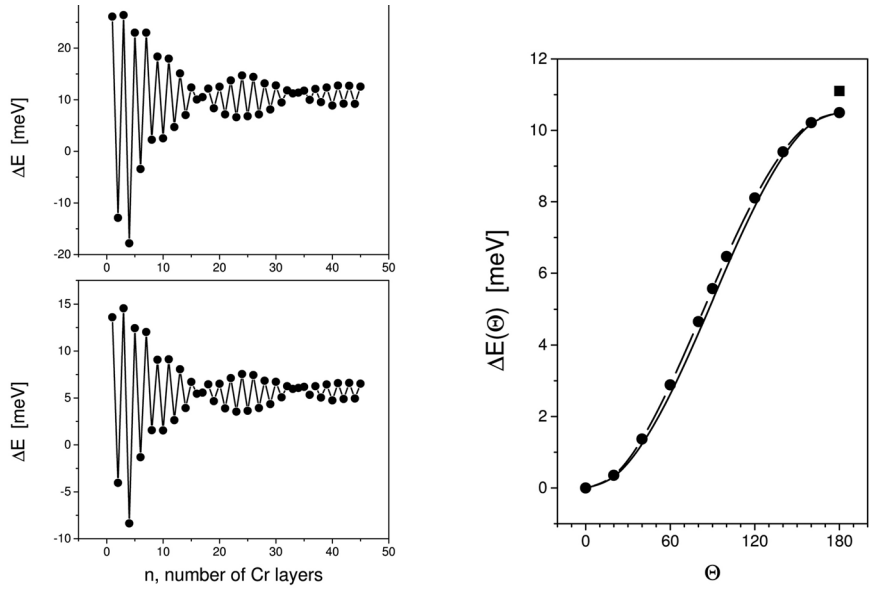

FIGURE 11.8: *Left: Antiparallel (top) and perpendicular (bottom) interlayer exchange coupling in bcc-Fe(100)/Fe$_6$Cr$_n$Fe$_6$/Vac. The reference ferromagnetic configuration is C_0, the antiferromagnetic configurations refer to C_1 and C_2; see Table 11.4. Right: Angular dependence of the interlayer exchange coupling energy in bcc-Fe(100)/FeCr$_{17}$Fe$_6$/Vac. The reference ferromagnetic configuration is C_0, the antiferromagnetic configuration C_1. Circles refer to the calculated values, and the full line to the function $\Delta E(\Theta) = \Delta E(1-\cos\Theta)/2$. The square refers to the absolute value of the interlayer exchange coupling energy when the (selfconsistent) antiferromagnetic configuration (C_1) is used as reference configuration. From Ref. [31].*

oscillations around a ferromagnetic ground state as n becomes large. The left half of Fig. 11.9 illustrates the dependency of the interlayer exchange energy defined in Eq. (11.19) on the number of Fe cap layers. For large enough n once again, just as in all other cases of capped free surfaces, oscillations with respect to n set in, seemingly with a periodicity of about 2 ML.

The best example for the importance of a strict definition of magnetic configurations (and actual reason for the bias) is to be found in the right half of Fig. 11.9. There energy differences of the type $E_b(C_{(k)}; r, n, m) - E_b(C_0, r, n, m)$, see Table 11.4, are considered for $m = 24, 25$ such that the number of Cr layers with orientations parallel to the one in the Fe substrate is successively increased.

Even more pronounced is the effect of a proper choice of magnetic configu-

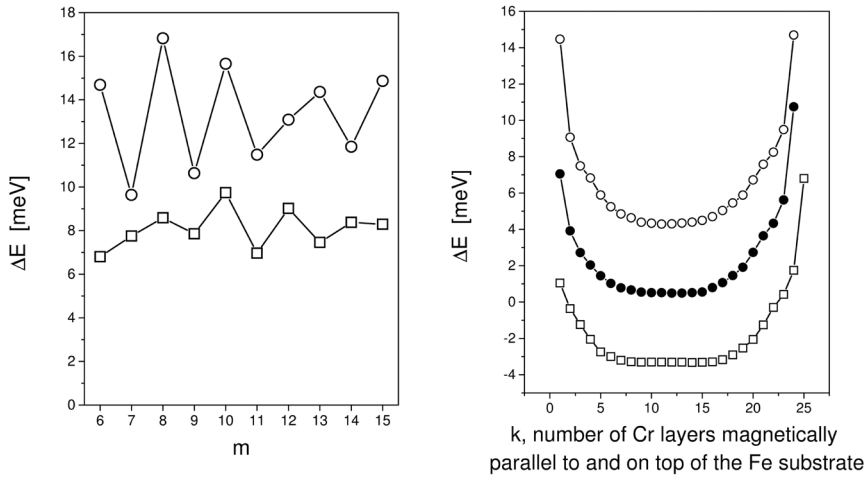

FIGURE 11.9: *Left: Interlayer exchange energy for bcc-Fe(100)/Fe$_6$Cr$_n$Fe$_m$/Vac for $n = 24$ (circles) and $n = 25$ (squares) with respect to increasing thickness (m) of the Fe cap. The reference ferromagnetic configuration is C_0, the antiferromagnetic configuration C_1; see Table 11.4. Right: Interlayer exchange energy for bcc-Fe(100)/Fe$_6$Cr$_n$Fe$_6$/Vac for $n = 24$ (open circles) and $n = 25$ (open squares) with respect to an increasing number k of Cr layers on top of and aligned magnetically parallel to the Fe substrate. Full circles correspond to the bias. The reference ferromagnetic configuration is C_0, the antiferromagnetic configurations refer to $C_{(k)}$. From Ref. [31].*

rations when considering layer-resolved band energies. In Fig. 11.10 the layer-resolved contributions to $E_b^i(C_1; r, n, m) - E_b^i(C_0, r, n, m)$ and $E_b^i(C_{(k)}; r, n, m) - E_b^i(C_0, r, n, m)$ are shown for $n = 24$ and 25. In the first case one would conclude that the cause for interlayer exchange coupling is mainly an interface effect that occurs at that boundary where the magnetization is reversed. From the second case, however, the conclusion is that although there are substantial interface effects the main contribution to the interlayer exchange energy arises from contributions in the interior of the Cr spacer.

Interesting in this context are the Cr moments in rather thick Cr slabs. As can be seen from Fig. 11.11 for $n > 40$ (in the ferromagnetic configuration, $\mathcal{C}_0$) the moments not only oscillate with a period of 2 ML, but also show characteristic long periods: for an even number of Cr layers a period of 8 ML is building up while for an odd number of Cr layers this period is doubled; i.e., for a large enough odd number of Cr layers the same long period is observed as in the interlayer exchange coupling. Whether or not this phenomenon con-

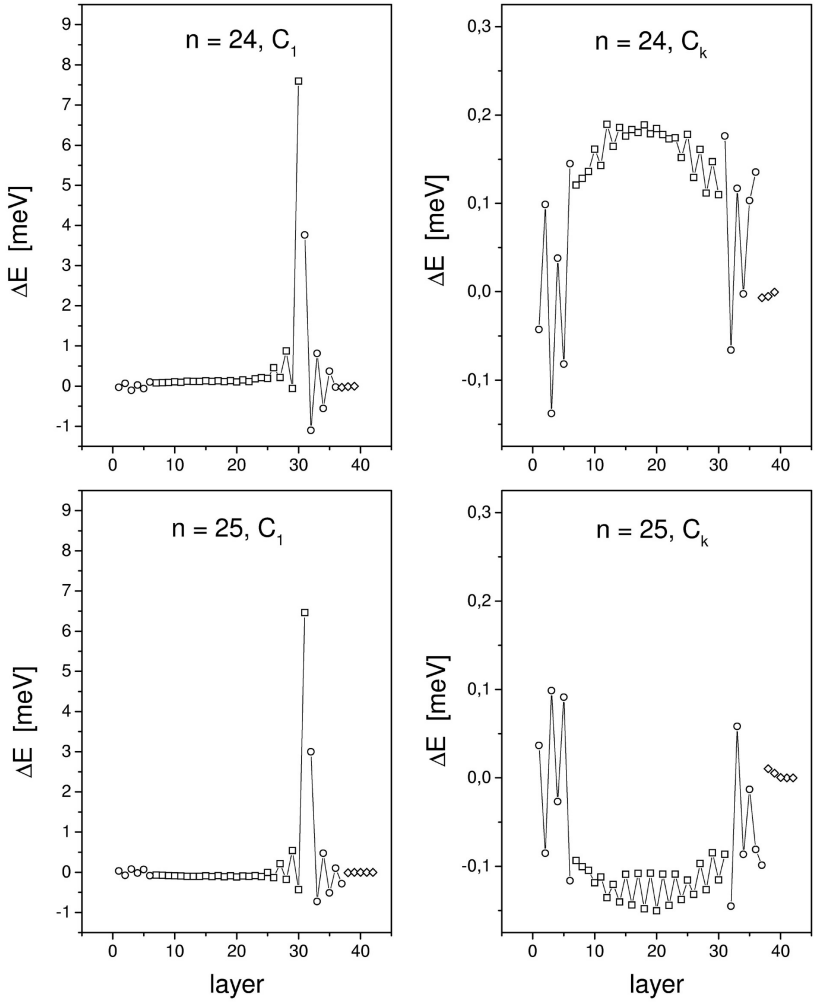

FIGURE 11.10: *Layer-resolved interlayer exchange energies for bcc-Fe(100)/Fe$_6$Cr$_n$Fe$_6$/Vac, $n = 24$ (top) and $n = 25$ (bottom). Squares refer to Cr contributions, circles to Fe contributions, and diamonds to contribution from the vacuum layers. The reference ferromagnetic configuration is C_0, the antiferromagnetic configurations are C_1 (left) and $C_{(k)}$ (right), $l_1 = 12$; see Table 11.4. The Fe substrate (origin of counting) is to the left, vacuum to the right. From Ref. [31].*

tributes to induce the long periods in the interlayer exchange coupling energy for very thick Cr spacers is a matter of belief since ΔE_b refers exclusively to an energy difference between two magnetic configurations.

The experimental facts for the Fe/Cr/Fe trilayer system seem to be already well confirmed [28, 29]: (1) the exchange coupling shows a short period of about 2 ML with respect to the Cr thickness (d_{Cr}, [ML]) and crosses to the antiferromagnetic (AF) coupling at 4ML of Cr, (2) between $4 \leq d_{Cr} \leq 12$ the samples are coupled antiferromagnetically [28, 29, 30], (3) opposite to the expectation that because of the 2ML oscillation the antiferromagnetic coupling would occur only for even numbers of Cr layers, independent measurements proved that this is not the case: antiferromagnetic coupling occurs at odd numbers of Cr layers, (4) the interlayer exchange energy depends on the thickness of the Fe cap [27], and (5) there is a first phase slip [26, 27] at 24 - 25 (38 - 39) ML of Cr at 310 K (550 K) followed by phase slips at 44 - 45 and 64 - 65 layers of Cr (at 310 K).

It should be noted that in order to properly interpret these facts one has to recall that the above cited experimental studies give only an indirect account of the interlayer exchange energy. Exactly this indirect mapping of interlayer exchange coupling is analyzed in the following for a well-defined system.

11.2.2 Trilayers: a direct comparison between theory and experiment

For $Cu_4Ni_8Cu_NNi_9/Cu(001)$, $N = 2 - 10$ ML, an attempt was made [32] to compare directly the results of experimental and theoretical studies and to analyze the interpretation predominately used by experimentalists of the experimental data in terms of anisotropy and exchange coupling constants and a phenomenological model of the free energy E (per unit area),

$$E = K - J_{inter} \frac{\mathbf{M}_1 \cdot \mathbf{M}_2}{M_1 M_2} \quad , \quad M_i = |\mathbf{M}_i| \quad , \tag{11.23}$$

where $\mathbf{M}_1$ and $\mathbf{M}_2$ denote the directions of the (macroscopic) magnetizations in the two magnetic slabs and K is the anisotropy energy,

$$K = \sum_{i=1}^{2} \left(2\pi M_i^2 - K_{2\perp,i}\right) d_i \cos^2 \theta_i \quad . \tag{11.24}$$

In Eq. (11.24) the d_i refer to the thicknesses of the individual Ni slabs, $2\pi M_i^2$ is the shape anisotropy and $K_{2\perp,i} = K_{2\perp,i}^V + (K_{2\perp,i}^{S_1} + K_{2\perp,i}^{S_2})/d_i$ denotes the intrinsic uniaxial anisotropy which in principle usually is split into a part arising from the slab volume ($K_{2\perp,i}^V$) and a contribution from the two surfaces ($K_{2\perp,i}^{S_1}$ upper surface, $K_{2\perp,i}^{S_2}$ lower surface). The angles θ_i measure the magnetization directions with respect to the surface normal. In the chosen trilayer $S_1 = S_2 = S$, since in $Cu_4Ni_8Cu_NNi_9/Cu(001)$ the Ni slabs face Cu

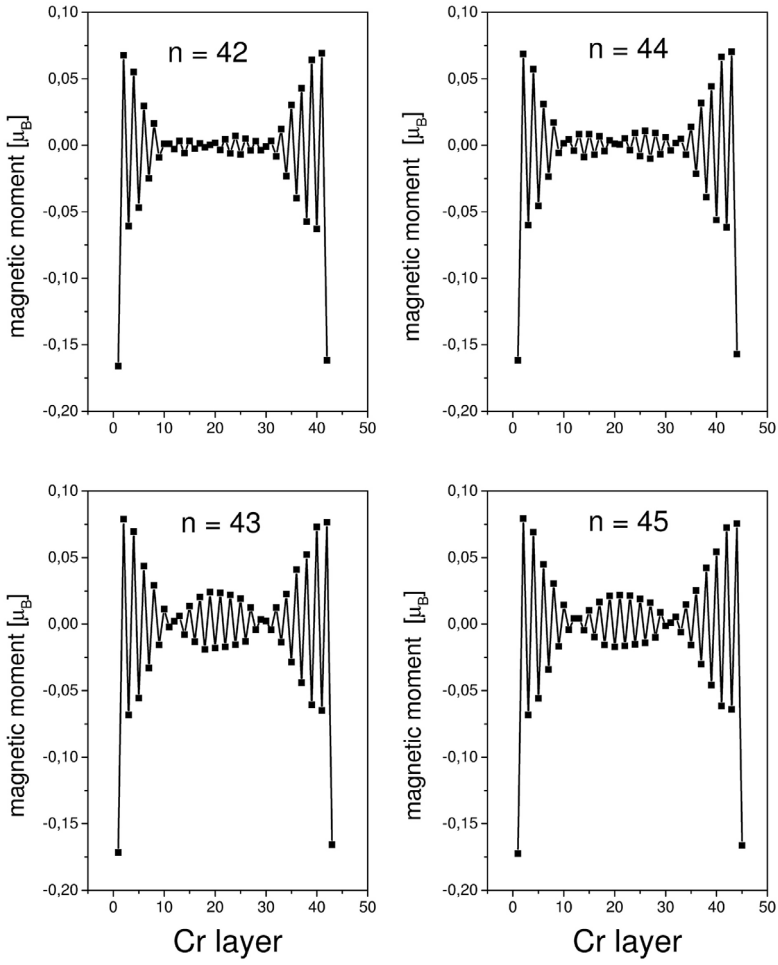

FIGURE 11.11: *Cr magnetic moments in bcc-Fe(100)/$Fe_6Cr_nFe_6$/Vac for a ferromagnetic configuration with the magnetization parallel to the surface normal (C_0, in Table 11.4) . The number of Cr layers is indicated explicitly. From Ref. [31].*

on both sides. For $2\pi M_i^2 - K_{2\perp,i} > 0$ (< 0) the easy axis of magnetization lies in (out of) the planes of atoms. The interlayer exchange coupling energy corresponds then to the *macroscopic* coupling constant J_{inter} [33] in Eq. (11.23).

The layer-resolved contributions to the interlayer exchange energy for trilayers with $N = 3$ and $N = 9$ are displayed in Fig. 11.12 (a) and (b). The layer numbering starts at the three Cu buffer layers (neighboring semi-infinite fcc Cu(001)) and comprises the trilayer, 4 Cu capping layers and three vacuum layers. The different parts of the system are separated in this figure by dotted lines. The lower part of this figure shows the experimental results extrapolated to $T = 0$ for (a) $Cu_4Ni_8Cu_NNi_9/Cu(001)$ trilayers (open squares) and (b) $Ni_7Cu_NCo_2/Cu(001)$ trilayers (open circles). Although the experimental values for the latter system are larger by about a factor of three, the overall behavior seems not to be smaller influenced upon substituting one Ni film with Co. In order to obtain the best agreement with the experiment, the theoretical curve had to be shifted by 0.7 ML, which in turn indicates that the *effective* experimental thickness seems to be smaller by 0.7 ML than the nominal evaporation rate. This can easily be understood considering a small amount of interdiffusion occurring during the film growth, a fact that is well known to happen for Ni as well as Co on Cu(001). Although the principal behavior of the IEC found experimentally is reproduced by the theoretical calculations rather well, the absolute strength of the coupling (amplitude) calculated for $Cu_4Ni_8Cu_NNi_9/Cu(001)$ is by a factor 10 larger than the experimental values.

This now is exactly the stage at which one has to separate clearly the actual experimental data from an interpretation in terms of existing models. The "measured values" displayed in Fig. 11.12 in fact refer to J_{inter} in Eq. (11.23), namely to a *macroscopic* Heisenberg model. The interaction parameter J_{inter} does not necessarily need to be identical with the *microscopically* defined interlayer exchange energy. It is even questionable whether a thermodynamically averaged microscopic Heisenberg model would eventually lead to a parameter J_{inter} as introduced in Eq. (11.23):

$$\begin{aligned} \langle E \rangle = \left\langle \sum_{i,j} J_{ij} \frac{\mathbf{m}_i \cdot \mathbf{m}_j}{m_i m_j} \right\rangle \Rightarrow \left\langle J \sum_{i,j} \frac{\mathbf{m}_i \cdot \mathbf{m}_j}{m_i m_j} \right\rangle \\ \Rightarrow \langle J \rangle \left\langle \sum_{i,j} \frac{\mathbf{m}_i \cdot \mathbf{m}_j}{m_i m_j} \right\rangle \Rightarrow J_{inter} \frac{\mathbf{M}_1 \cdot \mathbf{M}_2}{M_1 M_2} \quad . \end{aligned} \tag{11.25}$$

In Eq. (11.25) the $\mathbf{m}_i$ refer to magnetic moments at sites i, and J_{ij} is the (microscopic) coupling energy between two such moments, block arrows denote the assumptions made to arrive eventually at a global coupling parameter J_{inter}. It is indeed important to note that J_{inter} is *not* measured but is the result of an interpretation!

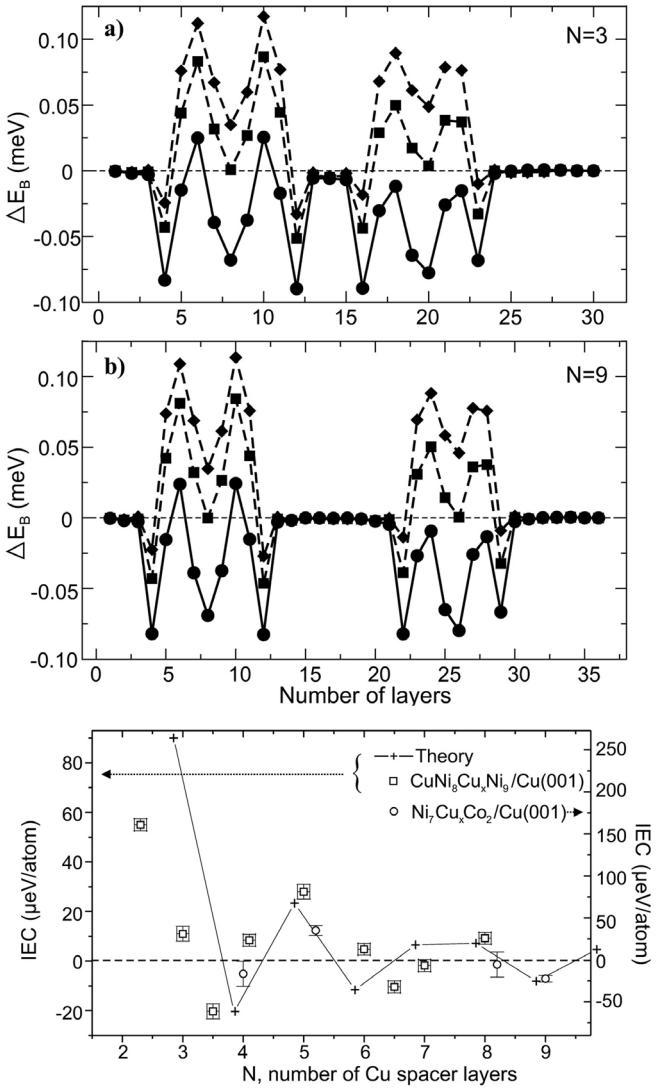

FIGURE 11.12: Top: l*ayer-resolved IEC for* $Cu_4Ni_8Cu_NNi_9/Cu(001)$ *with a)* $N = 3$ *and b)* $N = 9$. Bottom: *the experimental results are indicated by the open squares and circles; the theoretical IEC values (crosses) there have been upshifted on the x-axis by 0.7 ML. From Ref. [32].*

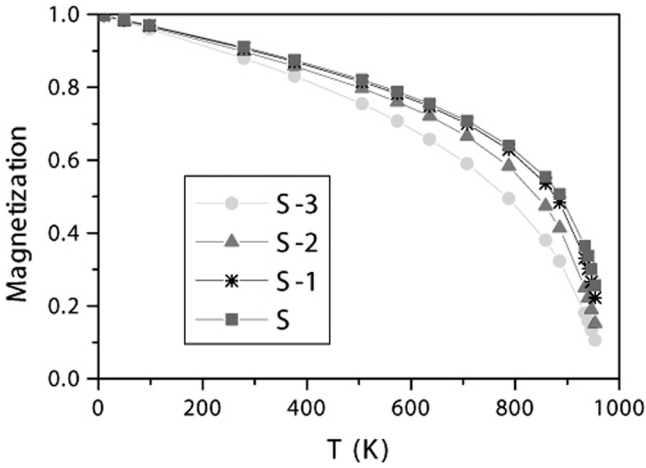

FIGURE 11.13: *Average magnetizations versus temperature for $Co_4/Cu(100)$. The label S refers to the surface Co layer, and $S-n$, $(n = 1, 2, 3)$ to the n-th Co layer beneath the surface. From Ref. [34].*

11.3 Temperature dependence

Chapter 8 gave a brief description of the so-called Disordered Local Moment Method, which ought to be applied when describing temperature effects of the magnetic anisotropy energy, so there is no need to repeat any kind of formal description.

In Figure 11.13 the calculated layer-dependent magnetizations are shown as a function of the temperature in the case of $Co_4/Cu(100)$. As can be seen from this figure the magnetization vanishes in all layers at a critical temperature of $T_C = 960$ K. The shape of the curves, however, differs from layer to layer: the largest overall magnetization corresponds to the surface layer (S), the lowest to the interface layer ($S-3$).

In the top part of Fig. 11.14 the calculated band energy contributions to the magnetic anisotropy energy, denoted there as $K_b(T)$, are plotted as a function of temperature. As in the few bulk systems studied so far [35, 36] the magnetic anisotropy constant decreases in the monolayer case almost monotonically in magnitude with increasing temperature. For thicker films, however, $K_b(T)$ shows a non-monotonic temperature behavior because of a more or less pronounced maximum. For n $\geq$ 3, K_b(T) even changes sign at a given temperature.

The magnetic dipole-dipole energy $K_{dd}(T)$ at finite temperatures can only be evaluated approximatively by using the averaged disordered local mag-

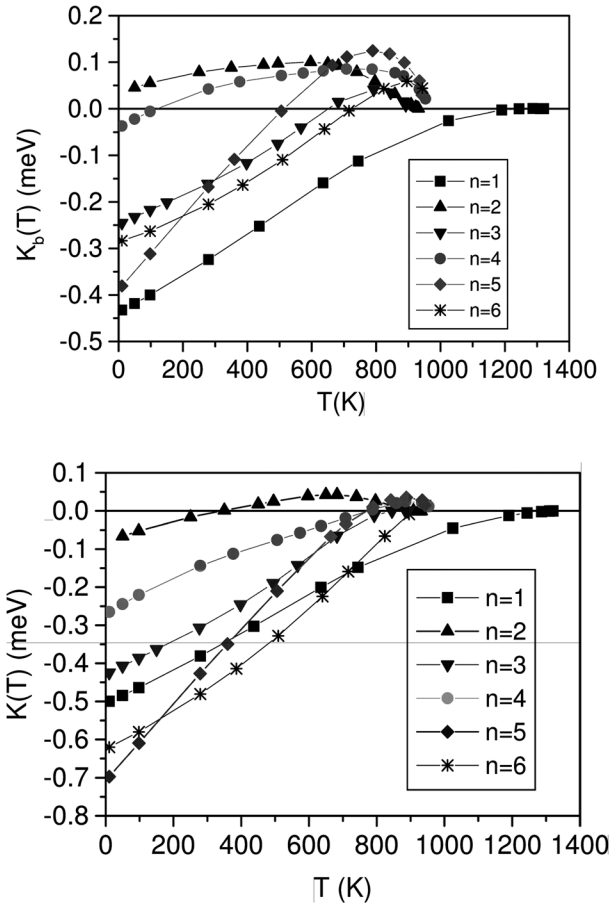

FIGURE 11.14: *Top: Band energy part of the magnetic anisotropy constant* $K_b(T)$ *for* $\overline{Co_n/Cu}(100)$. *Bottom: calculated total magnetic anisotropy constant,* $K(T) = K_b(T) + K_{dd}(T)$, *as a function of temperature for* $Co_n/Cu(100)$. *From Ref. [34].*

netic moments, Eqs. (8.18) - (8.20), see Chapter 6, valid in principle only for ordered magnetic systems at zero temperature. For Co on Cu(100) the magnetic anisotropy energies $K(T)$, namely the sum of the band and magnetic-dipole-dipole contributions, are displayed in the lower part of Fig. 11.14; the corresponding Curie temperatures are listed in Table 11.5.

Table 11.5: *Calculated Curie temperatures for Co_n/Cu(100). From Ref. [34].*

n	1	2	3	4	5	6
T_c	1330	933	897	960	945	960

It should be noted that for large thicknesses of Co on Cu(100) the experimental value [37] of T_C is about 950 K. The Curie temperature of thin magnetic films is perhaps a scientifically interesting quantity; however, more important is the value of the magnetic anisotropy energy at about room temperature. Taking for example the case of 6 Co layers on Cu(100), from Fig. 11.14 one immediately can see that the reduction with respect to zero temperature amounts to about 30%. This reduction of the magnetic anisotropy energy with temperature is indeed an important issue if perpendicular magnetism is used technologically.

Unfortunately, partially because of the computational effort involved, partially also because the relativistic Disordered Local Moment Theory for systems with only two-dimensional translational symmetry was proposed only very recently, further published studies of the temperature dependence of the magnetic anisotropy energy in layered systems are not available at present.

11.4 A short summary

Finally, a short summery of all the effects discussed in this chapter shall be given, to provide a characterization of anisotropy and interlayer exchange effects for free and capped magnetic surfaces in a nut-shell.

$$\Delta E = \begin{cases} E_a = \Delta E_b + \Delta E_{dd} \ , & \text{anisotropy energy} \\ E^{IEC} = \Delta E_b \ , & \text{interlayer exchange coupling energy} \end{cases}$$

$$\Delta E_b \equiv \Delta E_b(n, m, r, \ldots, T) = E(C_1; n, m, r, \ldots, T) - E(C_0; n, m, r, \ldots, T)$$

$n, m, \ldots$ thickness parameters, C_i magnetic configurations, T temperature

11.4.1 Magnetic anisotropy energy

$$\Delta E_b \equiv \Delta E_b(n, m, r, T) = E_b(C_1; n, m, r, T) - E_b(C_0; n, m, r, T)$$
$$\Delta E_{dd} \equiv \Delta E_{dd}(n, m, r, T) = E_{dd}(C_1; n, m, r, T) - E_{dd}(C_0; n, m, r, T)$$

C_0 refers to a *uniform perpendicular* to the planes of atoms orientation of the magnetization, C_1 to a *uniform in-plane* orientation. For free surfaces and "superstructures" E_a depends on

	thickness parameters	**effects**
n	number of magnetic layers	possible reorientation transition
m	number of cap layers	oscillations
r	number of repetitions	optimizing perpendicular magnetism

Characterization of magnetic anisotropy energies:

$$\Delta E_b(n, m, r, T) - \Delta E_{dd}(n, m, r, T) \quad \begin{cases} > 0 : \text{perpendicular} \\ \sim 0 : \text{reorientation} \\ < 0 : \text{in-plane} \end{cases}$$

11.4.2 Interlayer exchange coupling energy

$$\boxed{E^{IEC} = \Delta E_b(n, m, r, s, T)}$$

The reference magnetic configuration (C_0) is either uniformly in-plane or perpendicular to the planes of atoms. C_1 needs to be stated carefully in particular in the case of magnetic spacers: an appropriate number of atomic layers has to have an opposite to C_0 direction of the magnetization. The interlayer exchange energy depends on

	thickness parameters	**effects**
n	number of magnetic layers in the left magnetic slab	size of amplitudes
m	number of spacer layers	characteristic oscillations with one or more periods
r	number of magnetic layers in the right magnetic slab	size of amplitudes
s	number of cap layers	additional oscillations

- Both quantities, the magnetic anisotropy energy and as well as the interlayer exchange energy, are very sensitive with respect to interdiffusion at interfaces and/or other alloying effects.
- Both quantities depend crucially on temperature

It should be noted that in the case of interlayer exchange coupling, also a large number of publications dealing even with disorder or temperature effects, see for example [38] - [41], appeared, all of them based on a non-relativistic approach, since (mostly) only collinear magnetic structures had to be considered.

[1] C. Liu and S.D. Bader, J. Vac. Sci. Technol. A **8**, 2727 (1990).

[2] L. Szunyogh, B. Úfalussy and P. Weinberger, Phys. Rev. **B51**, 9552 (1995).

[3] M. Farle, B. Mirwald-Schulz, A.N. Anisimov, W. Platow, and K. Baberschke, Phys. Rev. B **55**, 3708 (1997).

[4] M. Farle, W. Platow, A.N. Anisimov, P. Poulopoulos, and K. Baberschke, Phys. Rev. B **56**, 5100 (1997).

[5] R. Vollmer, Th. Gutjahr-Löser, J. Kirschner, S. van Dijken, and B. Poelsma, Phys. Rev. B **60** 6277 (1999).

[6] S. van Dijken, R. Vollmer, B. Poelsema, and J. Kirschner: J. Magn. Magn. Mater. **210**, 316 (2000).

[7] W. L. O'Brien, T. Droubay, and B. P. Tonner, Phys. Rev. B **54**, 9297 (1997).

[8] C. Uiberacker, J. Zabloudil, P. Weinberger, L. Szunyogh and C. Sommers, Phys. Rev. Lett. **82**, 1289 (1999).

[9] F. Maca, A. B. Shick, J. Redinger, R. Podloucky, and P. Weinberger, Czech. J. Phys. **53**, 33 - 39 (2003).

[10] B. Schulz, R. Schwarzwald, and K. Baberschke, Sur.Sci. **307-309**, 1102 (1994).

[11] J. Lee, G. Lauhoff, and J. A. C. Bland, Phys. Rev. B **56**, R5728 (1997).

[12] C. Uiberacker, J. Zabloudil, P. Weinberger, L. Szunyogh and C. Sommers, Phys. Rev. B **62**, 5305 (2000).

[13] U. Pustogowa, J. Zabloudil, C. Uiberacker, C. Blaas, P. Weinberger, L. Szunyogh and C. Sommers, Phys. Rev. B **60**, 414 (1999).

[14] J. Zabloudil, L. Szunyogh, U. Pustogowa, C. Uiberacker and P. Weinberger, Phys. Rev. **58**, 6316 (1998).

[15] L. Szunyogh, P. Weinberger, and C. Sommers, Phys. Rev. B **60**, 11910 (1999).

[16] S. S. A. Razee, J. B. Staunton, and F. J. Pinski, Phys. Rev. B **56**, 8082 (1997).

[17] Th. Detzel, M. Vonbank, M. Donath, and V. Dose, J. Magn. Magn. Mater. **147**, L1 (1995).

[18] M. Kowalewski, C.M. Schneider, and B. Heinrich, Phys. Rev. B **47**, 8748 (1993).

[19] B. Újfalussy, L. Szunyogh, and P. Weinberger, Phys. Rev. B **54**, 9883 (1996).

[20] L. Szunyogh, B. Újfalussy, C. Blaas, U. Pustogowa, C. Sommers and P. Weinberger, Phys. Rev. B**56**, 14 036 (1997).

[21] L. Szunyogh, B. Újfalussy, and P. Weinberger, Phys. Rev. B **55**, 14392 (1997).

[22] A. Dittschar, M. Zharnikov, W. Kuch, M.-T. Lin, W. Kuch, C.M. Schneider, and J. Kirschner, Phys. Rev. B **57**, R3209 (1998).

[23] P. Grünberg, R. Schreiber, Y. Pang, M. B. Brodsky, and H. Sowers, Phys. Rev. Lett. **57**, 2442 (1986).

[24] M. N. Baibich, J. M. Broto, A. Fert, F. Nguyen Van Dau and F. Petroff, Phys. Rev. Lett. 61, 2472 (1988), received August 24, 1988.

[25] G. Binasch, P. Grünberg, F. Sauerbach and W. Zinn, Phys. Rev. B 39, 4828 (1989), received May 31, 1988.

[26] J. Unguris, R. J. Celotta, and D. T. Pierce, Phys. Rev. Lett. **67**, 140 (1991).

[27] D. T. Pierce, J. Unguris, R. J. Celotta, and M. D. Stiles, J. Magn. Magn. Mater. **200**, 290 (1999).

[28] B. Heinrich, J. F. Cochran, T. Monchesky, and R. Urban, Phys. Rev. B **59**, 14520 (1999).

[29] B. Heinrich, J. F. Cochran, T. Monchesky, and R. Urban, J Appl. Phys. **87**, 5449 (2000).

[30] J. J. Krebs, P. Lubitz, A. Chaiken, and G. A. Prinz, Phys. Rev. Lett. **63**, 1645 (1989).

[31] A. Vernes, P. Weinberger, P. Mohn, C. Blaas, L. Szunyogh, C. Sommers and P. M. Levy, Phil. Mag. B **82**, 85 (2002).

[32] R. Hammerling, J. Zabloudil, P. Weinberger, J. Lindner, E. Kosubek, R. Nünthel, and K. Baberschke, Phys. Rev. B **68**, 092406 (2003).

[33] P. Bruno, Phys. Rev. B **52**, 411 (1995) and references therein.

[34] Á. Buruzs, P. Weinberger, L. Szunyogh, L. Udvardi, and J. B. Staunton, Phys. Rev. B **76**, 064417 (2007).

[35] J. B. Staunton, S. Ostanin, S. S. A. Razee, B. L. Györffy, L.Szunyogh, B. Ginatempo, and E. Bruno, Phys. Rev. Lett. **93**, 257204 (2004).

[36] J. B. Staunton, L. Szunyogh, Á. Buruzs, B. L. Györffy, S. Ostanin, and L. Udvardi, Phys. Rev. B **74**, 144411 (2006).

[37] G. J. Mankey, S. Z. Wu, F. O. Schumann, F. Huang, M. T. Kief, and R. F. Willis, J. Vac. Sci. Technol. A **13** (3) , 1531 (1995).

[38] J. Kudrnovský, V. Drchal, C. Blaas, I. Turek and P. Weinberger, Phys. Rev. Lett. **76**, 3834 (1996)

[39] J. Kudrnovský, V. Drchal, I. Turek, M. Sob and P. Weinberger,Phys. Rev. **B53**, 5125 (1996)

[40] J. Kudrnovský, V. Drchal, P. Bruno, I. Turek and P. Weinberger,Phys. Rev. **B54**, R3738 (1996)

[41] V. Drchal, J. Kudrnovsky, P. Bruno, P.H. Dederichs and P. Weinberger, Phil. Mag. B **78**, 571 (1998)

12

Nanostructured in one dimension: spin valves

Properties of the anisotropy and the interlayer exchange energy of spin valve systems with metallic and non-metallic spacers are discussed putting the emphasis in particular on interdiffusion effects at the interfaces. Furthermore, the concept of twisting energies is introduced and their interpretation in terms of a phenomenological Landau-Lifshitz-Gilbert equation.

Perhaps the best way to explain that there are also quite a few physical reasons to distinguish between capped surfaces and spin valves is to go back to Table 11.2, from which a direct comparison between these two cases can be found. As can be seen from the last two rows, for a thin film consisting of 7 Fe ML on Cu(100) the magnetic moment in the surface layer (m_7) is oriented antiparallel to the one neighboring the Cu substrate. In the case of a spin valve (infinitely thick Cu cap) m_7 is parallel to the first one, since symmetric boundary conditions apply:

$$\boxed{\mathrm{Cu(100)/Fe_7/}\begin{cases}\mathrm{Vac} & m_7 = -2.232\\ \mathrm{Cu(100)} & m_7 = 2.520\end{cases}}$$

If the substrate and the cap are very much thicker than the actual film as is the case, e.g., when viewing these two parts of the system as leads in measurements of electric transport properties, then the term spin valve is justified. Of course there is another more practical difference between free magnetic surfaces and spin valves, namely in spin valves interdiffusion between spacer and substrate can occur at two interfaces, while interdiffusion effects for free surfaces of magnetic thin films on top of a substrate are in principle restricted to one interface.

It was already shown in the last chapter and will be again discussed in this one that interfaces and boundaries are rather important for the physical properties of systems nanostructured in one dimension. In particular a proper use of boundaries in any kind of theoretical description has perhaps unforeseen consequences. Take for example the case of Fe/Cr trilayers, $\mathrm{Fe}_{n_1}\mathrm{Cr}_m\mathrm{Fe}_{n_2}$ with fixed numbers n_1 and n_2 of Fe layers on both sides of the Cr slab. Treated as a "free standing" thin film for each combination of n_1, n_2 and m in principle a different Fermi energy $\epsilon_F(n_1, n_2, m)$ applies. If m becomes large, say M, then

$\epsilon_F(n_1, n_2, m)$ tends to the Fermi energy of "bulk Cr", $\epsilon_F(Cr)$. Considered as a semi-infinite system with Fe serving as substrate, e.g., $Fe(100)/Fe_{n_1}Cr_mFe_{n_2}$, the Fermi energy is always that of the substrate (electron reservoir), namely $\epsilon_F(Fe)$, i.e., remains constant for all finite m:

$$vac/Fe_{n_1}Cr_mFe_{n_2}/vac : \lim_{m\to M} \epsilon_F(n_1, n_2, m) \sim \epsilon_F(Cr)$$

$$\left.\begin{array}{l} Fe(100)/Fe_{n_1}Cr_mFe_{n_2}/Vac \\ \\ Fe(100)/Fe_{n_1}Cr_mFe_{n_2}/Fe(100) \end{array}\right\} = \lim_{m\to M} \epsilon_F(n_1, n_2, m) \equiv \epsilon_F(Fe) \quad .$$

In the following section the importance of interdiffusion and/or alloying shall be illustrated in terms of Fe/Cr spin valves before continuing with non-collinearity aspects and heterojunctions.

12.1 Interdiffusion at the interfaces

Usually Fe/Cr interfaces are not perfect: interdiffusion effects lead to the formation of FeCr alloys, the roughness of the interface being determined by the growth temperature. For growth temperatures well above room temperature the interface roughness is relatively small and the short period in the interlayer exchange coupling can be recorded even for finite interdiffusion, e.g., in Fe/Cr whiskers by Brillouin Light Scattering (BLS) experiments [1]. Similar results were reported [2] using other experimental probes.

Table 12.1: *Different types of Fe/Cr/Fe spin valves: c_d refers to the interdiffusion concentration, x to the homogeneous concentration.*

System		
$Fe/Cr_m/Fe$		$m \leq 42$
$Fe/Fe_{1-c_d}Cr_{c_d}/Fe_{c_d}Cr_{1-c_d}/Cr_{m-2}/\ldots/Fe$	$c_d \leq 0.2$	$m \leq 42$
$Fe/(Cr_{1-x}Mn_x)_m/Fe$	$x \leq 0.1$	$m \leq 42$

In Fig. 12.1 an at the two interfaces interdiffused trilayer Fe/Cr/Fe, see Table 12.1, which corresponds to the experimental situation of frozen disorder due to low growth temperatures, is compared to a (fictitious) trilayer with ideal interfaces (no disorder, no roughness). The case of alloying the Cr spacer homogeneously with Mn yields even another kind of oscillations in the interlayer exchange coupling; see Fig. 12.2. In both alloyed cases a RKKY

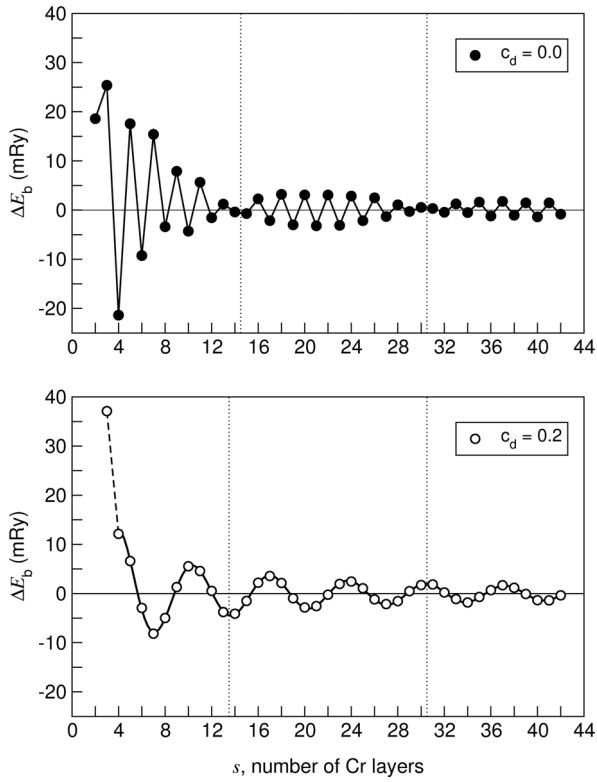

FIGURE 12.1: *Fe/Cr/Fe. Interlayer exchange energy ΔE_b versus the number of spacer layers s without interdiffusion ($c_d = 0$, top) and with a two-layer interdiffusion ($c_d = 0.2$,bottom). In the latter case the full line corresponds to a RKKY-type fit, see Eq. 12.1. From Ref. [3].*

type expression

$$J(m) \;=\; A_0 \frac{\sin\left(2\pi m/T_0 + \phi_0\right)}{m^2} + \; A_1 \frac{\sin\left(2\pi m/T_1 + \phi_1\right)}{m} \quad , \qquad (12.1)$$

was used to fit the calculated data points with respect to the number of Cr layers m. In Eq. (12.1) the first term on the *rhs* corresponds to the usual RKKY interaction, while the second term has to be related to the short period [4]. It turned out that in the case of interdiffused Fe/Cr/Fe trilayers there is only one period with $T_0 = T_1 = 6.74$ ML. Since homogeneous alloying of the Cr spacer with Mn gave about the same result, it seems that inhomogeneous disorder at the interfaces or homogeneous disorder in the spacer immediately suppresses the short period in the interlayer exchange coupling.

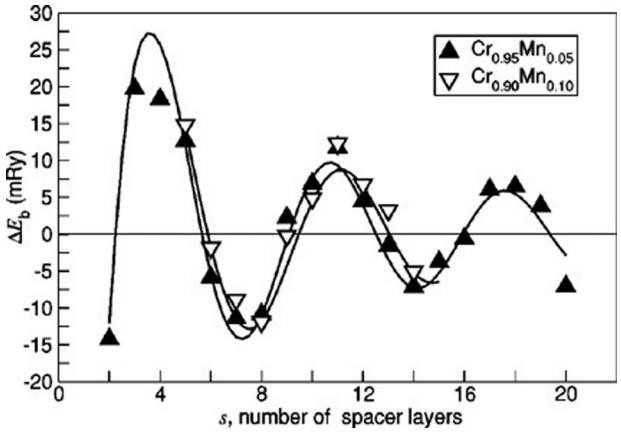

FIGURE 12.2: *$Fe/Cr_xMn_{1-x}/Fe$. Interlayer exchange coupling energy ΔE_b versus the number of spacer layers s for 5% (filled triangles) and 10% (open triangles) of Mn. Solid lines mark fits to the RKKY-type expression in Eq. 12.1. From Ref. [3].*

12.2 Spin valves and non-collinearity

Suppose for matters of simplicity that as indicated in Fig. 12.3 in a spin valve of the type $Cu(100)/Cu_x/Co_{m_1}Cu_sCo_{m_2}/Cu_x/Cu(100), m_1 > m_2$, the following orientations of the magnetizations $\mathbf{M}_1$ and $\mathbf{M}_2$ in the individual atomic layers apply

$$\underbrace{\{n_1, \ldots n_{m_1}\}, \{n_1, \ldots, n_{s/2},}_{= \mathbf{M}_2 \| \hat{z}} \underbrace{n_{(s/2+1)}, \ldots n_s\}, \{n_1, \ldots n_{m_2}\}}_{= \mathbf{M}_1} \quad . \tag{12.2}$$

Suppose further that by switching on an external magnetic field $\mathbf{M}_1$ is rotated around the y- or x-axis by an angle Θ while $\mathbf{M}_2$ remains unchanged. The band energy difference corresponding to these two magnetic configurations is then defined by

$$\begin{aligned} \Delta E(\Theta) &\equiv \Delta E(x, m_1, s, m_2, \Theta) \\ &= E(x, m_1, s, m_2, \Theta \neq 0) - E(x, m_1, s, m_2, \Theta = 0) \quad , \end{aligned} \tag{12.3}$$

and very often is referred to as *twisting energy*. Note that this now is a different case than shown in the previous chapter when discussing Fe/Cr/Fe trilayers, since there a uniform direction of the magnetization (applying for the whole system) was rotated around an in-plane axis. In the present case

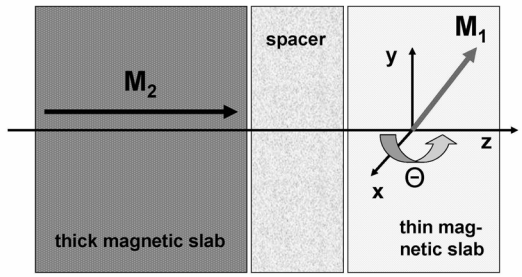

FIGURE 12.3: *Rotation of the magnetization in the thin magnetic slab by angle* Θ *around the y-axis.*

the main interest is directed to the questions (a) whether $\Delta E(\Theta)$ has any extrema with respect to Θ, and (b) does the ground state always correspond to a collinear configuration.

12.2.1 Co(100)/Cu$_n$/Co(100) & (100)Py/Cu$_n$/Py(100)

In Fig. 12.4 two almost spectacular cases are shown, namely the twisting energy for Co(100)/Cu$_{25}$/Co(100) and Cu(100)/Py$_{24}$/Cu$_{20}$/Py$_6$/Cu(100), where Py (permalloy) refers to $Ni_{85}Fe_{15}$.

As can be seen, for 25 Cu spacer layers in the Co/Cu/Co system the twisting energy shows a maximum at $\Theta = 90$, indicating that in switching the orientation in the right Co slab a positive anisotropy has to be overcome in order to reach the antiparallel configuration when starting with the parallel one. Furthermore, the energies for the parallel and the antiparallel configuration are nearly degenerated which in the language of interlayer exchange coupling means that at this spacer thickness there is a node in the oscillations with respect to the number of spacer layers,

$$\Delta E(\Theta) = (E(x, m_1, s, m_2, \Theta = 180) - E(x, m_1, s, m_2, \Theta)) \sim 0 \quad . \qquad (12.4)$$

However, this part of the figure implies also that once the external magnetic field is switching off, because of the positive anisotropy energy, the system remains in the switched configuration.

The other example in Fig. 12.4 shows just the opposite case. The anisotropy energy is negative, i.e., the twisting energy has a minimum at $\Theta = 90$. The magnetic ground state in the Py/Cu/Py system with Cu leads corresponds to a non-collinear magnetic configuration: the most favorable configuration is the perpendicular one. It was shown *[2]*, by the way, that in Py/Cu/Py between 20 and 30 Cu spacer layers the perpendicular arrangement always applies.

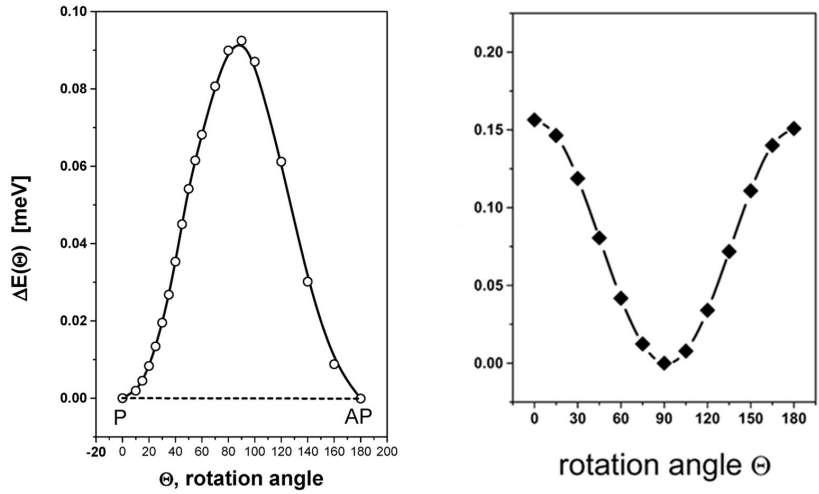

FIGURE 12.4: *Twisting energy as a function of the rotation angle* Θ. *Left:* $Co/Cu_{25}/Co$. *From Ref. [5]. Right:* $Py/Cu_{20}/Py$. *From Ref. [6].*

Switching on an external field can drive the system to either a parallel or an antiparallel configuration depending which of them has the lower energy.

12.2.2 Spin valves with exchange bias

A typical commercial GMR device contains an antiferromagnetic (AF) part used to pin a rather thick magnetic layer that in turn is separated by a metallic spacer such as Cu from a thin magnetic layer usually called free layer. This stack of layers very often is covered by a cap. The leads, which serve as electron reservoirs, are mostly made from Cu; see also Fig. 1.3. In principle the AF part can be any suitable material that combined with a metallic system produces a reasonably large *exchange bias*. The critical thickness of the AF part varies from about 400 Å in the case of NiO to only 80 Å for IrMn. The magnetic layers very often consist of Co/Fe alloys (hard magnets) and Ni/Fe alloys (soft magnets); the spacer material is usually Cu.

An exchange bias occurs when systems with ferro (F)-antiferromagnetic interfaces are cooled through the Néel temperature (T_N) of the AF part, whereby the Curie temperature (T_C) of the F part has to be larger than T_N. After the field cool procedure, at a temperature $T < T_N$, the hysteresis loop

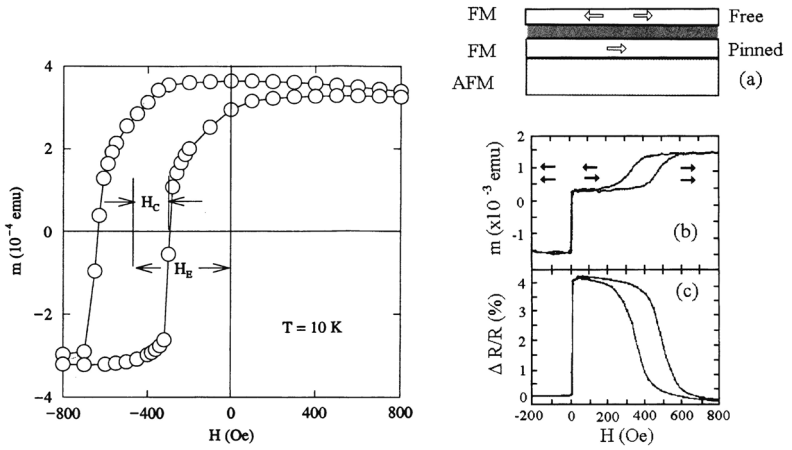

FIGURE 12.5: *Left: Hysteresis loop, $m(H)$, of a FeF_2/Fe bilayer at $T = 10$ K after field cooling. The exchange bias, H_E, and the coercivity, H_C, are indicated. Right: (a) Schematic diagram of a spin valve device. (b) Hysteresis loop, $m(H)$, and (c) magnetoresistance, $\Delta R/R(H)$, of a $Fe_{20}Ni_{80}/Cu/Fe_{20}Ni_{80}/FeMn$ spin valve at room temperature. From Ref. [7].*

of the F-AF system is shifted along the field axis generally in the opposite direction of the cooling field, i.e., the absolute value of the coercive field for decreasing and increasing field is different; see Fig. 12.5. This loop shift is usually termed *exchange bias* and was found and investigated in quite a few different experiments such as magnetization and magnetic torque measurements, ferromagnetic resonance, neutron diffraction, magnetoresistance, etc. For a review, see for example Ref. *[7].*

In the left part of Fig. 12.6 a prototype of such a GMR device is shown, namely

$$Cu(111)/Cu_6/(CoO)_{12}/Co_{24}/Cu_n/Co_6/Cu_{6+m}/Cu(111) \quad , \qquad (12.5)$$

$14 \leq n \leq 48$, in which CoO, known to exhibit one of the largest exchange bias effects [7], serves as AF part. The magnetic (spin only) moments in the antiferromagnetic part are typically 2.05 μ_B and -0.05 μ_B for Co and O, respectively. In the pinned Co layer they amount to about 1.71 μ_B. The magnetic moment of the Co layers adjacent to the Cu spacer is reduced to 1.65 μ_B; that of the penultimate plane of Co atoms in the free layer is slightly enhanced (1.72 μ_B) as compared to the moment of Co planes further off the Cu/Co interface. Within the spacer the Cu atoms are very weakly polarized; the magnitude of the induced moments oscillates approximately with a period of two monolayers.

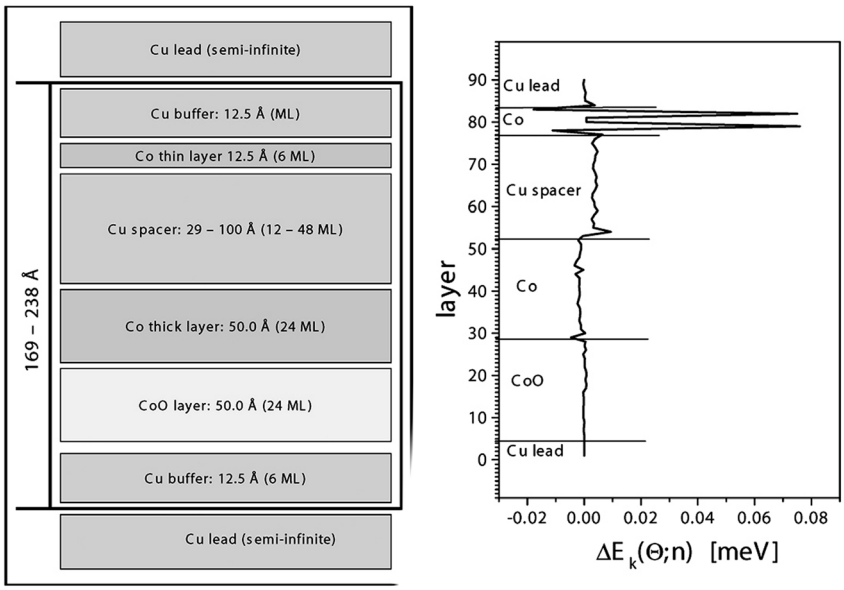

FIGURE 12.6: *Left: A typical Co/Cu/Co spin valve with semi-infinite Cu leads and a "thick" Co layer pinned by an antiferromagnetic CoO slab. Right: Layer-resolved band energies* $\Delta E_k(\Theta; n)$ *for the case of 23 Cu spacer layers and perpendicular coupling* ($\Theta = 90^0$). *From Ref. [8].*

The twisting energies for this set of systems, in which the thickness of the functional part varies between 21 and 30 ML, are displayed in Fig. 12.7 with respect to the rotation angle Θ. It is interesting to note that although there are cases in which the twisting energy changes as perhaps expected proportional to $(1 - \cos\Theta)$, in the majority of Cu spacer thicknesses a positive anisotropy seems to be present. Just as in the much simpler Co/Cu/Co system discussed above, at certain thicknesses the parallel and the parallel configuration are almost degenerated in energy; the twisting energy at such a spacer thickness is therefore entirely governed by the anisotropy energy.

Clearly enough in this context two questions have to be asked, namely (a) from which part of the system does the anisotropy energy arise, and (b) would it be destroyed if interdiffusion at the Co/Cu interface takes place. The first question can be answered by employing again the concept of layer-resolved band energies. In the right part of Fig. 12.6 these quantities are displayed for 23 Cu spacer layers and $\Theta = 90°$. Obviously, by changing the direction of the magnetization in the thin magnetic slab, by far the largest contributions to the anisotropy energy arise from the interface between the thin magnetic slab

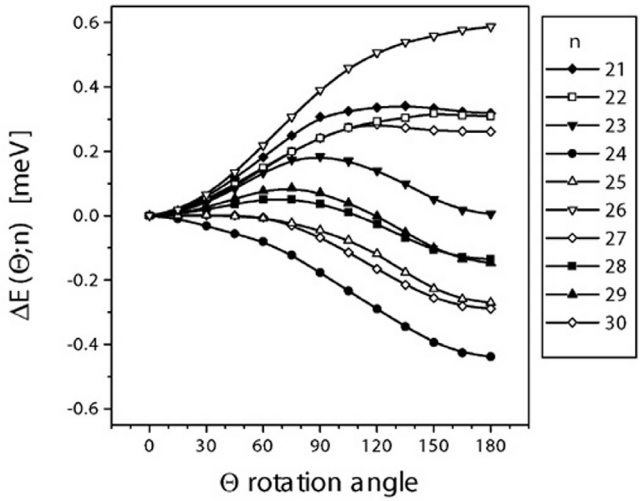

FIGURE 12.7: *Twisting energies $\Delta E(\Theta; n)$ for spacer thicknesses between 21 - 30 ML for the system shown in the left part of Fig. 12.6. From Ref. [8].*

and the spacer.

It is well known that in the binary bulk system Co/Cu the solubility of Co in Cu (and oppositely) is at best 1 - 2%. As this percentage not necessarily also applies for a possible interdiffusion at Co/Cu interfaces in Fig. 12.8 the following difference in total energies,

$$\Delta E_{tot}(\mathbf{c}, N) = E_{tot}(\mathbf{c}, N) - E_{tot}(\mathbf{c} = \mathbf{0}, N) \ , \tag{12.6}$$

is shown for the system Co(100)/Cu/Co(100) corresponding to a spacer thickness of 36.4 Å and a uniform orientation of the magnetization along the surface normal. In Eq. (12.6) the argument N denotes the total number of atomic layers considered in the functional part of Co(100)/Cu/Co(100), i.e., comprises all Co "buffer layers" and the Cu spacer layers. N serves as a reminder that the characteristic volume is N times the unit volume in each atomic layer. As can be seen from this figure, by assuming an error of about $\pm$ 0.025 mryd in the total energy calculations (indicated by horizontal dashed lines) $\Delta E_{tot}(c, N) \sim 0$ for all interdiffusion concentrations below about 1.5%. Fig. 12.8 clearly indicates that in Co/Cu/Co spin valves interdiffusion at the interfaces definitely has to be considered with interdiffusion concentrations ranging between about zero and 2%.

Surprisingly, however, it turns out that the main band energy contributions to the magnetic anisotropy energy in the spin valve listed in (12.5) come from the penultimate Co layer at the interface between the rotated Co slab and the spacer, and not from the Co layer immediately adjacent to the Cu spacer; see

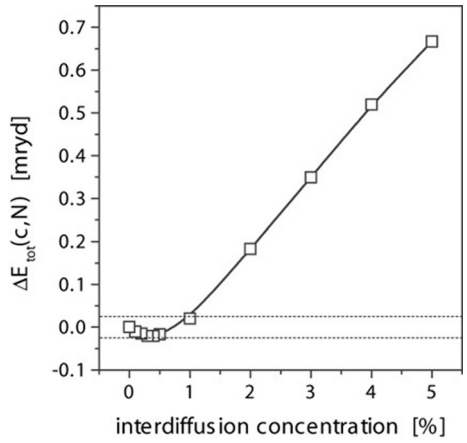

FIGURE 12.8: *Total energy difference with respect to the interdiffusion concentration for a spacer thickness of 36.4 Å in Co(100)/Cu/Co; see also Eq. (12.6). From Ref. [9].*

the left part of Fig. 12.9. Even more surprising is the fact that interdiffusion at the interfaces of the thin magnetic slab moves the maximum in the twisting energy to values of Θ larger than 90°. Altogether, however, the effects of interdiffusion at the Co/Cu interface are minute and because of the special behavior of the layer-resolved band energies (Fig. 12.9, right part) hardly change the functional form of the twisting energy.

12.3 Switching energies and the phenomenological Landau-Lifshitz-Gilbert equation

In using the phenomenological Landau-Lifshitz-Gilbert equation with a damping parameter G,

$$\frac{1}{\gamma_{\mathrm{G}}}\frac{d\mathbf{M}(t)}{dt} = -\mathbf{M}(t)\times\mathbf{H}^{\mathrm{eff}} + \frac{G}{\gamma_{\mathrm{G}}^2\,|\mathcal{M}(t)|^2}\left(\mathbf{M}(t)\times\frac{d\mathbf{M}(t)}{dt}\right) \quad , \tag{12.7}$$

$$\gamma_{\mathrm{G}} = \frac{g\mu_{\mathrm{B}}}{\hbar} = \frac{g\,|e|}{2m_{\mathrm{e}}} \quad , \tag{12.8}$$

where $\mathbf{M}(t)$ refers to the volume averaged total magnetic moment at a particular time t and $\mathbf{H}^{\mathrm{eff}}$ to the so-called effective field, it was found experimentally [10, 11, 12] that in multilayer systems the Gilbert damping parameter G

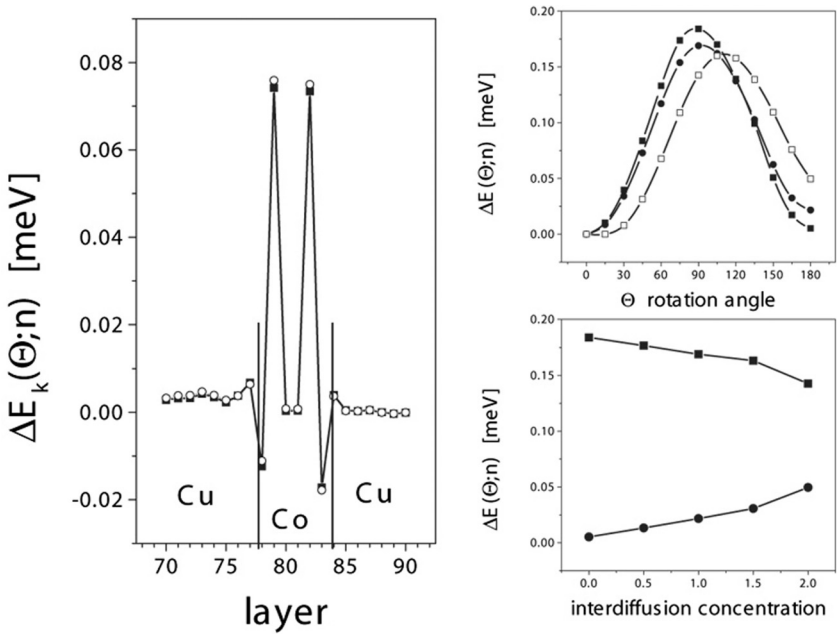

FIGURE 12.9: *Left: Layer-resolved twisting energies* $\Delta E_k(\Theta; n)$ *for* $\Theta = 90°$ *and* $n = 23$ *in the vicinity of the free layer of the spin valve specified in (12.5); see also Fig. 12.7. Circles: no interdiffusion, squares: 1% interdiffusion. Right: (top)* $n = 23$*, for the interdiffusion concentrations 0% (full squares), 1% (circles) and 2% (open squares) as a function of the rotation angle* Θ*. Lower part: twisting energy* $\Delta E(\Theta; n)$ *for* $n = 23$ *at* $\Theta = 90^0$ *(squares) and* 180^0 *(circles) versus the interdiffusion concentration. From Ref. [8].*

varies linearly with the inverse film thickness. In Eq. (12.8) e is the elementary charge, m_e the mass of an electron, μ_B the Bohr magneton, and g the (electronic) Landé–factor.

In the presence of two-dimensional translational invariance $\mathbf{M}$ can be replaced by a layer averaged magnetic moment $\mathbf{m}(t)$, or in terms of the magnetization direction $\mathbf{n}(t)$:

$$\frac{d\mathbf{n}(t)}{dt} = -\gamma \mathbf{n}(t) \times \mathbf{H}^{\text{eff}} + \alpha \mathbf{n}(t) \times \left(\mathbf{n}(t) \times \mathbf{H}^{\text{eff}}\right) \quad , \tag{12.9}$$

$$\mathbf{m}(t) = \frac{1}{N} \sum_{i=1,N} \mathbf{m}_i(t) \quad , \quad \mathbf{n}(t) = \frac{\mathbf{m}(t)}{|\mathbf{m}(t)|} \quad , \tag{12.10}$$

where N is the total number of magnetic layers in those parts of a spin valve, in which the averaged moment changes in time. It should be noted that obviously

the same type of Landau-Lifshitz-Gilbert equation is used as in Chapter 9, see, e.g., Eqs. (9.1) and (9.15), however, now for a different purpose.

12.3.1 Internal effective field

The local effective field $\mathbf{H}^{\text{eff}}$, which in principle includes the exchange energy, the magnetic anisotropy energy, external magnetic fields, etc., can in the case of layered systems be written in terms of the following derivative of the free energy F,

$$\mathbf{H}^{\text{eff}} = -\nabla_{\mathbf{m}(t)} F \quad , \tag{12.11}$$

Mapping now at zero temperature $\mathbf{H}^{\text{eff}}$ onto $\mathbf{H}^{\text{E}}$, namely onto changes of the total energy (band energy when using the magnetic force theorem, free energy at 0° K) with respect to $\mathbf{m}(t)$,

$$\mathbf{H}^{\text{eff}} \rightarrow \mathbf{H}^{\text{E}} : \mathbf{H}^{\text{E}} = -\frac{\partial E_b}{\partial \mathbf{m}(t)} = -\nabla_{\mathbf{m}(t)} E_b \quad , \tag{12.12}$$

Eq. (12.9) can be rewritten as *[5]*

$$\frac{d\mathbf{m}(t)}{dt} = \gamma \left(\mathbf{m}(t) \times \nabla_{\mathbf{m}(t)} E_b \right) - \alpha \mathbf{m}(t) \times \left(\mathbf{m}(t) \times \nabla_{\mathbf{m}(t)} E_b \right) \quad , \tag{12.13}$$

where α and γ are the properly reformulated parameters from Eq. (12.7).

Expanding therefore E_b at a given initial reference direction of the magnetic moment, $\mathbf{m}_0$, in terms of a Taylor series,

$$E_b(\mathbf{m}_0 + \mathbf{m}(t)) \simeq E_b(\mathbf{m}_0) + \sum_{k=1}^{p} \frac{1}{k!} \left(\mathbf{m}(t) \cdot \nabla_{\mathbf{m}(t)} \right)^k E_b(\mathbf{m}_0) \quad , \tag{12.14}$$

in principle Eq. (12.13) can be solved.

In particular, if the change in the moment $\mathbf{m}(t)$ is constrained to the yz-plane, see also Fig. 12.3,

$$\mathbf{m}(t) = m_{\text{y}}(t)\mathbf{e}_{\text{y}} + m_{\text{z}}(t)\mathbf{e}_{\text{z}} \quad , \quad (m_{\text{x}} = 0) \quad , \tag{12.15}$$

and $\mathbf{m}_0 = m_0 \mathbf{e}_{\text{z}}$ is the initial ground state moment,

$$m_0^2 = m_{\text{y}}^2 + m_{\text{z}}^2 \ = m^2 \quad , \tag{12.16}$$

then by using Eq. (12.15) up to third order ($p = 3$), one gets *[5]*

$$\begin{aligned} \Delta E_b \left(\mathbf{m}(t) \right) &= E_b(\mathbf{m}_0 + \mathbf{m}(t)) - E_b(\mathbf{m}_0) \\ &\simeq a - a\frac{m_{\text{z}}(t)}{m_0} + b\,\frac{m_{\text{z}}^2(t)}{m_0^2} + c\frac{m_{\text{z}}^3(t)}{m_0^3} \\ &= a - a n_{\text{z}}(t) + b\, n_{\text{z}}^2(t) + c n_{\text{z}}^3(t) \quad , \end{aligned} \tag{12.17}$$

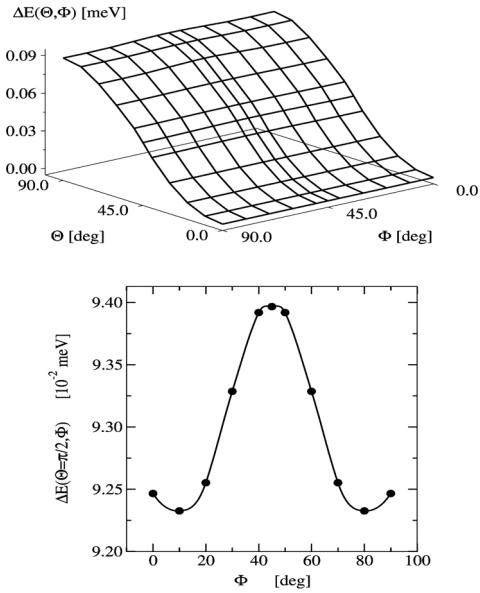

FIGURE 12.10: Top: Twisting energy as a function of both rotation angles in fcc Co(100)/Cu_{25}/Co(100). Bottom: precessional energy at $\Theta = 90^0$. From Ref. [5].

where the coefficients a, b and c can easily be obtained from the twisting energy as a function of Θ. Therefore, the energy torque rotating the moment, namely the first term on the *rhs* of Eq. (12.13) is given by

$$\mathbf{m}(t) \times \mathbf{H}^{\mathrm{E}} = \mathbf{e}_{\mathrm{x}} m_{\mathrm{y}}(t) H_{\mathrm{z}}^{\mathrm{E}} = -n_{\mathrm{y}}(t) \left(-a + 2b\, n_{\mathrm{z}}(t) + 3c n_{\mathrm{z}}^2(t)\right) \mathbf{e}_{\mathrm{x}} \quad , \quad (12.18)$$

and the second term by

$$\mathbf{m}(t) \times \left(\mathbf{m}(t) \times \mathbf{H}^{\mathrm{E}}\right) = -n_{\mathrm{y}}(t) \left(-a + 2b\, n_{\mathrm{z}}(t) + 3c n_{\mathrm{z}}^2(t)\right) \left(m_{\mathrm{z}}(t)\, \mathbf{e}_{\mathrm{y}} - m_{\mathrm{y}}(t) \mathbf{e}_{\mathrm{z}}\right) \quad (12.19)$$

12.3.2 The characteristic time of switching

Neglecting the energy torque term in Eq. (12.18) (absence of precession around the z-axis) since the in-plane anisotropy is by orders of magnitude smaller than the out-of-plane one, see Fig. 12.10, Eq. (12.13) is reduced to

$$\frac{d\mathbf{m}(t)}{dt} \simeq \alpha \frac{\mathbf{m}(t)}{M_0} \times \left(\mathbf{m}(t) \times \mathbf{H}^{\mathrm{E}}\right) \quad , \quad (12.20)$$

which in turn leads to *[5]*

$$m_0 \frac{dn_{\mathrm{x}}(t)}{dt} = 0 \quad , \tag{12.21}$$

$$m_0 \frac{dn_{\mathrm{y}}(t)}{dt} = -\alpha n_{\mathrm{y}}(t) n_{\mathrm{z}}(t) \left(-a + 2b\, n_{\mathrm{z}}(t) + 3c n_{\mathrm{z}}^2(t)\right) \quad , \tag{12.22}$$

$$m_0 \frac{dn_{\mathrm{z}}(t)}{dt} = \alpha n_{\mathrm{y}}^2(t) \left(-a + 2b\, n_{\mathrm{z}}(t) + 3c n_{\mathrm{z}}^2(t)\right) \quad . \tag{12.23}$$

Furthermore, since it was assumed that $n_{\mathrm{y}}^2(t) + n_{\mathrm{z}}^2(t) = 1$, only one equation, namely

$$m_0 \frac{dn_{\mathrm{z}}(t)}{dt} = \alpha \left(1 - n_{\mathrm{z}}^2(t)\right) \left(-a + 2b\, n_{\mathrm{z}}(t) + 3c n_{\mathrm{z}}^2(t)\right) \quad , \tag{12.24}$$

has to be solved. This equation can then be used to evaluate the time $\tau = t_f - t_i$ that is needed to change n_{z} from an initial direction at t_i, $n_{\mathrm{z}}^i = n_{\mathrm{z}}(t_i)$, to a particular direction at a given time t_f, $n_{\mathrm{z}}^f = n_{\mathrm{z}}(t_f)$.

Of particular interest is the time that is needed to switch in a spin valve system the orientation of the magnetization from the initial ground state configuration to a final (collinear) configuration. This exactly is shown in Fig. 12.11. There $\Theta_j = \pi/2$ denotes the ground state (perpendicular arrangement), $\Theta_i = 0$ the parallel and $\Theta_i = \pi$ the antiparallel configuration. As can be seen it takes the system about 35 picoseconds [ps] to switch from an excited collinear configuration to the non-collinear ground state. It also can be seen that there are indeed differences in time whether switching the direction of the magnetization in the thin magnetic layer is from a parallel or an antiparallel orientation to the non-collinear ground state; see the right part of Fig. 12.4.

12.4 Heterojunctions

Very soon it was found out [13] that not only metallic spacers showed oscillations in the interlayer exchange coupling, but also typical non-metallic materials such as "semiconductors" or metal oxides. The technical expression connected with this kind of system is Tunnelling Magnetoresistance (TMR) devices or heterojunctions. It should be noted that the term *semiconductor* was put in quotation marks, since colloquially a typical bulk property is used to characterize spacer materials such as Si or ZnSe, even so few tens of an Angstrom thick layers of such materials not necessarily are "semi-conducting". In the following two typical examples are discussed, namely Fe/ZnSe/Fe and Fe/Si/Fe, because different aspects of heterojunctions can be pointed out.

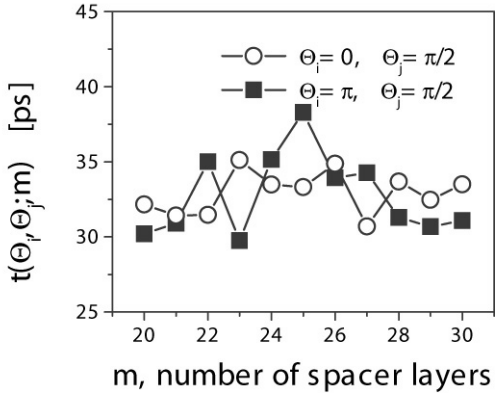

FIGURE 12.11: *Switching time $t(\Theta_i, \Theta_j; m)$ versus the number of Cu spacer layers in Cu(100)/Py/Cu_m/Py/Cu(100). See also the right half of Fig. 12.4. From Ref. [5].*

12.4.1 Fe(100)/$(ZnSe)_n$/Fe(100)

bcc-Fe(100)/ZnSe/Fe heterostructures can have two types of termination, namely either Zn or Se forming the interface with Fe, which in fact makes this system in particular interesting from a theoretical point of view. In the left part of Fig. 12.12 the interlayer exchange coupling is displayed, corresponding to an antiparallel configuration in which in the second (right) part of the atomic layers the magnetization is oriented antiferromagnetically. As can be seen from this figure, Zn-terminated heterostructures are antiferromagnetically coupled up to a spacer thickness of about 15 Å and then start to oscillate weakly between the ferro- and the antiferromagnetic configuration. The behavior of Se-terminated heterostructures is completely different: for thin spacers there are distinct regions of ferro- and antiferromagnetic coupling, only beyond about 20 Å weak oscillations set in.

The band energy part ΔE_b of the magnetic anisotropy energy is displayed in the right half of Fig. 12.12 for both types of termination. It is obvious that different terminations cause different characteristic behavior: for Zn-terminated heterostructures the orientation of the magnetization is predicted to be mostly in-plane, while for Se-terminated heterostructures a perpendicular orientation is favored. In Fig. 12.12, for a typical example, namely for 12 repetitions of ZnSe, a layer-wise decomposition of ΔE_b is shown. There one easily can see that the spacer part of the heterojunctions adds very little to ΔE_b: it is essentially the first 3 - 4 Fe layers next to the interface that account for the actual value of ΔE_b. It is interesting to note that in Zn-terminated heterostructures the contribution from the Fe layer forming the interface has a negative value, whereas from the same layer in the Se-terminated heterostructure the

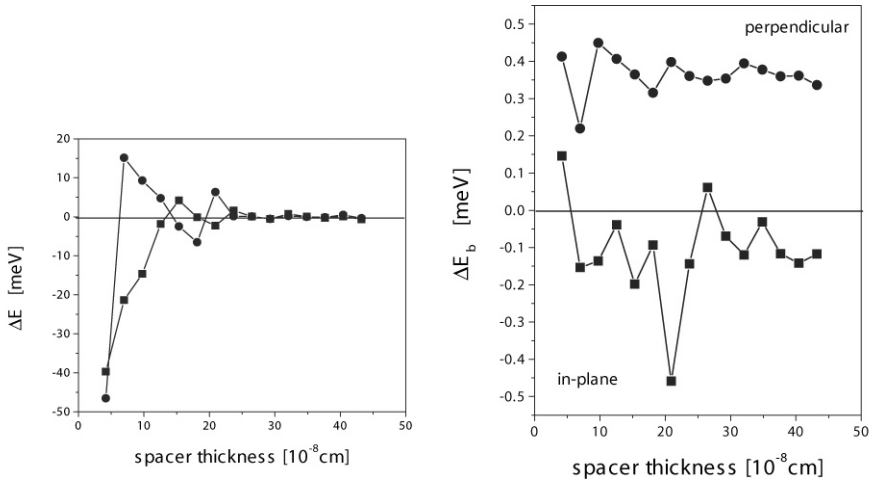

FIGURE 12.12: *Fe(100)/ZnSe/Fe(100). Left: Interlayer exchange coupling as a function of the spacer thickness. Squares: Zn-termination, circles: Se-termination. Right: Band energy part of the magnetic anisotropy energy as a function of the spacer thickness. Squares: Zn-termination, circles: Se-termination. From Ref. [14].*

contribution is reasonably large and positive: it is essentially this layer that generates the differences to be seen in the left part of Fig. 12.13.

12.4.2 Fe(000)/Si$_n$/Fe(100)

Trilayers as well as multilayers of Fe with nonmetallic amorphous Si [15] or metallic Fe-Si alloys [16] have been investigated experimentally already in the beginning 1990s. The occurrence of interlayer exchange coupling in antiferromagnetically coupled Fe/Si/Fe systems was first attributed to interdiffusion effects causing the spacer to become metallic [17]. Low-energy electron diffraction (LEED) and Auger spectroscopy measurements seemed to prove that the interlayer exchange coupling was not only due to alloying effects at the interface(s), but was also observed in systems with homogeneous Fe-Si alloy spacers [13, 18] with a slightly deformed B2 (c-FeSi) structure [19, 20]. Later on [16], Brillouin light scattering experiments, however, showed that in Fe/Fe$_{1-c}$Si$_c$/Fe, $0.4 \leq c \leq 1.0$, the interlayer exchange coupling constant increased with increasing Si content in the alloy, the oscillations in turn indicating a typical metallic behavior. The interlayer distance, by the way, as obtained from Bragg reflection experiments turned out to be about 1.4331 Å [20], which reflects closely the experimental bcc Fe lattice constant.

In the right part of Fig. 12.13 total energy differences $E(c_\mathrm{d}) - E(c_\mathrm{d} = 0)$

for Fe/Si/Fe are shown for particular spacer thicknesses with respect to the interdiffusion concentration c_d when considering a two-layer interdiffusion, i.e., considering a system with s Si layers of the following type

$$\ldots \mathrm{Fe}/\mathrm{Fe}_{1-c_\mathrm{d}}\mathrm{Si}_{c_\mathrm{d}}/\mathrm{Fe}_{c_\mathrm{d}}\mathrm{Si}_{1-c_\mathrm{d}}/\mathrm{Si}_{s-2}/\mathrm{Fe}_{c_\mathrm{d}}\mathrm{Si}_{1-c_\mathrm{d}}/\mathrm{Fe}_{1-c_\mathrm{d}}\mathrm{Si}_{c_\mathrm{d}}/\mathrm{Fe}\ldots \quad .$$

It turned out *[21]* that for interdiffusion concentrations larger than 20 % the formation of interface alloys is preferred, while below 20 % interdiffused interfaces as well as clean interfaces occur with equal probability.

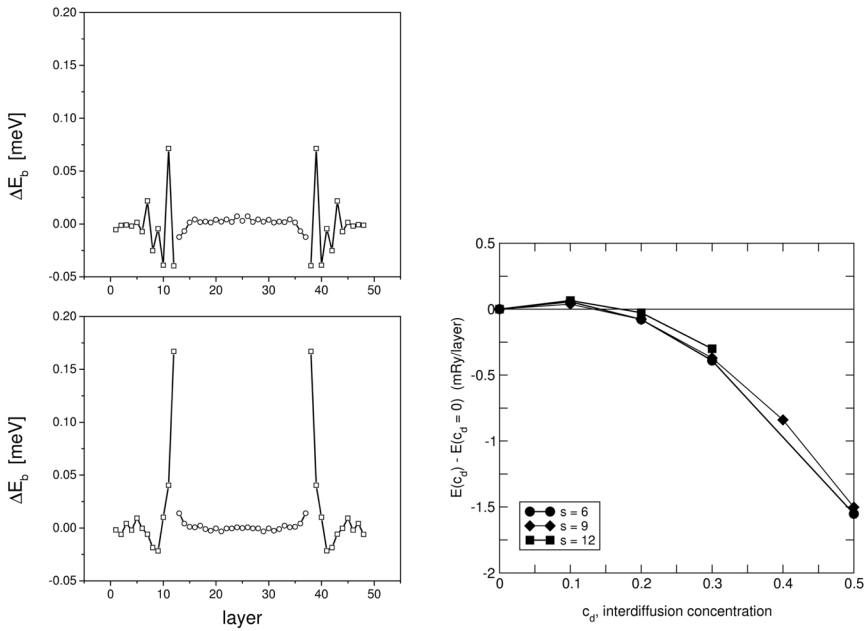

FIGURE 12.13: *Left: Layer-resolved band energy part of the magnetic anisotropy energy for Fe(100)/(ZnSe)$_{12}$/Fe(100). Top: Zn-termination, bottom: Se-termination. Squares: Fe-layers, circles: spacer layers. From Ref. [14]. Right: Total energy differences, $E(c_d) - E(c_d = 0)$, in Fe(100)/Si/Fe(100) with respect to the interdiffusion concentration c_d. The number of spacer layers s is marked explicitly. From Ref. [21].*

In the left part of Fig. 12.14 the interlayer exchange coupling is displayed for a variety of interdiffusion concentrations. As can be seen, increasing interdiffusion reduces the large oscillations for small spacer thicknesses dramatically, while for larger spacer thicknesses interdiffusion effects seem to be less important. For $c_\mathrm{d} > 0.15$ the regime of antiferromagnetic coupling is considerably

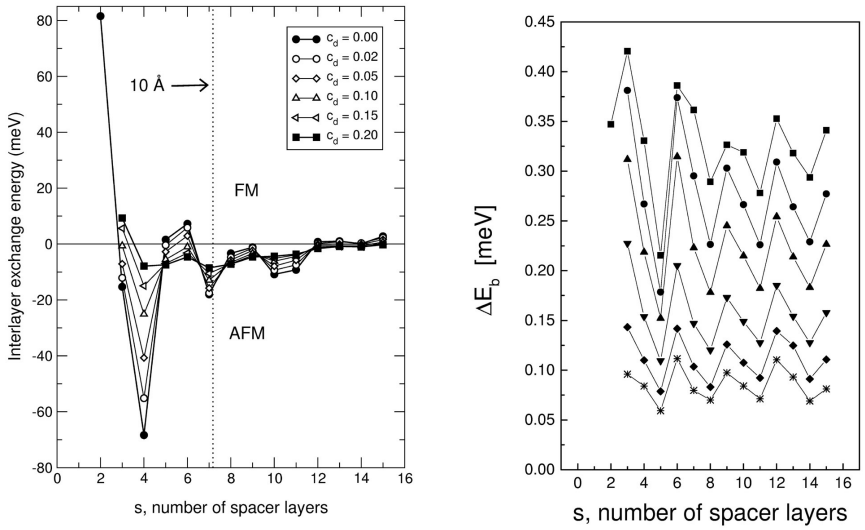

FIGURE 12.14: *Left: Changes of the interlayer exchange coupling with respect to the number of spacer layers for different interdiffusion concentrations c_d. Right: Band energy part of the magnetic anisotropy energy for Fe/Si/Fe systems with a two-layer interdiffusion at the interfaces versus the number of spacer layers. The results are shown for different interdiffusion concentrations c_d, whereby c_d increases from the top $c_d = 0.0$ (squares) to the bottom $c_d = 0.2$ (stars). From Ref. [21].*

enlarged extending for $c_{\mathrm{d}} = 0.2$ from $s = 4$ to $s = 12$. Thus strong interdiffusion at the interfaces helps to stabilize the antiferromagnetic coupling.

The right part of this figure contains the band energy contribution to the magnetic anisotropy energy, ΔE_b, considering a two-layer interdiffusion at the Fe/Si interfaces. With increasing interdiffusion concentration ΔE_b is reduced and shows an oscillation period of 3 ML. For all spacer thicknesses and interdiffusion concentrations ΔE_b favors a perpendicular orientation of the magnetization. Fig. 12.15, showing the concentration-dependent changes of the layer-resolved ΔE_b for the system with 9 Si layers, proves that again ΔE_b is essentially determined by contributions from the interfaces.

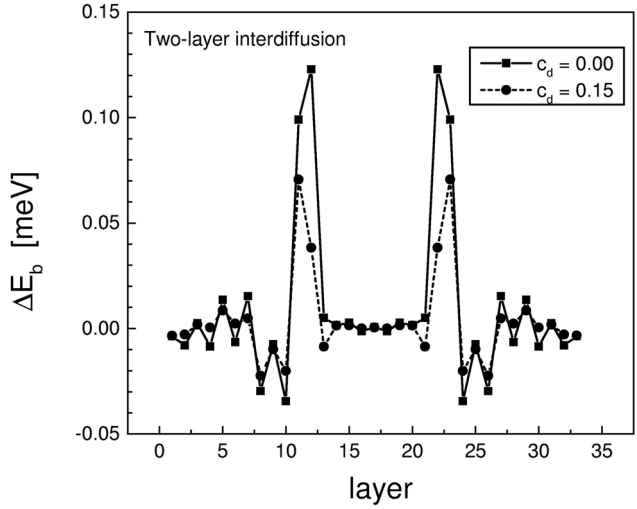

FIGURE 12.15: *Layer-resolved band energy part of the magnetic anisotropy energy for Fe(100)/Si$_9$/Fe(100) with a clean interface (squares) and corresponding to a finite interdiffusion concentration. From Ref. [21].*

12.5 Summary

Just like magnetic free surfaces spin valves can also be considered as systems nanostructured in one dimension, i.e., can be characterized by two-dimensional translational invariance and an orthogonal complement to the in-plane coordinates. They differ from free (capped) surfaces or trilayers by one important fact, namely the boundary conditions along the surface normal:

left boundary	**functional part**	**right boundary**	$r, s = \infty$
		$/\mathrm{Vac}_s$	: **free surface**
$\mathrm{Cu}_r/$	$\ldots \mathrm{Co}_n/\mathrm{Cu}_m/\ldots$		
		$/\mathrm{Cu}_s$	: **spin valve**

- Spin valves show all the properties already encountered with free magnetic surfaces such as oscillations with respect to the number of spacer layers in the interlayer exchange coupling as well as for the anisotropy energy (the band energy part).

- Again interdiffusion at the interfaces is a very important issue which seems to be even more crucial in the case of heterojunctions than in systems with a metallic spacer.
- The magnetic ground state of spin valves does not necessarily correspond to a collinear configuration.
- The so-called twisting energy can have considerable anisotropy contributions.
- The time needed to switch a spin valve from a given initial magnetic configuration to final one can be estimated by interpreting the twisting energy in terms of a phenomenological Landau-Lifshitz-Gilbert equation. Such switching times are typically of the order of a few ten picoseconds.

[1] B. Heinrich, J. F. Cochran, T. Monchesky, and R. Urban, Phys. Rev. B **59**, 14520 (1999).

[2] D. T. Pierce, J. Unguris, R. J. Celotta, and M. D. Stiles, J. Magn. Magn. Mater. **200**, 290 (1999).

[3] H. C. Herper, L. Szunyogh, P. Entel, and P. Weinberger, Phys. Rev. B **68**, 134421 (2003)

[4] S. Mirbt, A. M. N. Niklasson, B. Johansson, and H. L. Skriver, Phys. Rev. B **54**, 6382 (1996).

[5] P. Weinberger, A. Vernes, B. L. Gyorffy, and L. Szunyogh, Phys. Rev. B **70**, 094401 (2004).

[6] A. Vernes, P. Weinberger, and L. Szunyogh, Phys. Rev. B **72**, 0112401 (2005).

[7] J. Nogués and I. K. Schuller, J. Magn. Magn. Mater **192**, 203 (1999).

[8] P. Weinberger, Phys. Rev. B **75**, 064405 (2007).

[9] C. Sommers and P. Weinberger, Phys. Rev. B **72**, 054431 (2005).

[10] B. Heinrich, R. Urban, and G. Woltersdorf, IEEE Transactions on Magnetics **38**, 2496 (2002).

[11] R. Urban, G. Woltersdorf, and B. Heinrich, Phys. Rev. Letters **87**, 217204 (2001).

[12] B. Heinrich, G. Woltersdorf, R. Urban, and E. Simanek, J. Magn. Magn. Materials **258-259**, 376 (2003).

[13] E. E. Fullerton, J. E. Mattson, S. R. Lee, C. H. Sowers, Y. Y. Huang, G. Felcher, S. D. Bader, and F. T. Parker, J. Magn. Magn. Mater. **117**, L301 (1992).

[14] H. C. Herper, P. Weinberger, A. Vernes, L. Szunyogh, and C. Sommers, Phys. Rev. B **64**, 184442 (2001).

[15] S. Toscano, B. Briner, H. Hopster, and M. Landolt, J. Magn. Magn. Mater. **114**, L6 (1992).

[16] R. R. Gareev, D. E. Bürgler, M. Buchmeier, R. Schreiber, and P. Grünberg, J. Magn. Magn. Mater. **240**, 235 (2002).

[17] J. J. de Vries, J. Kohlhepp, F. J. A. de Broeder, R. Jungblut, R. Coehoorn, A. Reinders, and W. J. M. de Jonge, Phys. Rev. Lett. **78**, 3023 (1997).

[18] K. Inomata, K. Yusu, and Y. Saito, Phys. Rev. Lett. **74**, 1863 (1995).

[19] R. R. Gareev, D. E. Bürgler, M. Buchmeier, D. Olligs, R. Schreiber, and P. Grünberg, Phys. Rev. Lett. **87**, 157202 (2001).

[20] G. J. Strijkers, J. T. Kohlhepp, H. J. M. Swagten, and W. J. M. de Jonge, Phys. Rev. B **60**, 9583 (1999).

[21] H. Herper, P. Weinberger, L. Szunyogh, and C. Sommers, Phys. Rev. B **66**, 064426 (2002).

13

Nanostructured in two dimensions: single atoms, finite clusters & wires

Clusters (small ensembles of atoms, finite wires) on top of metallic substrates show anisotropic properties exceeding even those of systems nanostructured in one direction. Once again it will turn out that a proper definition of a characteristic volume is essential. The importance of "rim" atoms and the consequences of covering these clusters by protective metallic layers will be emphasized.

Surface-supported nanoparticles of magnetic atoms raised and still raise a lot of interest, because of potential applications in non-volatile magnetic storage media. In the last few years, magnetic nanostructures were investigated experimentally in terms of various experimental methods [1, 2, 3, 4, 5, 6] such as *Scanning Tunnelling Microscopy* (STM), *X-ray Magnetic Circular Dichroism* (XMCD) and the *Magneto-Optical Kerr Effect* (MOKE). In interpreting these techniques in terms of phenomenological models [7] and sum-rules [8], e.g., high anisotropies and orbital moments of single magnetic adatoms on a non-magnetic substrate were found or predicted. Eventually it was and is the ambition of experimental methods to produce and manipulate nanostructures on an atom-by-atom level using for example magnetic tunnel tips [9]. Furthermore, by combining magnetic and non-magnetic materials like Co and Pt [1], or two different magnetic species like Fe and Co [10], see also the next chapter, to form nanoclusters, tunable magnetic properties seem to be in reach.

A theoretical description of systems nanostructured in two dimensions is even more complex than those in one dimension, since in principle two-dimensional translational symmetry no longer helps to reduce the number of possible magnetic configurations. In systems lacking any translational symmetry every single atom has to be characterized by an individual orientation of the magnetization. In order to be still able to describe such systems one has to go back to Section 4.13 in which a scheme was introduced to embed an ensemble of adatoms on top of an otherwise perfect substrate (with two-dimensional translational invariance).

Suppose that as indicated in Fig. 13.1 a certain section ("cluster") of a solid system consisting of a substrate and adatoms is selected that contains the actual adatoms, perturbed and unperturbed substrate atoms and of course vacuum sites. Now let m be the total number of adatoms and perturbed

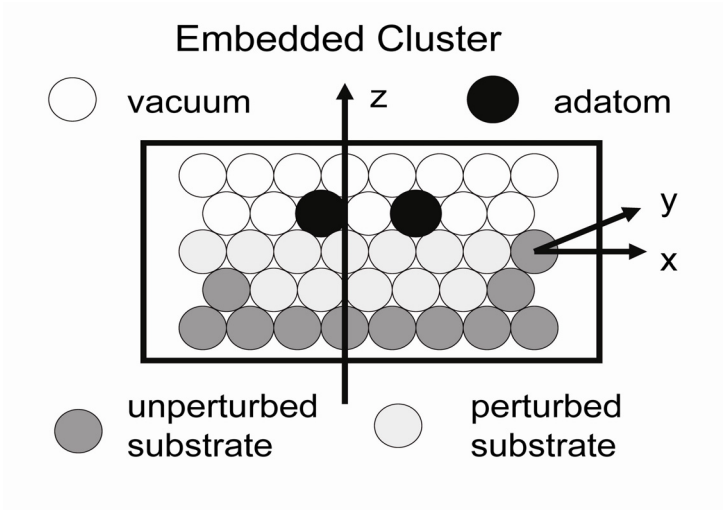

FIGURE 13.1: *Cluster section of a semi-infinite system.*

substrate atoms, s the total number of unperturbed substrate sites and v the number of included vacuum sites. A typical magnetic configuration in such a system is then defined by

$$C_\alpha = \{\mathbf{n}_1, \mathbf{n}_2, \ldots, \mathbf{n}_m, \{\mathbf{n}_k = \mathbf{n}_B, k = 1, \ldots, s\}\} \quad , \tag{13.1}$$

$$C_0 = \{\mathbf{n}_i = \hat{z}, i = 1, \ldots, (m+s)\} \quad , \tag{13.2}$$

where $\mathbf{n}_B$ contains all the information about the orientation of the magnetization in the unperturbed substrate (bulk). The total number N of atoms in a particular cluster amounts therefore to

$$N = m + s + v \quad . \tag{13.3}$$

In order to evaluate the band energy part of a characteristic anisotropy energy,

$$\Delta E_{\alpha-0} = E(C_\alpha) - E(C_0) \quad , \tag{13.4}$$

one can choose for example as a possible reference configuration C_0, see Eq. (13.2), in which the orientation of the magnetization in all atoms points uniformly along the z-axis (surface normal). Typically an anisotropy energy of particular interest is then of the following type

$$\Delta E_{\mu-z} = E_\mu - E_z = \begin{cases} > 0, & z, \text{ preferred} \\ \\ < 0, & \mu, \text{ preferred} \end{cases} \quad , \quad \mu = x, y \quad , \tag{13.5}$$

where the axes x and y refer to in-plane unit directions,

$$E_\alpha = \sum_{i=1}^{N} E_\alpha^i \quad , \quad \alpha \in (x, y, z) \quad , \tag{13.6}$$

$$E_\alpha^i = \int_{\epsilon_b}^{\epsilon_F} d\epsilon (\epsilon - \epsilon_F) n_\alpha^i(\epsilon) \quad , \tag{13.7}$$

and ϵ_b and ϵ_F, denote the (valence) band bottom and the Fermi energy, respectively. From Eq. (13.6) one immediately can guess that the by now familiar problem of defining a characteristic volume

$$\Omega = \sum_{i=1}^{N} \Omega_i \tag{13.8}$$

becomes an essential point, since *a priori* one cannot say how many unperturbed substrate and vacuum sites have to be included self-consistently in order to obtain an intrinsic anisotropy energy (or for that matter any other physical property).

13.1 Finite clusters

13.1.1 Fe, Co and Ni atoms on top of Ag(100)

Suppose that as indicated in Fig. 13.2 one considers a few atoms of Fe, Co or Ni to form a cluster on top of Ag(100). Then immediately just by considering the (two-dimensional) rotational symmetry of these clusters one can imagine that the information to be obtained from actual ab-initio type calculations simply explodes when increasing the number of adatoms, since in each site spin and orbital moments can be different and so are the magnetic interactions between the different sites within a particular cluster.

The above-mentioned problem of a characteristic volume is addressed in the left part of Fig. 13.3, in which typical properties of a single atom of Fe on Ag(100), such as the number of electrons, the spin and the orbital moment, are investigated by increasing the number of neighboring shells, i.e., by including more and more substrate (and vacuum) sites. As can be seen there, although the number of electrons in the cell corresponding to the Fe atom hardly changes beyond the third shell of neighbors, the orbital magnetic moment becomes intrinsic only after having included at least 4 shells. This implies that even in a hardly polarizable substrate such as silver, the number of perturbed substrate sites is quite high.

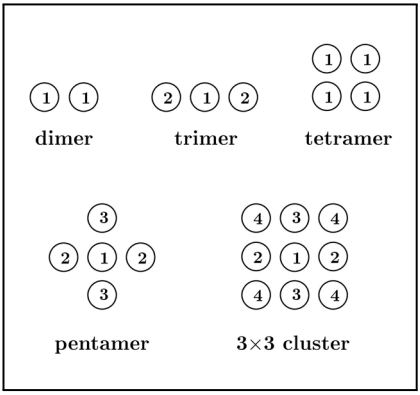

FIGURE 13.2: *Sketch of the planar clusters considered. For an orientation of the magnetization along the x or y axis, equivalent atoms in a cluster are labelled by the same number. From Ref. [11].*

A completely different case is shown in the middle part of Fig. 13.3, namely that of a cluster consisting of either two Fe or two Co atoms when changing the distance between the two magnetic atoms, i.e., by placing them on different in-plane positions of the parent Ag fcc lattice. Both the spin and orbital moments (per site) seem to indicate that being separated by only one in-plane lattice spacing they behave already like isolated atoms. The corresponding exchange energies, however,

$$\begin{aligned} E_x &= E(C_0) - E(C_1) \quad , \\ C_1 &= \{\mathbf{n}_1 = \hat{z}, \mathbf{n}_2 = -\hat{z}, \mathbf{n}_i = \hat{z}, i = 3, \ldots, (m+s)\} \quad , \\ C_0 &= \{\mathbf{n}_i = \hat{z}, i = 1, \ldots, (m+s)\} \quad , \end{aligned} \tag{13.9}$$

where $i = 1, 2$ refers to the magnetic atoms, show that this is not quite the case (right part of Fig. 13.3). With respect to an increase of the in-plane distance between the Fe atoms they first align parallel, then antiparallel, and from there on stay parallel. With the exception of being arranged as first neighbors the two Co atoms are aligned antiparallel even up to the 5-th shell.

As regards the anisotropy energies for small clusters of Fe , Co and Ni on top of Ag(100) the following situation applies (for the actual values see Ref.[11]):

$n \leq 4$	ΔE_{x-z}	ΔE_{y-z}
Fe clusters	> 0	> 0
Co clusters	$> 0, n = 1$	$> 0, n \leq 2$
	$< 0, n > 1$	$< 0, n > 2$
Ni clusters	< 0	< 0

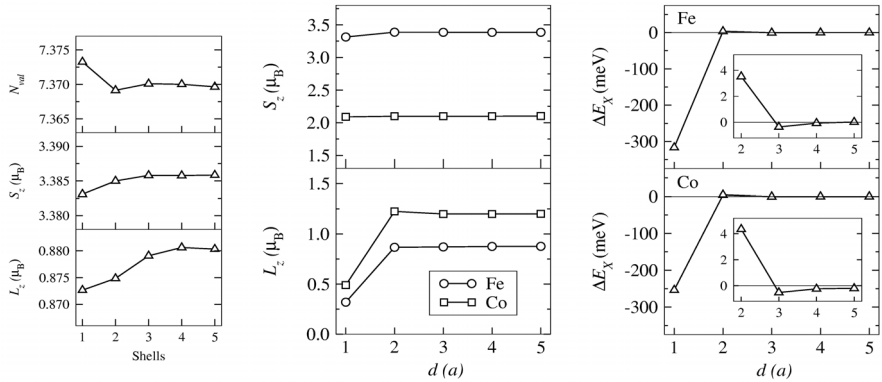

FIGURE 13.3: *Left: Calculated number of valence electrons (N_{val}), spin moment (S_z) and orbital moment (L_z) of a single Fe adatom on a Ag(100) surface as a function of the number of self-consistently treated atomic shells around the Fe atom. Middle: Calculated spin and orbital moments of two adatoms of Fe or Co on Ag(100) as a function of their distance d measured in units of the 2D lattice constant a. Right: Calculated exchange coupling energy, ΔE_x as a function of the distance d measured in units of the 2D lattice constant a. The insets show the range $2a \leq 5a$ on an enlarged scale. From Ref. [11].*

where for matters of simplicity n denotes the number of magnetic atoms in the cluster. This means that in all Fe clusters the orientation of the magnetization is perpendicular, in all Ni clusters it is in-plane, while in Co clusters not only the size of the cluster matters but also the chosen in-plane direction.

13.2 Finite wires & chains of magnetic atoms

With the arrival of advanced Scanning Tunnelling Microscope (STM) techniques, in particular spin-polarized versions thereof, it became very popular to arrange atoms in chains along steps of suitable substrates and to analyze their properties in terms of spectroscopy by means of selection-rule-based interpretations. Since in these interpretations mostly the spin and the orbital moments of the magnetic atoms were of main interest, in the following few sections these quantities will almost dominate the discussion of (anisotropic) magnetic properties of solid systems nanostructured in two dimensions.

A seriously meant warning, however, has to precede these sections: orbital

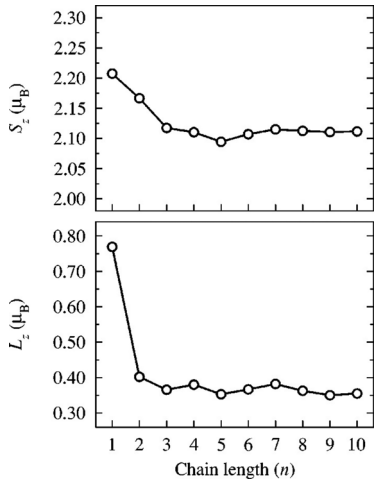

FIGURE 13.4: *Calculated spin moments (S_z) and orbital moments (L_z) of the central (most symmetric) atom in Co_n ($n = 1, \ldots, 10$) chains oriented along the (110) direction on the top of Pt(111) as a function of the chain length. From Ref. [12].*

(and spin) moments are *not* measured; they are the result of an interpretation using certain models ("*sum rules*"). If, therefore, in a particular publication it is claimed that orbital moments were "measured", don't believe it! Ask for the ansatz and the parameters used there, before making use of the published data.

The technological reason for all these investigations is quite clear: it is the search of the laterally tiniest patterns of magnetic atoms that could eventually serve as information medium.

13.2.1 Finite chains of Co atoms on Pt(111)

Suppose that a finite chain of n Co atoms is formed along the (110) direction on top of Pt(111). Then the obvious questions to be asked are (1) how does the spin and the orbital moment of a particular atom in the chain change when the length of the chain is increased, (2) how do the moments change viewing the various atoms in a particular chain of given length, and, of course, (3) to what extent do the individual atoms contribute to the total anisotropy energy.

The answer to the first question can be read immediately from Fig. 13.4, in which the most interior Co atom is considered in Co chains of increasing length. It is evident that only for $n > 7$ this particular Co atom becomes nearly independent of the length of the chain. In a kind of *Gedanken* experi-

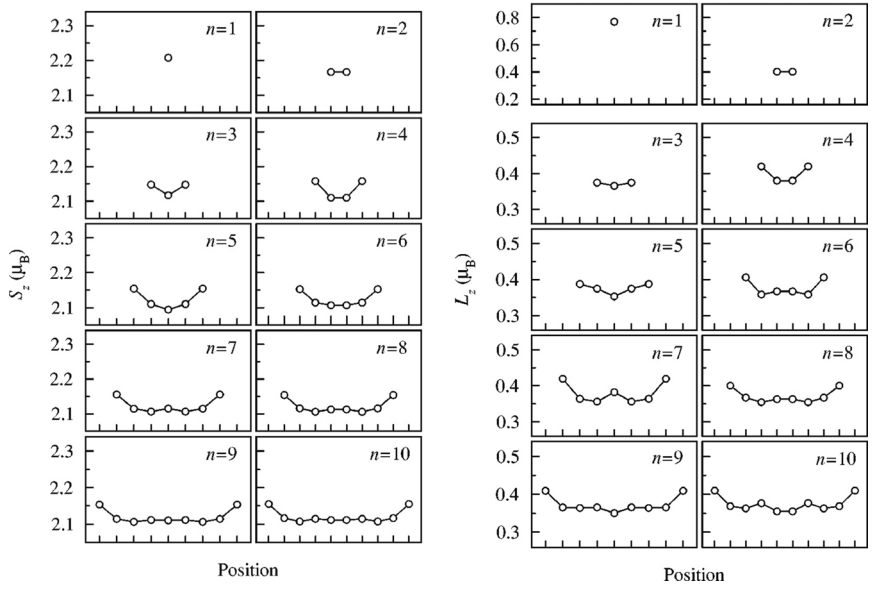

FIGURE 13.5: Left: Calculated spin moments (S_z) of the Co atoms in Co_n ($n = 1, \ldots, 10$) chains on Pt(111) with the magnetization pointing perpendicular to the surface. Right: Calculated orbital moments (L_z) of the Co atoms in Co_n ($n = 1, \ldots, 10$) chains on Pt(111) with the magnetization pointing perpendicular to the surface. From Ref. [12].

ment the length of the Co chains can obviously be increased simply by putting in more and more interior Co atoms into the chain without changing the total moment per Co atom. As can be seen from Fig. 13.5 the interior Co atoms were chosen intentionally, since they show an interesting behavior. For odd n the moments of the central atom seem to oscillate with a period of two; for even n it is the two most interior atoms that characteristically change. This can be seen best from the right part of this figure, in which the orbital moments are displayed.

Although this kind of very detailed information is of quite some interest, in view of the magnetic structure of such chains, in terms of the magnetic anisotropy energy as a function of the chain length it is of little importance, since as is shown in Fig. 13.6 ΔE_{x-z} as well as ΔE_{y-z} become already intrinsic beyond a chain length of $n > 3$.

13.2.2 Finite chains of Fe on Cu(100) & Cu(111)

Just as free surfaces of a magnetic element on a suitable substrate are extremely sensitive to oxidation and are very often covered by a cap of a chem-

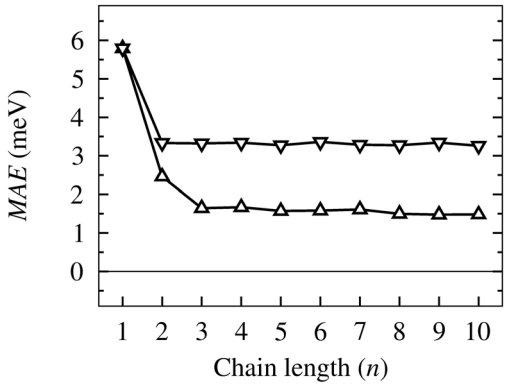

FIGURE 13.6: *Calculated magnetic anisotropy energies (MAE) for* Co_n $(n = 1, \ldots, 10)$ *chains on Pt(111) including also contributions from nearest neighbor Pt sites and normalized to one Co atom. Up- and down-triangles refer to* ΔE_{x-z} *and* ΔE_{y-z}*, respectively. From Ref. [12].*

ically inert metal, clusters of magnetic atoms are only stable in ultrahigh vacuum. The question that arises immediately in this context is therefore whether or not they can be protected by a suitable cap, and of course would a cap alter the magnetic properties in an undesirable manner.

In Fig. 13.7 the spin and orbital moments of a single Fe atom are considered when moving from a position on top of Cu(100) or Cu(111) to the interior of the substrate. As limiting cases the corresponding quantities of a single Fe impurity in an otherwise perfect host of (bulk) fcc Cu is shown. Very clearly the large orbital moment when positioned on top of the surface immediately disappears when embedded in the first (top) substrate layer. At least in terms of the orbital moment nearly no further changes occur when the Fe atom is moved into Cu layers farther away from the surface. The spin moment, however, approaches the limiting single impurity case much more slowly. Even in the second Cu layer beneath the actual surface layer distinct differences between a Cu(100) and Cu(111) substrate are visible. It is worthwhile to note that placed on top of the surface the orbital moment in the Cu(111) case is by about 0.2 μ_B larger than for the Cu(100) substrate!

A single atom is of course a very special case. However, considering a finite chain of Fe atoms "sinking" into a Cu substrate, very much the same effects occur. Concentrating on atom resolved anisotropy energies, see Eqs. (13.6) and (13.7), displayed in Fig. 13.8, it is evident that the anisotropy is substantially changed when covering these chains by additional layers of Cu. This is shown in Figs. 13.9 and 13.10 in terms of the anisotropy energies ΔE_{x-z},

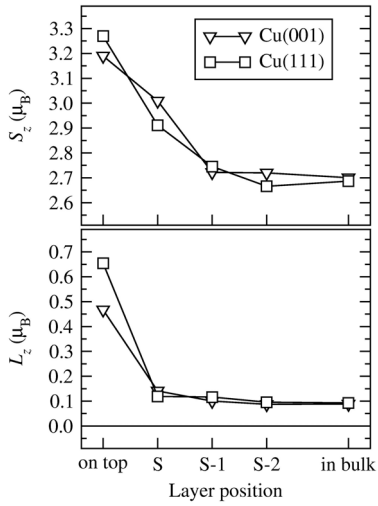

FIGURE 13.7: *Calculated spin (S_z) and orbital moments (L_z) of a single Fe impurity embedded at different distances from a Cu(001) and a Cu(111) surface with a magnetization along the surface normal (z). The position of the impurity is labelled as follows: on top – first vacuum layer, S – surface layer, S-1 – 1st subsurface layer, S-2 – 2nd subsurface layer, in bulk – perfect bulk host. From Ref. [13].*

ΔE_{y-z} and ΔE_{y-x}. It is interesting to note that while ΔE_{x-z} remains positive (perpendicular) for both surface orientations of the substrate when the chains are moved into the interior of the substrate, ΔE_{y-z} changes sign from in-plane to perpendicular. ΔE_{y-x} is always negative and shows a period of two with respect to the number of Fe atoms in the chain.

From this computer experiment of sinking slowly finite chains of Fe into the substrate two conclusions can be readily drawn, namely (1) the tendency for being perpendicularly arranged is reduced drastically already when the chains are embedded in the first substrate layer, and (2) the end ("rim") atoms always seem to contribute more to the anisotropy energy than the atoms in the interior of a chain. In particular the last observation can be important for a possible technological use of very small magnetic structures (supported by a substrate), since by increasing the number of rim atoms also the perpendicular anisotropy can be increased. However, before discussing a very special case of rim-only structures, namely quantum corrals, another very important issue of systems nanostructured in two dimensions has to be introduced, namely aspects of non-collinearity.

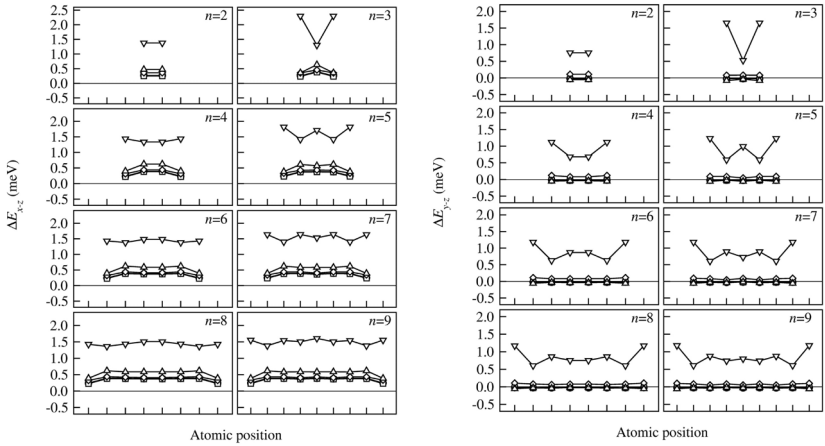

FIGURE 13.8: *Left: Calculated contributions to the magnetic anisotropy energy ΔE_{x-z} of Fe atoms in chains immersed at different distances from a Cu(001) surface ($\bigtriangledown$: on top ; $\bigtriangleup$: layer S; $\Diamond$: layer S-1; $\square$: layer S-2; $\circ$: in bulk). Right: Calculated contributions to the magnetic anisotropy energy ΔE_{y-z} of Fe atoms in chains immersed at different distances from a Cu(111) surface ($\bigtriangledown$: on top ; $\bigtriangleup$: layer S; $\Diamond$: layer S-1; $\square$: layer S-2;$\circ$: in bulk). From Ref. [13].*

13.3 Aspects of non-collinearity

Consider a seven-atom chain of Co embedded into the topmost Pt layer as schematically indicated in Fig. 9.1 in order to create a nascent step edge and nested Co chain. In using the spin dynamics scheme introduced in Chapter 9 and choosing initially arbitrary directions of the magnetizations (random number generator) for the Co atoms the magnetic ground state of this cluster consisting of Co and Pt atoms and vacuum sites can be found in terms of an iterative multi-scale approach. The time evolution of the orientations is then measured on a time scale with a unit (time step) of $1/\lambda$ (λ: Gilbert damping factor), since in the semi-classical Landau-Lifshitz-Gilbert equation, see Eq. (9.15), only the damping term needs to be considered. A stable ground state is achieved when the θ_i and ϕ_i angles of the individual Co atoms converge to a constant. For exactly the system to be discussed now the convergence was shown in Chapter 9 in order to illustrate there the methodological aspects and is repeated for matters of convenience on a smaller scale in the left part of Fig. 13.11.

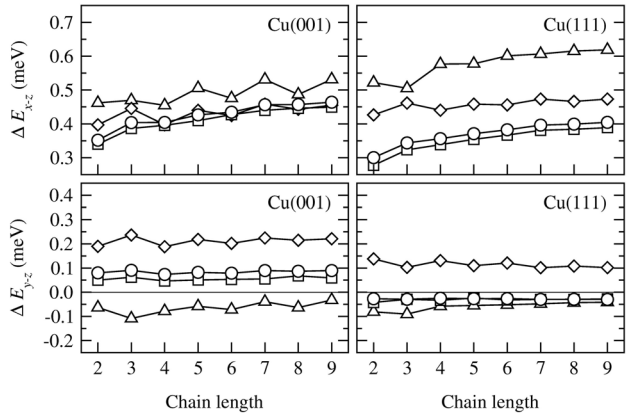

FIGURE 13.9: *Calculated magnetic anisotropy energies* ΔE_{x-z} *and* ΔE_{y-z} *(normalized to one Fe atom) for* Fe_n $(n = 2, \ldots, 9)$ *chains immersed at different distances from a Cu(111) and a Cu(001) surface. (*$\triangle$*: layer S;* $\Diamond$*: layer S-1;* $\square$*: layer S-2;* $\circ$*: in bulk). From Ref. [13].*

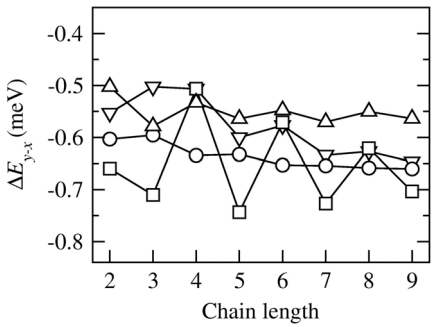

FIGURE 13.10: *Calculated in-plane magnetic anisotropy energy,* ΔE_{x-y}*, for* Fe_n $(n = 1, \ldots, 9)$ *chains on a Cu(001) and a Cu(111) surface including also contributions from nearest neighbor Cu sites and normalized to one Fe atom. (*$\bigtriangledown$*: Cu(001) on top ;* $\triangle$*: Cu(001) layer S;* $\square$*: Cu(111) on top;* $\circ$*: Cu(111) layer S). From Ref. [13].*

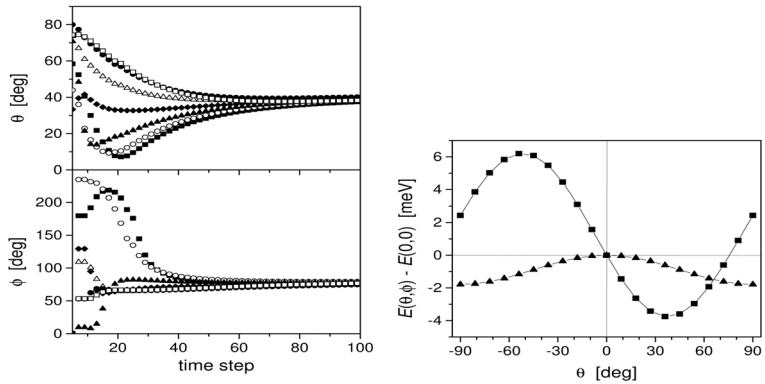

FIGURE 13.11: *Left: Time evolution of the angles θ_i (top) and ϕ_i (bottom) for i = 1: full squares, 2: open circles, 3: full triangles, 4: full diamonds, 5: open triangles, 6: full circles and 7: open squares. Right: Energy curves calculated using the magnetic force theorem for a ferromagnetic seven–atom Co wire at a Pt(111) surface step edge as a function of the azimuthal angle, θ. squares : $\phi = 90°$, triangles: $\phi = 0°$. Solid lines serve as a guide for eyes. From Ref. [14].*

In the left part of this figure the evolution of the θ_i and ϕ_i angles is plotted for the first 100 steps in this artificial time scale for each Co atom in the chain. The θ_i (ϕ_i) refer to the angle of orientation of the magnetization in an individual Co atom with respect to the z-axis (in-plane x-axis). The rapidly converging part (up to about 40 time steps) is caused by the strong ferromagnetic exchange coupling between the Co atoms, the following slow convergence is due to anisotropy effects. The final converged state is characterized by angles ϕ_i very close to 90° and θ_i close to 42°, see Table 13.1, which in turn is in remarkable agreement with experiment [15], namely $\phi = 90°, \theta = 43°$.

Assuming a uniform magnetization characterized by a single angle θ and a single angle ϕ clearly also the following general anisotropy energy

$$\Delta E(\theta, \phi) = E(\theta, \phi) - E(\theta = 0, \phi = 0)$$

can be calculated and compared to the results obtained using spin dynamics. In the right part of Fig. 13.11 this kind of anisotropy energy is displayed for the case of $\Delta E(\theta, \phi = 0°)$ and $\Delta E(\theta, \phi = 90°)$. From the results shown there, once can see that the easy axis corresponds to $\theta = 38°$ and $\phi = 90°$, the hard axis to $\theta = -52°$ and $\phi = 90°$, which is again in good agreement with experiment [15]. It is therefore quite assuring that although being based on quite different theoretical concepts, both approaches yield rather similar results (and agree well with the data elucidated from experiment).

Table 13.1: *Calculated magnitudes and orientations of the spin and orbital moments in a seven–atom Co chain along a Pt(111) step edge. From Ref. [14].*

atom	Spin moment		Orbital moment	
	moment(μ_B)	Θ(deg)	moment(μ_B)	Θ(deg)
1	2.23	41.1	0.25	39.1
2	2.18	42.5	0.20	41.5
3	2.18	42.3	0.19	40.1
4	2.18	42.4	0.20	41.3
5	2.18	42.3	0.19	40.2
6	2.18	42.5	0.20	41.5
7	2.23	41.1	0.25	39.1

[1] S. Rusponi, T. Cren, N. Weiss, M. Epple, P. Buluschek, L. Claude, and H. Brune, Nat. Mater. **2**, 546 (2003).

[2] A. Kubetzka, O. Pietzsch, M. Bode, and R. Wiesendanger, Phys. Rev. B **63**, 140407(R) (2001).

[3] P. Gambardella, S. Rusponi, M. Veronese, S.S. Dhesi, C. Grazioli, A. Dallmeyer, I. Cabria, R. Zeller, P.H. Dederichs, K. Kern, C. Carbone, and H. Brune, Science **300**, 1130 (2003).

[4] K. von Bergmann, M. Bode, and R. Wiesendanger, Phys. Rev. B **70**, 174455 (2004).

[5] J.T. Lau, A. Fohlisch, R. Nietubyc, M. Reif, and W. Wurth, Phys. Rev. Lett. **89**, 057201 (2002).

[6] D. Repetto, J. Honolka, S. Rusponi, H. Brune, A. Enders, and K. Kern, Appl. Phys. A **82**, 109 (2006).

[7] P. Bruno, Phys. Rev. B **39**, 865 (1989).

[8] P. Carra, B.T. Thole, M. Altarelli, and X. Wang, Phys. Rev. Lett. **70**, 694 (1993); B.T. Thole, P. Carra, F. Sette, and G. van der Laan, *ibid.* **68**, 1943 (1992).

[9] J. Kliewer, R. Berndt, and S. Crampin, Phys. Rev. Lett. **85**, 4936 (2000).

[10] M. Getzlaff, A. Kleibert, R. Methling, J. Bansmann, K.H. Meiwes-Broer, Surf. Sci. **566**, 332 (2004).

[11] B. Lazarovits, L. Szunyogh, and P. Weinberger, Phys. Rev. B **65**, 104441 (2002).

[12] B. Lazarovits, L. Szunyogh, and P. Weinberger, Phys. Rev. B **67**, 024415 (2003).

[13] B. Lazarovits, L. Szunyogh, P. Weinberger, and B. Ujfalussy, Phys. Rev. B **68**, 024433 (2003).

[14] B. Újfalussy, B. Lazarovits, L. Szunyogh, G. M. Stocks, and P, Weinberger, Phys. Rev. B **70**, 100404(R) (2004).

[15] P. Gambardella, A. Dallmeyer, K. Maiti, M. C. Malagoli, W. Eberhardt, K. Kern, and C. Carbone, Nature **416**, 301 (2002); P. Gambardella, J. Phys.: Condens. Matter **15**, S2533 (2003).

14

Nanostructured in two dimensions: nanocontacts, local alloys

Besides mentioning briefly the electronic structure and magnetic properties of quantum corrals and nano-contacts, and discussing the occurrence of spin-polarized surface states, the main emphasis in this chapter is put on the (geometrical) shape-, occupation- and configuration-dependence of spin and orbital magnetic moments and consequences thereof for the magnetic anisotropy energy of local alloys.

14.1 Quantum corrals

Quantum corrals are interesting examples of solid systems nanostructured in two dimensions, not only because in the semi-classical limit they can be associated with classical orbits of particles bouncing off confining walls giving in turn rise even to chaotic motions [1], but also since they can be considered as systems with only "rim" magnetic atoms. Experimentally single quantum corrals with about 50 - 100 magnetic atoms were already detected with the first generation of spin-polarized STM techniques; see e.g. Ref. [2]. Since quantum corrals were for a few years, so to say, the "show pieces" of nanoscience, they have to be mentioned in here at least shortly.

Fig. 14.1 shows the geometrical outlay of 48 Fe atoms on Cu(111) forming a corral with a diameter of 28 a, where a is the two-dimensional lattice constant of the fcc(111) Cu surface. It was found that the circular quantum well model, discussed in detail in Ref. [3], fitted rather well with the peaks in the density of states at the central site of the corral, see Fig. 14.2, a result that *per se* was essentially of theoretical interest. Following the spatial distribution of the density of states at the energy corresponding to the fifth peak in Fig. 14.2, however, gave a surprisingly illustrative image of the radial oscillations with respect to an increasing distance from the center. This particular view almost looks like an experimental STM image, in particular since the chosen energy $E - E_F \simeq 0.01$ Ryd refers to slightly excited electronic states.

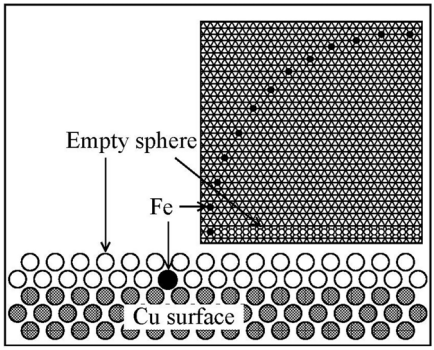

FIGURE 14.1: *Cross section of the surface showing the position of sites in the "vacuum layers" (open circles), the Cu surface layers (gray circles) and an Fe impurity in the first "vacuum layer" (black circle). Inset: the positions of the Fe atoms (black dots) and the empty spheres (open circles) along a diameter for a quadrant of the investigated corral. From Ref. [3].*

14.2 Magnetic adatoms & surface states

Since first experimental observations of a surface band at Cu(111) in terms of angle-resolved photoemission electron spectroscopy, electronic surface states of noble metals have been at the center of much experimental and theoretical attention. Unfortunately, until recently STM studies of adatoms on well defined Cu, Ag and Au (111) surfaces could only produce images of the charge distribution corresponding to these states. With spin-polarized STM, however, it is now possible to record also the spatial variation in the magnetization density, and to raise the question of the existence of spin-polarized surface states, see for example Ref. [4]. The problem to be addressed is therefore closely related to the previous example of quantum corrals.

Placing single atoms of Cr, Mn, Fe, Co, Ni and Cu on top of Cu(111) clearly gave the expected results [5], namely that with the exception of Cu all these adatoms were magnetic:

adatom	spin-only magnetic moments [μ_B]
Cr	4.21
Mn	4.39
Fe	3.27
Co	2.02
Ni	0.51

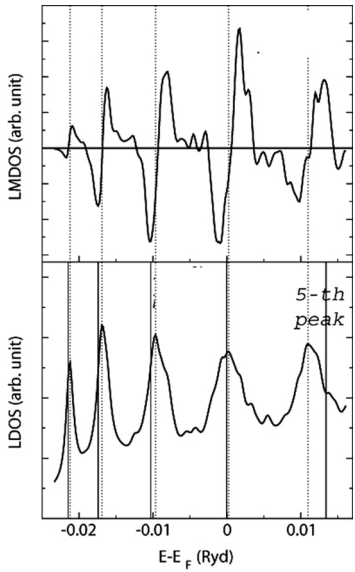

FIGURE 14.2: *Calculated local density of states (bottom) and local magnetic density of states (top) at the center of a quantum corral. The dotted lines indicate positions of maxima in the local density of states. Vertical solid lines refer to the energy eigenvalues, predicted by the circular quantum well model. From Ref. [3].*

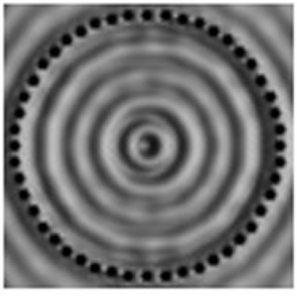

FIGURE 14.3: *Spatial distribution of the density of states at the energy corresponding to the fifth peak in Fig. 14.2. The local density of states of the Fe atoms is removed from the figure. From Ref. [3].*

As is probably well known and was amply discussed in the beginning, within a relativistic description the spin is not a constant of motion, a projection with respect to "up" and "down" spins, i.e., a projection with respect to the eigenspaces of S_z, is therefore a bit qualitative. However, since for the chosen magnetic adatoms the exchange splitting is much bigger than the spin-orbit splitting, for a better understanding the ("traditional") spin-polarized view of the electronic structure of these atoms is displayed in Fig. 14.4, putting the emphasis on the s-like channel. Clearly enough, as expected, at the site of the impurity also the s-like density of states is spin-polarized.

Then of course immediately the question arises: and how far out does this spin polarization induced by a single magnetic atom extend into the neighboring vacuum sites? At a distance of seven two-dimensional lattice constants ($\sim$ 17.9 Å) the s–density of states is practically the same as calculated for the clean Cu(111) surface. However, as the right part of Fig. 14.4 shows, a long–ranged oscillatory behavior of the densities of states can still be resolved even at distances much farther away from the impurity. In the right part of Fig. 14.4 the density of states at a selected energy, namely 34 mRyd above the bottom of the surface–state band is displayed for both spin channels as a function of the distance from an Fe adatom. A simple estimate of the wavelength of the two-dimensional Friedel oscillation,

$$\lambda = \frac{\pi}{\hbar\sqrt{2m^* E}} \quad , \tag{14.1}$$

where m^* is the effective mass, gives $\lambda \approx 15$ Å $\approx 6\, a_{2D}$ that immediately can be read off from the right part of Fig. 14.4. As shown in the inset of this figure, a single impurity of Fe on top of Cu(111) induces also long–range oscillations in the magnetization density of states (difference between the spin–projected densities of states) with the same period, which in turn lead to the well-known long–range magnetic (RKKY) interactions on noble metal (111) surfaces as discussed, e.g., in Ref. [6].

14.3 Nanocontacts

Because the possibility of using such systems in future nanoelectronic technologies, the number of theoretical and experimental investigations of the electronic structure and the transport properties of atomic-sized conductors has greatly been increased over the last decade. Widely applied methods for fabricating nanocontacts between macroscopic electrodes are the mechanically controllable break junction technique [7, 8, 9, 10] and scanning tunneling microscopy [11, 12, 13] by pushing the tip intentionally into the surface. The

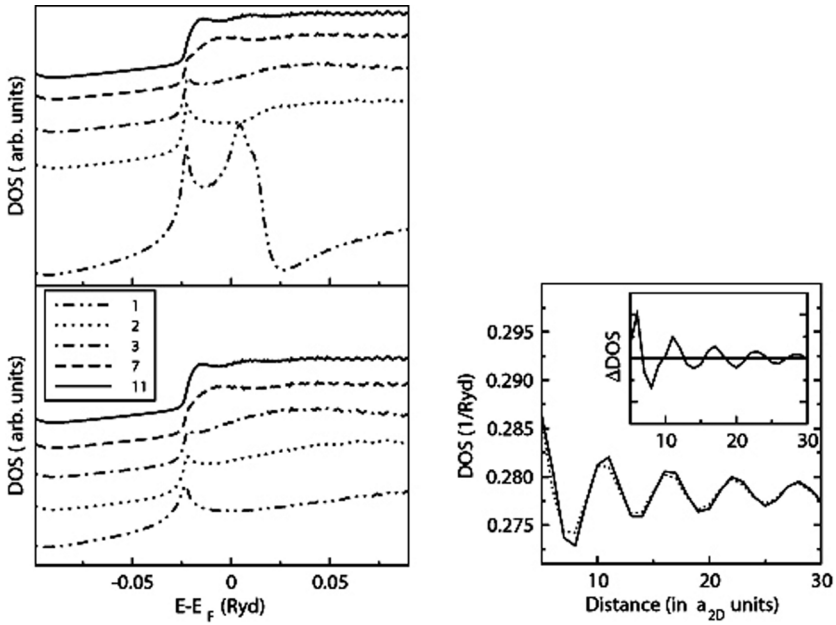

FIGURE 14.4: *Left: Calculated minority spin (upper panel) and majority spin (lower panel) s–like densities of states at a site in the same plane as a single Fe impurity on a Cu(111) surface with respect to the distance between these two sites. The distance (in units of the two–dimensional lattice constant) is indicated in the legend of the lower panel. Right: Calculated minority spin (solid line) and majority spin (dotted line) s–like densities of states at* $E - E_F = 0.012$ *Ryd of a site positioned in the same plane but at a certain distance from a single Fe impurity on a Cu(111) surface. Inset: s–like magnetization density of states. From Ref. [5].*

crucial problems [14] for both methods consist in the presence of contaminants and the mechanical stability. Since the electric properties of nanocontacts will be dealt with in Chapter 17, in this section only the electronic and magnetic properties of such contacts are discussed.

A schematic view of a typical contact is displayed in Fig. 14.5. In there C refers to the *central layer*, $C-1$ and $C+1$ to the layers below and above, etc. For the Au contacts shown in the top part of Fig. 14.6, e.g., the central layer contains 1 Au atom (the other sites in this plane are empty), layers $C-1$ and $C+1$ contain 4 Au atoms, layers $C-2$ and $C+2$ contain 9 Au atoms and, though not shown, all layers $C-n$ and $C+n$ ($n \geq 3$) are completely filled with Au atoms. All sites (Au, vacuum and impurity sites) correspond to an ideal fcc(001) parent lattice with a lattice constant of bulk Au, $a_{3D} = 7.68$ [a.u.].

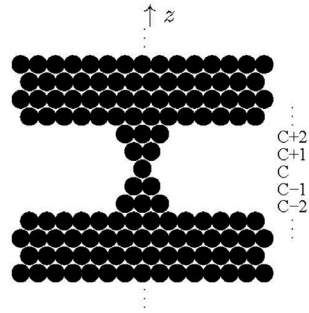

FIGURE 14.5: *Schematic side view of a point contact between two semi-infinite leads. The layers are labelled by C, $C \pm 1$, etc. From Ref. [15].*

Obviously, the question of the effect of magnetic impurities in Au point contacts is perhaps the most interesting one. It turns out, see Table 14.1, that as to be expected the position of the impurity atom with respect to the actual contact atom is absolutely crucial: the orbital moments change drastically when an Fe atom is moved from position A (being the contact atom) to positions B or C, see also the lower part of Fig. 14.6.

Table 14.1: *Calculated spin and orbital moments of magnetic impurities placed at different positions in a Au point contact; see also the lower part of Fig. 14.6. From Ref. [15].*

position	$S_z[\mu_B]$		$L_z[\mu_B]$	
	Fe	Co	Fe	Co
A	3.36	2.01	0.47	0.38
B	3.46	2.17	0.04	0.61
C	3.42	2.14	0.07	0.22

In order to pinpoint the difference of being placed in position A or B in Fig. 14.7 the minority d-like local densities of states of the Fe and Co impurities are resolved according to the canonical orbitals $d_{x^2-y^2}$, d_{xy}, $d_{xz,}$, d_{xy} and $d_{3z^2-r^2}$. Note that as already mentioned before, this kind of partial decomposition, usually referred to as the (ℓ, m, s) representation of the local density of states, is not unique within a relativistic formalism, since due to the spin-orbit interaction the different spin and orbital components are mixed. As can be seen from this figure, the local density of states of an impurity in position A is much narrower than in position C. This is an obvious consequence of the

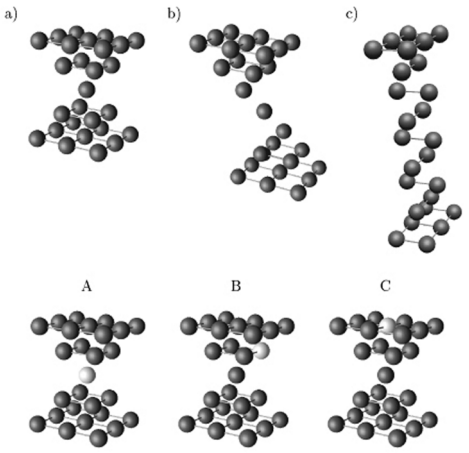

FIGURE 14.6: *Top: Perspective view of some contacts between two fcc(001) semi-infinite leads. Only the partially filled layers are shown. a) point contact b) slanted linear finite chain c) 2 x 2 finite chain. Bottom: Impurity positions (light grey spheres) in a Au point contact. From Ref. [15].*

difference in the coordination numbers (8 for position A and 12 for positions C). Thus an impurity in position A hybridizes less with the neighboring Au atoms and, as can be seen from Fig. 14.7, the corresponding d states are fairly localized. Also to be seen is a spin-orbit induced splitting of about 8 mRyd ($\sim$ 0.1 eV, about the spin-orbit splitting in an isolated atom) in the very narrow $d_{x^2-y^2}$-d_{xy} states of the impurities in position A. The difference of the band filling for the two kind of impurities shows up in a distinct downward shift of the local density of states of Co with respect to that of Fe.

In particular the s-like density of states at position A shows a very interesting shape which can indeed be correlated with the corresponding $d_{3z^2-r^2}$-like density of states at the impurity site; see bottom half of Fig. 14.8. Clearly, the center positions and the widths of the $d_{3z^2-r^2}$-like density of states peaks and those of the respective (anti-)resonant s-like density of states shapes coincide well with each other.

This kind of behavior in the density of states resembles the case studied by Fano [16] for a continuum band and a discrete energy level in the presence of configuration interaction (hybridization). Apparently in a Au point contact the s-like states play the role of a continuum and the $d_{3z^2-r^2}$-like state of the impurity acts as quasi-discrete energy level. Since the two kinds of states share the same cylindrical symmetry, interactions between them can occur due to backscattering effects.

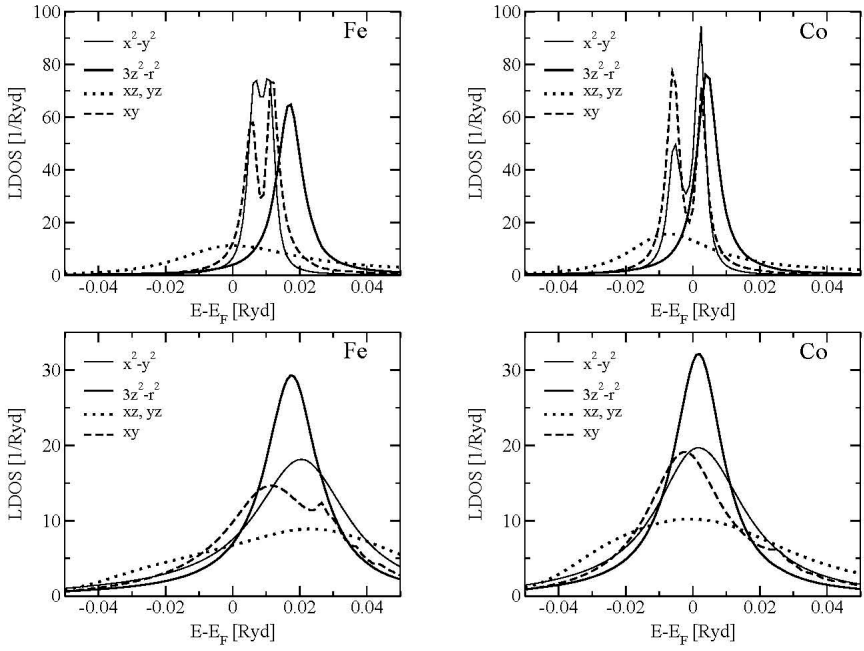

FIGURE 14.7: *Minority-spin orbital-resolved d-like local density of states of Fe and Co impurities in position A (upper panels) and in position C (lower panels) of a Au point contact; see lower part of Fig. 14.8. From Ref. [15].*

14.4 Local alloys

In view of the fabrication of so-called bit-patterned media [17, 18] it became the main goal of experimental methods to produce grains of controlled size and position, of known composition, and with sharply defined magnetic properties [19, 20]. Clearly, this eventually would lead to increased achievable areal densities [21] of magnetic recording media by several orders of magnitude [19, 22, 23, 24, 25].

One of the main issues is therefore the magnetic anisotropy energy which determines the orientation of the magnetization of a cluster with respect to the surface: a large enough magnetic anisotropy energy can stabilize the magnetization direction in the cluster and a stable magnetic bit can be created [26, 27]. The actual size of the magnetic anisotropy energy can in turn be manipulated by varying the shape, size and composition of clusters and – of course – is

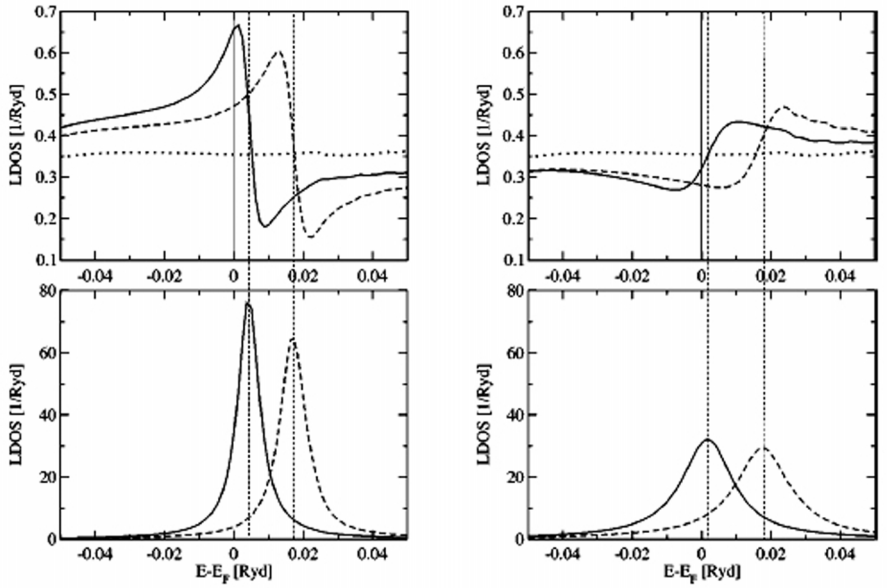

FIGURE 14.8: *Top: minority-spin s-like local density of states at the center site of a Au point contact with an impurity at position A (left) and B (right); see lower part of Fig. 14.8 (solid line: Co, dashed line: Fe). For matters of comparison, in both figures the corresponding local density of states for a pure Au contact (dotted line) is added. The solid vertical lines highlight the position of the Fermi energy. Bottom: minority-spin $d_{3z^2-r^2}$-like local density of states of the impurities (solid line: Co, dashed line: Fe) at positions A (left) and C (right). Vertical dashed lines mark the center positions of the peaks in the $d_{3z^2-r^2}$-like local density of states. From Ref. [15].*

influenced by the choice of the substrate.

It is exactly the problem of the shape, size and composition that is addressed in the following by considering clusters consisting of Fe and Co atoms on top of Cu(100) [28]. In this context an important question will be answered, namely when in a cluster of a certain size, geometry and composition (number of Fe and Co atoms), the magnetic anisotropy energy, averaged over all possible configurations of the Fe and Co atoms occupying the positions in the chosen cluster, resembles the magnetic anisotropy energy of a monolayer of a statistically disordered alloy Fe_xCo_{1-x} on the same substrate, where the concentration x corresponds to the composition in the cluster. Thus the magnetic anisotropy energy can be studied starting from two atoms, namely Fe and Co, via local alloys (configuration averaged clusters) up to larger islands of a certain composition, for which already statistical averages are justified.

In the following, first a 2 x 2 cluster, see also Fig. 13.2, of Co and Fe atoms with varying composition is considered, since the number of possible configurations is still rather small. In the left part of Fig. 14.9 the spin and the orbital moments of Fe and Co are displayed versus the configuration, shown explicitly in the right part of this figure. Note that each geometrical configuration has to be occupied with either Fe or Co atoms:

number of Co (A) atoms	number of Fe (B) atoms	configuration
0	4	1B
1	3	2,3 (A,B)
2	2	4,5 (A,B)
3	1	6 (A,B)
4	0	1A

In principle the composition in a particular cluster consisting of N_{Fe} Fe atoms and N_{Co} Co atoms is then given by

$$\xi \equiv \xi_{Fe} = \frac{N_{Fe}}{N} \quad , \quad \xi_{Co} = 1 - \xi \quad ,$$
$$N = N_{Fe} + N_{Co} \quad .$$

From this figure it is already evident that in comparison to a monolayer of statistical disordered Fe_xCo_{1-x} on Cu(100),

$$x = \lim_{N \to N_L} \xi \quad ,$$

where N_L is a sufficiently large number (e.g. Avogardo number), the spin moment of Co is hardly changed, while that of Fe is substantially increased. Amazingly enough with increasing ξ the L_x- and L_y-type orbital moments of Co show different slopes, the in-plane orbital moment (L_x) being much enhanced when ξ_{Co} is large. The Fe orbital moments do not differ a lot from each other and seem to be only little influenced by the actual composition of the cluster. This behavior of the orbital moments indicates already that great variations of the anisotropy energy can be expected when changing the composition of clusters.

But before conclusions are made perhaps too soon, the next bigger cluster with a total of 5 atoms shall be considered. In Fig. 14.10 first the spin and orbital moments for Co are shown, when a Co atom is placed either in the center (case A) or in a corner of a cross-like (case B) pentameter shaped cluster; Fig. 14.11 refers then to Fe.

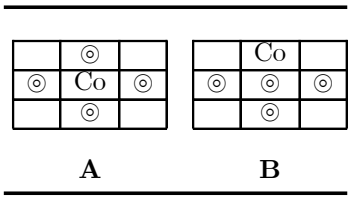

The comparison between these two possibilities, namely of having a Co (Fe) atom in the center and varying the occupation of the remaining sites or placing it in a corner, is indeed striking, because it shows that both the spin and the orbital moments can be greatly enhanced by fabricating clusters with enough corner ("rim") atoms. Viewing, e.g., Fig. 14.10 it is evident that in case A with increasing Co content the Co spin moment almost reaches its bulk value, while in case B it remains about three times as large! The same enormous differences apply for the orbital moments, which in case A hardly differ from those in a statistically disordered monolayer Fe_xCo_{1-x} on Cu(100), while in case B they vary between 0.3 and about 0.5 μ_B, i.e., are impressively big. Nearly the same trends can be read from Fig. 14.11 featuring the Fe component.

One can imagine now that the information to be obtained from this type of atomistic description simply "explodes" when going to even bigger clusters. Already in a "simple" 3 x 3 cluster three types of situations can be distinguished, namely center, edge and corner positions:

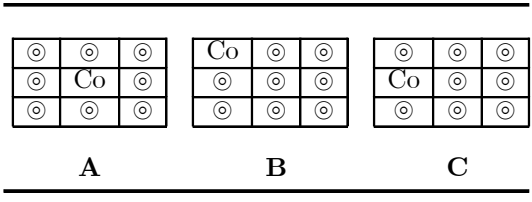

Since in experiments, but also in particular in view of any technological applications, such detailed arrangements of Fe and Co atoms are not very likely to be realized and also since for clusters with even more atoms an atomistic view becomes more and more intricate, an average over configurations can give a more condensed view of the magnetic properties of clusters obtained, e.g., by co-evaporation. Such configuration averages are shown in Fig. 14.12 for the spin and orbital moments and in Fig. 14.13 for the magnetic anisotropy.

From Fig. 14.12 one can see that the configuration-averaged spin moment decreases almost independent of the cluster size and geometry almost linearly with increasing Co content and follows rather closely the corresponding values for a monolayer of statistically disordered Fe_xCo_{1-x} on Cu(100). The orbital moments, however, show an impressive variation with respect to the cluster type. The values for clusters of pentameter type are by about 0.1 μ_B larger than those of the other types, which in turn is a consequence of the importance of corner atoms.

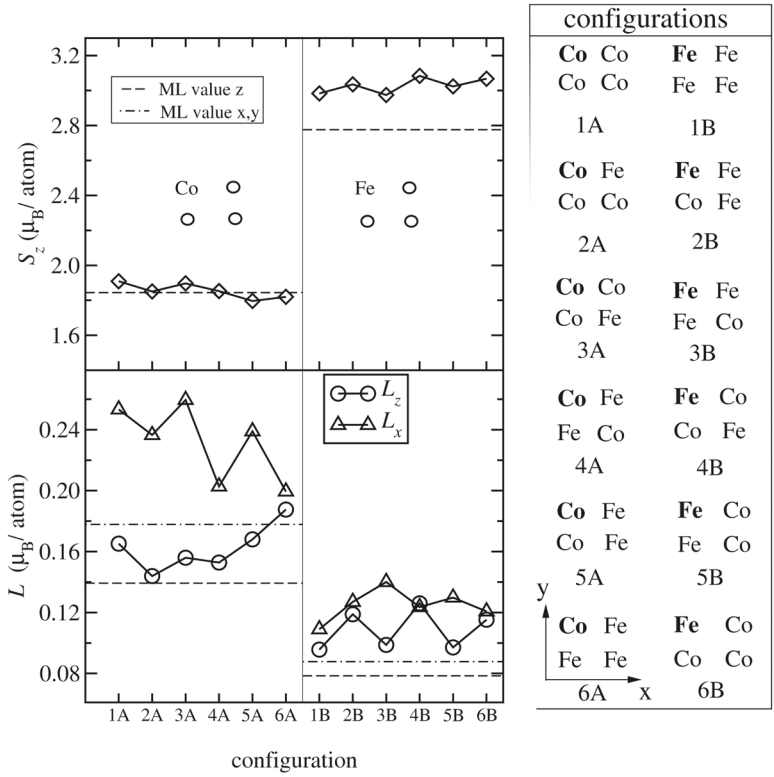

FIGURE 14.9: *Spin and orbital magnetic moments of selected Co (left panel) and Fe (right panel) atoms as a function of all cluster configurations possible (Co: iA, Fe: iB, $i = 1, \ldots, 5$); see the scheme to the right. Dashed horizontal lines refer to the corresponding Fe/Cu(100) or Co/Cu(100) monolayer values for a magnetization along the surface normal. Dash-dotted horizontal lines to those with the magnetization along the in-plane x(y)-axis. The investigated atom is indicated by boldface letters. From Ref. [28].*

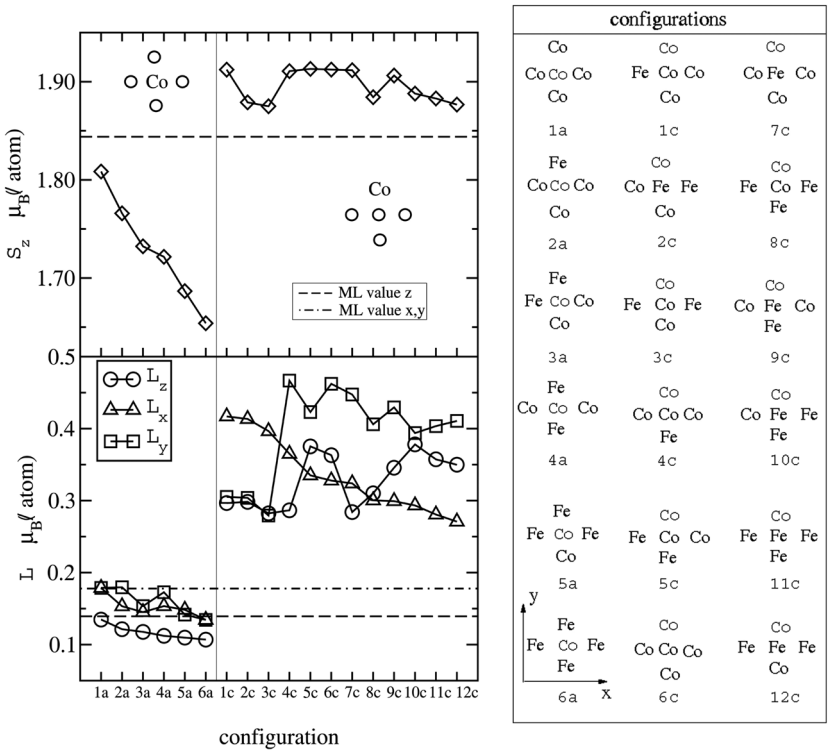

FIGURE 14.10: *Spin and orbital magnetic moments of a selected Co atom as a function of its position in the cluster and of the number of Fe neighbors. For the actual configuration see the panel to the right. Dashed horizontal lines refer to the corresponding Co/Cu(100) monolayer values with the magnetization along the surface normal. Dash-dotted horizontal lines to those with the magnetization along the in-plane x(y)-axis. From Ref. [28].*

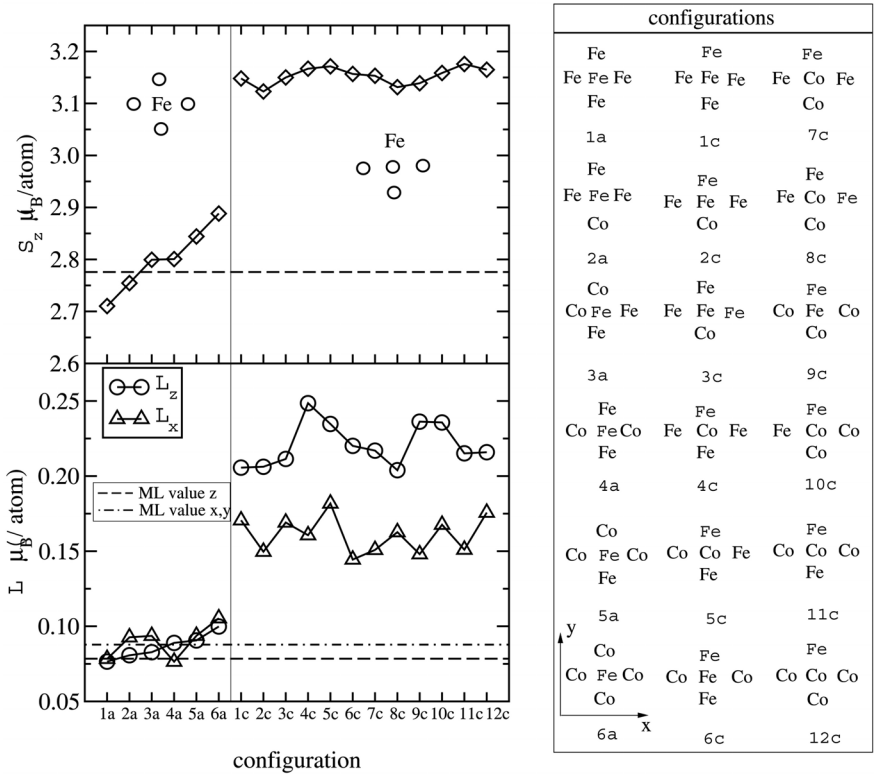

FIGURE 14.11: *Spin and orbital magnetic moments of a selected Fe atom as a function of the position occupied in the cluster and of the number of Co neighbors. For the actual configuration, see the panel to the right. Dashed horizontal lines refer to the corresponding Fe/Cu(100) monolayer values along the surface normal. Dash-dotted horizontal lines to those with the magnetization along the in-plane x(y)-axis. From Ref. [28].*

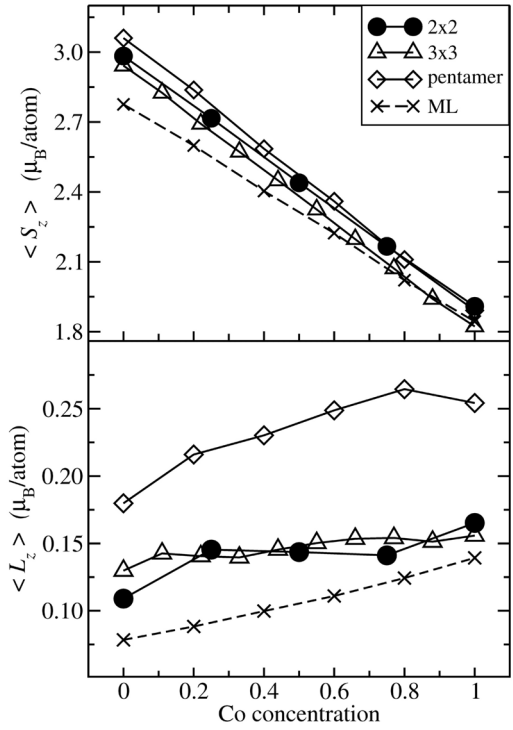

FIGURE 14.12: *Spin and orbital moments averaged over all the configurations for a given Co concentration. The dashed line refers to the case of a* Co_xFe_{1-x} *monolayer on Cu(100). From Ref. [28].*

The perhaps most surprising fact can be read from Fig. 14.13, in which not only the averaged magnetic anisotropy energy, but also the values for the individual configurations are displayed together with the data for a corresponding monolayer. The result is surprising, since (a) the reorientation transition from perpendicular to in-plane happens at exactly the same Co composition for the averaged clusters and the statistically disordered monolayer and (b) the spread in energy of the configuration-dependent anisotropy energies on the total scale from perpendicular to in-plane is perhaps less impressive than originally thought. This figure, however, also shows that as compared to a free surface of a monolayer of Co_xFe_{1-x} on Cu(100) anisotropy effects are quite a bit more enhanced in the case of small clusters of Fe and Co on Cu(100): there is a stronger tendency to be perpendicularly arranged for $x \leq 0.4$ as well as for an in-plane orientation for $x > 0.4$.

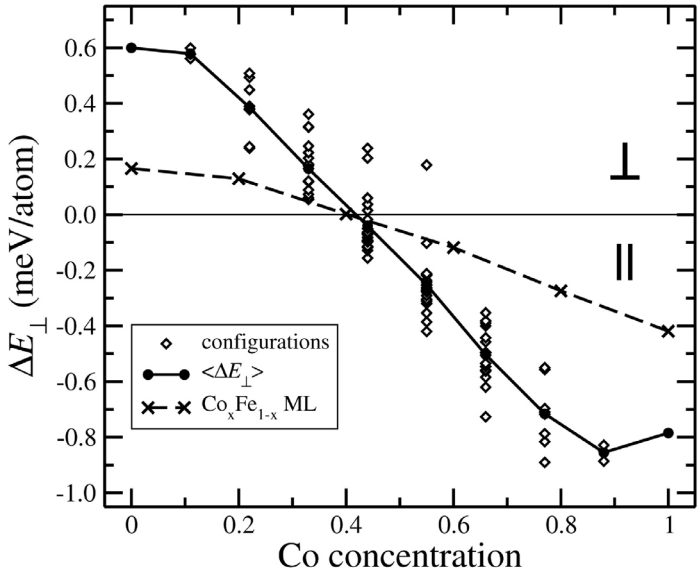

FIGURE 14.13: *Magnetic anisotropy energy as a function of the Co concentration. Shown is the distribution of the anisotropy energies for 3×3 clusters as a function of the clusters configuration (diamonds). The anisotropy energy is defined as* $\langle \Delta E_\perp \rangle = \langle (\Delta E_{xz} + \Delta E_{yz})/2 \rangle$*, where* $\langle\rangle$ *refers to the average over all configurations (solid line), z to the surface normal and x and y to the in-plane coordinates. Also displayed is the anisotropy energy for a* $Co_xFe_{1-x}/Cu(100)$ *monolayer (dashed line). From Ref. [28].*

14.5 Summary

- Clusters of magnetic atoms on suitable substrates have much higher magnetic anisotropy energies than even free surfaces of the same atomic species.

- The size of the magnetic anisotropy energy can be monitored by (a) maximizing the number of corner and edge magnetic atoms, (b) the geometric shape of clusters and (c) co-evaporation of two different types of magnetic atoms, or, (d) by choosing at least a neighborhood of easy polarizable material.

- Ensembles of magnetic atoms on top of a metallic substrate can induce

spin-polarized surface states.

- The extraordinary anisotropic properties of magnetic clusters on top of a metallic substrate are drastically reduced by the use of protective (metallic) cap layers.

[1] G. A. Fiete and E. J. Heller, Phys. Rev. Lett. **75**, 933 (2003); E. Doron and U. Smilansky, *Nonlinearity* **5**, 1055 (1992).

[2] O. Pietzsch, A. Kubetzka, M. Bode and R. Wiesendanger, Phys. Rev. Lett. **92**, 057202 (2004).

[3] B. Lazarovits, B. Újfalussy, L. Szunyogh, B. L. Gyorffy, and P. Weinberger, J. Phys. Cond. Matt.**17**, 1037 - 1048 (2005).

[4] L. Limot, E. Pehlke, J. Kröger, and R. Berndt, Phys. Rev. Lett. **94**, 036805 (2005).

[5] B. Lazarovits, L. Szunyogh, and P, Weinberger, Phys. Rev. B **73**, 045430 (2006).

[6] V. S. Stepanyuk, L. Niebergall, R. C. Longo, W. Hergert, and P. Bruno, Phys. Rev. B **70**, 075414 (2004).

[7] C. J. Muller, J. M. van Ruitenbeek, and L. J. de Jongh, Phys. Rev. Lett. **69**, 140 (1992).

[8] J. M. Krans, I. K. Yanson, Th. C. M. Govaert, R. Hesper, and J. M. van Ruitenbeek, Phys. Rev. B **48**, 14721 (1993).

[9] R. H. M. Smit, C. Untiedt, A. I. Yanson, and J. M. van Ruitenbeek, Phys. Rev. Lett. **87**, 266102 (2001).

[10] A. Halbritter, Sz. Csonka, O. Yu. Kolesnychenko, G. Mihály, O. I. Shklyarevskii, and H. van Kempen, Phys. Rev. B **65**, 045413 (2002); Sz. Csonka, A. Halbritter, G. Mihály, E. Jurdik, O. I. Shklyarevskii, S. Speller, and H. van Kempen, Phys. Rev. Lett. **90**, 116803 (2003).

[11] M. F. Crommie, C. P. Lutz, and D. M. Eigler, Science **262**, 219 (1993).

[12] J. K. Gimzewski and R. Möller, Phys. Rev. B **36**, 1284 (1987).

[13] M. Brandbyge, J. Schiøtz, M. R. Sørensen, P. Stoltze, K. W. Jacobsen, J. K. Nørskov, L. Olesen, E. Laegsgaard, I. Stensgaard, and F. Besenbacher, Phys. Rev. B **52** 8499 (1995).

[14] N. Agraït, A. L. Yeyati, and J. M. van Ruitenbeek, Phys. Rep. **377**, 81 (2003).

[15] K. Palotás, B. Lazarovits, L. Szunyogh, and P. Weinberger, Phys. Rev. B **70**, 134421 (2004).

[16] U. Fano, Phys. Rev. **124**, 1866 (1961).

[17] H. J. Richter, A. Y. Dobin, O. Heinonen, K. Z. Gao, R. J. M. v.d. Veerdonk, R. T. Lynch, J. Xue, D. Weller, P. Asselin, M. F. Erden, and R. M. Brockie, IEEE Trans. Magn. **42**, 2255 (2006).

[18] H. Brune, e-J. Surf. Sci. Nanotech. **4**, 478 (2006).

[19] N. Weiss, T. Cren, M. Epple, S. Rusponi, G. Baudot, S. Rohart, A. Tejeda, V. Repain, S. Rousset, P. Ohresser, F. Scheurer, P. Bencok, and H. Brune, Phys. Rev. Lett. **95**, 157204 (2005).

[20] G. A. Held, G. Grinstein, H. Doyle, S. Sun, and C. B. Murray, Phys. Rev. B **64**, 012408 (2001).

[21] H. Coufal, L. Dhar, and C. D. Mee, MRS Bull. **31**, 374 (2006); I. R. McFadyen, E. E. Fullerton, and M.J. Carey, *ibid.* 379; H. J. Richter, and S. D. Harkness IV, *ibid.* 385.

[22] K. Mitsuzuka, N. Kikuchi, T. Shimatsu, O Kitakami, H. Aoi, H. Muraoka, and J. C. Lodder, IEEE Trans. Magn. **43**, 3883 (2006).

[23] H. J. Richter, and A. Y. Dobin, J. Magn. Magn. Mat. **287**, 41 (2005).

[24] S. Sun, and C. B. Murray, J. Appl. Phys. **85**, 4325 (1999).

[25] C. E, D. Smith, S. Khizroev, D. Weller, and D. Litvinov, IEEE Trans. Magn., **42**, 2411 (2006).

[26] D. Weller, and A. Moser, IEEE Trans. Magn. **35**, 4423 (1999).

[27] C. P. Bean, and J. D. Livingston, J. Appl. Phys. **30**, 120S (1959).

[28] C. Etz, B. Lazarovits, J. Zabloudil, R. Hammerling, B. Újfalussy, L. Szunyogh, G. M. Stocks, and P. Weinberger, Phys. Rev. B **75**, 245432 (2007).

15

A mesoscopic excursion: domain walls

Based on the Ginzburg-Landau expansion an expression is introduced by which in a kind of multi-scale approach equilibrium domain wall widths of pure magnetic systems or binary magnetic alloys can be evaluated. This description will be important in particular for the discussion of domain wall resistivities in Chapter 17.

The interest in magnetic domains and domain-wall formation [1, 2] changed in recent years, in particular since the discovery of the giant magnetoresistance effect, from extended systems such as well-characterized thick layers on suitable substrates or single crystals to restricted systems in the form of thin wires or spin valve type arrangements, i.e., to nano-sized systems with structural or geometrical restrictions. Since domain wall widths are typically only between 100 to 500 nm, experimental techniques had to be improved continuously in order to map out sufficiently well domain walls, and, by making use of spin-polarized techniques. In the last few years they seem to head even for a resolution necessary to trace the spread of orientations of the magnetization within domain walls.

Suppose L denotes the width of a domain wall in a substitutional binary alloy A_cB_{1-c} viewed as a layered system (only two-dimensional translational symmetry) corresponding to the following magnetic configuration C_i

$$C_i = \{\mathbf{n}_l, \quad \underbrace{\mathbf{n}_1, \mathbf{n}_2, \ldots, \mathbf{n}_{L-1}, \mathbf{n}_{L-1}}_{\text{domain wall}}, \quad \mathbf{n}_r\} \quad , \tag{15.1}$$

where $\mathbf{n}_l$ and $\mathbf{n}_r$ denote the orientations of the magnetization in the "left" and the "right" domain and the $\mathbf{n}_i$ refer to those in the atomic planes forming the wall; see also Section 3.6. Each domain represents a semi-infinite system with a uniform orientation of the magnetization. Consider now the following special case

$$C_i = \{\mathbf{n}_l = \hat{x}, \quad \mathbf{n}_1, \mathbf{n}_2, \ldots, \mathbf{n}_{L-1}, \mathbf{n}_{L-1}, \quad \mathbf{n}_r = -\hat{x}\} \quad , \tag{15.2}$$

namely that the magnetization in the left domain points uniformly along the in-plane x-axis, and in the right domain the direction of the magnetization is uniformly antiparallel to x. Then in terms of the magnetic force theorem the energy difference between this configuration and the case that the system

forms a single domain with a magnetization aligned uniformly along $\hat{x}$,

$$C_0 = \{\mathbf{n}_l = \hat{x}, \quad \mathbf{n}_i = \hat{x}, i = 1, L, \quad \mathbf{n}_r = \hat{x}\} \quad , \tag{15.3}$$

is given by

$$\Delta E(\mathcal{C}_i, L) = E(\mathcal{C}_i, L) - E(\mathcal{C}_0, L) \quad , \tag{15.4}$$

where, as should be recalled, $E(\mathcal{C}_i, L)$ is defined by

$$E(\mathcal{C}_i, L) = \int_{E_b}^{E_F} n(\mathcal{C}_i, L; \epsilon)(\epsilon - E_F) d\epsilon \quad . \tag{15.5}$$

In principle in order to obtain at a given width L the *domain wall formation energy* the minimum over all configurations $\mathcal{C}_i$ has to be evaluated,

$$E(L) = \min_{\{\mathcal{C}_i\}} [\Delta E(\mathcal{C}_i, L)] \quad , \tag{15.6}$$

a procedure, which, however, is computationally beyond reach. The domain wall formation energy $E(L)$ is therefore approximated by a model in which the magnetization changes quasi-continuously from $\hat{x}$ to $-\hat{x}$

$$E(L) \sim E(\mathcal{C}_d, L) - E(\mathcal{C}_0, L) \quad , \tag{15.7}$$

$$C_d = \{\mathbf{n}_l = \hat{x}, \quad \mathbf{n}_i = D(\Phi_i)\hat{x}, \quad \mathbf{n}_r = -\hat{x} \quad ; \quad \Phi_i = 180 i/L \quad , \quad i = 1, L\} \quad , \tag{15.8}$$

where $D(\Phi_i)$ is a rotation by an angle Φ_i around the surface normal.

Based on the usual Ginzburg-Landau expansion [3] it was shown [4] that the domain wall formation energy in a magnetic substitutional binary alloy [5] $A_c B_{1-c}$ can be written as

$$E(L, c) = A_0(c) \left(\frac{\alpha(c)}{L} + \beta(c) L \right) \quad , \tag{15.9}$$

where $A_0(c)$ is the unit area, and the constants $\alpha(c)$ and $\beta(c)$ correspond to the *exchange* and *anisotropy energy*, respectively.

At a given concentration c, from the condition $dE(L)/dL = 0$ follows immediately that the equilibrium domain wall width L_0 is given by

$$L_0 = \sqrt{\alpha/\beta} \quad . \tag{15.10}$$

The coefficients α and β in Eq. (15.9) can easily be obtained by evaluating $E(L)$ in Eq. (15.7) at two different values of L, say L_1 and $L_2, L_2 > L_1$, since

$$\begin{aligned} \beta &= \left(L_2 E(L_2) - L_1 E(L_1)\right) / (L_2^2 - L_1^2) \quad , \\ \alpha &= L_1 E(L_1) - \beta L_1^2 \quad . \end{aligned} \tag{15.11}$$

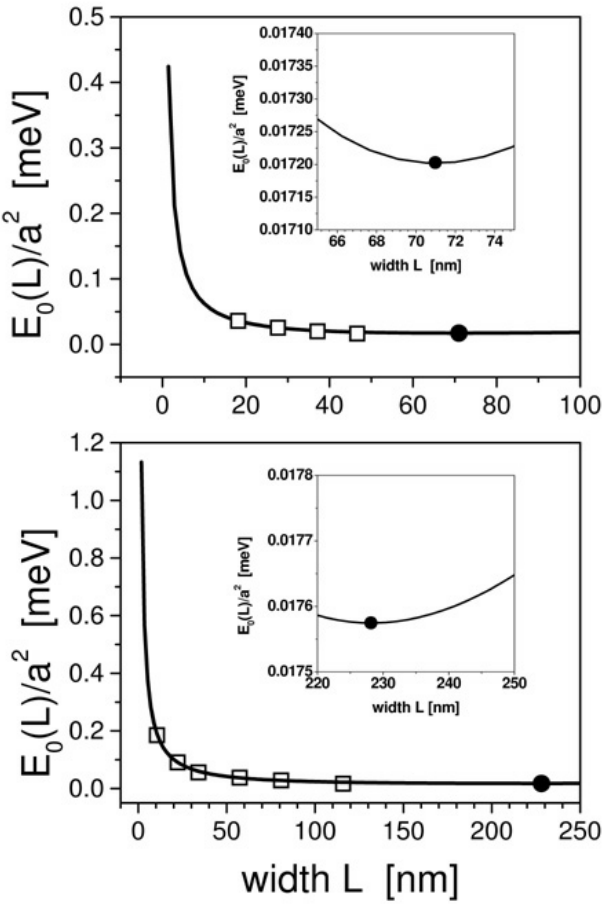

FIGURE 15.1: *Domain wall formation energies* $E(L)/a^2$ *for bcc* $Ni_{15}Fe_{85}$ *and fcc* $Ni_{85}Fe_{15}$ *as a function of the domain wall width* L*. Open squares refer to calculated values. The full line corresponds to a Landau-Ginzburg fit using* $L_1 = 126$ *and* $L_2 = 192$ *ML. The position of the equilibrium domain wall width* L_0 *is indicated as a full circle. The inset shows* $E(L)/a^2$ *in the vicinity of* L_0*. From Ref. [5].*

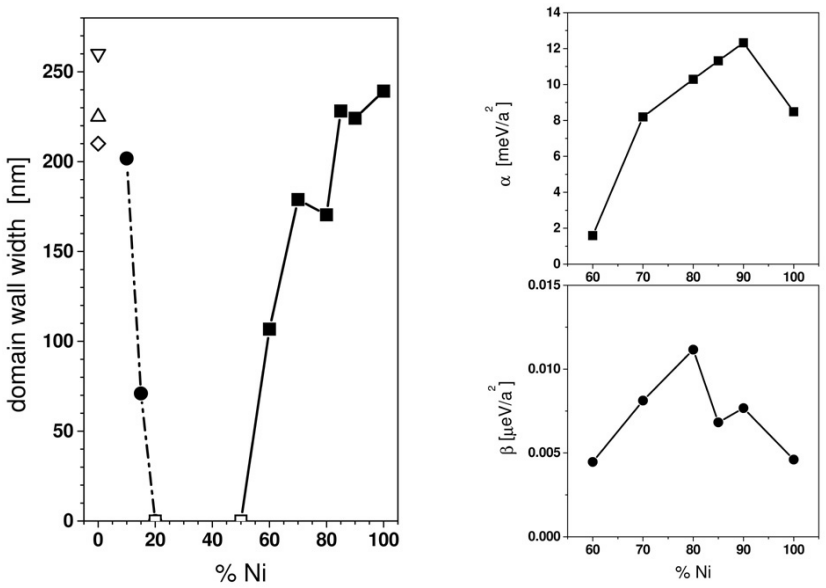

FIGURE 15.2: *Left: Equilibrium domain wall width L_0 (full circles: bcc, full squares: fcc) in Ni_cFe_{1-x} as a function of the Ni concentration. Note that between about 17.5 and 55% Ni no domain wall formation occurs. The open diamond, up-triangle and down-triangle refer respectively to the experimental data given in Refs. [7, 8, 9]. Right: Evaluated constants α and β for the fcc regime of Ni_xFe_{1-x}. From Ref. [5].*

Furthermore, for $L_2 - L_1 = n$ the corresponding energy difference $\Delta E(n) = E(L_1+n) - E(L_1)$ is simply given by $\Delta E(n) = -\alpha n / \left(L_1^2 + L_1 n\right) + n\beta \simeq n\beta$.

In Fig. 15.1 the domain wall formation energies $E(L)/a^2$ are displayed versus L (in nm) for bcc $Ni_{15}Fe_{85}$ and fcc $Ni_{85}Fe_{15}$. Since the functional form in Eq. (15.9) fits very well the ab-initio data evaluated fully relativistically, the occurring deviations being minute, Eq. (15.11) indeed can be used to predict L_0 (indicated in this figure as a full circle; see also the respective insets, in which $E(L)/a^2$ is depicted in the vicinity of L_0). The corresponding parameters α and β in Ni_cFe_{1-c} are shown in the right part of Fig. 15.2.

It is probably well known that in the Ni/Fe phase diagram a famous structural phase transition from bcc to fcc occurs around 35% Ni. In viewing Fig. 15.2, a perhaps surprising feature of this phase transformation becomes apparent: in Ni_cFe_{1-c} domain walls are only formed in the bcc regime for $x < 20\%$ and in the fcc regime for $x > 55\%$, since in the remainder of concentrations $\alpha/\beta < 0$.

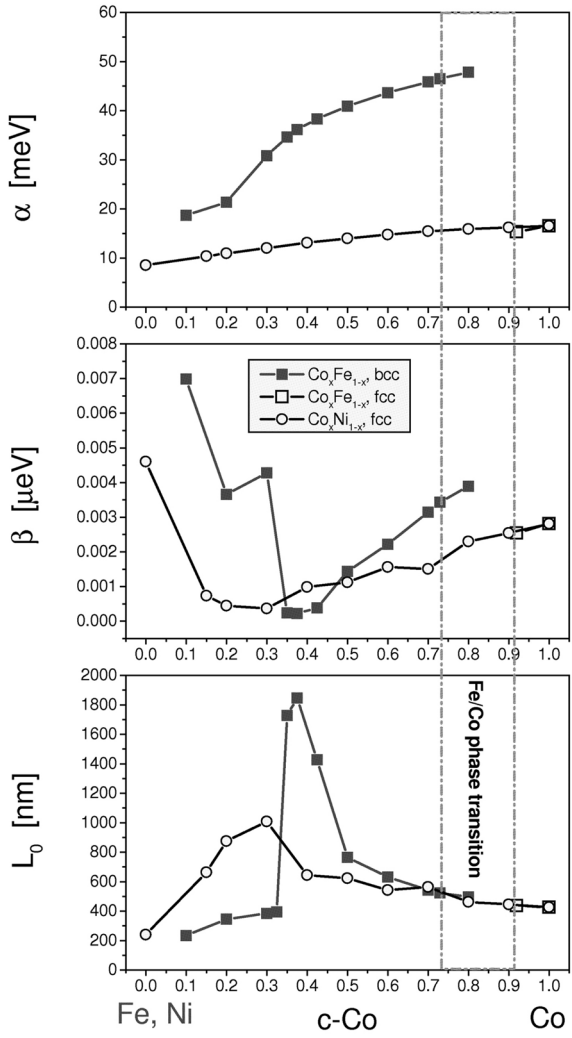

FIGURE 15.3: *Exchange and anisotropy parameters α and β, see Eq.(15.9), and equilibrium domain wall width [nm] in Co_cFe_{1-c} and Co_cNi_{1-c} with respect to the Co concentration. From Ref. [6].*

In Fig. 15.3 the exchange and anisotropy energies α and β for Co_cFe_{1-c} and Co_cNi_{1-c} are displayed versus the Co concentration together with the corresponding equilibrium domain wall width L_0. While for Co_cNi_{1-c} α, β and L_0 vary fairly smoothly with c, in Co_cFe_{1-c} both α and β show a break in the vicinity of the phase transition: they change from higher values in the bcc regime to lower values in the fcc regime. It is interesting to note that although there is this discontinuity for α and β across the regime of the phase transition, by continuing "artificially" the bcc regime to $c = 0.8$ no obvious jump in L_0 occurs at that concentration. Since the structural phase transition extends over about 20% in concentration and since the α and β are defined strictly only for either the bcc or the fcc regime, unfortunately nothing can be said about how they would change in the concentration range of the phase transition. Furthermore, since for Co_cFe_{1-c} β reaches a minimum while α increases continuously with c, there is a peak in L_0 near $c \sim 0.4$. This minimum in β looks like the system attempts to head for a structural phase transition.

The functional form of the equilibrium domain wall width versus concentration can be classified very simply using Eq. (15.10)

$$L_0^2 = \alpha/\beta \quad , \qquad \alpha, \beta \geq 0 : \begin{cases} \alpha \neq 0, \beta \to 0 : L_0 \to \infty \\ \\ \alpha \to 0, \beta \neq 0 : \; L_0 \to 0 \end{cases} . \tag{15.12}$$

Quite clearly it is the interplay between the exchange energy and the magnetic anisotropy that determines the width of magnetic domain walls, or expressed more drastically: in a non-relativistic description (no magnetic anisotropy) all magnetic systems are per definition single domain systems, since $\beta = 0$.

[1] F. Bloch, Z. Physik **74**, 295 (1932).

[2] L. Néel, Cahiers Phys. **25**, 1 (1944).

[3] see e.g. A. M. Kosevich, in *Modern Problems in Condensed Matter Sciences*, Vol 17, edited by V. M. Agranovich and A. A. Maradudin (North-Holland, Amsterdam, 1986), p. 495.

[4] J. Schwitalla, B. L. Gyorffy, and L. Szunyogh, Phys. Rev. B **63**, 104423 (2001).

[5] P. Weinberger, Phys. Rev. Lett. **98**, 027205 (2007).

[6] P. Weinberger, Phys. Rev. Lett. **100**, 017201 (2008).

[7] H. P. Oepen and J. Kirschner, Phys. Rev. Lett. **62**, 819 (1989).

[8] B. A. Lilley, Philos. Mag. **41**, 792 (1950)

[9] T. Suzuki and K, Suzuki, IEEE Transactions on Magnetics **13**, 1505 (1977).

16

Theory of electric and magneto-optical properties

Here, linear response theory, the Kubo and Kubo-Luttinger equations, is introduced in quite a general context from which for independent particles, namely in the context of density functional theory, a Kubo equation is derived that applies to electric as well as optical transport. For both aspects (zero and finite frequencies) a Green's function formulation in terms of multiple scattering is given. In particular, the importance of inherent boundary conditions and the concept of layer-resolved conductivities are discussed.

16.1 Linear response theory

In the 1950s Kubo developed a method of evaluating the response of a quantum mechanical system to an external potential, in particular to an electric field [1]. To first order, known as linear response, this kind of response theory [2, 3] is applicable to electric as well as to optical transport. In the following the underlying theoretical approach is introduced and will then be cast into a multiple scattering formulation [4, 5, 6].

16.1.1 Time-dependent perturbations

Assuming a time-dependent perturbation $\hat{H}'(t)$, the Hamilton operator of the perturbed system is of the form,

$$\hat{H}(t) = \hat{H}_0 + \hat{H}'(t) \quad . \tag{16.1}$$

For a grand-canonical ensemble the density operator of the unperturbed system can be written as

$$\hat{\varrho}_0 = \frac{1}{\mathcal{Z}} e^{-\beta \hat{\mathcal{H}}_0} \quad , \quad \hat{\mathcal{H}}_0 = \hat{H}_0 - \mu \hat{N} \quad , \quad \mathcal{Z} = Tr\left(e^{-\beta \hat{\mathcal{H}}_0}\right) \quad , \tag{16.2}$$

where μ is the chemical potential, $\beta = (k_B T)^{-1}$, $\hat{N}$ the (particle) number operator, and $\mathcal{Z}$ is the grand canonical partition function.

Since the expectation value of a physical observable A, associated with a Hermitian operator $\hat{A}$ corresponding to the unperturbed system, is given by

$$A_0 = \langle A \rangle = \frac{1}{\mathcal{Z}} Tr\left(\hat{A} e^{-\beta \hat{\mathcal{H}}_0}\right) = Tr\left(\hat{\varrho}_0 \hat{A}\right) \quad , \tag{16.3}$$

within the Schrödinger picture the equation of motion for the density operator can be written as

$$i\hbar \frac{\partial \hat{\varrho}(t)}{\partial t} = \left[\hat{\mathcal{H}}(t), \hat{\varrho}(t)\right] \quad , \quad \hat{\mathcal{H}}(t) = \hat{H}(t) - \mu \hat{N} = \hat{\mathcal{H}}_0 + \hat{H}'(t) \quad . \tag{16.4}$$

Clearly enough, in the absence of a perturbation, $\hat{\varrho}(t) = \hat{\varrho}_0$. Therefore, partitioning $\hat{\varrho}(t)$ as

$$\hat{\varrho}(t) = \hat{\varrho}_0 + \hat{\varrho}'(t) \quad , \tag{16.5}$$

and making use of the fact that $\left[\hat{\mathcal{H}}_0, \hat{\varrho}_0\right] = 0$, one gets in first order in $\hat{H}'$,

$$i\hbar \frac{\partial \hat{\varrho}'(t)}{\partial t} = \left[\hat{\mathcal{H}}_0, \hat{\varrho}'(t)\right] + \left[\hat{H}'(t), \hat{\varrho}_0\right] \quad , \tag{16.6}$$

or, by switching to the interaction (Dirac) picture,

$$\hat{\varrho}_D(t) = \hat{\varrho}_0 + \hat{\varrho}'_D(t) \ , \ \hat{\varrho}'_D(t) = e^{\frac{i}{\hbar}\hat{\mathcal{H}}_0 t} \hat{\varrho}'(t) e^{-\frac{i}{\hbar}\hat{\mathcal{H}}_0 t} \quad , \tag{16.7}$$

$$i\hbar \frac{\partial \hat{\varrho}'_D(t)}{\partial t} = \left[\hat{H}'_D(t), \hat{\varrho}_0\right] \quad . \tag{16.8}$$

This equation has to be solved now for a given initial condition. Turning on the external field adiabatically at $t = -\infty$, implies that the density operator of the system at $t = -\infty$ represents an ensemble of systems in thermal equilibrium, i.e.,

$$\lim_{t \to -\infty} \hat{\varrho}(t) = \hat{\varrho}_0 \quad , \quad \lim_{t \to -\infty} \hat{\varrho}'_D(t) = 0 \quad . \tag{16.9}$$

Using this boundary condition for $\hat{\varrho}'_D(t)$ results the following integral equation

$$\hat{\varrho}'_D(t) = -\frac{i}{\hbar} \int\limits_{-\infty}^{t} dt' \left[\hat{H}'_D(t'), \hat{\varrho}_0\right] \quad , \tag{16.10}$$

such that in the Schrödinger picture the density operator can be approximated in first order as

$$\hat{\varrho}(t) \approx \hat{\varrho}_0 - \frac{i}{\hbar} \int\limits_{-\infty}^{t} dt' e^{-\frac{i}{\hbar}\hat{\mathcal{H}}_0 t} \left[\hat{H}'_D(t'), \hat{\varrho}_0\right] e^{\frac{i}{\hbar}\hat{\mathcal{H}}_0 t} \quad . \tag{16.11}$$

Considering now the time evolution of a (time-dependent) physical observable $A(t)$,

$$A(t) = Tr\left(\hat{\varrho}(t)\hat{A}\right) = A_0 - \frac{i}{\hbar}\int_{-\infty}^{t} dt'\, Tr\left(e^{-\frac{i}{\hbar}\hat{\mathcal{H}}_0 t}\left[\hat{H}'_D(t'), \hat{\varrho}_0\right] e^{\frac{i}{\hbar}\hat{\mathcal{H}}_0 t}\hat{A}\right)$$
$$= A_0 - \frac{i}{\hbar}\int_{-\infty}^{t} dt'\, Tr\left(\left[\hat{H}'_D(t'), \hat{\varrho}_0\right]\hat{A}_D(t)\right) \quad , \qquad (16.12)$$

where A_0 is defined in Eq. (16.3) and the Dirac representation of operator $\hat{A}$ is given by

$$\hat{A}_D(t) = e^{\frac{i}{\hbar}\hat{\mathcal{H}}_0 t}\hat{A}e^{-\frac{i}{\hbar}\hat{\mathcal{H}}_0 t} \quad . \qquad (16.13)$$

Then by making use of the identity,

$$Tr\left(\left[\hat{A}, \hat{B}\right]\hat{C}\right) = Tr\left(\hat{A}\hat{B}\hat{C} - \hat{B}\hat{A}\hat{C}\right) = Tr\left(\hat{B}\hat{C}\hat{A} - \hat{B}\hat{A}\hat{C}\right)$$
$$= Tr\left(\hat{B}\left[\hat{C}, \hat{A}\right]\right) \quad , \qquad (16.14)$$

one arrives at

$$\delta A(t) = A(t) - A_0 = -\frac{i}{\hbar}\int_{-\infty}^{t} dt'\, Tr\left(\hat{\varrho}_0\left[\hat{A}_D(t), \hat{H}'_D(t')\right]\right) \quad . \qquad (16.15)$$

Assuming finally that the perturbation $\hat{H}'(t)$ is of the form,

$$\hat{H}'(t) = \hat{B}F(t) \quad , \qquad (16.16)$$

where $\hat{B}$ is a Hermitian operator and $F(t)$ is a complex function (classical field), Eq. (16.15) transforms to

$$\delta A(t) = -\frac{i}{\hbar}\int_{-\infty}^{t} dt' F(t') Tr\left(\hat{\varrho}_0\left[\hat{A}_D(t), \hat{B}_D(t')\right]\right) \quad , \qquad (16.17)$$

which can be written in terms of a (retarded) Green's function as,

$$G^{ret}_{AB}(t, t') = -i\Theta(t - t') Tr\left(\hat{\varrho}_0\left[\hat{A}_D(t), \hat{B}_D(t')\right]\right) \quad , \qquad (16.18)$$

or, by introducing a so-called generalized susceptibility,

$$\chi_{AB}(t, t') = \frac{1}{\hbar} G^{ret}_{AB}(t, t') \quad , \qquad (16.19)$$

as

$$\delta A(t) = \frac{1}{\hbar}\int_{-\infty}^{\infty} dt' F(t') G_{AB}^{ret}(t,t') = \int_{-\infty}^{\infty} dt' F(t') \chi_{AB}(t,t') \quad . \tag{16.20}$$

Suppose now that the operators $\hat{A}$ and $\hat{B}$ do not depend explicitly on time; then $G_{AB}^{ret}(t,t')$ and $\chi_{AB}(t,t')$ are only functions of the argument $(t-t')$. Consequently, the Fourier coefficients of $\delta A(t)$ can be written as

$$\delta A(\omega) = \frac{1}{\hbar} F(\omega) G_{AB}^{ret}(\omega) = F(\omega)\chi_{AB}(\omega) \quad , \tag{16.21}$$

where

$$X(\omega) = \int_{-\infty}^{\infty} dt\, X(t) e^{i\omega t} \quad , \quad X(t) = \frac{1}{2\pi}\int_{-\infty}^{\infty} d\omega\, X(\omega) e^{-i\omega t} \quad , \tag{16.22}$$

applies for any time-dependent quantity $X(t)$.

Since by definition $G_{AB}^{ret}(\omega)$ is analytical only in the upper complex semiplane, for a real argument ω the limit $\varpi \to \omega + i0$ has to be considered. The complex admittance $\chi_{AB}(\omega)$ can therefore be expressed in terms of the retarded Green function as

$$\chi_{AB}(\omega) = \frac{1}{\hbar} G_{AB}^{ret}(\omega + i0) = -\frac{i}{\hbar}\int_{0}^{\infty} dt\, e^{i(\omega+i0)t} Tr\left(\hat{\varrho}_0 \left[\hat{A}(t), \hat{B}(0)\right]\right) \quad . \tag{16.23}$$

The occurrence of the side-limit $\omega + i0$ in $\chi_{AB}(\omega)$ is usually termed *adiabatic switching on* of the perturbation, since it corresponds to a time-dependent classical field,

$$F'(t) = \lim_{s \to +0} \left(F(t) e^{st}\right) \quad . \tag{16.24}$$

16.1.2 The Kubo equation

Returning now to the second term on the *rhs* of Eq. (16.12),

$$\delta A(t) = -\frac{i}{\hbar}\int_{-\infty}^{t} dt'\, Tr\left(\left[\hat{H}'_H(t'), \hat{\varrho}_0\right] \hat{A}_H(t)\right) \quad , \tag{16.25}$$

where the operators are defined within the Heisenberg picture with respect to the unperturbed system and using *Kubo's identity*,

$$\frac{i}{\hbar}\left[\hat{X}_H(t), \hat{\varrho}\right] = \hat{\varrho}\int_{0}^{\beta} d\lambda\, \dot{\hat{X}}_H(t - i\lambda\hbar) \quad , \tag{16.26}$$

$$\hat{\varrho} = \frac{e^{-\beta \hat{H}}}{Tr\left(e^{-\beta \hat{H}}\right)} \quad , \tag{16.27}$$

$$\hat{X}_H(t) = e^{\frac{i}{\hbar}\hat{H}t}\hat{X}(t)e^{-\frac{i}{\hbar}\hat{H}t} \quad , \quad \dot{\hat{X}}_H(t) = -\frac{i}{\hbar}\left[\hat{X}_H(t), \hat{H}\right] \quad , \tag{16.28}$$

this term, namely Eq. (16.25), finally yields the famous *Kubo formula:*

$$\begin{aligned}\delta A(t) &= -\int_{-\infty}^{t} dt' \int_0^{\beta} d\lambda\, Tr\left(\hat{\varrho}_0 \dot{\hat{H}}'_H(t' - i\lambda\hbar)\hat{A}_H(t)\right) \\ &= -\int_{-\infty}^{t} dt' \int_0^{\beta} d\lambda\, Tr\left(\hat{\varrho}_0 \dot{\hat{H}}'(t')\hat{A}_H(t - t' + i\lambda\hbar)\right) \quad . \end{aligned} \tag{16.29}$$

16.1.3 The current-current correlation function

Suppose that the total electric field, $\mathbf{E}(\mathbf{r}, t)$ is associated with the perturbation $\hat{H}'(t)$ in terms of a scalar potential $\phi(\mathbf{r}, t)$ as

$$\hat{H}'(t) = \int d^3r\, \hat{\rho}(\mathbf{r})\phi(\mathbf{r}, t) \, , \quad \mathbf{E}(\mathbf{r}, t) = -\boldsymbol{\nabla}\phi(\mathbf{r}, t) \quad , \tag{16.30}$$

where $\hat{\rho}(\mathbf{r}) = e\psi(\mathbf{r})^+\psi(\mathbf{r})$ is the charge density operator, $\psi(\mathbf{r})$ a field operator and e the charge of an electron. Then the time-derivative of $\hat{H}'_H(t)$ can be calculated as follows,

$$\begin{aligned}\dot{\hat{H}}'(t) &= \int d^3r \underbrace{\frac{1}{i\hbar}\left[\hat{\mathcal{H}}_0, \hat{\rho}(\mathbf{r})\right]}_{\frac{\partial \hat{\rho}_H(\mathbf{r},t)}{\partial t}|_{t=0}} \phi(\mathbf{r}, t) = -\int d^3r\, \boldsymbol{\nabla}\hat{\mathbf{J}}(\mathbf{r})\, \phi(\mathbf{r}, t) \\ &= \int d^3r\, \hat{\mathbf{J}}(\mathbf{r})\, \boldsymbol{\nabla}\phi(\mathbf{r}, t) = -\int d^3r\, \hat{\mathbf{J}}(\mathbf{r})\, \mathbf{E}(\mathbf{r}, t) \quad , \end{aligned} \tag{16.31}$$

where the current-density operator is given by

$$\hat{\mathbf{J}}(\mathbf{r}) = \begin{cases} \frac{e\hbar}{2mi}\psi(\mathbf{r})^+\left(\overrightarrow{\nabla} - \overleftarrow{\nabla}\right)\psi(\mathbf{r}) \text{ , non-relativistic case} \quad , \\ \\ ec\psi(\mathbf{r})^+\, \hat{\boldsymbol{\alpha}}\, \psi(\mathbf{r}) \qquad \text{, relativistic case} \quad , \end{cases} \tag{16.32}$$

and the $\hat{\boldsymbol{\alpha}}$ denote Dirac matrices. Note that in Eq. (16.31) the continuity equation was used and periodic boundary conditions were assumed such that the corresponding surface term vanishes. The $\mu-$th component of the current density can thus be written as

$$J_\mu(\mathbf{r}, t) = \sum_\nu \int d^3r' \int_{-\infty}^{\infty} dt' \sigma_{\mu\nu}(\mathbf{r}, \mathbf{r}'; t, t')\, E_\nu(\mathbf{r}', t') \quad , \tag{16.33}$$

where the occurring space-time correlation function is given by

$$\sigma_{\mu\nu}(\mathbf{r},\mathbf{r}';t,t') = \Theta(t-t')\int_0^\beta d\lambda\, Tr\left(\hat{\varrho}_0\,\hat{J}_\nu(\mathbf{r},0)\hat{J}_\mu(\mathbf{r}',t-t'+i\lambda\hbar)\right) \quad , \quad (16.34)$$

by which the linear response of the current density at $(\mathbf{r},t)$ in direction μ is correlated to the local electric field at $(\mathbf{r}',t')$ applied in direction ν. Note that in the above equation the current-density operators are assumed to be Heisenberg operators.

Consider now the Fourier components of the electric field,

$$\mathbf{E}(\mathbf{q},\omega) = \int d^3r \int_{-\infty}^{\infty} dt\, \mathbf{E}(\mathbf{r},t)e^{-i\mathbf{q}\cdot\,\mathbf{r}+i\varpi t} \quad , \quad (16.35)$$

$$\mathbf{E}(\mathbf{r},t) = \frac{1}{2\pi V}\int d^3q \int_{-\infty}^{\infty} d\omega\, \mathbf{E}(\mathbf{q},\omega)e^{i\mathbf{q}\cdot\,\mathbf{r}-i\varpi t} \quad , \quad (16.36)$$

where $\varpi = \omega + i0$ and V is the volume of the system. While $\sigma_{\mu\nu}(\mathbf{r},\mathbf{r}';t,t')$ trivially depends only on $(t-t')$, in general, it is a function of the independent space variables $\mathbf{r}$ and $\mathbf{r}'$. In cases, however, when the current density is an average of the local current density in Eq. (16.31) over a large enough region, $\sigma_{\mu\nu}(\mathbf{r},\mathbf{r}';t,t')$ can be assumed to be homogeneous in space, i.e., $\sigma_{\mu\nu}(\mathbf{r},\mathbf{r}';t-t') = \sigma_{\mu\nu}(\mathbf{r}-\mathbf{r}';t-t')$. This usually is the case if $|\mathbf{q}|$ is small. The $(\mathbf{q},\omega)$ component of the current density per unit volume,

$$J_\mu(\mathbf{q},\omega) = \frac{1}{V}\int d^3r \int_{-\infty}^{\infty} dt\, J_\mu(\mathbf{r},t)e^{-i\mathbf{q}\cdot\,\mathbf{r}+i\varpi t} \quad , \quad (16.37)$$

can then be determined, i.e.,

$$J_\mu(\mathbf{q},\omega) = \sum_\nu \sigma_{\mu\nu}(\mathbf{q},\omega)\, E_\nu(\mathbf{q},\omega) \quad , \quad (16.38)$$

where $\sigma_{\mu\nu}(\mathbf{q},\omega)$ is the wave–vector and frequency dependent conductivity tensor,

$$\sigma_{\mu\nu}(\mathbf{q},\omega) = \frac{1}{V}\int_0^\infty dt\; e^{i\varpi t}\int_0^\beta d\lambda\; Tr\left(\hat{\varrho}_0\hat{J}_\nu(-\mathbf{q},0)\hat{J}_\mu(\mathbf{q},t+i\lambda\hbar)\right) \quad , \quad (16.39)$$

and

$$J_\mu(\mathbf{q},t) = \int d^3r\; J_\mu(\mathbf{r},t)e^{-i\mathbf{q}\cdot\,\mathbf{r}} \quad . \quad (16.40)$$

In using contour integration techniques one arrives at

$$\sigma_{\mu\nu}(\mathbf{q},\omega) = \frac{i}{\hbar V}\int_0^\infty dt\, e^{i\varpi t}\int_t^\infty dt'\, Tr\left(\hat{\varrho}_0\left[\hat{J}_\mu(\mathbf{q},t'),\hat{J}_\nu(-\mathbf{q},0)\right]\right) \quad , \tag{16.41}$$

such that by introducing the below current-current correlation function,

$$\Sigma_{\mu\nu}(\mathbf{q},\varpi) = \frac{1}{\hbar V}\int_0^\infty dt\, e^{i\varpi t}\, Tr\left(\hat{\varrho}_0\left[\hat{J}_\mu(\mathbf{q},t),\hat{J}_\nu(-\mathbf{q},0)\right]\right) \quad , \tag{16.42}$$

the conductivity tensor can finally be expressed as

$$\sigma_{\mu\nu}(\mathbf{q},\omega) = \frac{\Sigma_{\mu\nu}(\mathbf{q},\varpi) - \Sigma_{\mu\nu}(\mathbf{q},0)}{\varpi} \quad . \tag{16.43}$$

16.2 Kubo equation for independent particles

In the basis of the eigenfunctions of $\hat{H}_0$ (spectral representation),

$$\hat{H}_0\,|n\rangle = \varepsilon_n\,|n\rangle \;, \quad \langle\, m\,|\,n\,\rangle = \delta_{nm} \quad , \quad \sum_n |\,n\,\rangle\langle\,n\,| = \hat{I} \quad , \tag{16.44}$$

the equilibrium density operator and its matrix elements are given by

$$\hat{\varrho}_0 = \sum_n f(\varepsilon_n)|n\rangle\langle n| \;,\; \langle n\,|\hat{\varrho}_0|\,p\rangle = f(\varepsilon_n)\delta_{pn} \quad , \tag{16.45}$$

and the thermal average of the current–current commutator can be written as

$$Tr\left(\hat{\varrho}_0\left[\hat{J}_\mu(\mathbf{q},t'),\hat{J}_\nu(-\mathbf{q},0)\right]\right) = \sum_{nm}\{f(\varepsilon_n) - f(\varepsilon_m)\}\; e^{\frac{i}{\hbar}(\varepsilon_n-\varepsilon_m)t'} \times J_\mu^{nm}(\mathbf{q})J_\nu^{mn}(-\mathbf{q}) \quad , \tag{16.46}$$

with

$$J_\mu^{nm}(\mathbf{q}) \equiv \left\langle n\left|\hat{J}_\mu(\mathbf{q})\right|m\right\rangle \text{ and } J_\nu^{mn}(-\mathbf{q}) \equiv \left\langle m\left|\hat{J}_\nu(-\mathbf{q})\right|n\right\rangle \quad , \tag{16.47}$$

and $f(\varepsilon)$ being the Fermi-Dirac function. Substituting Eq. (16.46) into Eq. (16.42) then yields

$$\Sigma_{\mu\nu}(\mathbf{q},\omega) = \frac{1}{\hbar V}\sum_{nm}\{f(\varepsilon_n) - f(\varepsilon_m)\}\, J_\mu^{nm}(\mathbf{q})J_\nu^{mn}(-\mathbf{q})\int_0^\infty dt\, e^{\frac{i}{\hbar}(\varepsilon_n-\varepsilon_m+\hbar\varpi)t} \quad . \tag{16.48}$$

Since the integral with respect to t, however, is just the Laplace transform of the below identity,

$$\int_0^\infty dt\, e^{\left[\frac{i}{\hbar}(\varepsilon_n-\varepsilon_m+\hbar\omega)-s\right]t} \underset{(s>0)}{=} -\frac{e^{\left[\frac{i}{\hbar}(\varepsilon_n-\varepsilon_m+\hbar\omega)-s\right]}}{\frac{i}{\hbar}(\varepsilon_n-\varepsilon_m+\hbar\omega)-s} \quad , \tag{16.49}$$

Eq. (16.48) can be transformed to

$$\Sigma_{\mu\nu}(\mathbf{q},\omega) = \frac{i}{V}\sum_{nm}\frac{f(\varepsilon_n)-f(\varepsilon_m)}{\varepsilon_n-\varepsilon_m+\hbar\varpi}J_\mu^{nm}(\mathbf{q})J_\nu^{mn}(-\mathbf{q}) \quad . \tag{16.50}$$

Together with Eq. (16.41) this now provides a numerically tractable tool to calculate the conductivity tensor. Since

$$\frac{1}{\varepsilon_n-\varepsilon_m+\hbar\varpi}-\frac{1}{\varepsilon_n-\varepsilon_m} = \frac{-\hbar\varpi}{(\varepsilon_n-\varepsilon_m)(\varepsilon_n-\varepsilon_m+\hbar\varpi)} \quad ,$$

$\sigma_{\mu\nu}(\mathbf{q},\omega)$ can also be written in the following compact form,

$$\sigma_{\mu\nu}(\mathbf{q},\omega) = \frac{\hbar}{iV}\sum_{nm}\frac{f(\varepsilon_n)-f(\varepsilon_m)}{\varepsilon_n-\varepsilon_m}\frac{J_\mu^{nm}(\mathbf{q})J_\nu^{mn}(-\mathbf{q})}{\varepsilon_n-\varepsilon_m+\hbar\varpi} \quad , \tag{16.51}$$

where

$$\varpi = \omega + i\delta \quad . \tag{16.52}$$

16.2.1 Contour integrations

Considering a pair of eigenvalues, $\varepsilon_n$and ε_m, for a suitable contour C [5] in the complex energy plane (see Fig. 16.1) the residue theorem implies that

$$\begin{aligned}\oint_C dz\,\frac{f(z)}{(z-\varepsilon_n)(z-\varepsilon_m+\hbar\omega+i\delta)} &= -2\pi i\frac{f(\varepsilon_n)}{\varepsilon_n-\varepsilon_m+\hbar\omega+i\delta} \\ &+2i\delta_T\sum_{k=-N_2+1}^{N_1}\frac{1}{(z_k-\varepsilon_n)(z_k-\varepsilon_m+\hbar\omega+i\delta)} \quad ,\end{aligned} \tag{16.53}$$

where the $z_k = E_F + i(2k-1)\delta_T$ are the *Matsubara-poles* with E_F being the Fermi energy, $\delta_T \equiv \pi k_B T$, and T the temperature. In Eq. (16.53) it was supposed that N_1 and N_2 Matsubara-poles in the upper and lower semi-plane lie within the contour C, respectively. Eq. (16.53) can be rearranged as follows

$$\begin{aligned}i\frac{f(\varepsilon_n)}{\varepsilon_n-\varepsilon_m+\hbar\omega+i\delta} &= -\frac{1}{2\pi}\oint_C dz\,\frac{f(z)}{(z-\varepsilon_n)(z-\varepsilon_m+\hbar\omega+i\delta)} \\ &+i\frac{\delta_T}{\pi}\sum_{k=-N_2+1}^{N_1}\frac{1}{(z_k-\varepsilon_n)(z_k-\varepsilon_m+\hbar\omega+i\delta)} \quad .\end{aligned} \tag{16.54}$$

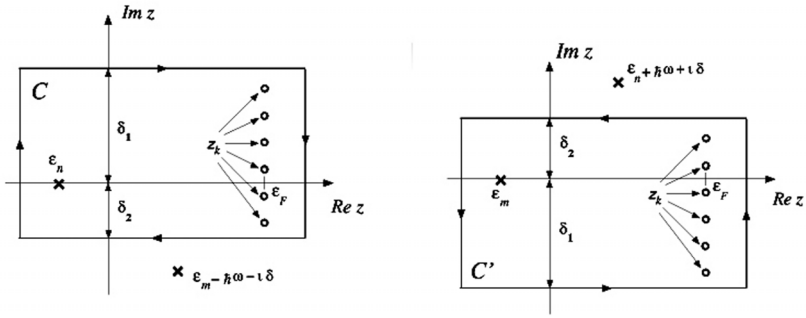

FIGURE 16.1: *Integrations along the contours C (left entry) and C' (right entry). From Ref. [5].*

Similarly, by choosing contour C', see Fig. 16.1, one gets [5]

$$-i\frac{f(\varepsilon_m)}{\varepsilon_n-\varepsilon_m+\hbar\omega+i\delta}=\frac{1}{2\pi}\oint_{C'}dz\,\frac{f(z)}{(z-\varepsilon_m)(z-\varepsilon_n-\hbar\omega-i\delta)}$$
$$+i\frac{\delta_T}{\pi}\sum_{k=-N_1+1}^{N_2}\frac{1}{(z_k-\varepsilon_m)(z_k-\varepsilon_n-\hbar\omega-i\delta)}\quad . \tag{16.55}$$

Deforming the contours such that the real axis is crossed at ∞ and $-\infty$, $\Sigma_{\mu\nu}(\mathbf{q},\varpi)$ can finally be expressed as

$$\Sigma_{\mu\nu}(\mathbf{q},\varpi)=-\frac{1}{2\pi V}\left\{\oint_C dz\,f(z)\sum_{mn}\frac{J_\mu^{nm}(\mathbf{q})J_\nu^{mn}(-\mathbf{q})}{(z-\varepsilon_n)(z-\varepsilon_m+\hbar\omega+i\delta)}-\right.$$
$$\left.\oint_{C'}dz\,f(z)\sum_{mn}\frac{J_\mu^{nm}(\mathbf{q})J_\nu^{mn}(-\mathbf{q})}{(z-\varepsilon_m)(z-\varepsilon_n-\hbar\omega-i\delta)}\right\}$$
$$+\,i\frac{\delta_T}{\pi V}\left\{\sum_{k=-N_2+1}^{N_1}\sum_{mn}\frac{J_\mu^{nm}(\mathbf{q})J_\nu^{mn}(-\mathbf{q})}{(z_k-\varepsilon_n)(z_k-\varepsilon_m+\hbar\omega+i\delta)}+\right.$$
$$\left.\sum_{k=-N_1+1}^{N_2}\sum_{mn}\frac{J_\mu^{nm}(\mathbf{q})J_\nu^{mn}(-\mathbf{q})}{(z_k-\varepsilon_m)(z_k-\varepsilon_n-\hbar\omega-i\delta)}\right\}\quad . \tag{16.56}$$

16.2.2 Formulation in terms of resolvents

Consider now the resolvent of the unperturbed Hamilton operator, i.e., of the Kohn-Sham Hamiltonian,

$$\hat{G}(z) = (z\hat{I} - \hat{H})^{-1} \quad , \tag{16.57}$$

and its adjoint,

$$\hat{G}(z)^{\dagger} = (z^{*}\hat{I} - \hat{H})^{-1} = \hat{G}(z^{*}) \quad , \tag{16.58}$$

$$\hat{G}(z) = \sum_{n} \frac{|\, n \,\rangle\langle\, n \,|}{z - \varepsilon_n} \quad ; \tag{16.59}$$

it is then straightforward to rewrite Eq. (16.56) as

$$\begin{aligned}\Sigma_{\mu\nu}(\mathbf{q},\varpi) = -\frac{1}{2\pi V}\Bigg\{ \oint_{C} dz\, f(z)\, Tr\left(\hat{J}_{\mu}(\mathbf{q})\,\hat{G}(z+\hbar\omega+i\delta)\,\hat{J}_{\nu}(-\mathbf{q})\,\hat{G}(z)\right) - \\ \oint_{C'} dz\, f(z)\, Tr\left(\hat{J}_{\mu}(\mathbf{q})\,\hat{G}(z)\hat{J}_{\nu}(-\mathbf{q})\,\hat{G}(z-\hbar\omega-i\delta)\right)\Bigg\} \\ + i\frac{\delta_T}{\pi V}\Bigg\{ \sum_{k=-N_2+1}^{N_1} Tr\left(\hat{J}_{\mu}(\mathbf{q})\,\hat{G}(z_k+\hbar\omega+i\delta)\,\hat{J}_{\nu}(-\mathbf{q})\,\hat{G}(z_k)\right) + \\ \sum_{k=-N_1+1}^{N_2} Tr\left(\hat{J}_{\mu}(\mathbf{q})\,\hat{G}(z_k)\,\hat{J}_{\nu}(-\mathbf{q})\,\hat{G}(z_k-\hbar\omega-i\delta)\right)\Bigg\} \quad .\end{aligned} \tag{16.60}$$

Introducing for matters of convenience the below quantities,

$$\widetilde{\Sigma}_{\mu\nu}(\mathbf{q};z_1,z_2) = -\frac{1}{2\pi V} Tr\left(\hat{J}_{\mu}(\mathbf{q})\hat{G}(z_1)\hat{J}_{\nu}(-\mathbf{q})\hat{G}(z_2)\right) \quad , \tag{16.61}$$

$$\widetilde{\Sigma}_{\nu\mu}(-\mathbf{q};z_2,z_1) = \widetilde{\Sigma}_{\mu\nu}(\mathbf{q};z_1,z_2) \quad , \tag{16.62}$$

$$\widetilde{\Sigma}_{\mu\nu}(\mathbf{q};z_1^{*},z_2^{*}) = \widetilde{\Sigma}_{\nu\mu}(\mathbf{q};z_1,z_2)^{*} = \widetilde{\Sigma}_{\mu\nu}(-\mathbf{q};z_2,z_1)^{*} \quad , \tag{16.63}$$

because of the reflection symmetry of the contours C and C', Eq. (16.60) can be written as

$$\begin{aligned}\Sigma_{\mu\nu}(\mathbf{q},\varpi) = \oint_{C} dz\, f(z)\, \widetilde{\Sigma}_{\mu\nu}(\mathbf{q};z+\hbar\omega+i\delta,z) \\ - \left(\oint_{C} dz\, f(z)\, \widetilde{\Sigma}_{\mu\nu}(-\mathbf{q};z-\hbar\omega+i\delta,z)\right)^{*} \\ -2i\delta_T \sum_{k=-N_2+1}^{N_1} \Big(\widetilde{\Sigma}_{\mu\nu}(\mathbf{q};z_k+\hbar\omega+i\delta,z_k) \\ + \widetilde{\Sigma}_{\mu\nu}(-\mathbf{q};z_k-\hbar\omega+i\delta,z_k)^{*}\Big) .\end{aligned} \tag{16.64}$$

16.2.3 Integration along the real axis: the limit of zero lifetime broadening

Deforming the contour C to the real axis such that the contributions from the Matsubara-poles vanish Eq. (16.64) trivially reduces to

$$\begin{aligned}\Sigma_{\mu\nu}(\mathbf{q},\varpi) = &\int_{-\infty}^{\infty} d\varepsilon\ f(\varepsilon)\ \Big\{\widetilde{\Sigma}_{\mu\nu}(\mathbf{q};\varepsilon+\hbar\omega+i\delta,\varepsilon+i0)\\ &-\widetilde{\Sigma}_{\mu\nu}(-\mathbf{q};\varepsilon+\hbar\omega+i\delta,\varepsilon-i0)\Big\}\\ &-\int_{-\infty}^{\infty} d\varepsilon\ f(\varepsilon)\ \Big\{\widetilde{\Sigma}_{\mu\nu}(\mathbf{q};\varepsilon-i0,\varepsilon-\hbar\omega-i\delta)\\ &-\widetilde{\Sigma}_{\mu\nu}(-\mathbf{q};\varepsilon+i0,\varepsilon-\hbar\omega-i\delta)\Big\}\quad ,\end{aligned} \tag{16.65}$$

or, by inserting the definition of $\widetilde{\Sigma}_{\mu\nu}(\mathbf{q};z_1,z_2)$ in Eqns. (16.61) - (16.63),

$$\begin{aligned}\Sigma_{\mu\nu}(\mathbf{q},\varpi) = -\frac{1}{2\pi V}\int_{-\infty}^{\infty} d\varepsilon\ f(\varepsilon)\Big\{ &Tr\left(\hat{J}_\mu(\mathbf{q})\hat{G}(\varepsilon+\hbar\omega+i\delta)\hat{J}_\nu(-\mathbf{q})\hat{G}^+(\varepsilon)\right)\\ &-Tr\left(\hat{J}_\mu(-\mathbf{q})\hat{G}(\varepsilon+\hbar\omega+i\delta)\hat{J}_\nu(\mathbf{q})\hat{G}^-(\varepsilon)\right)\\ &-Tr\left(\hat{J}_\mu(\mathbf{q})\hat{G}^-(\varepsilon)\hat{J}_\nu(-\mathbf{q})\hat{G}(\varepsilon-\hbar\omega-i\delta)\right)\\ &+Tr\left(\hat{J}_\mu(-\mathbf{q})\hat{G}^+(\varepsilon)\hat{J}_\nu(\mathbf{q})\hat{G}(\varepsilon-\hbar\omega-i\delta)\right)\Big\}\quad .\end{aligned} \tag{16.66}$$

Here $\hat{G}^+(\varepsilon)$ and $\hat{G}^-(\varepsilon)$ are the by-now-familiar up- and down-side limits of the resolvent

$$\hat{G}^\pm(\varepsilon) = \lim_{\theta\to+0}\hat{G}(\varepsilon\pm i\theta)\quad ,\quad \hat{G}^\pm(\varepsilon)^\dagger = \hat{G}^\mp(\varepsilon)\quad . \tag{16.67}$$

By taking the limit $\delta\to 0$, Eq. (16.66) reduces to

$$\begin{aligned}\Sigma_{\mu\nu}(\mathbf{q},\omega) = -\frac{1}{2\pi V}\int_{-\infty}^{\infty} d\varepsilon\ f(\varepsilon)\Big\{ &Tr\left(\hat{J}_\mu(\mathbf{q})\hat{G}^+(\varepsilon+\hbar\omega)\hat{J}_\nu(-\mathbf{q})\hat{G}^+(\varepsilon)\right)\\ &-Tr\left(\hat{J}_\mu(-\mathbf{q})\hat{G}^+(\varepsilon+\hbar\omega)\hat{J}_\nu(\mathbf{q})\hat{G}^-(\varepsilon)\right)\\ &-Tr\left(\hat{J}_\mu(\mathbf{q})\hat{G}^-(\varepsilon)\hat{J}_\nu(-\mathbf{q})\hat{G}^-(\varepsilon-\hbar\omega)\right)\\ &+Tr\left(\hat{J}_\mu(-\mathbf{q})\hat{G}^+(\varepsilon)\hat{J}_\nu(\mathbf{q})\hat{G}^-(\varepsilon-\hbar\omega)\right)\Big\}\quad ,\end{aligned} \tag{16.68}$$

which for $\mathbf{q} = 0$ yields

$$\Sigma_{\mu\nu}(\omega) = -\frac{1}{2\pi V}\int_{-\infty}^{\infty} d\varepsilon\, f(\varepsilon)\left\{ Tr\left(\hat{J}_\mu \hat{G}^+(\varepsilon+\hbar\omega)\hat{J}_\nu\left[\hat{G}^+(\varepsilon) - G^-(\varepsilon)\right]\right)\right.$$
$$\left. + Tr\left(\hat{J}_\mu\left[\hat{G}^+(\varepsilon) - G^-(\varepsilon)\right]\hat{J}_\nu \hat{G}^-(\varepsilon-\hbar\omega)\right)\right\} \quad . \tag{16.69}$$

16.3 Electric transport – the static limit

Making use of the analyticity of the Green's functions in the upper and lower complex semi-planes this then leads to the famous *Kubo-Luttinger formulation* [1, 7],

$$\sigma_{\mu\nu} = -\frac{\hbar}{2\pi V}\int_{-\infty}^{\infty} d\varepsilon\, f(\varepsilon) Tr\left(\hat{J}_\mu \frac{\partial \hat{G}^+(\varepsilon)}{\partial\varepsilon}\hat{J}_\nu\left[\hat{G}^+(\varepsilon) - \hat{G}^-(\varepsilon)\right]\right.$$
$$\left. - \hat{J}_\mu\left[\hat{G}^+(\varepsilon) - \hat{G}^-(\varepsilon)\right]\hat{J}_\nu \frac{\partial \hat{G}^-(\varepsilon)}{\partial\varepsilon}\right) \quad . \tag{16.70}$$

Integrating by parts yields

$$\sigma_{\mu\nu} = -\int_{-\infty}^{\infty} d\varepsilon \frac{df(\varepsilon)}{d\varepsilon} S_{\mu\nu}(\varepsilon) \tag{16.71}$$

with

$$S_{\mu\nu}(\varepsilon) = -\frac{\hbar}{2\pi V}\int_{-\infty}^{\varepsilon} d\varepsilon' Tr\left(\hat{J}_\mu \frac{\partial \hat{G}^+(\varepsilon')}{\partial\varepsilon'}\hat{J}_\nu\left[\hat{G}^+(\varepsilon') - \hat{G}^-(\varepsilon')\right]\right. \tag{16.72}$$
$$\left. - \hat{J}_\mu\left[\hat{G}^+(\varepsilon') - \hat{G}^-(\varepsilon')\right]\hat{J}_\nu \frac{\partial \hat{G}^-(\varepsilon')}{\partial\varepsilon'}\right) \quad ,$$

which has the meaning of a zero-temperature, energy-dependent conductivity.

For $T = 0$, $\sigma_{\mu\nu}$ is obviously given by

$$\sigma_{\mu\nu} = S_{\mu\nu}(E_F) \quad . \tag{16.73}$$

A numerically tractable expression can be obtained only for the diagonal elements of the conductivity tensor, the so-called *Kubo-Greenwood equation*

[8, 9] for the dc-conductivity at finite temperatures,

$$\sigma_{\mu\mu} = -\frac{\hbar}{4\pi V}\int_{-\infty}^{\infty} d\varepsilon \left(-\frac{df(\varepsilon)}{d\varepsilon}\right) Tr\left(\hat{J}_\mu\left[\hat{G}^+(\varepsilon) - \hat{G}^-(\varepsilon)\right] \times \hat{J}_\mu\left[\hat{G}^+(\varepsilon) - \hat{G}^-(\varepsilon)\right]\right) \quad , \tag{16.74}$$

which at $T = 0$ temperature obviously can be written as

$$\begin{aligned}\sigma_{\mu\mu} &= -\frac{\hbar}{4\pi V} Tr\left(\hat{J}_\mu\left[\hat{G}^+(E_F) - \hat{G}^-(E_F)\right]\hat{J}_\mu\left[\hat{G}^+(E_F) - \hat{G}^-(E_F)\right]\right) \\ &= \frac{\hbar}{\pi V} Tr\left(\hat{J}_\mu \operatorname{Im}\hat{G}^+(E_F)\hat{J}_\mu \operatorname{Im}\hat{G}^+(E_F)\right) \quad .\end{aligned} \tag{16.75}$$

Recalling finally the spectral resolution of the resolvent,

$$\operatorname{Im}\hat{G}^+(\varepsilon) = -\pi\sum_n |n\rangle\langle n|\,\delta(\varepsilon - \varepsilon_n) \quad , \tag{16.76}$$

it is easy to see that Eq. (16.75) is identical with the original *Greenwood equation* [8],

$$\sigma_{\mu\mu} = \frac{\pi\hbar}{V}\sum_{n,m} J_\mu^{nm}\, J_\mu^{mn}\,\delta(E_F - \varepsilon_n)\,\delta(E_F - \varepsilon_m) \quad . \tag{16.77}$$

16.4 The Kubo-Greenwood equation

Furthermore, for practical purposes Eq. (16.75) can be rewritten [9] as

$$\sigma_{\mu\mu} = \frac{1}{4}\left\{\widetilde{\sigma}_{\mu\mu}(\epsilon^+,\epsilon^+) + \widetilde{\sigma}_{\mu\mu}(\epsilon^-,\epsilon^-) - \widetilde{\sigma}_{\mu\mu}(\epsilon^+,\epsilon^-) - \widetilde{\sigma}_{\mu\mu}(\epsilon^-,\epsilon^+)\right\} \quad , \tag{16.78}$$

where $\epsilon^+ = \epsilon_F + i\delta,\ \epsilon^- = \epsilon_F - i\delta;\ \delta \to 0,$

$$\widetilde{\sigma}_{\mu\mu}(\epsilon_1,\epsilon_2) = -\frac{\hbar}{\pi N_0 \Omega_{at}} tr\ \langle J_\mu G(\epsilon_1) J_\mu G(\epsilon_2)\rangle \quad ; \quad \epsilon_i = \epsilon^\pm \quad ; \quad i = 1,2 \quad , \tag{16.79}$$

and $G(z)$ refers to the Green's function discussed at length in Chapter 4; see also Chapter 10.

16.4.1 Current matrices

Let $J_\mu^{i\alpha}(\epsilon_1,\epsilon_2)$ denote the angular momentum representation of the $\mu-$th component of the current operator according to component α of a binary substitutional alloy in a particular site i. Using a non-relativistic formulation for

the current operator, namely $\mathbf{J} = (e\hbar/im)\,\boldsymbol{\nabla}$, the elements of $J_{\mu}^{i\alpha}(\epsilon_1, \epsilon_2)$ are given by

$$J^{i\alpha}_{\mu,\Lambda\Lambda'}(\epsilon_1,\epsilon_2) = \frac{e}{m}\frac{\hbar}{i}\int\limits_{WS} Z^{i\alpha}_{\Lambda}(\mathbf{r}_i,\epsilon_1)^{\dagger}\frac{\partial}{\partial r_{i,\mu}} Z^{i\alpha}_{\Lambda'}(\mathbf{r}_i,\epsilon_2) d^3 r_i \quad , \quad \Lambda = (\ell m) \quad , \tag{16.80}$$

while within a relativistic formulation for the current operator, namely $\mathbf{J} = ec\boldsymbol{\alpha}$, one gets

$$J^{i\alpha}_{\mu,\Lambda\Lambda'}(\epsilon_1,\epsilon_2) = ec\int\limits_{WS} Z^{i\alpha}_{\Lambda}(\mathbf{r}_i,\epsilon_1)^{\dagger}\alpha_{\mu} Z^{i\alpha}_{\Lambda'}(\mathbf{r}_i,\epsilon_2) d^3 r_i \quad , \quad \Lambda = (\kappa\mu) \quad . \tag{16.81}$$

In Eqns. (16.80) and (16.81) the functions $Z^{i\alpha}_{\Lambda}(\mathbf{r}_i, z)$ are the usual (regular) scattering solutions as introduced in Chapter 4.

16.4.2 Conductivity in real space for a finite number of scatterers

If no translational symmetry at all is present then in principle one has to sum over all sites in the system including leads, contacts, etc.; i.e., a typical contribution in Eq. (16.79) to the conductivity is given by

$$\widetilde{\sigma}_{\mu\mu}(\mathcal{C};\epsilon_1,\epsilon_2) = \sum_{i,j=1}^{N_0} \widetilde{\sigma}^{ij}_{\mu\mu}(\mathcal{C};\epsilon_1,\epsilon_2) \quad , \tag{16.82}$$

$$\widetilde{\sigma}^{ij}_{\mu\mu}(\mathcal{C};\epsilon_1,\epsilon_2) = (w/N_0)tr\left\langle J^i_{\mu}(\epsilon_2,\epsilon_1)\tau^{ij}(\epsilon_1)J^j_{\mu}(\epsilon_1,\epsilon_2)\tau^{ji}(\epsilon_2)\right\rangle \quad , \tag{16.83}$$

where $\mathcal{C}$ specifies the magnetic configuration and $w = -\,(4m^2/\hbar^3\pi\Omega_{at})$, N_0 is the total number of scattering sites in the system, i.e., is of the order of 10^{23} and the $\tau^{ij}(\epsilon)$refer to the scattering path operator; see Chapter 4. As this is numerically not possible, one can define the following quantity

$$\widetilde{\sigma}_{\mu\mu}(\mathcal{C};\epsilon_1,\epsilon_2;n) = \sum_{i,j=1}^{n} \widetilde{\sigma}^{ij}_{\mu\mu}(\mathcal{C};\epsilon_1,\epsilon_2) \quad , \tag{16.84}$$

with n being the number of sites in a chosen region ("cluster"). This implies, however, that the convergence properties of $\widetilde{\sigma}_{\mu\mu}(\epsilon_1,\epsilon_2;n)$ with respect to n have to be investigated; i.e., once again the question of a characteristic volume becomes crucially important.

It should be recalled that in the absence of any translational symmetry in order to specify the magnetic configuration $\mathcal{C}$ the orientations of the magnetization in all sites of the chosen region have to be given.

16.4.3 Two-dimensional translational symmetry

Assuming that (one and the same) two-dimensional invariance applies in all layers under consideration, for a particular magnetic configuration $\mathcal{C}$, a typical contribution $\widetilde{\sigma}_{\mu\mu}(\mathcal{C};\epsilon_1,\epsilon_2)$ reduces to a double sum over all atomic layers (n) that have to be incorporated,

$$\widetilde{\sigma}_{\mu\mu}(\mathcal{C};\epsilon_1,\epsilon_2;n) = \sum_{p,q=1}^{n} \widetilde{\sigma}^{pq}_{\mu\mu}(\mathcal{C};\epsilon_1,\epsilon_2;n) \quad , \tag{16.85}$$

$$\widetilde{\sigma}^{pq}_{\mu\mu}(\mathcal{C};\epsilon_1,\epsilon_2;n) = w \left\{ \sum_{j\in I(\mathcal{L}^{(2)})} tr \left\langle J^{p0}_{\mu}(\epsilon_2,\epsilon_1)\tau^{p0,qj}(\epsilon_1) J^{qj}_{\mu}(\epsilon_1,\epsilon_2)\tau^{qj,p0}(\epsilon_2)\right\rangle \right\} \tag{16.86}$$

where $p0$ specifies the origin of the two-dimensional lattice $\mathcal{L}^{(2)}$ in the p-th layer and $I(\mathcal{L}^{(2)})$ simply refers to the set of indices corresponding to $\mathcal{L}^{(2)}$. The lattice sum in Eq. (16.86) can then be evaluated in terms of a two-dimensional lattice Fourier transformation. This implies, however, as already said, that in all atomic layers (including the substrate layers) *one and the same* two-dimensional translational invariance applies.

16.4.4 Vertex corrections

In the case of interdiffused interfaces, spacers, or substitutionally disordered alloys serving as leads, configurational averages have to be performed. Consider a typical contribution in Eq. (16.86). In principle the configurational average over the occurring products can be formulated as a product of averages

$$\begin{aligned} &\left\langle J^{p0}_{\mu}(\epsilon_2,\epsilon_1)\tau^{p0,qj}(\epsilon_1) J^{qj}_{\mu}(\epsilon_1,\epsilon_2)\tau^{qj,p0}(\epsilon_2)\right\rangle \\ &= \left\langle J^{p0}_{\mu}(\epsilon_2,\epsilon_1)\tau^{p0,qj}(\epsilon_1)\right\rangle (1-\Omega) \left\langle J^{qj}_{\mu}(\epsilon_1,\epsilon_2)\tau^{qj,p0}(\epsilon_2)\right\rangle \quad . \end{aligned} \tag{16.87}$$

Omitting the so-called vertex corrections Ω, i.e., in using $\Omega = 0$, one gets

$$\begin{aligned} &\left\langle J^{p0}_{\mu}(\epsilon_2,\epsilon_1)\tau^{p0,qj}(\epsilon_1) J^{qj}_{\mu}(\epsilon_1,\epsilon_2)\tau^{qj,p0}(\epsilon_2)\right\rangle \\ &= J^{p0}_{\mu}(\epsilon_2,\epsilon_1) \left\langle \tau^{p0,qj}(\epsilon_1)\right\rangle J^{qj}_{\mu}(\epsilon_1,\epsilon_2) \left\langle \tau^{qj,p0}(\epsilon_2)\right\rangle \quad , \end{aligned} \tag{16.88}$$

since due to two-dimensional translational invariance

$$\left\langle J^{p0}_{\mu}(\epsilon_2,\epsilon_1)\right\rangle = J^{p0}_{\mu}(\epsilon_2,\epsilon_1) \quad . \tag{16.89}$$

In order to average expressions of the type $\left\langle \tau^{pi,qj}(\epsilon)\right\rangle$ usually the Coherent Potential Approximation (CPA) introduced earlier in Chapter 5 is applied. One then obtains for the layer-diagonal terms

$$\widetilde{\sigma}^{pp}_{\mu\mu}(\epsilon_1,\epsilon_2) = w \sum_{\alpha=A,B} c_p^{\alpha} \left\{ tr\left[\widetilde{J}^{p\alpha}_{\mu}(\epsilon_2,\epsilon_1)\tau_c^{pp}(\epsilon_1) J^{p\alpha}_{\mu}(\epsilon_1,\epsilon_2)\tau_c^{pp}(\epsilon_2)\right] - \sum_{\beta=A,B} c_p^{\beta} tr\left[\widetilde{J}^{p\alpha}_{\mu}(\epsilon_2,\epsilon_1)\tau_c^{pp}(\epsilon_1)\widetilde{J}^{p\beta}_{\mu}(\epsilon_1,\epsilon_2)\tau_c^{pp}(\epsilon_2)\right]\right\} \quad , \tag{16.90}$$

while the layer-off-diagonal terms are given by

$$\widetilde{\sigma}^{pq}_{\mu\mu}(\epsilon_1,\epsilon_2) = (w/n\Omega_{SBZ}) \times \sum_{\alpha,\beta=A,B} c_p^{\alpha} c_q^{\beta} tr\left[\int \widetilde{J}^{p\alpha}_{\mu}(\epsilon_2,\epsilon_1)\tau_c^{pq}(\mathbf{k},\epsilon_1)\widetilde{J}^{q\beta}_{\mu}(\epsilon_1,\epsilon_2)\tau_c^{qp}(\mathbf{k},\epsilon_2) d^2k\right] \quad , \tag{16.91}$$

$$\widetilde{J}^{p\alpha}_{\mu}(\epsilon_2,\epsilon_1) = D^{pp}_{\alpha}(\epsilon_2)^t J^{p\alpha}_{\mu}(\epsilon_2,\epsilon_1) D^{pp}_{\alpha}(\epsilon_1) \quad , \tag{16.92}$$

where the matrices $D^{pp}_{\alpha}(\epsilon_i)$ are defined in Chapter 5 and the symbol t indicates a transposed matrix. Note that in Eq. (16.92) use has been made of a two-dimensional lattice Fourier transformation: Ω_{SBZ} is the unit area ("volume") in the surface Brillouin zone.

16.4.5 Boundary conditions

Although the summation within the layers is now exact, the convergence properties with respect to n, the number of layers, still have to be considered. In viewing n as a parameter the conductivity tensor elements for a layered system are then given by

$$\sigma_{\mu\mu}(\mathcal{C};n) = \frac{1}{n}\sum_{p,q=1}^{n} \sigma^{pq}_{\mu\mu}(\mathcal{C};n) \quad , \tag{16.93}$$

$$\sigma^{pq}_{\mu\mu}(\mathcal{C};n) = \frac{1}{4}\sum_{i,j=1}^{2} (-1)^{i+j} \widetilde{\sigma}^{pq}_{\mu\mu}(\mathcal{C};\epsilon_i,\epsilon_j;n) \quad . \tag{16.94}$$

For illustrative purposes the double sum in Eq. (16.93) can be rewritten as

$$\sigma_{\mu\mu}(\mathcal{C};n) = \frac{1}{n}\sum_{p=1}^{n} \sigma^{p}_{\mu\mu}(\mathcal{C};n) \quad ,$$

$$\sigma^{p}_{\mu\mu}(\mathcal{C};n) = \sum_{q=1}^{n} \sigma^{pq}_{\mu\mu}(\mathcal{C};n) \quad , \tag{16.95}$$

such that the $\sigma^{p}_{\mu\mu}(\mathcal{C};n)$ can be regarded as layer-resolved conductivities.

A beautiful example for the importance of boundary conditions is to be found in Fig. 16.2, considering the multilayer system $Co_{12}Cu_{12}Co_{12}$ as a free

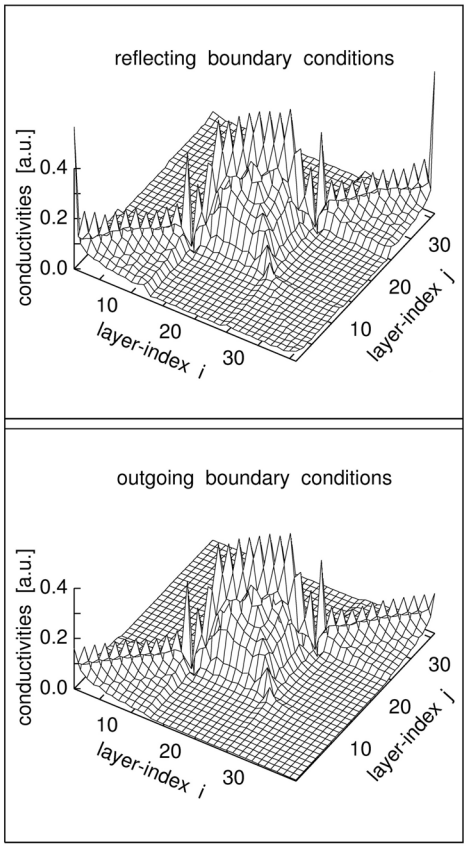

FIGURE 16.2: *Layer-resolved contributions* σ_{xx}^{ij} *to the CIP conductivity corresponding to an imaginary part of the Fermi energy of* δ*=2 mRyd for the parallel configuration of a model spin-valve structure with (top) reflecting (Vacuum / Co*$_{12}$ *Cu*$_{12}$ *Co*$_{12}$ */ Vacuum; open squares) and (bottom) outgoing (Co(100) / Co*$_{12}$ *Cu*$_{12}$ *Co*$_{12}$ */ Co(100); full circles) boundary conditions. From Ref. [10].*

standing film (reflecting boundary conditions) and with Co leads (outgoing boundary conditions). In both cases the main contributions to the in-plane (CIP) conductivity tensor element σ_{xx} is due to the Cu spacer. In the case of reflecting boundary conditions the contributions from the Cu layers next to the vacuum barrier suddenly increase, while for outgoing boundary conditions only the contributions due to the imaginary part of the Fermi energy are repeated (the peaks for outer Co layers). It is surprising to find out from this figure that viewed from a particular site contributions from sites farther off than about 15 atomic layers seem to be of little importance for the sum over all layers.

16.5 Optical transport

In the case of finite frequencies, i.e., in the case of optical transport, one only has to return to Eqns. (16.61) - (16.64), for a definition of the optical conductivity tensor, repeated for matter of convenience below

$$\begin{aligned}\Sigma_{\mu\nu}(\mathbf{q},\varpi) = & \oint_C dz\, f(z)\, \widetilde{\Sigma}_{\mu\nu}(\mathbf{q}; z+\hbar\omega+i\delta, z) \\ & - \left(\oint_C dz\, f(z)\, \widetilde{\Sigma}_{\mu\nu}(-\mathbf{q}; z-\hbar\omega+i\delta, z) \right)^* \\ -2i\delta_T & \sum_{k=-N_2+1}^{N_1} \Big(\widetilde{\Sigma}_{\mu\nu}(\mathbf{q}; z_k+\hbar\omega+i\delta, z_k) \\ & + \widetilde{\Sigma}_{\mu\nu}(-\mathbf{q}; z_k-\hbar\omega+i\delta, z_k)^* \Big) \quad ,\end{aligned}$$

$$\widetilde{\Sigma}_{\mu\nu}(\mathbf{q}; z_1, z_2) = -\frac{1}{2\pi V} Tr\left(\hat{J}_\mu(\mathbf{q}) \hat{G}(z_1) \hat{J}_\nu(-\mathbf{q}) \hat{G}(z_2) \right) \quad ,$$

$$\varpi = \omega + i\delta \quad ,$$

in which $\vec{q} = 0$ can be chosen, since in the visible regime the leading interaction is the electric dipole one. In using, as before in the case of electric transport, Green's functions and multiple scattering, in principle a double sum over all sites has to be performed,

$$\Sigma_{\mu\nu}(\varpi) = \sum_{i,j=1}^{n} \Sigma_{\mu\nu}^{ij}(\varpi) \quad , \tag{16.96}$$

or, provided that two-dimensional translational symmetry applies, by making use of two-dimensional lattice Fourier transformations, a double sum over

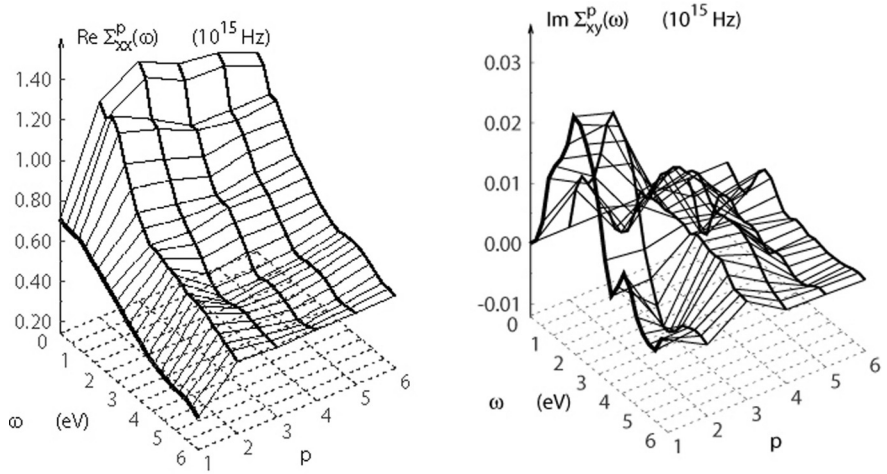

FIGURE 16.3: *Absorptive parts of the layer–resolved complex optical conductivity* $\Sigma^p_{\mu\nu}(\omega)$ *for fcc(111)–*$Co\,|\,Pt_5$ *as a function of the optical frequency* ω *and the layer index* p*. Heavy line marks the Co–layer resolved optical conductivity* $\Sigma^{p=1}_{\mu\nu}(\omega)$*. From Ref. [11].*

(atomic) layers

$$\Sigma_{\mu\nu}(\varpi) = \sum_{p,q=1}^{n} \Sigma^{pq}_{\mu\nu}(\varpi) \quad . \tag{16.97}$$

For reasons that will be become clear in Chapter 18 it is useful to define again layer-resolved quantities

$$\Sigma^p_{\mu\nu}(\varpi) = \sum_{p,q=1}^{n} \Sigma^{pq}_{\mu\nu}(\varpi) \quad , \quad \Sigma_{\mu\nu}(\varpi) = \sum_{p=1}^{n} \Sigma^p_{\mu\nu}(\varpi) \quad . \tag{16.98}$$

In Fig. 16.3 an example for layer-resolved optical conductivities is shown, namely for fcc(111)–Co/Pt_5 as a function of the optical frequency ω and the layer index p.

A discussion of boundary conditions with respect to the number of atomic layers to be included will be given in Chapter 18 in the context of the magneto-optical Kerr effect. It should be noted in particular that in the case of finite frequencies the off-diagonal elements of the conductivity tensor are well-defined and can of course be calculated.

[1] R. Kubo, M. Toda, N. Hashitsume, *Statistical Physics II: Non-equilibrium Statistical Mechanics*, Springer, Berlin (1985); R. Kubo, J. Phys. Soc. Jpn. **12**, 570 (1957).

[2] A. Vernes and P. Weinberger, Phys. Rev. **B 71**, 165108 (2005).

[3] K. Palotas, B. Lazarovits, L. Szunyogh and P. Weinberger, *Electric properties of nanostructures, Handbook of Theoretical and Computational Nanotechnology*, Edited by M. Rieth and W. Schommers, Volume 10, Chapter 6, Pages (363-408), American Scientific Publishers, Los Angeles, 2006.

[4] P. Weinberger, P. M. Levy, J. Banhart, L. Szunyogh and B. Úfalussy, J. Phys. Cond. Matt. **8**, 7677 (1996).

[5] L. Szunyogh and P. Weinberger, J. Phys. Cond. Matt. **11**, 10451 (1999).

[6] P. Weinberger, Physics Reports **377**, 281 (2003).

[7] J. M. Luttinger, in *Mathematical Methods in Solid State and Superfluid Theory* (Oliver and Boyd, Edinburgh) Chap. 4, pp. 157 (1962).

[8] D. A. Greenwood, Proc. Phys. Soc. London **71**, 585 (1958).

[9] W. H. Butler, Phys. Rev. B **31**, 3260 (1985).

[10] C. Blaas, L. Szunyogh, P. Weinberger, C. Sommers, P. M. Levy, and J. Shi, Phys. Rev. B **65**, 134427 (2002).

[11] A. Vernes, L. Szunyogh, and P. Weinberger, J. Phys. Condens. Matter **13**, 1529 (2001).

17

Electric properties of magnetic nanostructured matter

At least for the time being electric properties of magnetic nanostructures are probably the most important outcome of nanoscience, creating even a new field of research, usually termed now "spintronics" or "nanoelectronics". This chapter comprises not only characteristic aspects of current-in-plane (CIP) and current-perpendicular to the planes of atoms (CPP) electric transport, of the giant magnetoresistance (GMR) and the tunnelling magnetoresistance (TMR), but also of nanocontacts and domain wall resistivities.

All discussions in this chapter are based on the use of the fully relativistic version of the Kubo-Greenwood equation, see Chapter 16,

$$\boxed{\sigma_{\mu\mu} = \frac{\hbar}{\pi V} Tr\left(\hat{J}_\mu \,\mathrm{Im}\,\hat{G}^+(E_F)\hat{J}_\mu \,\mathrm{Im}\,\hat{G}^+(E_F)\right)} \tag{17.1}$$

$\hat{J}_\mu$ being the μ-th component of the current operator, $\mu \in (x, y, z)$, V the characteristic volume, and $\hat{G}^+(E_F)$ referring to the positive side-limit of the resolvent of a single particle (Kohn-Sham) Dirac Hamiltonian.

17.1 The bulk anisotropic magnetoresistance (AMR)

Although not directly a nano-related quantity the so-called anisotropic magnetoresistance (AMR) in bulk magnetic alloys is an important anisotropy effect, well suited to demonstrate and check the realization of the Kubo-Greenwood equation in terms of fully relativistic multiple scattering theory. This is in particular valid, since it is quite well known by now that in disordered magnetic alloys the non-relativistic two-spin current model, in which each "spin channel" is treated independently, fails. Considering for example statistically disordered fcc $Ni_{1-c}Fe_c(001)$, $c \leq 0.5$, as a layered system of the type $Ni_{1-c}Fe_c(001)/(Ni_{1-c}Fe_c)_n/Ni_{1-c}Fe_c(001)$ and using a complex Fermi energy,

$E_F = \epsilon_F + i\delta$, the resistivity for a particular magnetic configuration C is given by the following limiting procedure, which, as will be demonstrated further on, can be used as a valuable computational tool,

$$\rho_{\mu\mu}(C;c) = \lim_{\delta\to 0} \rho_{\mu\mu}(C;c,\delta) \quad , \quad \mu \in (x,y,z) \quad , \tag{17.2}$$
$$\rho_{\mu\mu}(C;c,\delta) = \sum_{i,j=1}^{n} \rho_{\mu\mu}^{ij}(C;c,\delta) \quad ,$$

since it turns out that $\rho_{\mu\mu}(C;c,\delta)$ is linear in δ. The so-called *residual resistivity* is therefore given as the analytical continuation of $\rho_{\mu\mu}(C;c,\delta)$ to the real axis. In Fig. 17.1 such a continuation is shown for the case of $Ni_{80}Fe_{20}$. Adopting for a moment the more traditional notation,

$$\rho_{av}(c) = 1/3(\rho_{\parallel}(c) + 2\rho_{\perp}(c)) \; , \quad \rho_{\parallel}(c) = \rho_{zz}(\hat{z};c) \quad , \quad \rho_{\perp}(c) = \rho_{zz}(\hat{x};c) \quad , \tag{17.3}$$

the AMR ratio of bulk alloys is usually defined as

$$\frac{\Delta\rho(c)}{\rho_{av}(c)} = \frac{\rho_{\parallel}(c) - \rho_{\perp}(c)}{\rho_{av}(c)} \quad . \tag{17.4}$$

The theoretical resistivities and the corresponding AMR ratios are displayed in Fig. 17.2 for the fcc regime of $Ni_{1-c}Fe_c(001)$ and compared to available experimental low temperature values. As can be seen the AMR ratios fit rather well the corresponding experimental data. The experimental data, by the way, are defined as an extrapolation of the measured results to zero applied magnetic field. It should be noted in particular that experimental "bulk resistivities" are in principle fictitious quantities, since they are usually determined by growing films of the same material as the substrate and performing measurements at different film thicknesses. So-called bulk values correspond to an extrapolation of the obtained values for infinite thickness.

It will turn out later that the concept of anisotropic magnetoresistances will be important once again when considering the electric properties of domain walls.

17.2 Current-in-plane (CIP) & the giant magnetoresistance (GMR)

The so-called giant magnetoresistance effect (GMR) not only revolutionized the computer and storage media industry, but also its discovery was (finally) awarded with the top academic honors, namely the Nobel Prize in Physics in 2007 to Albert Fert and Peter Grünberg. Although today GMR switches

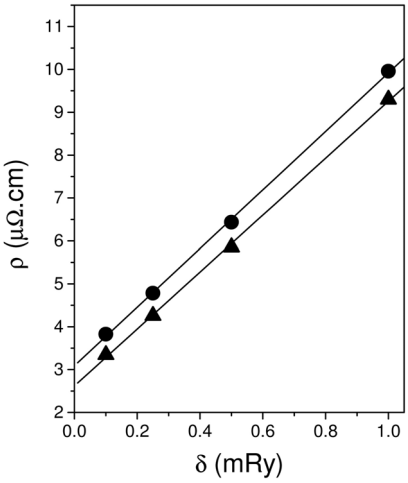

FIGURE 17.1: *Calculated resistivities $\rho_{zz}(C;\delta)$ of $Ni_{80}Fe_{20}$ with with respect to the imaginary part of the Fermi energy δ. Circles and triangles refer to the cases when the current is perpendicular or parallel to the direction of the magnetization, pointing either uniformly along the in-plane $\hat{x}$ axis or along the surface normal $\hat{z}$. Solid lines correspond to a least square fit to the data. The residual resistivity is defined by the interception of respective lines with the ordinate. From Ref. [1].*

are rather complicated systems nanostructured in one dimension, see, e.g., Fig. 1.3, and consist of different magnetic, spacer and capping materials, there are a few typical effects that characterize the electric properties of such devices.

17.2.1 Leads

When dealing with the electric properties of magnetic multilayer systems, of course not only the problem of interdiffusion at the interfaces has to be tackled, but also the question of an appropriate choice of leads has to be addressed, since the leads (semi-infinite systems) serve as electron reservoirs, i.e., provide the Fermi energy.

As reported in Ref. [6] for a carefully grown $Au_{20}Fe_{10}Au_7Fe_{28}$ multilayer on GaAs(100) not only the temperature dependence of the GMR but also the conductivities in the parallel and the antiparallel alignment were investigated experimentally using Au leads; see the left half of Fig. 17.3. In the corresponding simultaneous theoretical study of the following quantities

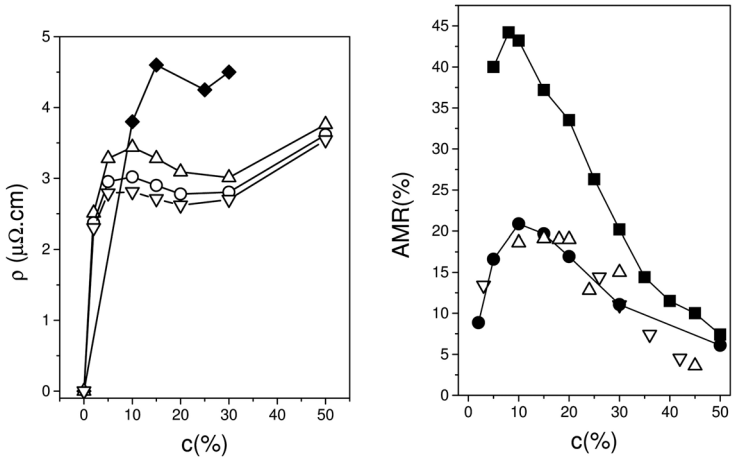

FIGURE 17.2: *Left: Calculated (open symbols) and experimental (diamonds) residual resistivities of $Ni_{1-c}Fe_c$ alloys with respect to the concentration c. For the definitions of $\rho_{\parallel} = \rho_{zz}(c;\hat{z})$ (up-triangles) $\rho_{\perp} = \rho_{zz}(c;\hat{x})$ (down-triangles) and $\rho_{\rm av} = 1/3(\rho_{\parallel}(c) + 2\rho_{\perp}(c))$ (circles), see Eq. (17.3). Right: Calculated and experimental AMR ratios of $Ni_{1-c}Fe_c$ alloys. Full circles: calculations of [1], full squares: calculations of Ref.[2], up-triangles: experiment [3], down-triangles: experiment [4, 5]. From Ref. [1].*

$$\rho_{xx}(P) = \lim_{\delta\to 0}\rho_{xx}(P;\delta) \quad , \quad \lim_{\delta\to 0}\rho_{xx}(AP) = \rho_{xx}(AP;\delta) \quad , \tag{17.5}$$

$$GMR = \frac{\rho_{xx}(AP) - \rho_{xx}(P)}{\rho_{xx}(AP)} \quad , \tag{17.6}$$

P (AP) denoting a parallel (antiparallel) alignment of the magnetic slabs, it was additionally assumed that in this system the electric contacts could have been placed in the Fe or the Au layers; i.e., Fe leads as well as Au leads were considered. Furthermore, a two-monolayer interdiffusion at the Fe/Au interfaces was considered in order to study the dependence of the GMR with respect to disorder; see Table 17.1. In particular from Eq. (17.6) it is obvious that it is very important that not only GMR values are recorded (or theoretically evaluated) but also the corresponding individual resistivities, since the GMR value is independent of a uniform arbitrary scaling factor for $\rho_{xx}(AP)$ and $\rho_{xx}(P)$.

As can be seen from the right part of Fig. 17.3 it does indeed make quite a big difference what kind of leads are used. For system C, see Table 17.1, which in fact corresponded to the experimental set-up, namely to the use

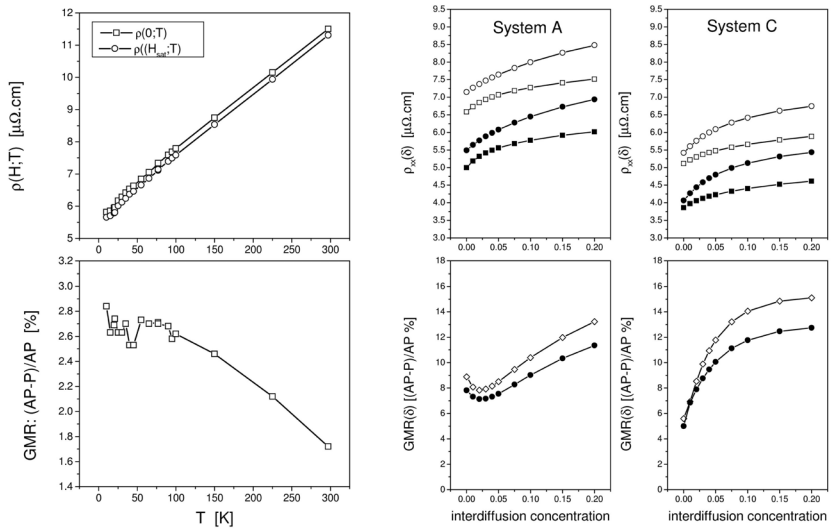

FIGURE 17.3: *Left: Experimental field- and temperature-dependent resistivities (top) and temperature-dependent giant magnetoresistance (bottom) in Fe/Au/Fe multilayers. Right: calculated CIP-resistivity and GMR. Squares refer to the parallel aligment, circles to the antiparallel aligment. For systems A and C full symbols apply, for system B open symbols, see also Table 17.1. From Ref. [6].*

of Au contacts, not only the calculated GMR ratio fitted very well indeed to the experimental data, but also the involved in-plane (CIP) resistivities. Although the experimental characterization of the Fe/Au multilayer did not show any traces of interdiffusion effects at the interfaces, it was the theoretical investigations that in the end seemed to prove the quality of the grown interfaces. As can be seen from Fig. 17.3, for system A as well as for system C the resistivities do increase with increasing interdiffusion, creating in this particular circumstance increased GMR values.

Even more striking are the differences between cases B and C when displaying the difference between the parallel (P) and the antiparallel (AP) conductivities in a layer-resolved manner:

$$\begin{aligned}\Delta^i_{xx}(\delta) &= \rho^i_{xx}(P;\delta) - \rho^i_{xx}(AP;\delta) \\ &= \sum_{j=1}^{n} \left(\rho^{ij}_{xx}(P;\delta) - \rho^{ij}_{xx}(AP;\delta)\right) \quad , \end{aligned} \tag{17.7}$$

where i and j denote atomic planes. It has to be remembered that of course

Table 17.1: Fe/Au multilayer systems with different leads. From Ref. [6].

system A	system B	system C
2 ML inter-diffusion at two Fe/Au interfaces	2 ML inter-diffusion at all Fe/Au interfaces	2 ML inter-diffusion at all Fe/Au interfaces
bcc-Fe(100)	bcc-Fe(100)	fcc-Au(100)
Fe_{11}	Fe_{11}	Au_5
$[Fe_cAu_{1-c}]$	$[Fe_cAu_{1-c}]$	$[Au_cFe_{1-c}]$
$[Au_cFe_{1-c}]$	$[Au_cFe_{1-c}]$	$[Fe_cAu_{1-c}]$
Au_5	Au_5	Fe_8
$[Au_cFe_{1-c}]$	$[Au_cFe_{1-c}]$	$[Fe_cAu_{1-c}]$
$[Fe_cAu_{1-c}]$	$[Au_cFe_{1-c}]$	$[Au_cFe_{1-c}]$
Fe_9	Fe_8	Au_5
Au_5	$[Fe_cAu_{1-c}]$	$[Au_cFe_{1-c}]$
vac	$[Au_cFe_{1-c}]$	$[Fe_cAu_{1-c}]$
	Au_4	Fe_{10}
	vac	vac

in principle only the total sum,

$$\Delta_{xx}(\delta) = \sum_{i=1}^{n} \Delta_{xx}^{i}(\delta) \quad , \quad \Delta_{xx} = \lim_{\delta \to 0} \Delta_{xx}(\delta) \quad , \tag{17.8}$$

is well defined. From Fig. 17.4 one easily can see that Δ_{xx} is of completely different origin in systems B and C. While for a Fe/Au multilayer with Fe leads (system B) most contributions come from the Au spacer, in using Au leads the two Fe slabs contribute most to Δ_{xx}.

17.2.2 Rotational properties

As is well-known a function $f(\Theta)$ can be fitted very accurately by means of the following expansion in powers of $\cos(\Theta)$, often used also for characterizing the magnetic anisotropy energy,

$$f(\Theta) = f(0) + \sum_{m=1}^{\infty} a_m \left(1 - \cos^m \Theta\right) \quad , \tag{17.9}$$

where the first two fitting coefficients can be approximated to first order by

$$a_1 = \frac{1}{2}\left[f(\pi) - f(0)\right] \quad , \tag{17.10}$$

$$a_2 = f(\frac{\pi}{2}) - \frac{1}{2}\left[f(\pi) + f(0)\right] \quad . \tag{17.11}$$

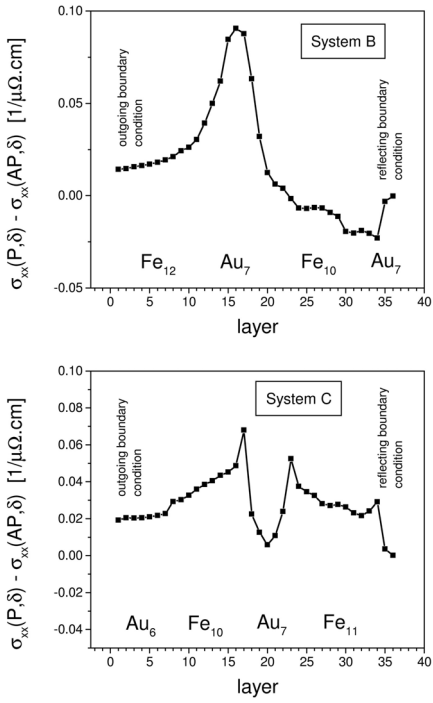

FIGURE 17.4: *Layer-resolved difference of conductivities, see Eq. (17.7), corresponding to an imaginary part of the Fermi energy of 2 mryd and an interdiffusion concentration of* $c = 0.05$. *From Ref. [6].*

In Fig. 17.5 an interesting comparison between the twisting energy $\Delta E(\Theta; n)$ and the magnetoresistance ratio $GMR(\Theta; n)$,

$$\Delta E(\Theta; n) = E(\Theta; n) - E(0; n) \quad , \tag{17.12}$$

$$GMR(\Theta; n) = \frac{\rho_{xx}(\Theta; n) - \rho_{xx}(0; n)}{\rho_{xx}(\Theta; n)} \quad , \tag{17.13}$$

expanded up to second order using the above expansion, can be found for the $Co/Cu_n/Co$ spin valve listed in Table 17.2.

As can be seen these two coefficients characterize impressively the importance of anisotropy effects. For 6 Cu spacer layers the interlayer coupling energy is very close to a node (with respect to the number of spacer layers); the anisotropy term, i.e., coefficient a_2, in the twisting energy is therefore by

Table 17.2: *Cu/Co spin valve with interdiffused magnetic slabs. From Ref. [7].*

Cu(100)	lead
Cu_3	buffer
$Cu_{0.9}Co_{0.1}$ $Cu_{0.2}Co_{0.8}$ $Cu_{0.9}Co_{0.1}$	magnetic slab
Cu_6	spacer
$Cu_{0.9}Co_{0.1}$ $Cu_{0.2}Co_{0.8}$ $Cu_{0.9}Co_{0.1}$	magnetic slab
Cu_3	buffer
Cu(100)	lead

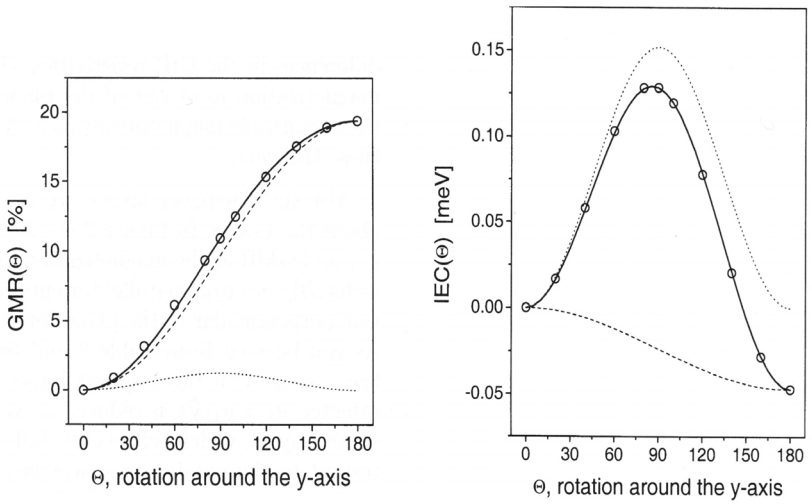

FIGURE 17.5: *Left: MR ratio, $GMR(\Theta; n)$. Right: Twisting energy (denoted as $IEC(\Theta)$)* for the system listed in Table 17.2. *The magnetization is rotated around the y-axis (out of the plane of the layers). Circles represent calculated values, solid lines are the result of a two term fit according to Eqs. (17.10) - (17.11), dashed and dotted lines display the first and second term, respectively. From Ref. [7].*

far the leading one, whereas for the corresponding resistances and the magnetoresistance ratio the contributions from the second coefficient are minute. This indicates very clearly, that although in this particular case the twisting energy is governed mostly by anisotropy effects, for the magnetoresistance ratio these effects are rather unimportant. The system shown in Fig. 17.5 is again a nice example for a perfect switch, since after turning off the external magnetic field, due to the anisotropy energy the system remains in the switched state.

By the way, a similar behavior as shown in the left part of Fig. 17.5 was found in quite a few other cases and seems to indicate that for current-in-plane geometries the GMR changes essentially proportional to $(1 - \cos\Theta)$, which in fact confirms the usual experience made in experimental or technological studies.

17.3 Current-perpendicular to the planes of atoms (CPP)

17.3.1 Sheet resistances

As the current is independent of z in the steady state one can write the CPP resistivity within the Kubo approach as [8, 9, 10]

$$\rho_{CPP} = \frac{1}{L}\int\int \rho(z,z')dzdz' \quad , \tag{17.14}$$

where $\rho(z,z')$ is the inverse of $\sigma(z,z')$,

$$\int \sigma(z,z'')\rho(z'',z')dz'' = \delta(z-z') \quad , \tag{17.15}$$

and L is the distance between the two contacts used to measure the resistivity. The sheet resistance r and resistance R are then defined by the following relations

$$r = AR = L\rho_{CPP} = \int\int \rho(z,z')dzdz' \quad , \tag{17.16}$$

with A being the unit area.

In the following the conductivity tensor $\sigma(z,z')$ as defined in terms of Eq. (17.15) is mapped ($f:$) onto the (zz-components of the) conductivity tensor for a layered system, $\sigma_{ij}(n), i,j = 1,n$, with i and j denoting planes of atoms,

$$\boxed{f : \sigma(z,z''), \rho(z'',z') \rightarrow \sigma_{ij}(n), \rho_{ij}(n)} \tag{17.17}$$

such that the algebraic structure as defined by Eq. (17.15), namely

$$\sum_{k=1}^{N} \sigma_{ik}(n)\rho_{kj}(n) = \delta_{ij} \quad , \tag{17.18}$$

is conserved. Clearly enough the sheet resistance r then serves as measure $(g:)$

$$\boxed{g : r \to r(n)} \tag{17.19}$$

$$r(n) = \sum_{i,j=1}^{N} \rho_{ij}(n) \quad , \tag{17.20}$$

for the mapping f, since according to the Cauchy convergence criterion the integral in Eq. (17.16) can be replaced by a sum, i.e., by $r(n)$, if and only if,

$$\left| r - \lim_{n\to\infty} r(n) \right| < \Delta \quad , n \in \mathbb{N}^+ \quad , \tag{17.21}$$

or

$$|r(n+m) - r(n)| < \Delta; \qquad n, m \in \mathbb{N}^+ \quad , \tag{17.22}$$

where Δ is an infinitesimal small number.

Using again complex Fermi energies, $E_F = \epsilon_F + i\delta$, the sheet resistance for a given magnetic configuration $\mathcal{C}$ is then defined by

$$r(C;n) = \lim_{\delta\to 0} r(C;n;\delta) \quad , \tag{17.23}$$

where

$$r(C;n;\delta) = \sum_{i,j=1}^{n} \rho_{ij}(C;n;\delta) \quad . \tag{17.24}$$

In addition to this sheet resistance, layer-resolved sheet resistances $r_i(\mathcal{C};n)$ can be defined

$$r_i(\mathcal{C};n;\delta) = \sum_{j=1}^{n} \rho_{ij}(\mathcal{C};n;\delta) \quad , \tag{17.25}$$

which relate the electric field in layer i qualitatively to the steady state current (CPP) which is independent of the layer index j . It should be noted, however, that only $r(C;n;\delta)$ in Eq. (17.24) is well-defined. Similar as in the case of the in-plane elements of the resistivity (conductivity) tensor, see Fig. 17.4, these layer-resolved sheet resistances are useful illustrative quantities in pursuing the question from which part of a layered system the main contributions to the sheet resistance of a given magnetic configuration arise.

17.3.2 Properties of the leads

Consider for matters of simplicity bcc Fe as a layered system, namely to be of the form bcc Fe(100)/Fe_n/Fe(100). In principle, for a large enough n $(n \geq n_0)$ because of a given imaginary part δ of the complex Fermi energy $\epsilon_F + i\delta$, the corresponding sheet resistance $r(\mathcal{C};n;\delta)$ varies linearly with n,

$$k_1(\mathcal{C};\delta) = \frac{r(\mathcal{C};n+m;\delta) - r(\mathcal{C};n;\delta)}{m} \quad ; \quad m, n \in \mathbb{N}^+ \quad , \tag{17.26}$$

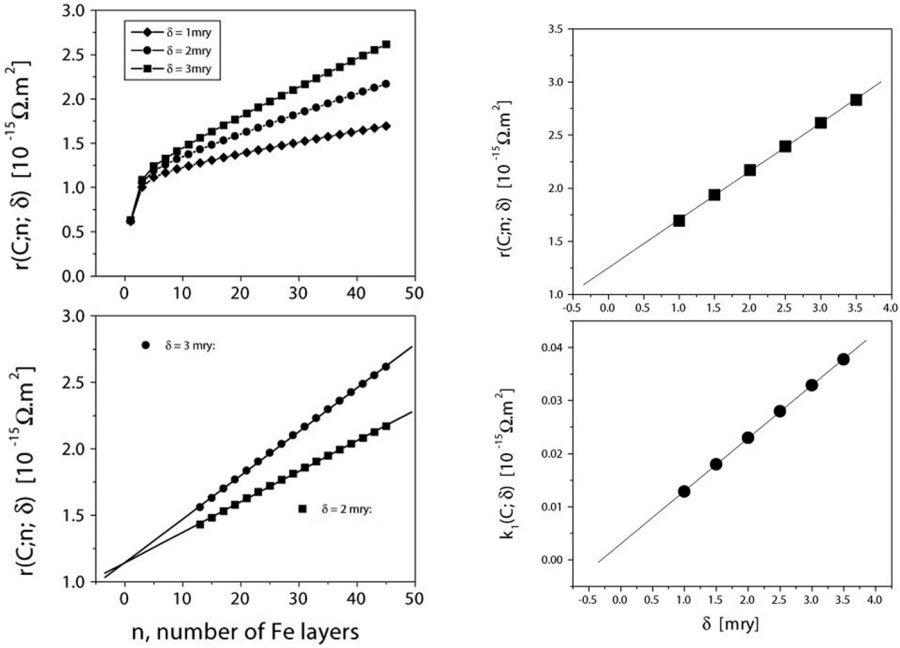

FIGURE 17.6: Top, left: variation of the sheet resistance $r(\mathcal{C};n;\delta)$ for ferromagnetic bcc Fe(100)/Fe$_n$/Fe with respect to n for three values of the imaginay part δ to the Fermi energy. Bottom, left: numerical extrapolation (full line) of the linear regime of the sheet resistance $r(\mathcal{C};n;\delta)$ for ferromagnetic bcc Fe(100)/Fe$_n$/Fe. Top, right: variation of $r(\mathcal{C};n;\delta)$ for Fe(100)/Fe$_{45}$/Fe with respect to δ. The linear fit is shown as a full line. Bottom, right: variation of $k_1(\mathcal{C};\delta)$ with respect to δ for the same system. From Ref. [11].

i.e., the following relation applies

$$r(\mathcal{C};n;\delta) = r_0(\mathcal{C};\delta) + nk_1(\mathcal{C};\delta) \quad , \tag{17.27}$$

with $r_0(\mathcal{C};\delta)$ being the value of the linear form defined by Eq. (17.26) at $n = 0$.

In the top left part of Fig. 17.6 the sheet resistance $r(\mathcal{C};n;\delta)$ for bcc Fe(100)/Fe$_n$/Fe(100) is shown for three values of δ by varying n in terms of $N - m$, $N = 45$, whereby $\mathcal{C}$ trivially refers to the ferromagnetic configuration. As can be seen for $n \geq 9$ the $r(\mathcal{C};n;\delta)$ vary indeed linearly with n; i.e., n_0 ought to be at least 9 in order to yield a linear behavior. The rapid fall off for $n < n_0$ reflects the fact that the size of the $\sigma_{ij}(\mathcal{C};n;\delta)$ matrix to be inverted becomes too small: for $n = 1$ only one diagonal element, namely $\sigma_{ii}(\mathcal{C};n)$, survives. In the lower left part of this figure the extrapolation defined in Eq. (17.27) is performed numerically for $n_0 \leq n \leq 45$, $n_0 = 12$, for two different values of

δ. As can be seen in both cases the extrapolation leads to virtually the same value for $n = 0$.

Investigating now for a given value of n the dependence of $r(\mathcal{C}; n; \delta)$ with respect to δ one can see from the top right part of Fig. 17.6 that $r(\mathcal{C}; n, \delta)$ varies as in the cases discussed before linearly in δ:

$$k_2(\mathcal{C}; n) = \frac{1}{n} \frac{r(\mathcal{C}; n; \delta_2) - r(\mathcal{C}; n; \delta_1)}{\delta} \quad , \quad \delta = \delta_2 - \delta_1 \quad , \tag{17.28}$$

i.e.,

$$r(\mathcal{C}; n; \delta) = r_0(\mathcal{C}; n) + n\delta k_2(\mathcal{C}; n) \quad , \tag{17.29}$$

where as will become clear in a moment the constant $k_2(\mathcal{C}; n)$ is chosen to be normalized per layer.

Combining now Eq. (17.26) with Eq. (17.29),

$$r_0(\mathcal{C}; \delta) = r_0(\mathcal{C}; n) + n(\delta k_2(\mathcal{C}; n) - k_1(\mathcal{C}; \delta)) \quad , \tag{17.30}$$

by taking the limit of $\delta \to 0$ it is easy to see that in demanding that

$$r_0(\mathcal{C}; n) = \lim_{\delta \to 0} r_0(\mathcal{C}; \delta) \quad , \tag{17.31}$$

this in turn implies that

$$\lim_{\delta \to 0} k_1(\mathcal{C}; \delta) = 0 \quad , \tag{17.32}$$

since $\delta k_2(\mathcal{C}; n)$ trivially vanishes for $\delta \to 0$. In the lower left part of Fig. 17.6 $k_1(\mathcal{C}; \delta)$ is linearly extrapolated to $\delta = 0$. As can be seen $k_1(\mathcal{C}; \delta)$ indeed tends to zero for $\delta \to 0$. The very small remainder of $k_1(\mathcal{C}; \delta)$ at $\delta = 0$ has to be regarded as an inherent error of the applied numerical procedure.

17.3.3 Resistivities and boundary conditions

From Eqs. (17.27) and (17.31), it follows that for $n \geq n_0$

$$\lim_{\delta \to 0} r(\mathcal{C}; n + m; \delta) = r_0(\mathcal{C}; n) \equiv r_0(\mathcal{C}) \quad ; \quad m, n \in \mathbb{N}^+ \quad , \tag{17.33}$$

which, however, is nothing but the Cauchy convergence criterion for the sheet resistance stated in Eq. (17.22):

$$\lim_{\delta \to 0} [r(\mathcal{C}; n + m; \delta) - r(\mathcal{C}; n; \delta)] = 0 \quad ; \quad m, n \in \mathbb{N}^+, n \geq n_0 \quad . \tag{17.34}$$

Quite clearly since $r_0(\mathcal{C})$ is a constant for a pure metal by performing the limit $n \to \infty$ this leads to a correct resistivity $\rho_{CPP}(\mathcal{C})$,

$$\rho_{CPP}(\mathcal{C}) = \lim_{n \to \infty} \left[\frac{r_0(\mathcal{C})}{L} \right] = \frac{r_0(\mathcal{C})}{d} \lim_{n \to \infty} \frac{1}{n} = 0 \quad , \tag{17.35}$$

where d is the interplanar distance. For a substitutionally disordered alloy $r(\mathcal{C};n;\delta)$ has to vary with respect to n in the following manner, see also Eq. (17.27),

$$r(\mathcal{C};n;\delta) = r_0(\mathcal{C};\delta) + n\left(k_1(\mathcal{C};\delta) + \overline{k}_1(\mathcal{C};\delta)\right) \quad , n \geq n_0 \quad , \tag{17.36}$$

where

$$\overline{k}_1(\mathcal{C}) = \lim_{\delta\to 0} \overline{k}_1(\mathcal{C};\delta) \tag{17.37}$$

simply is the resistivity caused by disorder (residual resistivity). In general for a bulk system $\rho_{CPP}(\mathcal{C})$ can be formulated in terms of sheet resistances such that

$$\rho_{CPP}(\mathcal{C}) = \frac{1}{d}\lim_{\delta\to 0}\left\{\lim_{n\to\infty}\frac{r(\mathcal{C};n;\delta)}{n}\right\} \quad . \tag{17.38}$$

17.3.4 Rotational properties

Let $R(\Theta)$ be an angle-dependent resistance,

$$R(\Theta) = r(\Theta)/A_0 \quad , \tag{17.39}$$

where A_0 is the unit area and Θ denotes the rotation angle around the in-plane y-axis (angle between the orientations of the magnetization in the two magnetic slabs), by which the orientation of the magnetization is rotated from perpendicular (parallel to the applied current) to in-plane (perpendicular to the current), such that the following magnetoresistance can be defined by

$$MR(\Theta) = \frac{\Delta r(\Theta)}{r(\Theta)} \quad , \quad \Delta r(\Theta) = r(\Theta) - r(0) \quad . \tag{17.40}$$

As in the case of in-plane resistivities the difference in sheet resistances can again be expanded in a power series in $\cos\Theta$ of the following form,

$$\Delta r(\Theta) = \alpha(1-\cos(\Theta)) + \beta\cos^2(\Theta) + \gamma\cos^3(\Theta) + \ \ldots \ , \tag{17.41}$$

in order to discuss anisotropy effects in a CPP geometry. Examples for the rotational properties of the magnetoresistance as well as for the dependence on the thickness of the spacer will be shown later, but first another important feature of electric transport in a CPP geometry has to be discussed, namely the occurrence of tunneling.

17.4 Tunnelling conditions

Suppose that in the Kubo-Greenwood equation, see Eq. (17.1) or Chapter 16, the current operator can be approximated by a constant,

$$\overline{\sigma} \sim tr \ \left\langle \operatorname{Im} G^{+}(\epsilon_F) \operatorname{Im} G^{+}(\epsilon_F) \right\rangle \sim n^2(\epsilon_F) \quad , \tag{17.42}$$

which in turn implies that the sheet resistance can approximately be written as

$$\overline{r} = L\overline{\sigma}^{-1} = Ln^{-2}(\epsilon_F) \quad . \tag{17.43}$$

Furthermore, suppose the density of states is calculated for complex Fermi energies, $E_F = \epsilon_F + i\delta$,

$$\overline{r}(\delta) = Ln^{-2}(\epsilon_F + i\delta) \quad ; \tag{17.44}$$

then from the properties of the density of states,

$$\frac{d\left[n(\epsilon_F + i\delta)\right]}{d\delta} = \begin{cases} > 0; \text{ “non-metallic”} \\ \\ < 0; \text{ “metallic”} \end{cases} \quad , \tag{17.45}$$

follows immediately

$$\frac{d\left[\overline{r}(\delta)\right]}{d\delta} = \begin{cases} > 0; \text{ “metallic”} \\ \\ < 0; \text{ “non-metallic”} \end{cases} \quad . \tag{17.46}$$

The functional form of the actually calculated sheet resistance with respect to the imaginary part of the Fermi energy can therefore be used to qualitatively interpret the underlying type of conductance

$$\frac{d\left[r\left(\mathcal{C}; s; \delta\right)\right]}{d\delta} = \begin{cases} > 0; \text{ “metallic”} \\ \\ < 0; \text{ “non-metallic”} \end{cases} \quad . \tag{17.47}$$

The last equation means *inter alia* that in the case of a negative slope of the sheet resistance with respect to δ "tunneling" might occur. The parameter δ obviously acts like a (small) constant self-energy: in the regime of metallic conductance an increase of the self-energy implies an increased resistivity (sheet resistance); in the non-metallic regime an increase of δ reduces the resistance, and the system becomes more metallic.

It should be noted that from an experimental point of view the temperature dependence of the resistance of a system is probably the only safe criterion for the occurrence of tunnelling. Eq. (17.47) seems to pinpoint the experimental experience, since the imaginary part of the Fermi energy can also be interpreted as an additional "thermal energy".

This particular feature of sheet resistances (or resistances for that matter) is illustrated in Fig. 17.7 for a model system consisting of two Fe leads separated by vacuum, namely by

$$\text{bcc-Fe(100)/Fe}_{n_0}\text{Vac}_s\text{Fe}_{n_0}\text{/Fe(100)}$$

The sheet resistances $r(\mathcal{C}; 2n_0+s; \delta)$, $2n_0+s$ being the total number of layers, are displayed in this figure for the parallel as well as the antiparallel configuration of the two Fe subsystems for $s \leq 4$. As can be seen in the parallel configuration the slope of the sheet resistance with respect to the imaginary part of the Fermi energy is positive only for one and three vacuum layers; in all other cases this slope is negative. Beyond 4 vacuum layers all slopes are always negative. Clearly the most interesting case arises with 3 vacuum layers, since the parallel and the antiparallel configuration obviously behave differently.

The fact that indeed in the parallel configuration a weak metallic conductance is predicted can be read also from Fig. 17.8, in which for the center vacuum layer the density-of-states at the Fermi energy, $n(\epsilon_F)$, is displayed versus the imaginary part of the Fermi energy. For $s = 3$ a very weak negative slope is observed, while for $s \geq 4$ the slope in $n(\epsilon_F)$ is positive! It is perhaps very informative to find out that only when the distance between the two Fe is beyond 12 monolayers, $n(\epsilon_F)$ is actually zero in the center layer, i.e., only then the two Fe subsystems can be viewed as separated, individual systems.

Equally amusing is to consider the usual so-called "exponential growth condition for tunnelling". Abbreviating $r(\mathcal{C}; 2n_0 + s; \delta)$ for a moment simply by $r_{\mathcal{C}}(s)$, $\mathcal{C}$ referring to the parallel ($\mathcal{P}$) or antiparallel configuration ($\mathcal{AP}$), and assuming that the growth of $r_{\mathcal{C}}(s)$ with s (number of vacuum layers) is of exponential form,

$$r_{\mathcal{P}}(s) = A_{\mathcal{P}} \exp\left(K_{\mathcal{P}} s\right) \quad \textit{and} \quad r_{\mathcal{AP}}(s) = A_{\mathcal{AP}} \exp\left(K_{\mathcal{AP}} s\right) \ , \tag{17.48}$$

then quite clearly the corresponding magnetoresistance $R(s)$ is given by

$$R(s) = 1 - C \exp\left[\left(K_{\mathcal{P}} - K_{\mathcal{AP}}\right) s\right] \quad , \tag{17.49}$$

where $C = A_P / A_{\mathcal{AP}}$. This now implies that the following cases have to be distinguished

$$K_{\mathcal{AP}} < K_{\mathcal{P}} \quad \rightarrow \quad \lim_{s\to\infty} R(s) = -\infty \tag{17.50}$$

$$K_{\mathcal{AP}} = K_{\mathcal{P}} \quad \rightarrow \quad \lim_{s\to\infty} R(s) = 1 - C \in [0, 1) \tag{17.51}$$

$$K_{\mathcal{AP}} > K_{\mathcal{P}} \quad \rightarrow \quad \lim_{s\to\infty} R(s) = 1 \tag{17.52}$$

leaving the conclusion that with "strict" exponential growth of the sheet resistance in the limit of infinitely separated magnetic leads $R(s)$ tends to zero only in the particular case of $A_P = A_{AP}$ ($C = 1$) and $K_P = K_{AP}$, i.e., $r_P(s) = r_{AP}(s)$ ($\forall s$). In physical terms this particular case implies that the two Fe subsystems have to be independent of each other; i.e., the domains of their Hamiltonians don't overlap.

Finally the question can be posed of how much in this particular case the vacuum barrier has to be reduced in order to force the system to conduct

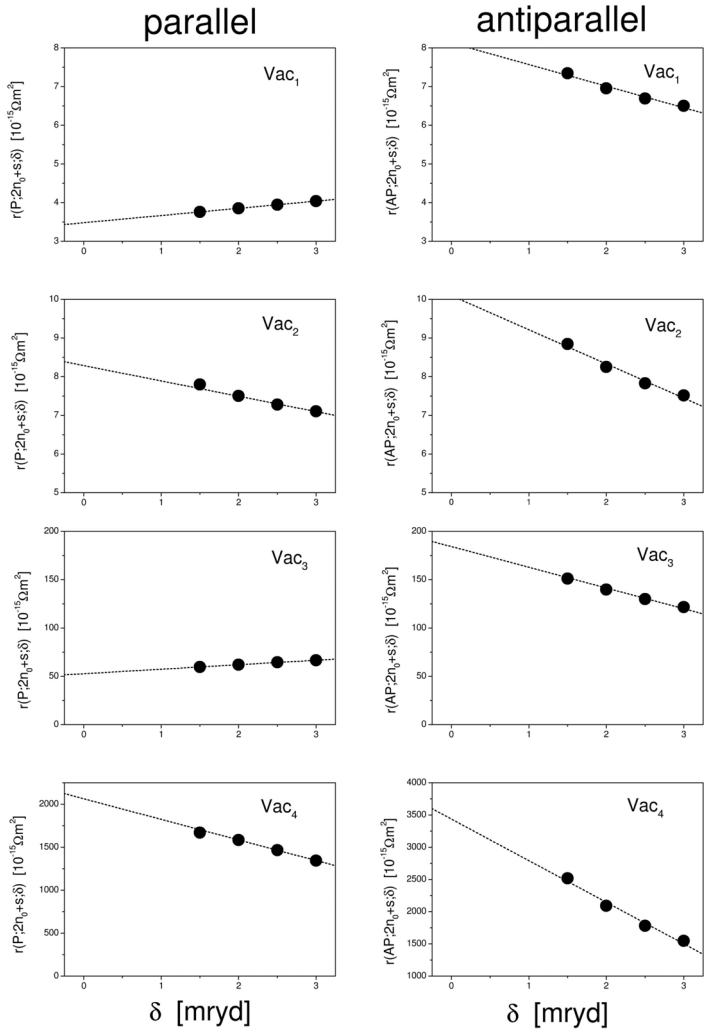

FIGURE 17.7: *Analytical continuation of the sheet resistances* $r(C; 2n_0+s; \delta)$, $n_0 \geq 11$, *in bcc-Fe(100)/*$Fe_{n_0}\,Vac_s\,Fe_{n_0}$*/Fe(100) to the real energy axis. Left: parallel configuration. Right: antiparallel configuration. Full circles refer to calculated values, dotted lines to the corresponding linear fit. From Ref. [12].*

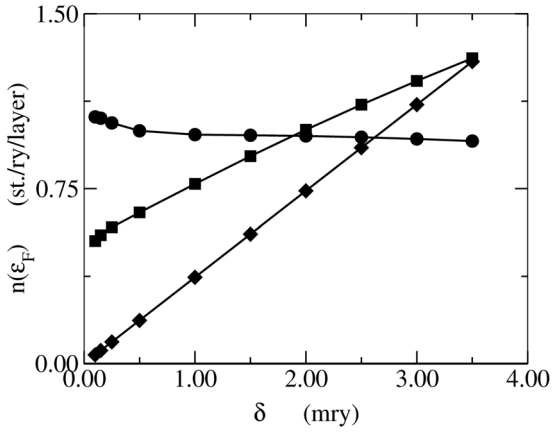

FIGURE 17.8: *Density of states of the center vacuum layer at the complex Fermi energy $\epsilon_F + i\delta$ as a function of δ in bcc-Fe(100)/$Fe_{12}\,Vac_s\,Fe_{12}$/Fe(100) for $s = 3$ (circles), $s = 6$ (squares; multiplied by 100), and $s = 9$ (diamonds; multiplied by 250). From Ref. [12].*

electrons like a metal. Again a computer experiment can help to solve this question. Consider that the actually self-consistently determined Madelung potentials for the 12 vacuum layers between the two Fe slabs are altered in the following manner

$$V_M^i = \begin{cases} V_M^i & ; \quad i \leq n_0 + 1; i \geq n_0 + s - 1 \\ V_M^i + V_C & ; \quad \text{otherwise} \end{cases} , \tag{17.53}$$

where i denotes atomic layers. As can be seen from the top of Fig. 17.9 by reducing the value of the potential barrier the layer-resolved sheet resistance immediately drops in the interior of the vacuum barrier and the magnetoresistance (bottom) increases. It should be noted that Fig. 17.9 offers an interesting aspect of the transition between metallic behavior of electric transport and tunneling: at $V_M^i + V_C = 0$ there is a cusp that separates these two regimes of electric transport. Once $V_M^i + V_C \leq 0$ a situation as in a (metallic) spin valve is reached. If $0 \leq V_M^i + V_C \leq V_0$, where V_0 is a reasonably small, but a positive constant, a tunnelling magnetoresistance can be expected even for very thick spacers, since the case of $s = 12$ already corresponds to a spacer thickness of about 17 Å.

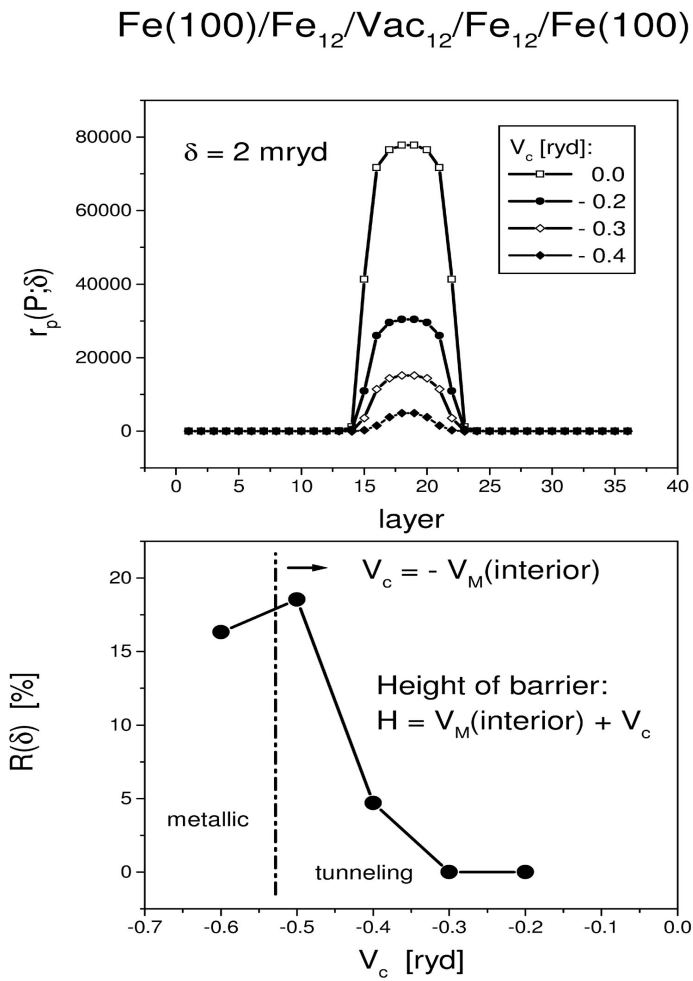

FIGURE 17.9: *Sheet resistance $r(P;\delta)$ (top) and magnetoresistance $R(\delta)$ (bottom), $\delta = 2$ mryd, in bcc-Fe(100)/Fe_{12} $\overline{Vac}_{12}Fe_{12}$/Fe(100) as a function of the constant shift V_C, see also Eq. (17.53). In the top part squares, triangles, circles and diamonds refer to $V_C = 0, -0.2, -0.3$ and -0.4 ryd, respectively; in the lower part the regimes of metallic and tunnelling behavior of electric transport are separated by the condition $V_M^i = -V_C$ (vertical line). From Ref. [12].*

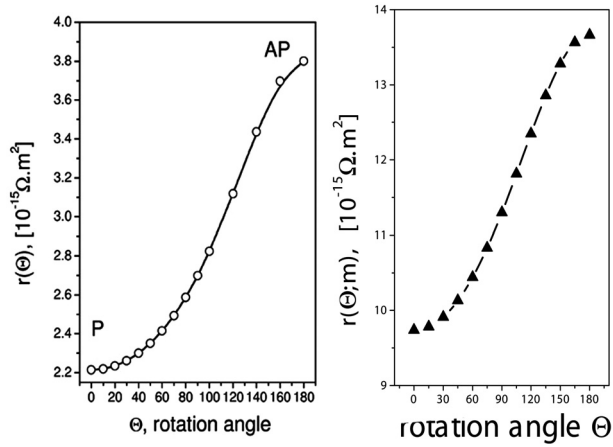

FIGURE 17.10: *Sheet resistance $r(\Theta)$ as a function of the rotation angle Θ. Left: $Co/Cu_{25}/Co$, from Ref. [13]. Right: $Cu/Py_{24}/Cu_{20}/Py_6/Cu$, from Ref. [14].*

17.5 Spin-valves

It turns out that in most cases investigated in the CPP geometry the angle dependent difference in sheet resistances, $\Delta r(\Theta)$, see Eq. (17.41), is of the form $\alpha(1 - \cos(\Theta))$; i.e., it turned out that also in CPP anisotropy effects in the magnetoresistance are of little importance. In Fig. (17.10) two very different systems are shown. In both cases Cu leads are assumed; the magnetic parts, however, are distinctly different and so are also the magnetic ground states. In the Co/Cu system collinear magnetic configurations form the ground states, whereas in the Cu/Py system a perpendicular arrangement is preferred; see also Fig. 12.4.

Even for spin valves with antiferromagnetic parts serving for exchange biasing purposes, little anisotropy effects in the CPP magnetoresistance as a function of the rotation angle Θ can be traced; see the left part of Fig. 17.11. The right part of this figure serves as a nice illustration of the ohmic properties of the sheet resistances, i.e., of the linearity of the product $nr(n)$, where n denotes the number of spacer layers.

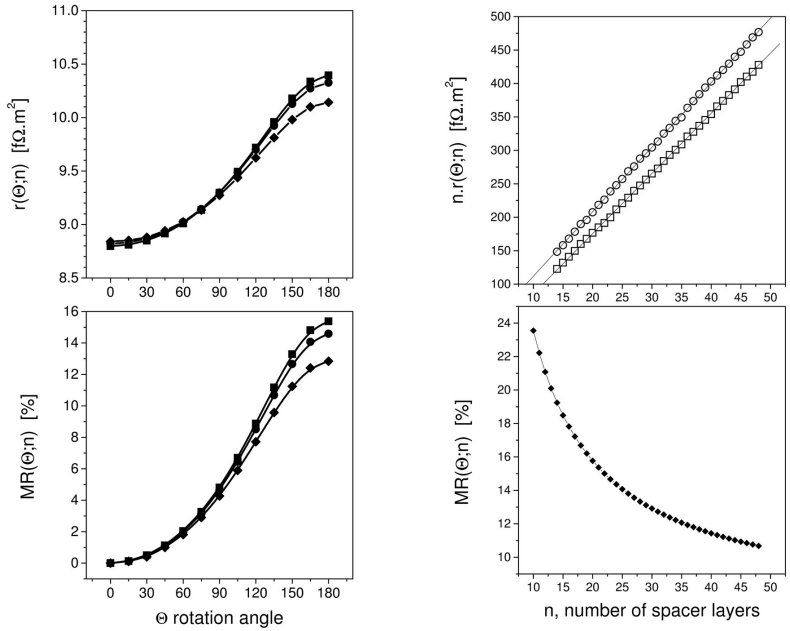

FIGURE 17.11: *$Cu(111)/Cu_6/(CoO)_{12}/Co_{24}/Cu_n/Co_6/Cu_{6+m}/Cu(111)$: Left: Variation of the sheet resistance (upper part) and the magnetoresistance (lower part) with respect to the rotation angle for n=21 (squares), n=24 (circles), and n=30 (diamonds). Right: Upper part: variation of $nr(\Theta;n)$ for $\Theta = 0°$ (parallel, diamonds) and $\Theta = 180°$ (antiparallel, circles) and of the respective fits (full lines) with respect to the spacer thickness (ML). Lower part: the magnetoresistance $MR(\Theta;n)$ at $\Theta = 180°$ for spacer thicknesses between 14 and 48 ML. From Ref. [15].*

17.6 Heterojunctions

It was already discussed in Chapter 12 that heterojunctions are extremely sensitive with respect to interdiffusion at the interfaces or alloying in the spacer. This applies in particular to spacer materials that easily form chemical compounds with the magnetic slabs of a spin valve; i.e., this applies always when the solubility of the spacer material in the magnetic parts is rather high. See for example the right parts of Fig. 12.13 and Fig. 12.15. In the left part of Fig. 17.12 the effect of a two-layer interdiffusion at the non-metal/magnetic slab interface is shown for the system $Fe(100)/Si_n/Fe(100)$. In the right part

of this figure two different "dirt effects" are assumed, namely homogeneous alloying of Si with Fe and the case that the Si spacer is statistically rough, i.e., contains statistically distributed holes. From all situations displayed in Fig. 17.12 it is obvious that Si as a spacer material is not suitable to be used in actual applications: any kind of disorder immediately pushes the magnetoresistance into an uninteresting regime. Fig. 17.12 also suggests that the magnetoresistance effect in the CPP geometry is mostly located in interface near regions of spin valve type systems.

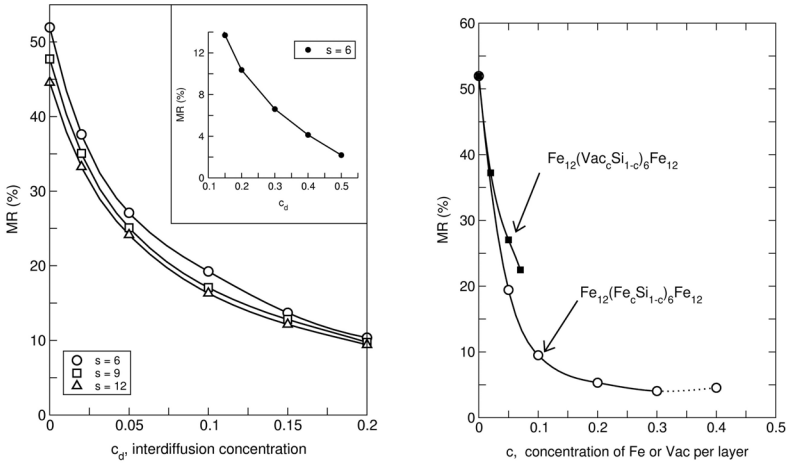

FIGURE 17.12: *Left: Dependence of the magnetoresistance on the interdiffusion concentration in $Fe/Si_s/Fe$ systems. Right: Magnetoresistance for systems with homogeneous Fe_cSi_{1-c} (circles) or Vac_cSi_{1-c} (squares) spacers depending on the Fe content c per layer. From Ref. [16].*

Turning now to the second example for a heterojunction involving a spacer material that considered as a bulk system is a semiconductor, namely to bcc-(100)Fe/$(ZnSe)_t$/Fe, one easily can show from the linearity of the sheet resistance times spacer thickness that

$$r(\mathcal{P}; 2\,(n_0 + t) + 1)t \equiv r(\mathcal{P}; t)t = C_{\mathcal{P}} + k_{\mathcal{P}}t \quad , \tag{17.54}$$

$$r(\mathcal{AP}; 2\,(n_0 + t) + 1)t \equiv r(\mathcal{AP}; t)t = C_{\mathcal{AP}} + k_{\mathcal{AP}}t \quad . \tag{17.55}$$

In Eqs.(17.54) and (17.55) t denotes the number of repetitions of a ZnSe unit, n_0 the number of Fe layers that have to be included, see Section 17.3.2, and

P and AP refer to the parallel and the antiparallel configuration of the Fe subsystems. By using the above two equations the difference in the sheet resistance between the antiparallel and the parallel alignments can be formulated as

$$\Delta r(t) \equiv r(\mathcal{AP};t) - r(\mathcal{P};t) \;=\; \frac{C_{\mathcal{AP}} - C_{\mathcal{P}}}{t} + k_{\mathcal{AP}} - k_{\mathcal{P}} \quad , \tag{17.56}$$

which in turn implies that

$$\lim_{t\to\infty} [\Delta r(t)] \;=\; k_{\mathcal{AP}} - k_{\mathcal{P}} \quad ; \tag{17.57}$$

i.e., with increasing spacer thickness $\Delta r(t)$ becomes a constant. It is important to note that since $\Delta r(t)$ and $r(\mathcal{AP};t)$ remain finite as t becomes very large, the corresponding magnetoresistance also becomes a constant; see the left part of Fig. 17.13.

By making use of the fact that for $\Delta r(t)$,

$$\Delta r(t) \;= \sum_{i=1}^{n} \left(\sum_{j=1}^{n} (\rho_{ij}(\mathcal{AP};t) - \rho_{ij}(\mathcal{P};t)) \right) \quad , \tag{17.58}$$

the summation over i can be taken in parts – in the right part of Fig. 17.13 $\Delta r(t)$ is partitioned into contributions arising from different parts of the heterostructure, namely the left and right electrodes (leads) L_{left} and L_{right}, the interface regions between electrodes and spacer, I_{left} and I_{right}, and the remaining spacer part S,

$$\begin{aligned} \Delta r(t;\delta) \;=\; & \Delta r_{L_{left}}(t;\delta) + \Delta r_{L_{right}}(t;\delta) + \Delta r_{I_{left}}(t;\delta) \\ & + \Delta r_{I_{right}}(t;\delta) + \Delta r_{S}(t;\delta) \quad . \end{aligned} \tag{17.59}$$

In this part of Fig. 17.13 $t = 21$ repetitions of ZnSe are considered and the interface region is chosen to consist of the actual interface plus three atomic layers to the left and right of it; i.e., for the Zn-terminated heterostructure the interface region is of the form Fe_3/FeZn/SeZnSe. As can be seen for the Se-terminated structure, the magnetoresistance $\Delta r(s;\delta)$ is entirely determined by the contributions from the two interface regions, while in the Zn-terminated structure the spacer part reduces these contributions. From both cases it is obvious that the interface regions contribute most to the difference in the sheet resistances and therefore also to the magnetoresistance.

In an electric transport study [17] of Fe on top of ZnSe it was found that the conductivities did not depend greatly on the thickness of the ZnSe layers. When putting an 18 Å thick layer of Fe on top of 150 Å of ZnSe a "*metallic contribution*" to the conductivity, was observed, whose temperature dependence is still "*semiconductor-like to some extent*". Interestingly enough, in

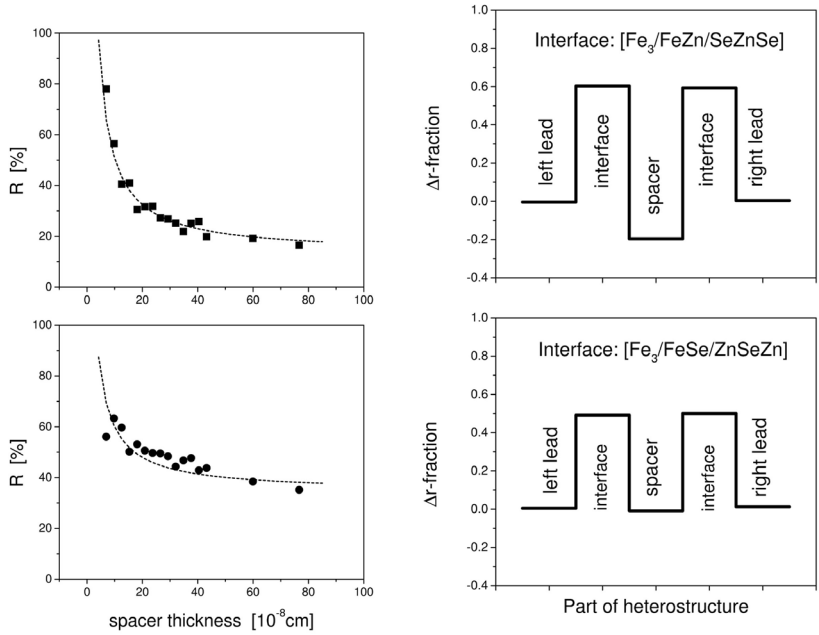

FIGURE 17.13: *Left: Magnetoresistance $R(t)$ in Fe(100)/ZnSe/Fe(100) heterostructures as a function of the spacer thickness. Top: Zn-termination, bottom: Se-termination. The squares refer to the actual calculated values, the dashed lines to the magnetoresistance using the fitted sheet resistances. Right: Normalized fractions of the difference in the sheet resistance between the antiferromagnetic and the ferromagnetic configuration in Fe(100)/$(ZnSe)_{21}$/Fe(100); see Eq. (17.59). The various regions of the heterostructure are shown explicitly. From Ref. [18].*

the theoretical Fe/$(ZnSe)_t$/Fe study [18], it was found that in all cases investigated the constant $k_2(\mathcal{C};n)$ in Eq. (17.28) had the following properties,

$$k_2(\mathcal{C};n) = \begin{cases} > 0\ ; & \text{parallel configuration} \\ \\ < 0\ ; & \text{antiparallel configuration} \end{cases} \quad ; \tag{17.60}$$

i.e., that in the parallel configuration metallic conduction applies, whereas in the antiparallel configuration tunnelling seems to be present. This obviously is exactly what was observed in the cited experiment.

17.7 Systems nanostructured in two dimensions

Up-to-now only electric transport properties of magnetic nanostructures characterized by two-dimensional translational symmetry were discussed. Once lattice Fourier transformations can no longer be used, the summations in the Kubo-Greenwood equation have to be performed over all sites i and j,

$$\sigma_{\mu\mu} = \sum_{i,j} \sigma_{\mu\mu}^{ij} \quad . \tag{17.61}$$

Computationally this implies to evaluate the following quantities

$$\rho_{\mu\mu} = \lim_{\delta \to 0} \rho_{\mu\mu}(r_0; \delta) \quad , \tag{17.62}$$

$$\rho_{\mu\mu}(r; \delta) \simeq \left[\sigma_{\mu\mu}^{0}(r; \delta)\right]^{-1} \quad , \quad \sigma_{\mu\mu}^{0}(r; \delta) = \sum_{|\mathbf{R}_{0j}| \leq r} \sigma_{\mu\mu}^{0j}(\delta) \quad , \tag{17.63}$$

where $|\mathbf{R}_{0j}|$ is the distance from a chosen origin in an embedded cluster to site j, and r is a sufficiently large distance such that by increasing r the resistivity $\rho_{\mu\mu}$ no longer changes.

17.7.1 Embedded magnetic nanostructures

As in the following only examples of square- or diamond-shaped clusters of atoms on a (100) surface with C_{4v} symmetry are chosen. The resistivity tensor $\boldsymbol{\rho}(r; \delta)$ is of the form

$$\boldsymbol{\rho}(r; \delta) = \begin{pmatrix} \rho_{xx}(r; \delta) & 0 & 0 \\ 0 & \rho_{yy}(r; \delta) & 0 \\ 0 & 0 & \rho_{zz}(r; \delta) \end{pmatrix} \quad . \tag{17.64}$$

Taking for illustrative purposes the simple example of a Ag atom (origin) "self-embedded" in the top (surface) layer of Ag(100), a two-dimensional map of ρ_{yy} and ρ_{zz} is displayed in Fig. 17.14. By comparing with the corresponding layer-resolved conductivity as obtained using two-dimensional translational symmetry it turned out that a reliable convergence of the resistivity determined via Eq. (17.63) can be achieved only for $r > 15\ a_{2D}$, where a_{2D} is the two-dimensional lattice constant of Ag.

Of course much more interesting are magnetic structures such as short wires embedded in the surface of Ag(100). In Fig. 17.16 the case of a short wire consisting of 4 Co atoms is displayed. In this figure one can see very well the difference between Ag and Co atoms neighboring a Co atom at the origin, i.e., the fall off of $\sigma_{\mu\mu}^{0j}$ with increasing distance of site j from the origin in different directions. In this sense clearly $\sigma_{\mu\mu}$ is highly anisotropic!

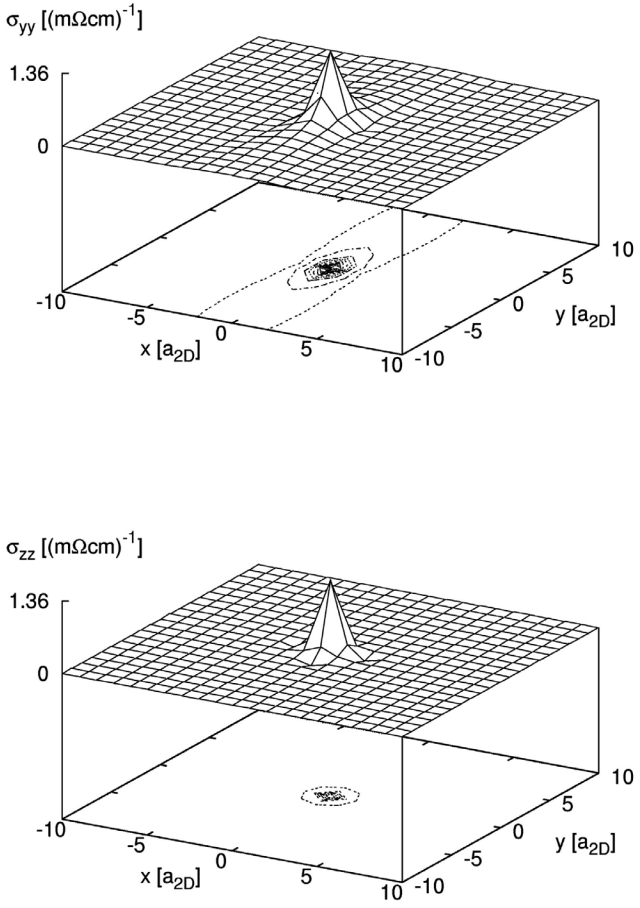

FIGURE 17.14: $\sigma_{\mu\mu}^{0j}(x_j, y_j)$ *for bulk fcc-Ag. The atom labelled by* 0 *is at the position* $(0, 0)$*, while the position of atom* j *is varied in a (100)-oriented plane* (δ *corresponds to 1 mryd). From Ref. [19].*

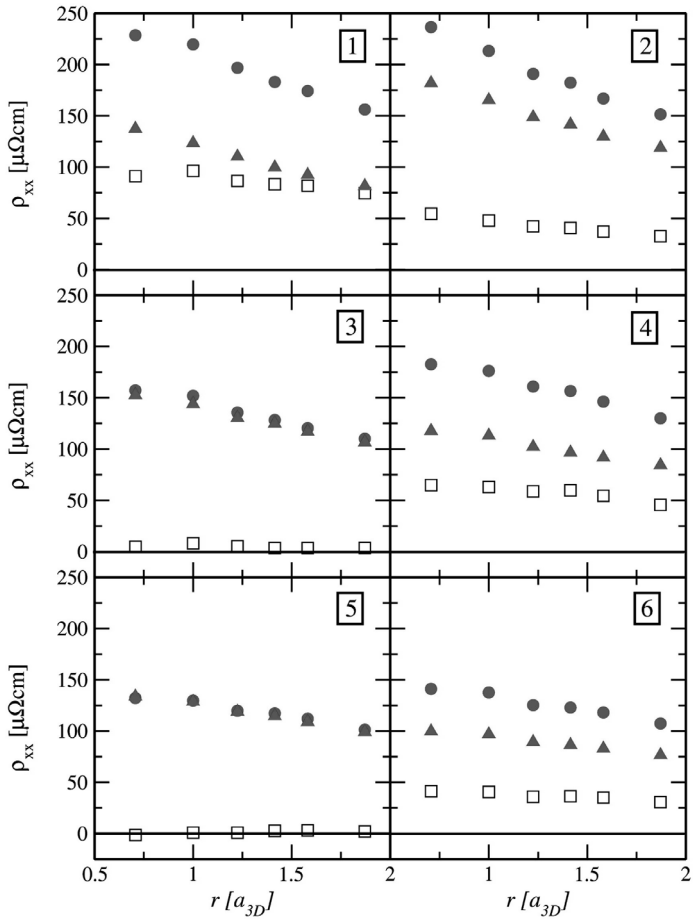

FIGURE 17.15: *Residual resistivities of finite chains of Fe (circles) and Co (triangles) atoms embedded in the surface plane of Ag(100). Open squares refer to the difference between the Fe and the Co residual resistivity. The length of the chains is shown explicitly. From Ref. [19].*

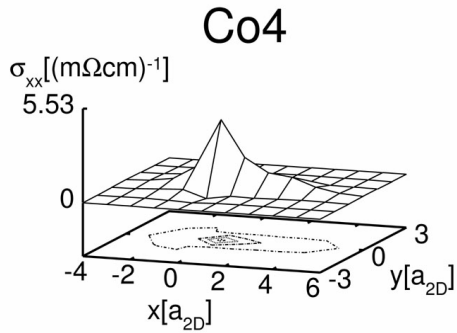

FIGURE 17.16: $\sigma^{oj}_{xx}(x_j, y_j)$ *for a chain of 4 Co atoms on Ag(100). The first atom in the chain is at position* $(0, 0)$*; all further atoms (index* j*) are varied in the (100)-oriented surface plane,* ($\delta = 1$ *mryd). From Ref. [20].*

Since clearly enough a summation over all sites in the embedded cluster plus those of the semi-infinite substrate would yield only the resistivity of the substrate, namely zero in the case of Ag(100), a kind of "residual resistivity" for finite clusters has to be defined,

$$\sigma^{\alpha}_{\mu\mu}(m;n) = \frac{1}{m}\sum_{i=1}^{m}\sum_{j=1}^{n}\left[\sigma^{ij}_{\mu\mu}\right]_{i=\alpha} \quad , \tag{17.65}$$

$$\rho^{\alpha}_{\mu\mu}(m;n) = \sigma^{\alpha}_{\mu\mu}(m;n)^{-1} \quad , \tag{17.66}$$

where m denotes the number of impurities of type α at sites i. The summation over the second index (j) is restricted as in the previous cases by a certain length of the difference vector $\mathbf{R}_{ij}$, which in turn determines the convergence of $\sigma^{\alpha}_{\mu\mu}(m;n)$

$$\left|\sigma^{\alpha}_{\mu\mu}(m;n+k) - \sigma^{\alpha}_{\mu\mu}(m;n)\right| \leq \Delta \quad . \tag{17.67}$$

In Fig. 17.15 such residual resistivities are shown for finite chains of Fe and Co embedded along the x (110) direction in the surface layer of Ag(100). As can be seen in this figure, chains with an even number of atoms differ distinctly from those with an odd number of atoms. Furthermore, for an odd chain length ($m > 1$) there is almost no difference whether Fe or Co atoms form the chains; i.e., the following difference,

$$\Delta\rho_{xx}(m;n) = \rho^{Fe}_{xx}(m;n) - \rho^{Co}_{xx}(m;n) \quad . \tag{17.68}$$

is nearly vanishing for all n considered, whereas in the case of even chain lengths $\Delta\rho_{xx}(m;n)$ is finite and varies slowly with respect to the cluster size.

17.7.2 Nanocontacts

17.7.2.1 Expression of the conductance

Let E_z^p be a constant electric field applied in all cells of layer p pointing along the z axis; i.e., E_z^p is normal to the planes of atoms. Denoting the z component of the current density averaged over cell i in layer q by j_z^{qi}, the microscopic Ohm's law is given by

$$j_z^{pi} = \frac{1}{V_{at}} \sum_j \sigma_{zz}^{pi,qj} E_z^q \quad , \tag{17.69}$$

where V_{at} is the volume of the unit cell in layer p. The total current flowing through layer p can be written as

$$I_{tot} = A_\parallel \sum_i j_z^{pi} = gU \quad , \tag{17.70}$$

where the applied voltage U is

$$U = E_z^J d_\perp \quad , \tag{17.71}$$

and $A_\parallel$ and $d_\perp$ denote the area of the two-dimensional unit cell and the interlayer spacing, respectively ($V_{at} = A_\parallel\, d_\perp$). Assuming that the same V_{at} applies in all layers and combining all three equations results in the following expression for the conductance,

$$g = \frac{1}{d_\perp^2} \sum_i \sum_j \sigma_{zz}^{pi,qj} \quad , \tag{17.72}$$

where the summations should, in principle, be carried out over all the cells in layers p and q.

It has to be emphasized that because of the use of linear response theory and current conservation, in principle the choice of layers p and q has to be arbitrary in the above formula. By the way, if the layers p and q are asymptotically far away from each other, the present formulation naturally recovers the Landauer-Büttiker approach [21, 22].

17.7.2.2 Gold contacts

Nanocontacts made of gold show a dominant peak very close to the conductance quantum, 1 $G_0 = 2e^2/h$ in the conductance histogram [23, 24].

A schematic view of a typical contact is displayed in Fig. 14.5; see also section 14.3. In the left part of Fig. 17.17 for the particular contact depicted there the numerically tedious required independence of the layer indices p and q, see Eq. (17.72), is shown in terms of the convergence with respect to the number of atoms in the layers. Convergence with about 20 atoms can already be obtained placing p and q in the first two full layers ($p = C - 3, q = C + 3$),

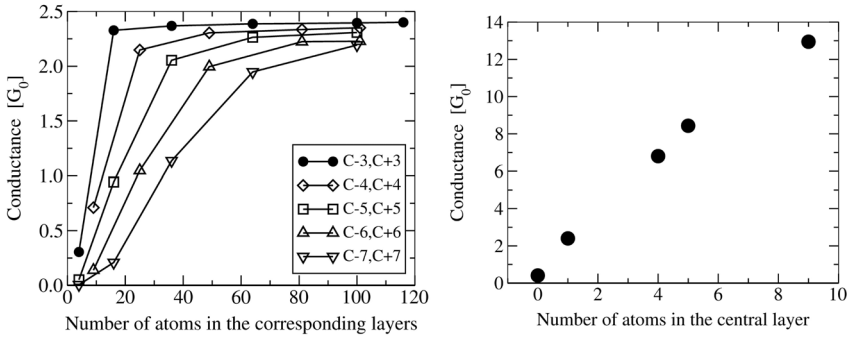

FIGURE 17.17: *Left: Conductance versus the number of sites included in the sum in Eq. (17.72) for the contact shown as entry (a) in Fig. 14.6. The different curves show conductances as calculated between different pairs of layers. For a definition of the layer numbering see Fig. 14.5. Right: Conductance versus the number of Au atoms in the central layer for the Au contacts. Zero atoms refer to a broken contact. From Ref. [25].*

C referring to the central layer, whereas the number of sites needed to get convergent sums gradually increases if pairs of layers farther away from the center of the contact are chosen. Since the current flows from the contact atom forming a cone of some opening angle that cuts out sheets of increasing area from the corresponding layers, this – at a first glance – strange kind of convergence property is qualitatively quite understandable.

This part of Fig. 17.17 also implies that an application of the Landauer-Büttiker approach to calculate the conductance of nanocontacts is numerically more tedious than the above described one, since in principle two layers situated infinitely far from each other have to be chosen in order to represent the leads.

For $p, q = C \pm 3$ a linear continuation of the conductivities in Eq. (17.69) to the real axis yielded a conductance for Au nanocontacts of 2.38 G_0. Repeating this calculation with an imaginary part of the Fermi energy of only 1 μRyd resulted in $g = 2.4$ G_0, which again proves that the use of complex Fermi energies is a very valuable numerical tool. For a 2×2 Au chain of finite length sandwiched between two semi-infinite Au systems, see entry (c) in Fig. 14.6, a conductance of 2.58 G_0 was obtained [25].

The right part of Fig. 17.17 shows the dependence of the conductance on the thickness of the nanocontacts in terms of the number of Au atoms in the central layer; see also Fig. 14.5. It should be noted in particular that the case of zero Au atoms refers to a broken contact! It can be seen that the conductance is nearly proportional to the number of Au atoms in the central layer.

17.7.2.3 Gold contacts with a magnetic impurity

As can be seen from Table 17.3, by placing impurities in the vicinity of the contact atom, see entries (A) - (C) in Fig. 14.6, at position B the conductance is changed only a little. Being placed at position A, however, Fe and Co atoms increase the conductance by 11 % and 24 %, while at position C they decrease the conductance by 19 % and 27 %, respectively.

Table 17.3: *Calculated conductances of a Au point contact with impurities at different positions in the vicinity of the contact atom, see entries (A) - (C) in Fig. 14.6. From Ref. [25].*

impurity position	Conductance $[G_0]$ Pd	Fe	Co
A	2.22	2.67	2.97
B	2.24	2.40	2.26
C	2.36	1.95	1.75
pure Au		2.40	

The change in the conductance caused by the impurities at positions A and C can qualitatively be explained by comparing the *s*-like density of states at the contact atom, shown in Fig. 14.4, with the corresponding $d_{3z^2-r^2}$-like density of states at the impurity site in Fig. 14.5; see also the corresponding section in Chapter 14.

The enhanced *s*-like density of states at the Fermi level of the contact atom seem to correlate nicely with the enhancement of the conductance when an Fe and Co impurity is placed at position A, while placed at position C a decreased value of the *s*-like density of states at the Fermi level seemingly causes a decreased conductance; see Table 17.3. However, since the effects are larger in the case of a Co impurity than for an Fe impurity, this simple picture can only serve as a very qualitative argument.

17.8 Domain wall resistivities

One of the most fascinating new ideas in the field of spintronics is the concept of race track memories [26, 27, 28], which is based on the experimental finding that in a given length of a nanowire the size of the anisotropic magnetoresistance (AMR) changes whether a domain wall is present or not. Since domain

walls can be moved in and out of such a predefined region by applying an electric field [29], it was proposed to use this effect for a new, all-solid-state archival storage with about the same density of magnetic disks, however, with no moving parts at all.

Suppose that C_0 and C_1 denote the following magnetic reference configurations corresponding to a magnetic domain wall of width L in a substitutional magnetic alloy A_cB_{1-c} viewed as a layered system (only two-dimensional translational symmetry)

$$C_0 = \{\mathbf{n}_l = \hat{x}, \quad \mathbf{n}_i = \hat{x}, \quad \mathbf{n}_r = \hat{x}, \quad i = 1, L\} \quad , \tag{17.73}$$

$$C_1 = \{\mathbf{n}_l = \hat{z}, \quad \mathbf{n}_i = \hat{z}, \quad \mathbf{n}_r = \hat{z}, \quad i = 1, L\} \quad , \tag{17.74}$$

where $\mathbf{n}_l$ and $\mathbf{n}_r$ denote the orientations of the magnetization in the "left" and the "right" domain, the $\mathbf{n}_i$ in the atomic planes forming the wall, $\hat{x}$ is parallel to the in-plane x-axis, and $\hat{z}$ is parallel to the surface normal. Consider further a magnetic configuration C_d such that within the atomic layers forming the domain wall the orientation of the magnetization in the individual planes changes quasi-continuously from $\hat{x}$ to $-\hat{x}$

$$C_d = \{\mathbf{n}_l = \hat{x}, \quad \mathbf{n}_i, \quad \mathbf{n}_r = -\hat{x}, \quad i = 1, L\} \quad , \tag{17.75}$$

$\mathbf{n}_i = D(\Phi_i)\hat{x}$, $\quad \Phi_i = 180i/L, \quad i = 1, \ldots, L$, $D(\Phi_i)$ being a rotation by an angle Φ_i around the surface normal.

As discussed in Chapter 15 the equilibrium domain wall width L_0 can be evaluated by minimizing the domain wall formation energy $E(L; C_d, c)$ with respect to L. It should be noted that by adding L_l and/or L_r layers from the left or right domain, of course the domain wall formation energy has to remain unchanged, i.e., $E(L + L_l + L_r; C_d, c) = E(L; C_d, c)$.

For large enough L the resistivity $\rho_{CPP}(L; C_i, c)$ for a particular chosen configuration C_i, see Eqs. (17.15) - (17.25), and the corresponding sheet resistance $r(L; C_i, c)$ or resistance $R(L; C_i, c)$,

$$r(L; C_i, c) = L\rho_{CPP}(L; C_i, c) = AR(L; C_i, c) \quad , \tag{17.76}$$

A being the unit area, can approximatively be obtained from the zz-component of the conductivity tensor, $\sigma_{zz}(L; C_i, c)$,

$$\rho_{CPP}(L; C_i, c) \sim \rho_{zz}(L; C_i, c) = \sigma_{zz}^{-1}(L; C_i, c) \quad . \tag{17.77}$$

Furthermore, one can make use of the fact that $r(L; C_i, c)$ is linear in L, see, e.g., Eq. (17.54),

$$r(L; C_i, c) = L\rho_{zz}(L; C_i, c) = a(C_i, c) + b(C_i, c)L \quad . \tag{17.78}$$

In using Eq. (17.77) this linear form has to yield the below limiting properties already discussed previously, namely

$$0 < c < 1 : \lim_{L \to \infty} \rho_{zz}(L; C_d, c) = b(C_d, c) = \rho_{zz}(C_0, c) \quad , \tag{17.79}$$

$$c = 0, 1 : \lim_{L \to \infty} \rho_{zz}(L; C_d, c) = \rho_{zz}(C_0, c) = 0 \quad , \tag{17.80}$$

where $\rho_{zz}(C_0, c), 0 < c < 1$, is the zz-component of the residual ("bulk") resistivity corresponding to configuration C_0; see Eq. (17.73). It should be recalled that for pure systems ($c = 0, 1$) the constant $b(C, c)$ has to be exactly zero. Eq. (17.80) can therefore be used to check the accuracy of the applied numerical procedure, in particular, since $\rho_{zz}(L; C, c)$ is evaluated like in all other cases discussed up-to-now by means of an analytical continuation of resistivities defined for complex Fermi energies to the real axis.

Clearly enough the "standard" expression for the anisotropic magnetoresistance [1] for bulk cubic systems, $c \neq 0, 1$, see Eq. (17.4), no longer makes sense in the presence of domain walls. However, one can define a similar ratio,

$$AMR(L_0; C_i, c) = \frac{\rho_{zz}(L_0; C_1, c) - \rho_{zz}(L_0; C_i, c)}{\rho_{zz}(L_0; C_1, c)} \quad , \tag{17.81}$$

$C_i = C_0, C_d$, where L_0 now refers to the equilibrium domain wall width. Similarly, in the absence of domain walls use can be made of the procedure indicated in Eq. (17.79), i.e.,

$$AMR(c) = \left(\rho_{zz}(C_1, c) - \rho_{zz}(C_0, c)\right) / \rho_{zz}(C_1, c) \quad . \tag{17.82}$$

By combining the last two equations a difference in these anisotropic magnetoresistances can be evaluated,

$$\begin{aligned} \Delta_{AMR} &= AMR(L_0; C_i, c) - AMR(c) \\ &= \frac{(r(L_0; C_i, c) - r(C_0, c))}{r(L_0; C_1, c)} = \frac{(R(L_0; C_i, c) - R(C_0, c))}{R(L_0; C_1, c)} \quad , \end{aligned} \tag{17.83}$$

which indicates how much the AMR is changed due to the presence of a domain wall. Obviously this reduction is determined by the difference in sheet resistances (resistances) in the presence and absence of a domain wall, normalized to the case that in the distance that separates the contacts, see Fig. 17.18, no domain wall is present and the magnetization is parallel to the electric current.

In Fig. 17.19 the resistivities $\rho(C_0, c)$ and $\rho(C_1, c)$, namely the so-called bulk residual resistivities, see Eq. (17.79), are displayed versus the Co concentration together with the domain wall resistivities $\rho(L_0; C_0, c)$, $\rho(L_0; C_1, c)$ and $\rho(L_0; C_d, c)$ for Co_cFe_{1-c} (left) and Co_cNi_{1-c} (right). In the case of Co_cNi_{1-c} also the experimental room temperature values [31] are shown. Note that for illustrative purposes these values were shifted uniformly by -5 [$\mu\Omega$.cm] such that for pure Co the experimental value is zero. As can be seen from the right part of Fig. 17.19 for Co_cNi_{1-c} the experimental and the theoretically calculated "bulk" resistivities vary in a similar manner with respect to the Co concentration. There is a peak at about $c = 0.15$; for higher Co concentrations the resistivities fall off continuously. In both systems $\rho(L_0; C_0, c)$ and

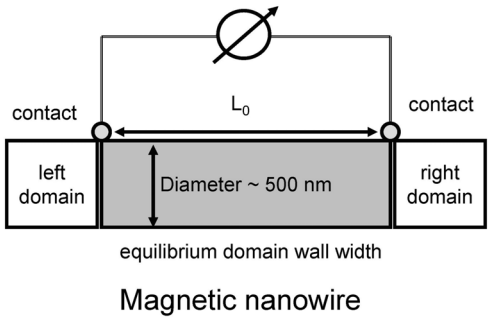

FIGURE 17.18: *Electric contacts placed on a nanowire, separated by the equilibrium domain wall width.*

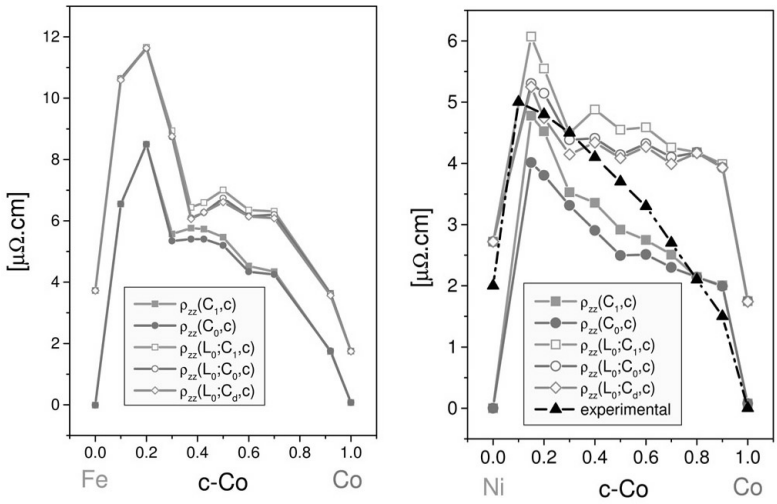

FIGURE 17.19: *Domain wall resistivities $\rho_{zz}(L_0;C_i,c)$ and "bulk" resistivities $\rho_{zz}(C_i,c)$ for Co_cFe_{1-c} (left) and Co_cNi_{1-c} (right). The various entries are denoted explicitly; the experimental values [31] at 273° K, are shifted uniformly by -5 [$\mu\Omega.cm$]. From Ref. [30].*

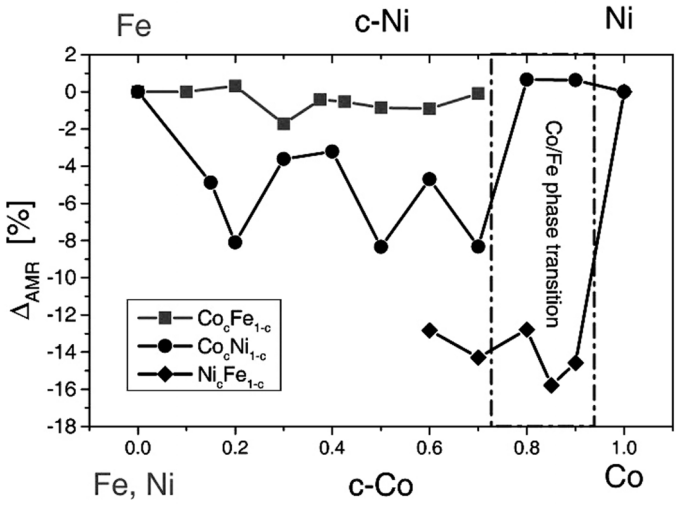

FIGURE 17.20: *Reduction of the AMR in the presence of a domain wall. From Refs. [30, 32].*

$\rho(L_0; C_d, c)$ are very similar in value, since the so-called in-plane anisotropy is very small. It should be noted that in Co_cFe_{1-c} there is a phase transition from bcc to fcc in the concentration regime of about 70 - 90% Co. For these Co concentrations the connecting lines in the left part of Fig. 17.19 serve merely as a guide for the eye.

Finally in Fig. 17.20 the difference in the anisotropic magnetoresistance with respect to the presence and the absence of a domain wall is shown for all three possible binary alloy combinations of Fe, Co and Ni. From this figure one immediately can see that Co_cFe_{1-c} obviously is not suitable for technological purposes, while the results for Co_cNi_{1-c} suggest that for $0.15 \leq c \leq 0.75$ on the average a reduction of the AMR amounting to about 6% can be expected. The best choice by far seems to be – one is almost tempted to say as usual – permalloy with a Ni content of about 85%.

17.9 Summary

This chapter was based on the use of the "relativistic" Kubo-Greenwood equation, which can be uniformly applied to all the different topics mentioned. Clearly enough, quite a few of these aspects, in particular CPP in the case of

spin valves and heterojunctions, could have been discussed using also a non-relativistic approach or applying the so-called "Kubo-Landauer" approach, see e.g. [33].

- **CIP, GMR:** the interface conditions and the type of leads are important; the GMR changes proportional to $(1 - \cos\Theta)$ between the initial and the final magnetic configuration. The stability of switching depends on the switching energy. Close to a node in the interface coupling energy (with respect to the thickness of the metallic spacer), a positive magnetic anisotropy energy guarantees that the system remains in the switched state. The actual performance of GMR devices usually can be tuned by making use of the dependence on the thickness parameter for the free magnetic slab, the spacer, the antiferromagnetic pinning layer and – of course – by combining different magnetic materials ("soft" and "hard" magnets). The switching time most likely is below 100 ps.

- **Heterojunctions, CPP, TMR:** the interface conditions are essential for the TMR ratio. A combination of materials with strong intermixing tendencies such Fe and Si is not suitable for applications. The magnetoresistance ratio changes proportional to $(1 - \cos\Theta)$ between the initial and the final magnetic configuration. Conditions for the occurrence of tunnelling can be best checked via the temperature dependence of the resistance. Systems with oxidic spacers like MgO with nearly perfect interfaces show by far the best results in terms of the TMR ratio.

- **Nanocontacts:** the conducting properties of nanocontacts depend very much on the geometrical shape of the contact in the vicinity of the contact atoms. Impurities, in particular magnetic ones, can enhance or reduce the conductance. Au nanocontacts still seem to be the most useful ones.

- **Domain walls:** the presence or absence of a domain wall between two electric contacts can be used for a new type of nano-switching. In particular for permalloy the reduction in the anisotropic magnetoresistance seems to be quite large.

[1] S. Khmelevskyi, K. Palotás, P. Weinberger, and L. Szunyogh, Phys. Rev. B **68**, 012402 (2003).

[2] J. Banhart, amd H. Ebert, Europhys. Lett. **32**, 517 (1995).

[3] J. Smith, Physica **16**, 612 (1951).

[4] I. A. Campbell, A. Fert, and O. Jaoul, J. Phys. C **3**, S95 (1970).

[5] I. A. Campbell, J. Phys. F **4**, L181 (1974).

[6] P. Weinberger, L. Szunyogh, J. Zabloudil, R. Hammerling, T. L. Mochesky, and B. Heinrich, Phys. Rev. B **67**, 054404 (2003).

[7] C. Blaas, P. Weinberger, L. Szunyogh, J. Kudrnovsky, V. Drchal, P.M. Levy, and C. Sommers, Eur. Phys. J. B **9**, 245 (1999).

[8] P. M. Levy, Solid State Physics Vol. 47, eds. H. Ehrenreich and D. Turnbull (Academic Press, Cambridge, MA, 1994) pp. 367-462.

[9] H. E. Camblong, P. M. Levy, and S. Zhang, Phys. Rev. B **51**, 16052 (1995).

[10] P. M. Levy and I. Mertig, In: *Spin-dependent Transport in Magnetic Nanostructures*, Eds. T. Shinjo and S. Maekawa, Gordon and Breach Science Publisher (2001).

[11] P. Weinberger, L. Szunyogh, C. Blaas, and C. Sommers, Phys. Rev. B **64**, 184429 (2001).

[12] P. Weinberger, V. Drchal, J. Kudrnovsky, I. Turek, H. Herper, L. Szunyogh and C. Sommers, Phil. Mag. B **82**, 1027 - 1045 (2002).

[13] P. Weinberger, A. Vernes, B. L. Gyorffy, and L. Szunyogh, Phys. Rev. B **70**, 094401 (2004).

[14] A. Vernes, P. Weinberger, and L. Szunyogh, Phys. Rev. B **72**, 0112401 (2005).

[15] P. Weinberger, Phys. Rev. B **75**, 064405 (2007).

[16] H. Herper, P. Weinberger, L. Szunyogh, and C. Sommers, Phys. Rev. B **66**, 064426 (2002).

[17] M. Hunziker, and M. Landolt, Surf. Sci. **468**, 187 (2000).

[18] H. C. Herper, P. Weinberger, A. Vernes, L. Szunyogh, and C. Sommers, Phys. Rev. B **64**, 184442 (2001).

[19] K. Palotas, B. Lazarovits, L. Szunyogh, and P. Weinberger, Phys. Rev. B **67**, 174404 (2003).

[20] K. Palotás, B. Lazarovits, P. Weinberger, and L. Szunyogh, J. Magnetism and Magnetic Materials **272-276**, 1594 - 5 (2004).

[21] R. Landauer, IBM J. Res. Dev. **1**, 223 (1957).

[22] M. Büttiker, Phys. Rev. Lett. **57**, 1761 (1986).

[23] J. M. Krans, I. K. Yanson, Th. C. M. Govaert, R. Hesper, and J. M. van Ruitenbeek, Phys. Rev. B **48**, 14721 (1993).

[24] M. Brandbyge, J. Schiøtz, M. R. Sørensen, P. Stoltze, K. W. Jacobsen, J. K. Nørskov, L. Olesen, E. Laegsgaard, I. Stensgaard, and F. Besenbacher, Phys. Rev. B **52** 8499 (1995).

[25] K. Palotás, B. Lazarovits, L. Szunyogh, and P. Weinberger, Phys. Rev. B **70**, 134421 (2004).

[26] D. A. Allwood, G. Xiong, C. C. Faulkner, D. Atkinson, D. Petit, and R. P. Cowburn, Science **309**, 1688 (2005).

[27] S. S. P. Parkin, U. S. Patent No. US 683 400 5 (2004).

[28] S. A. Wolf, D. Treger, and A. Chtchelkanova, MRS Bulletin **31**, 400 (2006).

[29] M. Kläui, P.-O- Jubert, R. Allenspach, A. Bischof, J. A. C. Bland, G. Faini, U. Rüdinger, C. A. F. Vaz, L. Vila, and C. Vouille, Phys. Rev. Lett. **95**, 026601 (2005).

[30] P. Weinberger, Rev. Lett. **100**, 017201 (2008).

[31] J. Bass, In: Landolt-Börnstein, Vol. **15b**, (Springer Verlag, 1985).

[32] P. Weinberger, MRS Proceedings, Boston, 2007, in press (2008).

[33] J. Kudrnovsky, V. Drchal, I. Turek, P. Weinberger, and P. Bruno, Computational Materials Science **25**, 584 - 589 (2002).

18

Magneto-optical properties of magnetic nanostructured matter

A concept of evaluating Kerr rotation and ellipticity angles is introduced based on a macroscopic model that takes into account all possible reflections and interferences of incident light. This concept is then applied to typical applications in the context of magnetic nanostructured matter, in particular to interlayer exchange coupling and magnetic anisotropy-driven phenomena such as reorientation transitions.

In 1876 J. Kerr discovered [1] that reflected from iron the polarization plane of linearly polarized light is rotated. Since in his first experiments the pole of an Fe magnet was used, this magneto–optical effect has been called the *polar Kerr effect*. Two years later Kerr demonstrated that the same effect shows up even when iron is magnetized in–plane. This particular set up is known today as the *longitudinal geometry*. Nowadays, the magneto–optical Kerr effect (MOKE) is a widely used powerful experimental tool, e.g., for magnetic domain imaging, mapping of hysteresis loops, etc., and technologically is applied in magneto–optical high–density recording.

MOKE is usually identified with a change in the polarization state of incident linearly polarized light when reflected from a magnetic system [2], namely with a rotation of the main polarization plane (characterized by the Kerr rotation angle θ_{K}) and the ellipticity of the reflected light (ellipticity angle ϵ_{K}) [3]. In viewing linearly polarized incident light as a superposition of right– and left–handed circularly polarized waves of equal amplitudes, from a purely optical stand-point of view, the magneto–optical Kerr effect is caused by different reflections of these two circularly polarized components of the incident light.

Based on the relative orientation of the magnetization with respect to the surface of the system and the plane of incidence, one distinguishes between three basic Kerr geometries, which are most frequently used in experiments. In the *polar Kerr effect*, the magnetization of the system is in the plane of incidence and perpendicular to the reflective surface. The *longitudinal Kerr effect* occurs, when the magnetization is parallel to both, the plane of incidence and the reflective surface. If the magnetization is in–plane and perpendicular to the plane of incidence, the Kerr effect is said to be *transverse* and, unlike in other geometries [3], magnetization dependent intensity differences

are measured. Because only the polar Kerr effect and a specific transverse configuration go linearly with the magnitude of magnetization [2], presently, all optical data storage technologies use these geometries [4]. The longitudinal Kerr effect, on the other hand, is mainly applied for investigating domain structures [3].

In this chapter all microscopic descriptions are based on the complex optical conductivity tensor $\sigma_{\mu\nu}(\omega)$ [5], see Chapter 16, as given by

$$\boxed{\sigma_{\mu\nu}(\omega) = \frac{\Sigma_{\mu\nu}(\omega) - \Sigma_{\mu\nu}(0)}{\hbar\omega + i\delta}} \tag{18.1}$$

where the current–current correlation functions $\Sigma_{\mu\nu}(\omega)$ are defined by

$$\boxed{\Sigma_{\mu\nu}(\omega) = \frac{i\hbar}{V} \sum_{m,n} \frac{f(\varepsilon_m) - f(\varepsilon_n)}{\varepsilon_m - \varepsilon_n + \hbar\omega + i\delta} \; J^{\mu}_{mn} J^{\nu}_{nm}} \tag{18.2}$$

with $f(\varepsilon)$ being the Fermi–Dirac distribution function, ε_m and ε_n a pair of eigenvalues of the effective one–electron (Kohn-Sham-) Dirac Hamiltonian, δ the life-time broadening, J^{μ}_{mn} the matrix elements of the electronic current operator ($\mu = x, y, z$) and V the reference volume.

18.1 The macroscopic model

18.1.1 Layer–resolved permittivities

Within linear response theory the Fourier transformed *macroscopic material equations* [6] averaged over a given reference volume V directly yield the total electric displacement,

$$\frac{1}{V}\int_V d^3r \; \mathbf{D}(\mathbf{r},\omega) = \frac{1}{V}\int_V d^3r \int_V d^3r' \; \boldsymbol{\epsilon}(\omega;\mathbf{r},\mathbf{r}')\,\mathbf{E}(\mathbf{r}',\omega) \quad , \tag{18.3}$$

provided that the dielectric function $\boldsymbol{\epsilon}(\omega;\mathbf{r},\mathbf{r}')$ and the Fourier components of the electric field $\mathbf{E}(\mathbf{r},\omega)$ at a particular frequency ω are known. As is probably well-known by now, by using non–overlapping cells in configuration space (the multiple scattering requirement), the reference volume can be written as

$$V = \sum_{p=1}^{N} \left(N_{\parallel} \sum_i \Omega_{pi} \right) \equiv \sum_{p=1}^{N} \Omega^p \quad , \tag{18.4}$$

where $N_{\parallel}$ is the number of atoms per layer (order of the two-dimensional translational group $\mathcal{L}^{(2)}$, one and the same group has to apply in each layer

p), N the total number of layers, and Ω_{pi} is the volume of the $i-$th atomic cell in layer p.

Assuming that (for matters of simplicity) the Atomic Sphere Approximation (ASA) is applied, that plane waves propagate in a layer like in a two–dimensional unbound homogeneous medium,

$$\mathbf{D}_{pi}\left(\mathbf{r},\omega\right)=\mathbf{D}_{p}\left(\mathbf{r},\omega\right)\quad,\quad\forall i\in I(\mathcal{L}^{(2)})\quad, \tag{18.5}$$

the integral on the left hand side of Eq. (18.3) can be written as [7]

$$\int_{V}d^{3}r\ \mathbf{D}\left(\mathbf{r},\omega\right)=N_{\parallel}\sum_{p=1}^{N}\mathbf{D}_{p}\sum_{i}\Omega_{pi}\left[1+6\sum_{k=1}^{\infty}\frac{\left(-1\right)^{k}\left(k+1\right)}{\left(2k+3\right)!}\left(\frac{2\pi}{\lambda_{0}}n_{p}S_{pi}\right)^{2k}\right] \tag{18.6}$$

In Eq. (18.6) the vector $\mathbf{D}_p$ is the *amplitude of the electric displacement*, $\mathbf{n}_p$ the *refraction vector*,

$$\mathbf{n}_{p}=\mathbf{q}_{p}/q_{0}\quad, \tag{18.7}$$

$\mathbf{q}_p$ the wave vector ($q_0=2\pi/\lambda_0$ refers to the constant of propagation in vacuum), and S_{pi} is the radius of the $i-$th atomic sphere in layer p. The double integral on the *rhs* of Eq. (18.6) reduces therefore to

$$\begin{aligned}\int_{V}d^{3}r\int_{V}d^{3}r'\boldsymbol{\epsilon}\left(\omega;\mathbf{r},\mathbf{r}'\right)\mathbf{E}\left(\mathbf{r}',\omega\right)&=\left(4\pi\right)^{2}N_{\parallel}\sum_{p,q=1}^{N}\mathbf{E}_{q}\sum_{i,j}\int_{0}^{S_{pi}}dr\ r^{2}\\&\times\int_{0}^{S_{qj}}dr'\ \left(r'\right)^{2}\boldsymbol{\epsilon}^{pi,qj}\left(\omega;r,r'\right)\ \left[1+\sum_{k=1}^{\infty}\frac{\left(-1\right)^{k}}{\left(2k+1\right)!}\left(\frac{2\pi}{\lambda_{0}}n_{q}r'\right)^{2k}\right]\quad,\end{aligned} \tag{18.8}$$

where the vector $\mathbf{E}_q$ refers to the amplitude of the electric field in layer q, and $\boldsymbol{\epsilon}^{pi,qj}\left(\omega;r,r'\right)$ is the dielectric function $\boldsymbol{\epsilon}\left(\omega;\mathbf{r},\mathbf{r}'\right)$ at $\mathbf{r}\in\Omega_{pi}$ and $\mathbf{r}'\in\Omega_{qj}$.

In the case of visible light the wave vector dependence of the permittivity is negligible [2]. Therefore, e.g., in Eq. (18.6), only the first term in the power series expansion has to be kept, which immediately leads to

$$\sum_{p=1}^{N}\left[\mathbf{D}_{p}-\sum_{q=1}^{N}\boldsymbol{\epsilon}^{pq}\left(\omega\right)\mathbf{E}_{q}\right]\sum_{i}\Omega_{pi}=0\ , \tag{18.9}$$

where the *inter–* ($p\neq q$), *intra–*layer ($p=q$) *permittivities* are given by

$$\boldsymbol{\epsilon}^{pq}\left(\omega\right)=\frac{\left(4\pi\right)^{2}}{\sum_{i}\Omega_{pi}}\sum_{i,j}\int_{0}^{S_{pi}}drr^{2}\int_{0}^{S_{qj}}dr'\ \left(r'\right)^{2}\boldsymbol{\epsilon}^{pi,qj}\left(\omega;r,r'\right)\quad. \tag{18.10}$$

By using the relation

$$\mathbf{D}_{p}=\boldsymbol{\epsilon}^{p}\left(\omega\right)\mathbf{E}_{p}\quad,$$

the layer–resolved permittivities $\boldsymbol{\epsilon}^p(\omega)$ are then solutions of the following system of equations:

$$\boldsymbol{\epsilon}^p(\omega)\,\mathbf{E}_p = \sum_{q=1}^{N} \boldsymbol{\epsilon}^{pq}(\omega)\;\mathbf{E}_q \;, \qquad p = 1,\ldots,N \quad . \tag{18.11}$$

18.1.2 Mapping: $\boldsymbol{\sigma} \rightarrow \boldsymbol{\epsilon}$

By mapping finally the *inter* $(p \neq q)$– and *intra* $(p = q)$–layer contributions of the microscopically (quantum mechanically) well-defined optical conductivity tensor $\boldsymbol{\sigma}(\omega)$,

$$\boldsymbol{\sigma}(\omega) = \sum_{p=1}^{N}\sum_{q=1}^{N} \boldsymbol{\sigma}^{pq}(\omega) \quad , \tag{18.12}$$

onto the corresponding contributions of the permittivity tensor

$$\boxed{f : \boldsymbol{\sigma}(\omega) \rightarrow \boldsymbol{\epsilon}(\omega)}$$

such that

$$\boldsymbol{\epsilon}^{pq}(\omega) = \frac{1}{N}\left[1 - \frac{4\pi i}{\omega}\boldsymbol{\sigma}^{pq}(\omega)\right] \quad , \tag{18.13}$$

one then can establish a well–defined macroscopical model for the evaluation of Kerr spectra.

18.1.3 Multiple reflections and optical interferences

By assuming that when put between two boundaries each atomic layer acts as a homogeneous, anisotropic medium and is characterized by a layer–resolved dielectric tensor $\boldsymbol{\epsilon}^p$ all optical reflections and interferences within a multilayer system $(p = 1,\ldots,N)$ can be determined [4, 8] using classical optics.

18.1.3.1 The Fresnel equation

First the Fresnel or characteristic equation [9]

$$\left|n_p^2\delta_{\mu\nu} - n_{p\mu}n_{p\nu} - \epsilon^p_{\mu\nu}\right| = 0 \quad , \quad (\mu,\nu = x,y,z) \quad , \tag{18.14}$$

has to be solved [3] in order to determine the *normal modes* of the electromagnetic waves in a particular layer p, where $\mathbf{n}_p = \mathbf{q}_p/q_0$ is the (complex) refraction vector in layer p; see Eq. (18.7).

18.1.3.2 The Helmholtz equation

For each normal mode the Helmholtz equation,

$$\sum_{\nu}\left(n_p^2\delta_{\mu\nu} - n_{p\mu}n_{p\nu} - \epsilon^p_{\mu\nu}\right)E_{p\nu} = 0 \quad , \quad (\mu,\nu = x,y,z) \quad , \tag{18.15}$$

Table 18.1: *Key quantities and relations for the polar and the longidutional Kerr effect.*

Layer-resolved quantity	polar geometry	logitudinal geometry
M_p	$(0, 0, M_{pz})$	$(0, M_{py}, 0)$
$q_p = q_0 n_p$	$(0, 0, n_{pz})$	$(0, -\sin\Theta, n_{pz}\cos\Theta)$
$\boldsymbol{\epsilon}^p(\omega)$	$\begin{pmatrix} \varepsilon^p_{xx} & \varepsilon^p_{xy} & 0 \\ -\varepsilon^p_{xy} & \varepsilon^p_{xx} & 0 \\ 0 & 0 & \varepsilon^p_{zz} \end{pmatrix}$	$\begin{pmatrix} \varepsilon^p_{xx} & 0 & \varepsilon^p_{xz} \\ 0 & \varepsilon^p_{yy} & 0 \\ \varepsilon^p_{zx} & 0 & \varepsilon^p_{zz} \end{pmatrix}$
normal modes	$n_{pz} = \pm\sqrt{\varepsilon^p_{xx} \pm i\varepsilon^p_{xy}}$ $\varepsilon^p_{xx} - \varepsilon^p_{zz} \sim 0$	$n^4_{pz} + a n^2_{pz} + b = 0$ $a = \left(1 + \varepsilon^p_{yy}/\varepsilon^p_{zz}\right)\sin^2\theta$ $+ \left(\varepsilon^p_{xz}\varepsilon^p_{zx}\right)/\varepsilon^p_{zz} - \varepsilon^p_{xx} - \varepsilon^p_{yy}$ $b = \left[\left(\varepsilon^p_{xx} - \sin^2\theta\right)\left(\varepsilon^p_{zz} - \sin^2\theta\right)\right.$ $\left. -\varepsilon^p_{zx}\varepsilon^p_{xz}\right]\left(\varepsilon^p_{yy}/\varepsilon^p_{zz}\right)$

has then to be solved [3], from which the corresponding components of the electric field $\mathbf{E}_p$ in layer p can be obtained.

18.1.3.3 The curl Maxwell equation

For a given set of layer-resolved electric fields the curl Maxwell equation [4, 8],

$$\mathbf{H}_p = \mathbf{n}_p \times \mathbf{E}_p \quad , \tag{18.16}$$

provides then the amplitudes of the magnetic fields $\mathbf{H}_p$ for each normal mode in layer p. It should be noted that in an anisotropic medium the refraction vector $\mathbf{n}_p$ is direction and frequency dependent [9].

18.1.3.4 The 2×2 matrix approach

Finally, continuity of the tangential components of the electric and the magnetic field at a boundary between adjacent layers leads to a set of equations, which has to be solved recursively, e.g., by means of the 2×2 matrix technique [4, 8], in order to determine, e.g., the surface reflectivity. Inspecting

Table 18.2: *Permittivity tensor in a (cubic) homogeneous, paramagnetic system and in vacuum.*

	Cubic paramagnetic homogeneous system	Vacuum
$\boldsymbol{\epsilon}^p(\omega)$	$\begin{pmatrix} \varepsilon^p_{xx} & 0 & 0 \\ 0 & \varepsilon^p_{xx} & 0 \\ 0 & 0 & \varepsilon^p_{xx} \end{pmatrix}$	$\begin{pmatrix} 1 & 0 & 0 \\ 0 & 1 & 0 \\ 0 & 0 & 1 \end{pmatrix}$

for a moment the key quantities and relations for the polar and longitudinal Kerr effect, compiled in Table 18.1, where $\mathbf{M}_p, \mathbf{q}_p, \mathbf{n}_p$ and $\boldsymbol{\epsilon}^p(\omega)$ refer in turn to the layer-resolved magnetization, direction of the incident light, (complex) refraction vector and the permittivity tensor for a system with cubic parent lattice, one can see, e.g., that there are 4 normal modes, namely the solutions of the Fresnel equation; see Eq. (18.14).

Table 18.3: *Solutions of the Helmholtz Eq. (18.15) for polar geometry and normal incidence neglecting for matters of simplicity the difference in the diagonal elements of the layer–resolved permittivity.* $E^{(k)}_{p\mu}$ *is the amplitude of the electric field in layer* p *for solution (beam)* k*. From Ref. [10].*

k	1	2	3	4
$E^{(k)}_{px}$	arbitrary	$iE^{(2)}_{py}$	arbitrary	$iE^{(4)}_{py}$
$E^{(k)}_{py}$	$iE^{(1)}_{px}$	arbitrary	$iE^{(3)}_{px}$	arbitrary
$E^{(k)}_{pz}$	0	0	0	0

Two of these four solutions are always situated in the lower half and the other two in the upper half of the complex plane. The first two solutions, $n^{(1)}_{pz}$ and $n^{(2)}_{pz}$, correspond to a "downward" (negative z-direction) and the other two, $n^{(3)}_{pz}$ and $n^{(4)}_{pz}$, to an "upward" (positive z–direction) propagation of the electromagnetic waves [4, 8].

For polar geometry these two different kinds of cases are given by

$$\begin{cases} n^{(1)}_{pz} = -\sqrt{\epsilon^p_{xx} + i\epsilon^p_{xy}} \\ n^{(2)}_{pz} = -\sqrt{\epsilon^p_{xx} - i\epsilon^p_{xy}} \end{cases} , \quad \begin{cases} n^{(3)}_{pz} = \sqrt{\epsilon^p_{xx} + i\epsilon^p_{xy}} \\ n^{(4)}_{pz} = \sqrt{\epsilon^p_{xx} - i\epsilon^p_{xy}} \end{cases} . \tag{18.17}$$

Since the polar Kerr effect is probably the conceptually easiest magneto-optical phenomenon, in the following the so-called 2×2 matrix technique

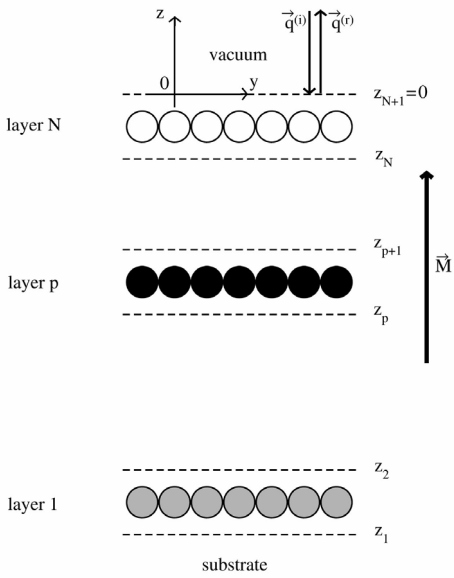

FIGURE 18.1: *The macroscopic model for polar geometry and normal incidence. The $x-$axis is perpendicular to the plane of the figure, $\vec{q}^{(i)}$ refers to the incident, $\vec{q}^{(r)}$ to the reflected wave vector. $\vec{M}$ denotes the total spontaneous magnetization of the system. From Ref. [10].*

shall be considered [10] only for this geometry. In all other cases reference will be given to the original publications.

Consider as indicated in Fig. 18.1 a multilayer system, in which each individual atomic layer acts like an anisotropic optical medium. Each of these media has two boundaries: a plane perpendicular to the surface normal at positions z_p and z_{p+1} separated by the layer thickness. The first plane to be considered lies deep inside the substrate, the last one $(N+1)$ in the vacuum.

For each solution $n_{pz}^{(k)}, k = 1, \ldots, 4$, the Helmhotz equation, see Eq. (18.15), has to be satisfied. Because not all of the equations there are independent, only two components of the electric field can be determined, keeping the others arbitrary. Following the approach originally proposed by Mansuripur [4, 8], for $n_{pz}^{(1)}$ and $n_{pz}^{(3)}$ the $x-$components of the corresponding electric field $E_{px}^{(k)}$ are chosen arbitrarily, while for $n_{pz}^{(2)}$ and $n_{pz}^{(4)}$ the $y-$components $E_{py}^{(k)}$ are arbitrary.

For polar geometry and normal incidence, the solutions of the Helmholtz equation, Eq. (18.15), are given in Table 18.3 and the corresponding components of the magnetic field as obtained from Eq. (18.16) are listed in Table 18.4.

Table 18.4: *Solutions of the curl Maxwell equation, see Eq. (18.16), for polar geometry and normal incidence neglecting the difference in the diagonal elements of the layer–resolved permittivity ϵ^p. $H^{(k)}_{p\mu}$ is the amplitude of the magnetic field in layer p for solution ("beam") k. From Ref. [10].*

k	1	2
$H^{(k)}_{px}$	$iE^{(1)}_{px}\sqrt{\epsilon^p_{xx}+i\epsilon^p_{xy}}$	$E^{(2)}_{py}\sqrt{\epsilon^p_{xx}-i\epsilon^p_{xy}}$
$H^{(k)}_{py}$	$-E^{(1)}_{px}\sqrt{\epsilon^p_{xx}+i\epsilon^p_{yx}}$	$-iE^{(2)}_{py}\sqrt{\epsilon^p_{xx}-i\epsilon^p_{xy}}$
$H^{(k)}_{pz}$	0	0
k	3	4
$H^{(k)}_{px}$	$-iE^{(3)}_{px}\sqrt{\epsilon^p_{xx}+i\epsilon^p_{xy}}$	$-E^{(4)}_{py}\sqrt{\epsilon^p_{xx}-i\epsilon^p_{xy}}$
$H^{(k)}_{py}$	$E^{(3)}_{px}\sqrt{\epsilon^p_{xx}+i\epsilon^p_{xy}}$	$iE^{(4)}_{py}\sqrt{\epsilon^p_{xx}-i\epsilon^p_{xy}}$
$H^{(k)}_{pz}$	0	0

18.1.4 Layer-dependent reflectivity matrices

The 2×2 reflectivity matrix $\mathcal{R}_p$ at the lower boundary z_p of layer p is given by [4, 8]

$$\begin{pmatrix} E^{(3)}_{px} \\ E^{(4)}_{py} \end{pmatrix} = \mathcal{R}_p \begin{pmatrix} E^{(1)}_{px} \\ E^{(2)}_{py} \end{pmatrix} = \begin{pmatrix} r_p & 0 \\ 0 & r'_p \end{pmatrix} \begin{pmatrix} E^{(1)}_{px} \\ E^{(2)}_{py} \end{pmatrix} \quad , \tag{18.18}$$

such that the tangential components of the electric and magnetic field at z_p^+, namely just above the boundary z_p, are defined by

$$\begin{cases} \begin{pmatrix} E_{px} \\ E_{py} \end{pmatrix}_{z_p^+} = \mathcal{A}\left(\mathcal{I}+\mathcal{R}_p\right) \begin{pmatrix} E^{(1)}_{px} \\ E^{(2)}_{py} \end{pmatrix} \\ \begin{pmatrix} H_{px} \\ H_{py} \end{pmatrix}_{z_p^+} = \mathcal{B}^{12}_p \left(\mathcal{I}-\mathcal{R}_p\right) \begin{pmatrix} E^{(1)}_{px} \\ E^{(2)}_{py} \end{pmatrix} \end{cases} , \tag{18.19}$$

where according to Tables 18.3 and 18.4,

$$\mathcal{A} \equiv \begin{pmatrix} 1 & i \\ i & 1 \end{pmatrix} \quad , \quad \mathcal{B}^{12}_p = \begin{pmatrix} -in^{(1)}_{pz} & -n^{(2)}_{pz} \\ n^{(1)}_{pz} & in^{(2)}_{pz} \end{pmatrix} \quad , \tag{18.20}$$

and $\mathcal{I}$ is the 2×2 unit matrix.

Using the lower boundary z_{p-1} as reference plane for the four beams in layer $p-1$, the tangential components of the electric and magnetic field at

z_p^-, situated just below the boundary z_p, are of the form

$$\begin{cases} \begin{pmatrix} E_{px} \\ E_{py} \end{pmatrix}_{z_p^-} = \mathcal{A}\left(\mathcal{C}_{p-1}^{12} + \mathcal{C}_{p-1}^{34}\mathcal{R}_{p-1}\right)\begin{pmatrix} E_{p-1x}^{(1)} \\ E_{p-1y}^{(2)} \end{pmatrix} \\ \begin{pmatrix} H_{px} \\ H_{py} \end{pmatrix}_{z_p^-} = \mathcal{B}_{p-1}^{12}\left(\mathcal{C}_{p-1}^{12} - \mathcal{C}_{p-1}^{34}\mathcal{R}_{p-1}\right)\begin{pmatrix} E_{p-1x}^{(1)} \\ E_{p-1y}^{(2)} \end{pmatrix} \end{cases} , \tag{18.21}$$

where

$$\mathcal{C}_{p-1}^{k,k+1} \equiv \begin{pmatrix} e^{-i\varphi_{p-1}^{(k)}} & 0 \\ 0 & e^{-i\varphi_{p-1}^{(k+1)}} \end{pmatrix} \quad , \quad k = 1, 3 \quad , \tag{18.22}$$

with

$$\varphi_{p-1}^{(k)} \equiv q_0 n_{p-1z}^{(k)} d_{p-1} \quad , \quad k = 1, \ldots, 4 \quad . \tag{18.23}$$

Here $d_p \equiv z_{p+1} - z_p$ is the thickness of layer p, and q_0 is the propagation constant in vacuum.

Based on Eqs. (18.19) and (18.21), the continuity of the tangential components of the electric and magnetic field at the boundary z_p implies

$$\begin{cases} \left(\mathcal{I} + \mathcal{R}_p\right)\begin{pmatrix} E_{px}^{(1)} \\ E_{py}^{(2)} \end{pmatrix} = \left(\mathcal{C}_{p-1}^{12} + \mathcal{C}_{p-1}^{34}\mathcal{R}_{p-1}\right)\begin{pmatrix} E_{p-1x}^{(1)} \\ E_{p-1y}^{(2)} \end{pmatrix} \\ \mathcal{B}_p^{12}\left(\mathcal{I} - \mathcal{R}_p\right)\begin{pmatrix} E_{px}^{(1)} \\ E_{py}^{(2)} \end{pmatrix} = \mathcal{B}_{p-1}^{12}\left(\mathcal{C}_{p-1}^{12} - \mathcal{C}_{p-1}^{34}\mathcal{R}_{p-1}\right)\begin{pmatrix} E_{p-1x}^{(1)} \\ E_{p-1y}^{(2)} \end{pmatrix} \end{cases} , \tag{18.24}$$

such that by eliminating the electric field vectors, one immediately gets

$$\mathcal{D}_{p-1}\left(1 + \mathcal{R}_p\right) = \mathcal{B}_p^{12}\left(\mathcal{I} - \mathcal{R}_p\right) \quad , \tag{18.25}$$

where

$$\mathcal{D}_{p-1} \equiv \mathcal{B}_{p-1}^{12}\left(\mathcal{C}_{p-1}^{12} - \mathcal{C}_{p-1}^{34}\mathcal{R}_{p-1}\right)\left(\mathcal{C}_{p-1}^{12} + \mathcal{C}_{p-1}^{34}\mathcal{R}_{p-1}\right)^{-1} \quad . \tag{18.26}$$

The layer-dependent reflectivity matrices $\mathcal{R}_p$ are therefore given in terms of the following simple recursion relation:

$$\mathcal{R}_p = \left(\mathcal{B}_p^{12} + \mathcal{D}_{p-1}\right)^{-1}\left(\mathcal{B}_p^{12} - \mathcal{D}_{p-1}\right) \quad , \quad p = 1, \ldots, N \quad . \tag{18.27}$$

To start this procedure one needs to know the 2×2 matrix $\mathcal{D}_0$ corresponding to the substrate. This in turn implies that the tangential components of the electric and magnetic field at z_1^- have to be taken into account properly. However, since the substrate is considered to be (and treated as) a semi–infinite bulk without any boundaries, $\mathcal{R}_0 = 0$ [4, 8] and therefore $\mathcal{D}_0 = \mathcal{B}_0^{12}$, which according to Eq. (18.20) requires to specify the permittivity of the substrate.

18.1.4.1 Surface reflectivity matrix

In the vacuum region, see the corresponding permittivity tensor in Table 18.2, only the superposition of the incident (i) and reflected (r) electromagnetic waves ("beams") has to be dealt with. For polar geometry and normal incidence these beams are related to each other via the so-called *surface reflectivity matrix* R_{surf} ,

$$\begin{pmatrix} E^{(\mathrm{r})}_{vac,x} \\ E^{(\mathrm{r})}_{vac,y} \end{pmatrix} = R_{surf} \begin{pmatrix} E^{(\mathrm{i})}_{vac,x} \\ E^{(\mathrm{i})}_{vac,y} \end{pmatrix} \equiv \begin{pmatrix} r_{xx} & r_{xy} \\ -r_{xy} & r_{xx} \end{pmatrix} \begin{pmatrix} E^{(\mathrm{i})}_{vac,x} \\ E^{(\mathrm{i})}_{vac,y} \end{pmatrix} \quad , \tag{18.28}$$

The tangential components of the electric and magnetic field at z^{+}_{N+1}, namely just above the interface between the vacuum and the surface, are given by

$$\begin{cases} \begin{pmatrix} E_{vac,x} \\ E_{vac,y} \end{pmatrix}_{z^{+}_{N+1}} = (\mathcal{I} + R_{surf}) \begin{pmatrix} E^{(\mathrm{i})}_{vac,x} \\ E^{(\mathrm{i})}_{vac,y} \end{pmatrix} \\ \begin{pmatrix} H_{vac,x} \\ H_{vac,y} \end{pmatrix}_{z^{+}_{N+1}} = \left(B^{12}_{vac} + B^{34}_{vac} R_{surf}\right) \begin{pmatrix} E^{(\mathrm{i})}_{vac,x} \\ E^{(\mathrm{i})}_{vac,y} \end{pmatrix} \end{cases} , \tag{18.29}$$

where

$$B^{12}_{vac} = \begin{pmatrix} 0 & 1 \\ -1 & 0 \end{pmatrix} \quad , \quad B^{34}_{vac} = \begin{pmatrix} 0 & -1 \\ 1 & 0 \end{pmatrix} \ . \tag{18.30}$$

The continuity of the tangential components of the electric and magnetic fields at the vacuum and surface layer interface, $z_{N+1} = 0$, can now be written as

$$\begin{cases} (\mathcal{I} + R_{surf}) \begin{pmatrix} E^{(\mathrm{i})}_{vac,x} \\ E^{(\mathrm{i})}_{vac,y} \end{pmatrix} = \mathcal{A} \left(\mathcal{C}^{12}_{N} + \mathcal{C}^{34}_{N} \mathcal{R}_{N}\right) \begin{pmatrix} E^{(1)}_{Nx} \\ E^{(2)}_{Ny} \end{pmatrix} \\ \left(B^{12}_{vac} + B^{34}_{vac} R_{surf}\right) \begin{pmatrix} E^{(\mathrm{i})}_{vac,x} \\ E^{(\mathrm{i})}_{vac,y} \end{pmatrix} = \mathcal{B}^{12}_{N} \left(\mathcal{C}^{12}_{N} - \mathcal{C}^{34}_{N} \mathcal{R}_{N}\right) \begin{pmatrix} E^{(1)}_{Nx} \\ E^{(2)}_{Ny} \end{pmatrix} \end{cases} , \tag{18.31}$$

or, by eliminating the electric field vectors, as

$$\mathcal{F}_{N} \left(1 + R_{surf}\right) = B^{12}_{vac} + B^{34}_{vac} R_{surf} \quad , \tag{18.32}$$

where

$$\mathcal{F}_{N} \equiv \mathcal{B}^{12}_{N} \left(\mathcal{C}^{12}_{N} - \mathcal{C}^{34}_{N} \mathcal{R}_{N}\right) \left(\mathcal{C}^{12}_{N} + \mathcal{C}^{34}_{N} \mathcal{R}_{N}\right)^{-1} \mathcal{A}^{-1} = \mathcal{D}_{N} \mathcal{A}^{-1} \quad . \tag{18.33}$$

Thus for the surface reflectivity matrix one finally gets

$$R_{surf} = \left(\mathcal{F}_{N} - B^{34}_{vac}\right)^{-1} \left(B^{12}_{vac} - \mathcal{F}_{N}\right) \quad , \tag{18.34}$$

where as defined in Eq. (18.28)

$$R_{surf} = \begin{pmatrix} r_{xx} & r_{xy} \\ -r_{xy} & r_{xx} \end{pmatrix} \quad . \tag{18.35}$$

18.1.4.2 Self–consistent layer–resolved permittivities

In order to calculate for a homogeneous, anisotropic layer p the corresponding dielectric tensor from the *inter–* and *intra–*layer permittivities based on Eq. (18.13), the following linear system of equations,

$$\begin{pmatrix} \epsilon^p_{xx} & \epsilon^p_{xy} \\ -\epsilon^p_{xy} & \epsilon^p_{xx} \end{pmatrix} \begin{pmatrix} E_{px} \\ E_{py} \end{pmatrix} = \sum_{q=1}^{N} \begin{pmatrix} \epsilon^{pq}_{xx} & \epsilon^{pq}_{xy} \\ -\epsilon^{pq}_{xy} & \epsilon^{pq}_{xx} \end{pmatrix} \begin{pmatrix} E_{qx} \\ E_{qy} \end{pmatrix} \quad , \tag{18.36}$$

has to be solved; see Eq. (18.11). For E_p one can make the following ansatz [11]:

$$\begin{pmatrix} E_{px} \\ E_{py} \end{pmatrix} \equiv \begin{pmatrix} E_{px} \\ E_{py} \end{pmatrix}_{z=z_p^+ + \frac{d_p}{2}} = \mathcal{A} \left[\left(\mathcal{C}_p^{12}\right)^{\frac{1}{2}} + \left(\mathcal{C}_p^{34}\right)^{\frac{1}{2}} \mathcal{R}_p \right] \begin{pmatrix} E^{(1)}_{px} \\ E^{(2)}_{py} \end{pmatrix} \quad , \tag{18.37}$$

where, as in Eq. (18.22),

$$\left(\mathcal{C}_p^{k,k+1}\right)^{\frac{1}{2}} \equiv \begin{pmatrix} e^{-iq_0 \tilde{n}^{(k)}_{pz} \frac{d_p}{2}} & 0 \\ 0 & e^{-iq_0 \tilde{n}^{(k+1)}_{pz} \frac{d_p}{2}} \end{pmatrix} \quad , \quad k = 1, 3 \quad . \tag{18.38}$$

By using the corresponding continuity equation of the tangential components of the electric field at the boundaries, one then obtains the layer–resolved permittivities as a weighted sum of permittivities,

$$\begin{pmatrix} \epsilon^p_{xx} & \epsilon^p_{xy} \\ -\epsilon^p_{xy} & \epsilon^p_{xx} \end{pmatrix} = \sum_{q=1}^{N} W_{pq} \, \boldsymbol{\epsilon}^{pq} \quad . \tag{18.39}$$

where

$$W_{pq} = \mathcal{A} \left(\prod_{k=0}^{N-q} \mathcal{W}_{q+k} \right) \left(\prod_{k=0}^{N-p} \mathcal{W}_{p+k} \right)^{-1} \mathcal{A}^{-1} \quad , \tag{18.40}$$

with

$$\mathcal{W}_{p+k} = \left(\mathcal{I} + \mathcal{R}_{p+k}\right) \left(\mathcal{C}^{12}_{p+k} + \mathcal{C}^{34}_{p+k} \mathcal{R}_{p+k}\right)^{-1} \quad , \quad k = 1, \ldots, N-p \quad , \tag{18.41}$$

and

$$\mathcal{W}_p = \left[\left(\mathcal{C}_p^{12}\right)^{\frac{1}{2}} + \left(\mathcal{C}_p^{34}\right)^{\frac{1}{2}} \mathcal{R}_p \right] \left(\mathcal{C}^{12}_{p} + \mathcal{C}^{34}_{p} \mathcal{R}_{p}\right)^{-1} \quad , \quad k = 0 \quad . \tag{18.42}$$

Because the matrices $\mathcal{W}_{p+k}$ contain $\mathcal{R}_p$, $\mathcal{C}_p^{12}$ and $\mathcal{C}_p^{34}$, which in turn depend on the layer–resolved permittivities $\epsilon^p_{\mu\nu}(\omega)$, Eq. (18.39) has to be solved iteratively. This self–consistent procedure can, e.g., be started by setting all weighting matrices W_{pq} in Eq. (18.40) to unity, i.e., by neglecting the phase

differences of the electromagnetic waves between the lower and upper boundaries in each layer p. In the zero-th iteration the layer-resolved permittivities $\epsilon^{p}_{\mu\nu}(\omega)$ are simply given by

$$\epsilon^{p}_{\mu\nu}(\omega)^{(0)} = \sum_{q=1}^{N} \epsilon^{pq}_{\mu\nu}(\omega) \quad . \tag{18.43}$$

It turned out, however, that in most cases the $\epsilon^{p}_{\mu\nu}(\omega)^{(0)}$ differ only very little from their self-consistent counterparts and can therefore be used as such to describe magneto-optical phenomena sufficiently accurately [11].

18.1.5 Kerr rotation and ellipticity angles

It should be noted that in evaluating the surface reflectivity matrix in terms of the approach outlined above for the polar Kerr effect, all (optical) reflections and interferences have been taken into account.

18.1.5.1 Polar magneto-optical Kerr effect

Expressed in spherical coordinates, one immediately obtains the complex reflectivity of the right (+) and left–handed (-) circularly polarized light as

$$r_{\pm} = r_{xx} \mp i r_{xy} \; = \frac{E^{(\mathrm{r})}_{\pm}}{E^{(\mathrm{i})}} = |r_{\pm}|\, e^{i\Delta_{\pm}} \quad , \tag{18.44}$$

where $E^{(\mathrm{r})}_{\pm}$ is the complex amplitude of the reflected right- and left-handed circularly polarized light and $E^{(\mathrm{i})}$ that of the incident light. The Kerr rotation θ_{K} and ellipticity ϵ_{K} angles are then given by

$$\theta_{\mathrm{K}} = -\frac{1}{2}(\Delta_{+} - \Delta_{-}) \quad , \tag{18.45}$$

$$\epsilon_{\mathrm{K}} = -\frac{|r_{+}| - |r_{-}|}{|r_{+}| + |r_{-}|} \quad , \tag{18.46}$$

or, expressed as a complex Kerr angle, as

$$\Phi_{\mathrm{K}} = \theta_{\mathrm{K}} + i\epsilon_{\mathrm{K}} \quad . \tag{18.47}$$

18.1.5.2 Longitudinal magneto-optical Kerr effect

In the case of the longitudinal magneto-optical Kerr effect and p-polarized incident light the complex Kerr angle is given by

$$\Phi_{\mathrm{K}} \sim -\frac{r_{xy}}{r_{yy}} \cos\Theta \quad , \tag{18.48}$$

see also Table 18.1, where the elements of the surface reflectivity matrix have to be calculated according to the procedure described in Ref. [12].

18.1.5.3 Approximate formulations

In viewing a layered system to consist only of two media, namely vacuum and the rest, an approximate formulation of the complex Kerr angle (polar geometry) was suggested [2] in an attempt to extract the optical conductivity tensor directly from experimental measurements,

$$\Phi_{\mathrm{K}}^{[2]} = \frac{\sigma_{xy}(\omega)}{\sigma_{xx}(\omega)}(1 - \frac{4\pi i}{\omega}\sigma_{xx}(\omega))^{-1/2} \quad . \tag{18.49}$$

Since this formulation can still be found in the literature, it has to be pointed out that of course $\Phi_{\mathrm{K}}^{[2]}$ in Eq. (18.49) cannot account for any contributions from the interior or surface near layers in a multilayer system: the vacuum and the actual system are considered as homogeneous bulk-like systems. For matters of distinction to Kerr angles evaluated using the above introduced 2×2 matrix techniques, those based on the two-media approach carry a suffix "two".

18.2 The importance of the substrate

Just as in the case of electric transport experimentally determined optical properties are mostly only available for "bulk"-like systems. For this reason in Fig. 18.2 the calculated reflectance of fcc bulk Pt for the (100), (110) and (111) surface orientations is compared with available experimental data. In the theoretical data shown there and in Fig. 18.3 bulk Pt was considered as a layered system (two-dimensional translational symmetry!) of the type (hkl)Pt/Pt$_n$/Pt(hkl), where (hkl) denotes the surface orientation, and n layers of Pt separate the two semi-infinite systems. For this system it was found that for $n \geq 15$ very good agreement with the various available experimental data can be achieved.

Fig. 18.3, by the way, indicates that by using Eqs. (18.1) - (18.2) to calculate the optical conductivity tensor the range of accessible photon energies is restricted from below by δ, namely the so-called life-time broadening.

In Fig. 18.4 the convergence of the permittivity for fcc Cu with respect to the number of Cu layers between the two semi-infinite Cu is displayed; i.e., the permittivity of Cu(100)/Cu$_n$/Cu(100) is shown as a function of n. It should be noted that – as was explained above – the permittivity of the substrate has to be known in order to calculate the surface reflectivity matrix for a chosen magnetic multilayer system. Again it seems that for $n \geq 15$ the diagonal elements of the permittivity tensor no longer change when increasing n. This, as should be noted, is an equivalent way to express the boundary conditions to be fulfilled in theoretical magneto-optical descriptions. Using, for example,

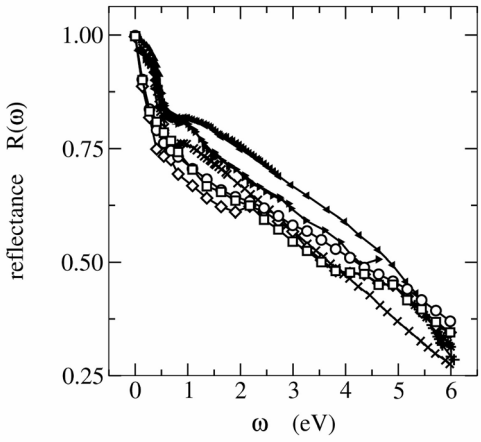

FIGURE 18.2: *Reflectance of fcc Pt bulk as calculated for the (100), (110) and (111) surface orientation (diamonds, circles and squares). Crosses, pluses, stars, and triangle right, left and up refer to various experimental data. From Ref. [11].*

Cu as a substrate implies, therefore, one must consider the following system (boundary conditions)

$$\mathrm{Cu}(100)/\mathrm{Cu}_{n\geq 15}/\text{magnetic multilayer}$$

for a reliable evaluation of Kerr rotation and ellipticity angles.

18.3 The Kerr effect and interlayer exchange coupling

In Chapter 11 a direct comparison between the experimental data and theoretical calculations was shown for $\mathrm{Cu_4Ni_8Cu}_n\mathrm{Ni_9/Cu}(001)$ trilayers considering there the interlayer exchange and the magnetic anisotropy energy. The type of coupling (ferromagnetic or antiferromagnetic) can in principle be also determined experimentally by measuring Kerr angles at vanishing external (magnetic) field as a function of the spacer thickness n.

In Fig. 18.5 a comparison between the calculated interlayer exchange energy and Kerr rotation and ellipticity angles is displayed. As can be seen from this figure the Kerr angles map very nicely to the different types of coupling: in the case of antiferromagnetic coupling both Kerr angles are negative and distinctly different in size from those when ferromagnetic coupling applies.

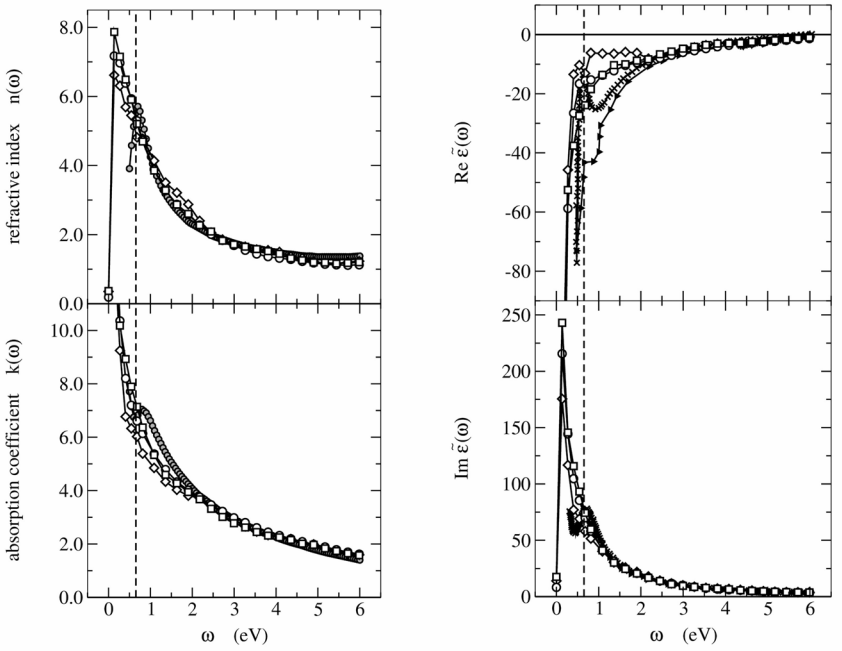

FIGURE 18.3: *Left: Optical constants of fcc Pt bulk as calculated for the (100), (110) and (111) surface orientation (diamonds, circles and squares). Available experimental data are displayed as grey circles. Right: Permittivity of fcc Pt bulk as calculated for the (100), (110) and (111) surface orientation (diamonds, circles and squares). Crosses, pluses, stars, triangles right and down refer to various experimental data. The dotted line marks the photon energy that equals the used lifetime broadening of* $\delta = 0.653$ *eV. From Ref. [11].*

In order to find out which elements of the layer-resolved permittivity tensor give rise to positive or negative Kerr angles, in Figs. 18.6 and 18.7 the xx- and xy-elements are displayed for one particular system, namely $Cu_4Ni_8Cu_{10}Ni_9$/Cu(001) considering a ferro- as well as an antiferromagnetic configuration. As can be seen the xx-elements reflect hardly any dependence on the magnetic configuration (the zz-elements, not shown here are even more boring), all the differences to be eventually mapped in the Kerr angles arise from the xy-elements in the rotated Ni slab and the adjacent half of the Cu spacer.

Although the Kerr angles cannot be directly related to the total magnetic moment of the system,

$$m = \sum_{p=1}^{N} m_p \quad ,$$

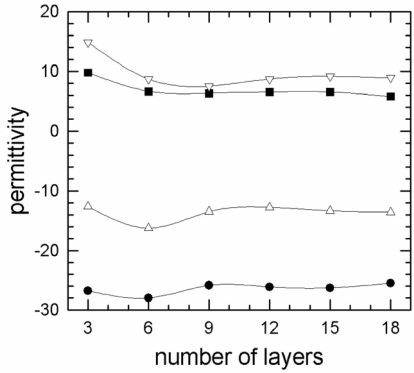

FIGURE 18.4: *Convergence of the permittivity of Cu bulk with respect to the number of sandwiched Cu layers in Cu(100)/Cu$_n$/Cu(100). Circles, squares, up and down triangles denote in turn Re(ε_{xx}), Im(ε_{xx}), Re(ε_{zz}) and Im(ε_{zz}). From Ref. [14].*

it is tempting to give at least an interpretation of Fig. 18.7 in terms of layer-dependent magnetic moments weighted by "optical factors". Neglecting multiple reflections and interferences, it is simple to analyze an incident wave reflected at a particular layer p. Assuming no further reflections, the light travels back to the surface with a reduced amplitude A'. The space-like part of a plane wave traveling in z direction is given by $A\exp(ikz)$. The wave number k is complex; thus the real part is responsible for the oscillation and the imaginary part for the absorption of the wave. Using layer-resolved complex wave numbers the damped amplitude A'_p can be obtained as

$$\begin{aligned} A'_p &= A_0 \prod_{q=0}^{N-p+1} \prod_{q=N-p+1}^{0} \exp\left[i\, Im(k_{N-q}) \cdot d_{N-q}\right] \\ &= A_0 \prod_{q=0}^{N-p+1} \exp\left[2i\, Im(k_{N-q}) \cdot d_{N-q}\right] \quad . \end{aligned} \tag{18.50}$$

If the penetration depth is defined as the thickness at which the amplitude of the incident wave is reduced to A_0/e, where e is Euler's constant, the number of layers s needed for this purpose has to be determined from the below relation

$$\sum_{q=0\in\{1,\ldots,s\}} Im(k_{N-q}) \cdot d_{N-q} = -1 \quad . \tag{18.51}$$

It should be noted that for the penetration depth only light traveling in direction of the substrate is considered; therefore in Eq. (18.51) the factor 2 is

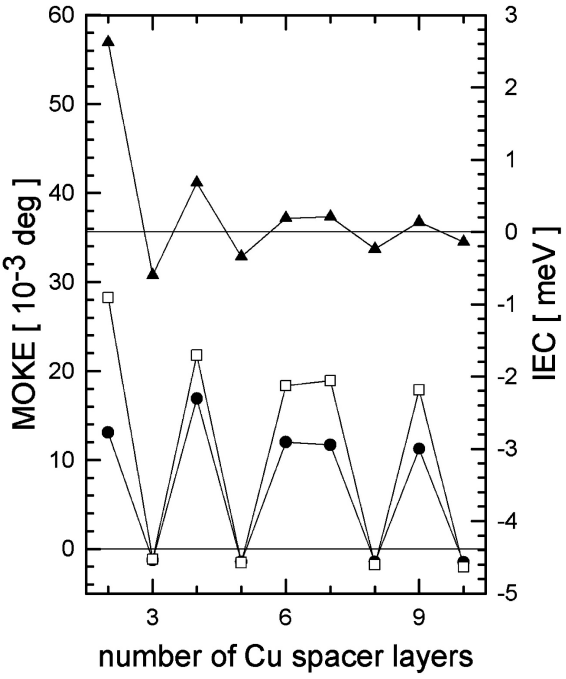

FIGURE 18.5: *Comparison between the theoretical interlayer exchange energy and the magneto-optical Kerr angles for* $Cu_4Ni_8Cu_nNi_9/Cu(100)$ *with respect to the number of Cu spacer layers. Triangles denote the theoretical interlayer exchange energy results of Ref. [13], circles and squares the calculated Kerr angles* θ_K *and* ε_K*, respectively. From Ref. [14].*

dropped. The bulk-value of the refractive index of pure Cu, e.g., leads to a penetration depth of $s = 68.5$ layers.

Assuming that the Kerr data in Fig. 18.5 can be interpreted by a sum of layer-resolved magnetic moments weighted by the damping factor of a wave reflected at the respective atomic layer, the total "damped" magnetic moment is given by

$$m' = \sum_{p=1}^{N} m'_p \quad , \quad m'_p = \frac{A'_p}{A_0} \cdot m_p \quad . \tag{18.52}$$

As can be seen from Table 18.5 this total damped magnetic moment m' turns out to show the same pattern with respect to the coupling as the Kerr angles.

Clearly enough this is only a very qualitative interpretation, which, however, indicates strongly that whenever spectroscopic data are to be interpreted appropriate penetration depths have to be taken into account.

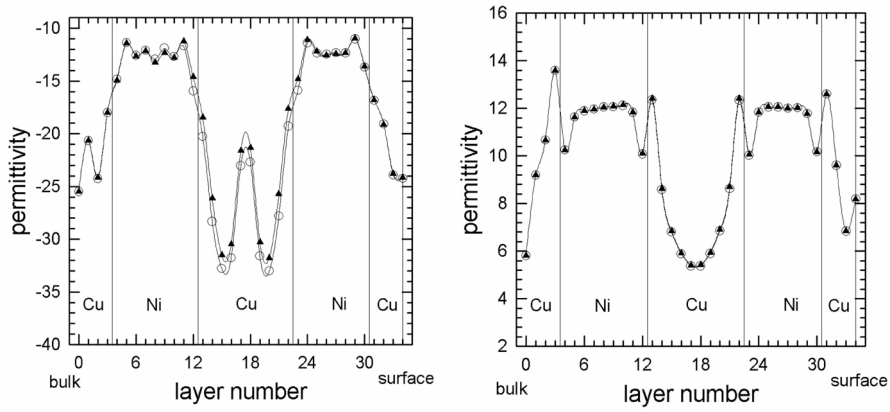

FIGURE 18.6: *Comparison of the layer-resolved complex permittivity for* $Cu_4Ni_8Cu_{10}Ni_9/Cu(100)$ *in the antiferromagnetic (triangles) and the ferromagnetic (circles) configuration.* Left: $Re(\varepsilon_{xx})$. Right: $Re(\varepsilon_{yy})$. *From Ref. [14].*

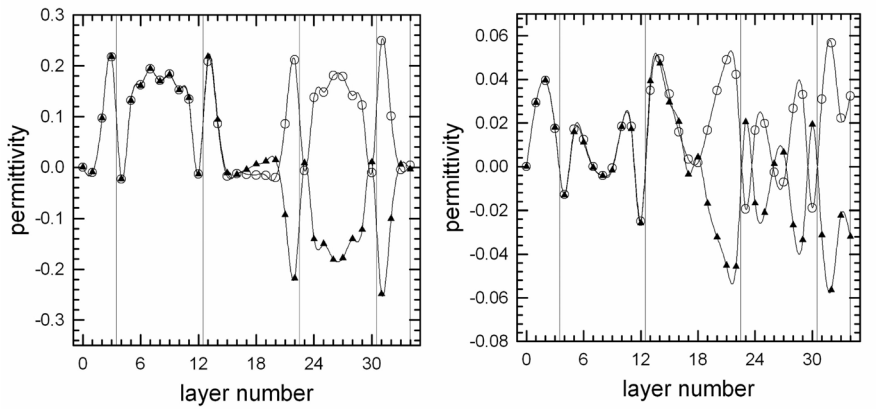

FIGURE 18.7: *Comparison of the layer-resolved complex permittivity for* $Cu_4Ni_8Cu_{10}Ni_9/Cu(100)$ *in the antiferromagnetic (triangles) and the ferromagnetic (circles) configuration.* Left: $Re(\varepsilon_{xy})$. Right: $Im(\varepsilon_{xy})$. *From Ref. [14].*

Table 18.5: *Comparison of the theoretical Kerr angles θ_K and ϵ_K with the damped (m') and undamped (m) total magnetic moments; see Eq. (18.52). From Ref. [14].*

	FM	AFM
θ_K, ϵ_K	> 0	< 0
m'	> 0	< 0
m	> 0	> 0

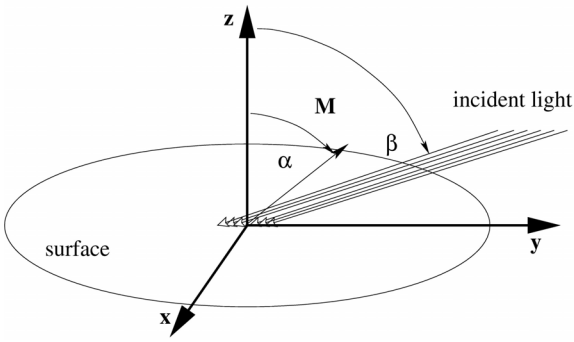

FIGURE 18.8: *Kerr set-up in the case of p-polarized incident light. Here α and β specify the orientation of the magnetization* **M** *and the direction of the incident light, respectively. Both are specified with respect to the surface normal. Note that the magnetization always lies in the plane of incidence. From Ref. [16].*

18.4 The Kerr effect and the magnetic anisotropy energy

Another system that was already discussed in the context of reorientation transitions, namely Fe_n/Au(100), see Chapter 11, was first studied experimentally using the Kerr effect. The experimental evidence [15] for the reorientation transition seemed to be quite clear: if the easy axis was in-plane then the longitudinal Kerr signal yielded a square hysteresis loop while the polar Kerr signal produced no hysteresis. If, however, the easy axis was normal to the film surface then the polar signal yielded a square hysteresis loop and the longitudinal one showed no hysteresis. In the regime of canted magnetization, hysteresis loops related to both configurations occurred. At a given film thickness the Kerr intensity was identified with the height of the hysteresis loop in the remanent state.

In order to describe this experiment properly, in principle both the angle of the incident light as well as that of the orientation of the magnetization with respect to the surface normal, see Fig. 18.8, has to be varied. In the theoretical investigations reported in [16], however, the range of angles investigated was restricted to the following cases:

angle	range	restriction
$\alpha:$	$0 \leq \alpha \leq 90^\circ$	$;\beta = 0$
$\beta:$	$0 \leq \beta \leq 90^\circ$	$;\alpha = 0, 90^\circ$

Since in the experimental study [15] the polar and longitudinal Kerr intensities are given by the height of the hysteresis loops in the remanent state, the reorientation transition from a perpendicular to an in-plane orientation of the magnetization shows up in a strong decrease of the Kerr intensity for normal incidence ($\beta = 0^0$) and a rather moderate increase of the Kerr intensity for grazing incidence ($\beta = 90^0$); see the upper part of Fig. 18.9. By considering the actual ground-state orientations of the magnetization resulting from magnetic anisotropy energy calculations, see also Fig. 11.1, the lower part of this figure shows the calculated Kerr rotation angles for two different angles of incidence, namely, for $\beta = 0^0$ and 70^0. Although Kerr angles and Kerr intensities cannot be directly related to each other, it is not surprising at all that their respective dependence on the number of Fe layers is in good qualitative agreement with the experimental data.

As can be immediately seen from Fig. 18.9, the calculated Kerr rotation angles for the system $Fe_n/Au(100)$ in the magnetic ground state, describe remarkably well the magnetic reorientation transition: the perpendicular orientation of the magnetization is preferred below 3 ML, whereas above this Fe thickness the ground state is characterized by an in-plane orientation of the magnetization, which for normal incidence yields zero Kerr rotation angles.

In the case of oblique incidence (say for $\beta = 70^0$) non-vanishing Kerr rotation angles are obtained for both normal-to-plane ($n \leq 3$) and in-plane ($n > 4$) ground-state magnetizations and the reorientation transition appears as a drop in θ_K. It is interesting to note that for $\beta = 70^0$ the value of θ_K is by a factor of 2 to 3 larger than that for $\beta = 0^0$ ($n \leq 3$).

It should be noted that the theoretical results shown in Fig. 18.9 are – as already mentioned – based on the magnetic ground states ($\alpha = 0$ or 90°) found from magnetic anisotropy calculations. Fig. 18.9 serves as an impressive example for the claim that whenever all theoretical descriptions are included on the same footing, quantities actually measured in experiment can be reproduced very well.

As can be seen from the left part of Fig. 18.10 the Kerr rotation angle for oblique incidence increases independent of the Fe thickness until $\beta = 70^0$, where a maximum of θ_K is reached; increasing the incidence angle β beyond 70^0 causes a continuous decrease of the Kerr rotation angle. It seems therefore

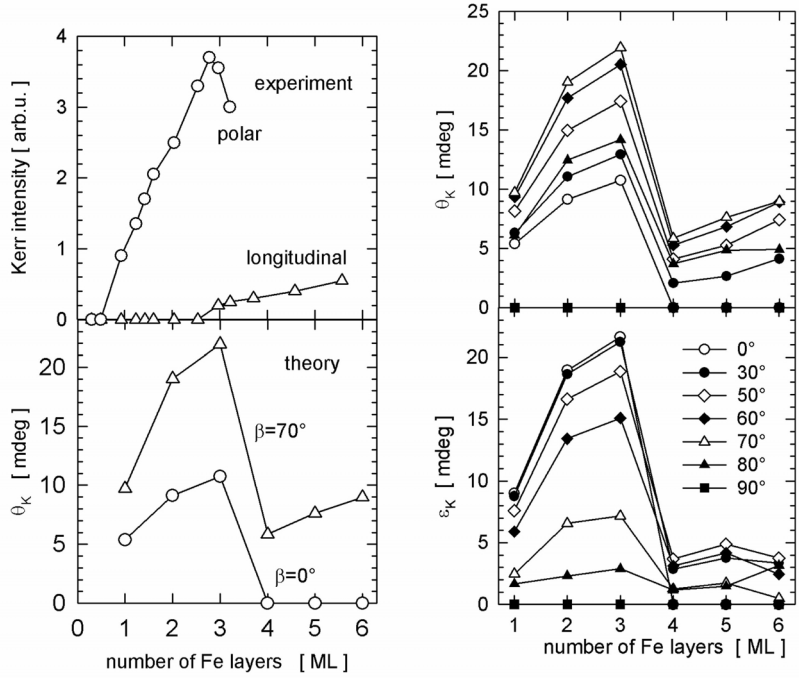

FIGURE 18.9: *Left: Top: Surface magneto-optical Kerr experiments by Liu and Bader [15]. Circles denote the measured data for the polar, triangles for the longitudinal Kerr set-up. Bottom: calculated values of the Kerr rotation angle θ_K in the case of p-polarized incident light and for the magnetic ground state of $Fe_n/Au(100)$. Circles mark the theoretical results for a normal incidence ($\beta = 0^0$) and triangles for an incidence of $\beta = 70^0$. Right: Calculated Kerr rotation angle (upper part) and ellipticity angle (lower part) for different angles of incidence for the corresponding magnetic ground state of $Fe_n/Au(100)$. See also Fig. 18.8. From Ref. [16].*

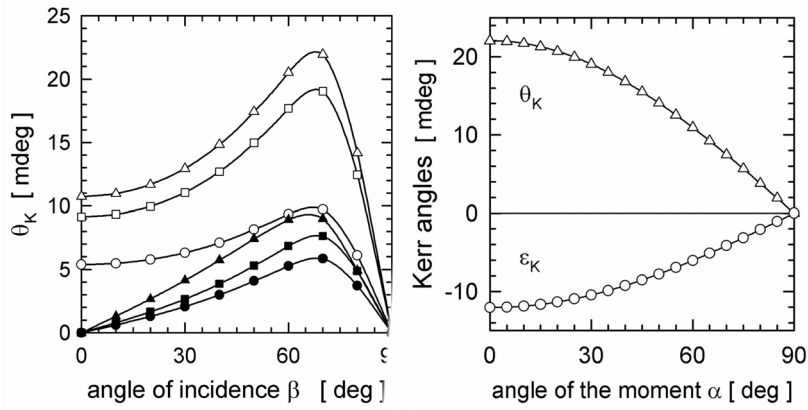

FIGURE 18.10: *Left: Calculated Kerr rotation angle as a function of the angle of incidence β and for different thicknesses of Fe films on Au(100). Open circles, squares and triangles refer to* 1, 2 *and* 3, *full circles, squares and triangles to* 4, 5 *and* 6 *ML of Fe on the top of Au(100). Right: Calculated Kerr angles in the case of normal incidence for Fe_4/Au(100), $\beta = 0^0$, as a function of the angle α; see also Fig. 18.8. From Ref. [16].*

that two regimes of $\theta_K(\beta)$ values can be distinguished: one for $n \leq 3$ ($\alpha = 0^0$) where $\theta_K(\beta = 0^0) \neq 0$, and one for $n > 4$ ($\alpha = 90^0$) with $\theta_K(\beta = 0^0) = 0$.

For the particular case of Fe_4/Au(100) the Kerr angles are displayed in the right part of Fig. 18.10 for normal incidence ($\beta = 0^0$) and different orientations of the magnetization, $0 \leq \alpha \leq 90^0$. As can be seen from this figure, both $\theta_K(\alpha)$ and $\varepsilon_K(\alpha)$ show an almost perfect $\cos(\alpha)$ dependence. This finding supports independently the experimentally known fact that for normal incidence the Kerr rotation angle is direct proportional to the normal component of the magnetization.

For the case of normal incidence Fig. 18.11 offers an interesting view of the Kerr angles, $\theta_K(\alpha)$ and $\varepsilon_K(\alpha)$, since in this figure each entry refers to a particular value of α, the abscissa being, however, the anisotropy energy $E_a(\alpha)$. Obviously points along the ordinate ($E_a = 0$) correspond to $\alpha = 90^0$, while those along the abscissa belong to $\alpha = 0^0$. For $n \leq 3$ all curves fall into the regime of positive anisotropy energies (perpendicular orientation of the magnetization), while those for $n \geq 4$ refer to that of negative anisotropy energies (in-plane orientation). The reorientation transition in Fe_n/Au(100) is thus particularly clearly visualized.

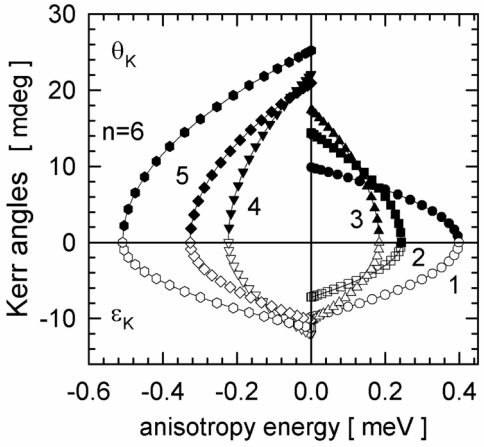

FIGURE 18.11: *Calculated Kerr angles displayed as a function of the magnetic anisotropy energy for different thicknesses of the Fe film on Au(100). Full symbols refer to Kerr rotation, open symbols to Kerr ellipticity angles. The data for this figure were obtained by varying the angle of magnetization α while the angle of incidence is fixed to $\beta = 0^0$; see also Fig. 18.8. From Ref. [16].*

18.5 The Kerr effect in the case of repeated multilayers

Magneto-optical storage media still promise to provide the highest storage densities with high data security at respectable data transfer rates. It is generally believed that the highest areal densities can be achieved by means of perpendicular recording. In particular, systems containing Co/Pd or Co/Pt multilayers appear to be most suitable for this purpose.

Experimental investigations of Co/Pt superstructures showed that the magneto-optical and the magnetic properties are not independent of each other: the former scale with the ratio of the thicknesses of Co to Pt, t_{Co}/t_{Pt}, the latter depend inversely on this ratio [17]. The superstructure with a Co thickness of $t_{Co} = 4$ Å and a Pt thickness of $t_{Pt} = 12.7$ Å showed the highest Kerr rotation with a 100% remanence and a positive nucleation field at a wave length of $\lambda = 820$ nm. Assuming a (111) surface orientation and a perpendicular lattice spacing of 2.265 Å, the thicknesses of this superstructure in monolayers (ML) are $t_{Co} = 1.8$ ML and $t_{Pt} = 5.6$ ML. According to Ref. [18] a Co thickness t_{Co} of less than 4 Å (1.8 ML) and a Pt thickness t_{Pt} greater than 12 Å (5.3 ML) is needed to achieve perpendicular magnetism and a 100% remanence.

Fig. 18.12 shows the diagonal elements of the dielectric tensor, ε^p_{xx} and ε^p_{zz}

for $(Co_2Pt_6)_5$/Pt(111), i.e., for a Co/Pt superstructure with the unit Co_2Pt_6 five times repeated. As can be seen the dielectric tensor is quite anisotropic, since $\varepsilon^p_{xx} \neq \varepsilon^p_{zz}$. This difference results from effects of spin-orbit coupling in the presence of an internal magnetic field. Note that $\varepsilon^p_{xx} = \varepsilon^p_{zz}$ only for the paramagnetic layers of the substrate Pt(111).

As was seen already in the previous example of the trilayer system Cu_4Ni_8 $Cu_{10}Ni_9$/Cu(001) it is mostly the non-vanishing off-diagonal elements of the dielectric tensor ε^p_{xy} that lead to magneto-optical effects. From Fig. 18.12, it is evident that $\left|\varepsilon^p_{xy}\right|$ is not largest in the Co layers as the layer-dependent moments in this figure perhaps suggest, but in the Pt layers adjacent to the Co layers. This implies that the presence of the Pt slabs is decisive for the magneto-optical Kerr effect.

Assuming a finite penetration depth with an exponential damping behavior the Kerr rotation angle $\theta_K(n)$, n denoting the number of repetitions of the unit Co_2Pt_6, can be extrapolated to an arbitrary large n in the following manner

$$\theta_K(n) = \theta_K(1) \sum_{l=0}^{n-1} e^{-\gamma l} = \theta_K(1)\, \frac{1 - e^{-\gamma n}}{1 - e^{-\gamma}} \quad , \tag{18.53}$$

where γ is the damping factor. From Eq. (18.53) it immediately follows that the Kerr rotation angle shows the below asymptotic behavior

$$\lim_{n\to\infty} \theta_K(n) = \theta_K(1)\, \frac{1}{1 - e^{-\gamma}} \quad . \tag{18.54}$$

In the left part of Fig. 18.14 the Kerr angles θ_K and ε_K are shown versus the number of repetitions of the unit Co_2Pt_5; the right part of this figure illustrates the use of Eq. (18.54). In using this fitting procedure the asymptotic value of θ_K for Co_2Pt_6 superstructures on Pt(111) amounts to 0.2106°.

In Fig. 18.14 the experimental and the calculated data for the magneto-optical Kerr rotation angle θ_K, the Kerr ellipticity angle ε_K, and the magnitude of the complex Kerr angle $\Phi_K = \sqrt{\varepsilon_K^2 + \theta_K^2}$ are displayed versus the photon energy. As can be seen, θ_K exhibits a maximum at about 3.5 eV for $n = 1, 3, 6$, for $n = 6$ a local maximum occurs at about 1.5 eV. The dependence of θ_K on the repetition number is clearly visible: the peak at approximately 3.5 eV becomes more pronounced. Most experimental studies reported a peak at about 4 eV, depending a bit on the Kerr geometrical set-up actually used and – of course – on the composition of the Co/Pt units.

18.6 How surface sensitive is the Kerr effect?

ROTMOKE was originally suggested by Mattheis and Quednau [21] and is based on the longitudinal magneto–optical Kerr effect using a sufficiently large

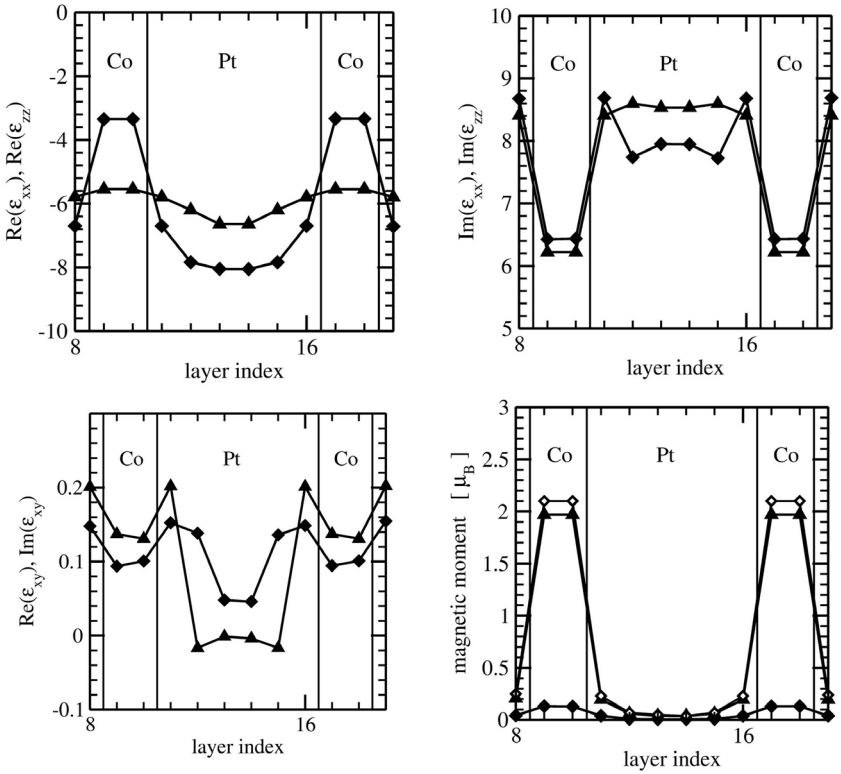

FIGURE 18.12: *$(Co_2Pt_6)_5/Pt(111)$. Top: diagonal elements of the layer-resolved complex dielectric tensor ε^p_{xx} and ε^p_{zz}. Note that only one unit Co_2Pt_6 is shown. Diamonds refer to xx-elements, triangles to the zz-elements. Bottom, left: off-diagonal elements of the layer-resolved complex dielectric tensor, ε^p_{xy}. Diamonds denote $Re(\varepsilon^p_{xy})$, triangles $Im(\varepsilon^p_{xy})$. Bottom, right: Layer-resolved magnetic moments. Full diamonds denote the spin-only, full triangles the orbital-only magnetic moments, the sum of both is represented by open diamonds. In all figures the atomic layers are labeled beginning with the last layer of the previous bilayer ($p = 8$), vertical lines denote the interfaces between Pt and Co. From Ref. [19].*

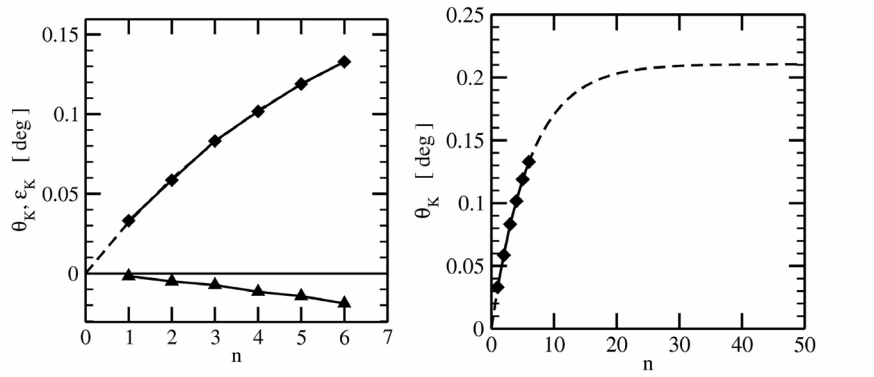

FIGURE 18.13: *Kerr rotation (and ellipticity) angles for $(Co_2Pt_6)_n/Pt(111)$ superstructures at an energy of $\hbar\omega = 3$ eV. In the left part diamonds denote the Kerr rotation angle θ_K, triangles the Kerr ellipticity angle ε_K, and the dashed line refers to an interpolation for θ_K. In the right part also the extrapolation according to Eq. (18.53) to large n is shown. From Ref. [19].*

rotating magnetic field in order to ensure a single domain behavior of ferromagnetic probes. Applying ROTMOKE to a thick "bcc" Ni film deposited on GaAs(001) the claim was put forward [22] of having been able to determine the magneto–crystalline anisotropy constant of bulk bcc Ni, surely a curiosity, since – as is well known – the ground state of bulk Ni refers to an fcc structure. In what follows it will be shown this claim was inappropriate because an intrinsic property of the Kerr effect, namely the surface sensitivity was overlooked.

Of course the easiest way to approve or disapprove that claim is simply to perform corresponding evaluations of the (in-plane) magnetic anisotropy energy of bulk "bcc" Ni, bcc $Ni(100)/Ni_{N_0}/Ni(100)$, and of a corresponding free surface bcc $Vac_{N_{vac}}/Ni_{N_{lay}}/Ni(100)$, see also Chapter 6,

$$\Delta E = E(110) - E(100) \quad , \tag{18.55}$$

shown in the right part of Fig. 18.15 together with the respective spin and orbital moments. As easily can be seen, once again the moments in the surface layer are much enhanced, falling off slowly towards the bulk values, i.e., to those values at which the moments become intrinsic. Layer-resolving the anisotropy energy yields the by now well-known pattern: the contribution from the surface layer is much bigger than for all following layers. It needs about 15 atomic layers to get into a regime of constant contributions. In viewing the anisotropy energy per layer results in oscillations which eventually settle down to the respective intrinsic values. Fig. 18.15 hints in the right

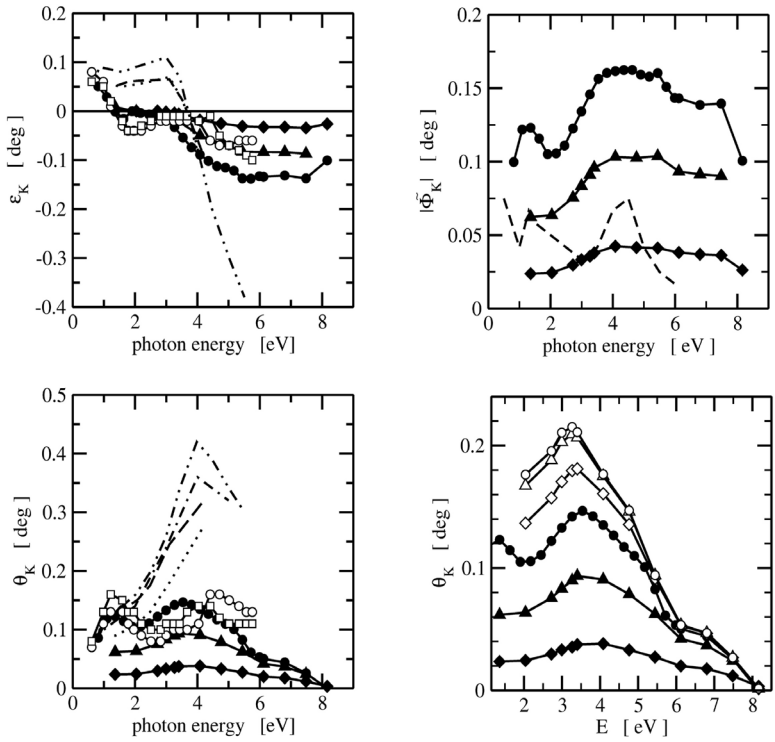

FIGURE 18.14: *Kerr rotation and ellipticity angles (left column), θ_K and ε_K, and the magnitude of the complex Kerr angle (top right entry), $|\Phi_K|$, for different photon energies. In all three entries diamonds, triangles, and circles denote the calculated Kerr quantities of $(Co_2Pt_6)_n/Pt(111)$ superstructures with repetition number $n = 1, 3,$ and 6, respectively. Open circles and squares refer to the calculated data for θ_K and ε_K of Ref. [20] in Co_2Pt_7 and Co_3Pt_6 as bulk superstructures. Dashed, dash-dotted, etc., lines refer to various experimental investigations. Bottom, right: Extrapolation to higher values of n. Full symbols denote the ab-initio calculated θ_K for n =1 (diamonds), 3 (triangles), and 6 (circles), respectively, open symbols denote data extrapolated to n =10 (diamonds), 20 (triangles) and $n \to \infty$ (circles) respectively. From Ref. [19].*

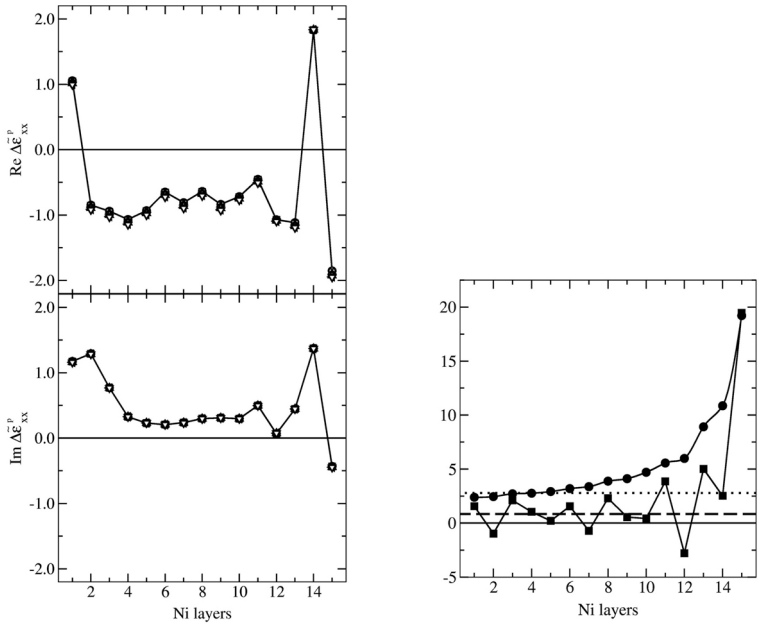

FIGURE 18.15: *Left: Layer–resolved spin (circles) and orbital (squares) magnetic moments in bcc $Vac_3/Ni_{15}/Ni(100)$. Dashed and dotted lines mark the corresponding ab–initio average moments and the average experimental spin moment, [22] respectively. Layer 15 corresponds to the surface Ni layer. Right: Layer–resolved in–plane magnetic anisotropy constants (circles) and their averaged value (squares) in bcc $Vac_3/Ni_{15}/Ni(100)$. Dashed and dotted lines refer to the ab–initio and experimental [22] cubic anisotropy constants, respectively. Layer 15 corresponds to the surface Ni layer. From Ref. [23].*

direction of a surface-driven effect seen experimentally but does not explain the experiment itself. This can only be achieved using the concepts introduced in this chapter.

Let $\varphi_{\mathbf{M}}$ be the polar angle between the (in-plane) x–axis and a uniform in–plane magnetization $\mathbf{M} = \mathbf{M}_p$, $\forall p = 0, 1, \ldots, N$, where N includes also all vacuum layers. By using the following abbreviations

$$m_x = \cos\varphi_{\mathbf{M}} \quad , \quad m_y = \sin\varphi_{\mathbf{M}} \quad , \tag{18.56}$$

for bcc $\mathrm{Vac}_{N_{\mathrm{vac}}}/\mathrm{Ni}_{N_{\mathrm{lay}}}/\mathrm{Ni}(100)$, $N_{\mathrm{vac}} \geq 3$, the layer-resolved permittivity ten-

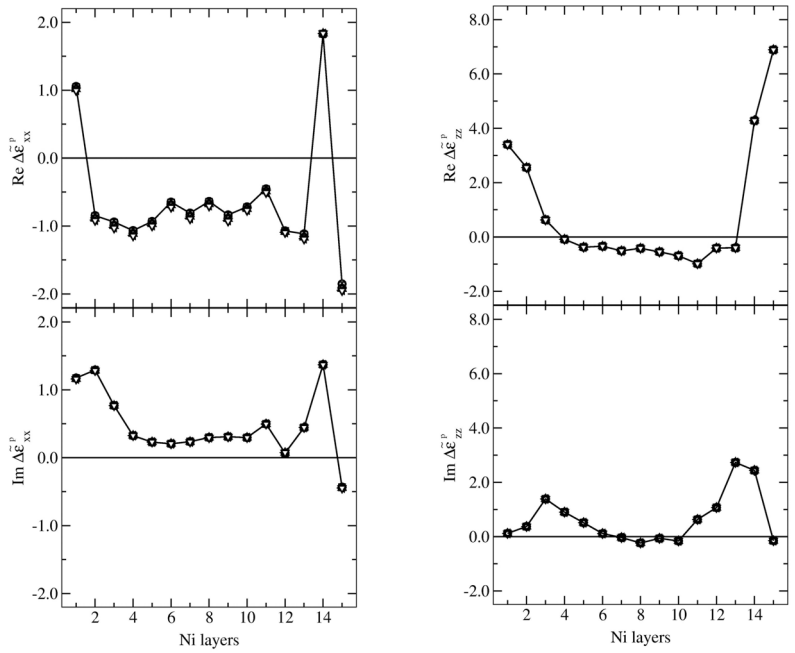

FIGURE 18.16: *Difference in the diagonal elements of the layer–resolved permittivities in bcc $Vac_3/Ni_{15}/Ni(100)$ and bcc $Ni(100)/Ni_{24}/Ni(100)$ corresponding to a photon wave length $\lambda \simeq 633$ nm. Circles, squares, diamonds and triangles (up, left and down) refer to differences corresponding to $\varphi_{\vec{M}} = 15°, 30°, 45°, 60°, 75°, 90°$; see also Eq. (18.56). The layer numbering starts with the first layer on top of the semi–infinite bulk substrate. From Ref. [23].*

sors are of the form [23]:

$$\epsilon^p = \begin{pmatrix} \epsilon^p_{xx} & \epsilon^p_{xy}\, m_x m_y & -\epsilon^p_{xz}\, m_y \\ \epsilon^p_{xy}\, m_x m_y & \epsilon^p_{xx} & \epsilon^p_{xz}\, m_x \\ \epsilon^p_{zx}\, m_y & -\epsilon^p_{zx}\, m_x & \epsilon^p_{zz} \end{pmatrix} . \tag{18.57}$$

For the substrate, however, described as bcc $Ni(100)/Ni_{N_0}/Ni(100)$, where N_0 is the number of Ni layers between the two semi-infinite bcc-Ni subsystems,

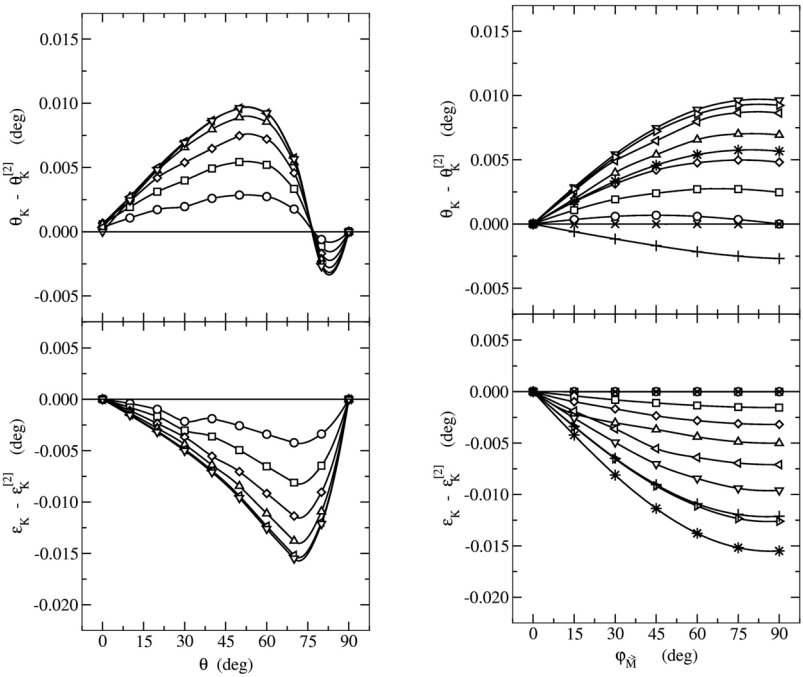

FIGURE 18.17: *Differences* ($\Theta_K - \Theta_K^{[2]}$) *and* ($\epsilon_K - \epsilon_K^{[2]}$) *for bcc Ni/Ni(100) corresponding to oblique incidence of p–polarized light in the yz plane* ($\lambda \simeq 633$ *nm) as a function of the incidence angle* θ *(left) and the polar angle* $\varphi_{\mathbf{M}}$ *(right). In the left panel circles, squares, diamonds and triangles (up, left and down) refer to Kerr angles obtained for a polar angle of* $\varphi_{\mathbf{M}} = 15°, 30°, 45°, 60°, 75°, 90°$ *(open symbols); in the right panel circles, squares, diamonds and triangles (up, left, down and right) represent Kerr angles obtained for an angle of incidence* $\theta = 0, 10, \ldots, 60°$ *(open symbols), stars, pluses and crosses stand for* $\theta = 70°, 80°, 90°$. *From Ref. [23].*

see section 18.2, the permittivity tensor for all Ni planes is given by

$$\varepsilon^0 = \begin{pmatrix} \epsilon^0_{xx} & \epsilon^0_{xy}\, m_x m_y & -\epsilon^0_{xz}\, m_y \\ \epsilon^0_{xy}\, m_x m_y & \epsilon^0_{xx} & \epsilon^0_{xz}\, m_x \\ \epsilon^0_{xz}\, m_y & -\epsilon^0_{xz}\, m_x & \epsilon^0_{zz} \end{pmatrix} \quad . \tag{18.58}$$

Therefore, independent of the direction of **M**, the below difference in layer–resolved permittivities,

$$\Delta\varepsilon^p = \varepsilon^p - \varepsilon^0 \quad , \quad \forall p = 1, \ldots, N_{\mathrm{lay}} + N_{\mathrm{vac}} \quad , \tag{18.59}$$

can be viewed as a measure of the surface sensitivity.

From Fig. 18.16 one immediately can see that these differences are quite large and nearly independent of the in-plane orientation of the magnetization. The difference between the Kerr angles obtained from a proper evaluation of the surface reflectivity matrix and those resulting from the two–media approach, see section 18.1.5.3, unambiguously reveals the contribution of the surface-near region to the Kerr data, since in the two-media approach all Ni layers are treated as one (bulk-like) homogeneous medium [23]. Only for normal incidence both approaches would yield identical results for the Kerr angles.

As can be seen from Fig. 18.17 the contributions from surface-near layers are not only extremely significant, but in fact are decisive for the actual magnitude of the Kerr angles, which for moderately thick "bcc"-like Ni films grown on a suitable substrate range between -0.015° and 0.015°, depending on the orientation of the magnetization. It seems therefore very unlikely that from the experimental ROTMOKE measurements in [22] any conclusions about a "bulk" magneto-crystalline anisotropy energy of "bcc-Ni" can be drawn.

18.7 Summary

The magneto-optical Kerr effect surely is one of the most used experimental tools in dealing with magnetic systems nanostructured in one dimension. Since there are quite a few variations of this technique only very general concluding remarks can be made:

- Any interpretation of experimental Kerr data has to take into account finite penetration depths.

- The magneto-optical Kerr effect is well suited to map out regimes of (a) parallel or antiparallel coupling in multilayers systems or (b) of an in-plane or perpendicular orientation of the magnetization.

- Besides these rather obvious and well-known aspects of Kerr spectroscopy, there is one property that very easily is overlooked, but might turn out to become very important in the future: since "classical optics" is involved Kerr measurements can in principle be performed on a very short time scale. The Kerr effect is ideally suited for pump-probe phenomena, probing physical phenomena which usually last only a few femtoseconds. See also the following chapter!

[1] J. Kerr, Rept. Brit. Assoc. Adv. Sci. 40 (1876); Phil. Mag. **3**, 321 (1877); Phil. Mag. **5**, 161 (1878).

[2] W. Reim and J. Schoenes, in *Magneto–optical spectroscopy of f–electron systems*, ferromagnetic materials ed., edited by K. H. J. Buschow and E. P. Wohlfarth (North–Holland, Amsterdam, 1990), Vol. 5, Chap. 2, p. 133.

[3] A. K. Zvezdin and V. A. Kotov, *Modern magnetooptics and magnetooptical materials*, *Studies in condensed matter physics* (Institute of Physics Publishing, Bristol, 1997).

[4] M. Mansuripur, *The principles of Magneto-Optical Recording* (Cambridge University Press, Cambridge, 1995).

[5] L. Szunyogh and P. Weinberger, J. Phys. Cond. Matt. **11**, 10451 (1999).

[6] V. M. Agranovich and V. L. Ginzburg, in *Spatial dispersion in crystal optics and the theory of excitons*, Vol. XVIII of *interscience monographs and texts in physics and astronomy*, edited by R. E. Marshak (John Wiley & Sons, London, 1966).

[7] A. Vernes, L. Szunyogh, and P. Weinberger, J. Phys. Condens. Matter **13**, 1529 (2001).

[8] M. Mansuripur, J. Appl. Physics **67**, 6466 (1990).

[9] L. D. Landau and E. M. Lifshitz, *Electrodynamics of continuous media*, Vol. 8 of *Course of Theoretical Physics* (Butterworth–Heinemann, Oxford, 1999).

[10] A. Vernes, L. Szunyogh, and P. Weinberger, Phys. Rev. B **65**, 144448 (2002).

[11] A. Vernes, L. Szunyogh and P. Weinberger, Phys. Rev. B **66**, 214404 (2002).

[12] A. Vernes, I. Reichl, P. Weinberger, L. Szunyogh and C. Sommers, Phys. Rev. B **70**, 195407 (2004).

[13] R. Hammerling, J. Zabloudil, P. Weinberger, J. Lindner, E. Kosubek, R. Nünthel, K. Baberschke, Phys. Rev. B **68**, 092406 (2003).

[14] I. Reichl, R. Hammerling, A. Vernes, C. Sommers, L. Szunyogh, and P. Weinberger, Phys. Rev. B **70**, 214417 (2004).

[15] C. Liu and S.D. Bader, J. Vac. Sci. Technol. **A8**(3), 2727 (1990).

[16] I. Reichl, A. Vernes, P. Weinberger, C. Sommers, and L. Szunyogh, Phys. Rev. B **71**, 214416 (2005).

[17] W. B. Zeper, F. J. A. M. Greidanus, P. F. Garcia, and C. R. Fincher, J. Appl. Phys. **65**, 4971 (1989).

[18] E. R. Moog, J. Zak, and S. D. Bader, J. Appl. Phys. **69** (2), 880 (1991).

[19] I. Reichl, J. Zabloudil, R. Hammerling, A. Vernes, L. Szunyogh, and P. Weinberger, Phys. Rev. B **73**, 054402 (2006).

[20] S. Uba, L. Uba, A. N. Yaresko, A. Ya. Perlov, V. N. Antonov, and R. Gontarz, J. Mag. Magn. Mater. **193**, 159 (1999).

[21] R. Mattheis and G. Quednau, phys. stat. sol. (a) **172**, R7 (1999); J. Magn. Magn. Mater. **205**, 143 (1999).

[22] C. S. Tian, D. Qian, D. Wu, R. H. He, Y. Z. Wu, W. X. Tang, L. F. Yin, Y. S. Shi, G. S. Dong, X. F. Jin, X. M. Jiang, F. Q. Liu, H. J. Qian, K. Sun, L. M. Wang, G. Rossi, Z. Q. Qiu, and J. Shi, Phys. Rev. Letters **94**, 137210 (2005).

[23] C. Etz, A. Vernes, L. Szunyogh, J. Zabloudil, and P. Weinberger, Phys. Rev. B **77**, 064420 (2008).

19

Time dependence

In order to deal with pump-probe experiments, first the Kubo-Luttinger approach is carried over to the femtosecond scale. Ultimately, however, the time-dependent Dirac equation in the presence of an external electro-magnetic field, introduced here, has to identify properly, for example, spin currents and spin torques. It is quite likely that this equation is the entrance gate to new types of theoretical descriptions dealing with physical phenomena that occur only on the time scale of femto- to nanoseconds.

19.1 *Terra incognita*

At least from a microscopic (quantum mechanical) standpoint the description of time-dependent physical phenomena in the realm of magnetic nanostructures is still in its infancy, is mostly *terra incognita*, in particular when physical properties have to be described that occur only on a pico- or femtosecond scale. However, since quite a few of these properties, such as current-induced switching (nano- to picosecond regime) or pump-probe experiments, e.g., in connection with time-resolved Kerr measurements (pico- to femtosecond scale), might change completely the direction of research in the field of magnetic nanostructured matter, an attempt is made here (a) to extend the Kubo formulation to the regime of femtosecond magneto-optics and (b) to introduce the time-dependent Dirac equation in the presence of an external electro-magnetic field in order to describe time-dependent "spin-polarized" phenomena such as spin currents and spin torques.

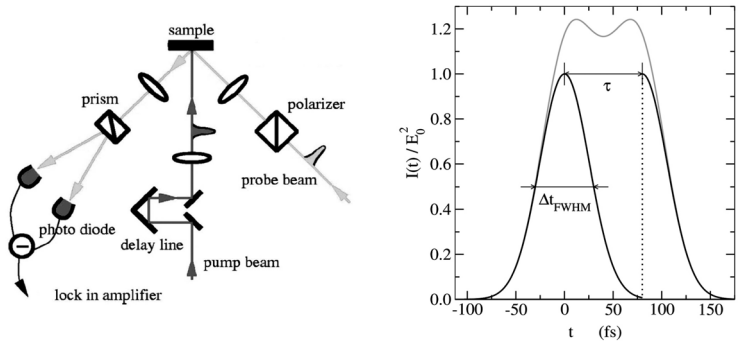

FIGURE 19.1: *Left: A typical experimental set-up for performing pump-probe experiments. The probe laser is usually delayed with respect to the pump laser by (much) less than 100 fs. Right (from Ref. [1]): Time–dependent normalized intensity resulting from two time-delayed ($\tau = 20$ fs) identical, linearly polarized Gaussian femtosecond ($t_{\mathrm{FWHM}} = 60$ fs) laser pulses (parallel configuration) neglecting the time overlap of the pulses.*

19.2 Pump-probe experiments

In the left part of Fig. 19.1 a typical set-up for pump-probe experiments is shown. The right part corresponds to a simulation [1] of this situation in terms of a superposition of two laser pulses assumed for matters of computational simplicity to be independent from each other.

According to this assumption, in principle two time-dependent processes have to be considered, namely first the one corresponding to the pump pulse, abbreviated in the following by "pu" and thereafter that for the probe pulse ("pr"). Linearizing for near-equilibrium states the probability density for the pump–excited state ρ_{pu}

$$\rho_{\mathrm{pu}} \simeq \rho_0 - \frac{i}{\hbar}\int_{-\infty}^{\tau} dt\ [H_{\mathrm{pu}}(t), \rho_0] \equiv \rho_{\mathrm{pu}}^{(0)} + \rho_{\mathrm{pu}}^{(1)} \quad , \tag{19.1}$$

the leading term $\rho_{\mathrm{pu}}^{(0)}$ has to fulfill the following condition for $t_0 \to -\infty$,

$$t_0 \to -\infty : \rho_{\mathrm{pu}}^{(0)} = \rho_0 \quad , \tag{19.2}$$

$$\rho_0 = \frac{\exp\left(-\beta H_0\right)}{\mathrm{Tr}\ \left[\exp\left(-\beta H_0\right)\right]} \quad , \tag{19.3}$$

where ρ_0 is the equilibrium density, $\beta = \left(k_{\mathrm{B}}T\right)^{-1}$ the Boltzmann constant and T the temperature. In a similar manner the probability density for the

probe pulse can be written as

$$\rho_{\rm pr}(t) \simeq \rho_{\rm pu} - \frac{i}{\hbar}\int_{\tau}^{t} dt' \; [H_{\rm pr}(t'), \rho_{\rm pu}] \quad . \tag{19.4}$$

In Eqs. (19.1) and (19.4) $H_{\rm pu}(t)$ and $H_{\rm pr}(t)$ are of the form

$$H_{\rm x}(t) = H_0 + H_x(t) \quad , \quad x = {\rm pr},\, {\rm pu} \quad ,$$

where by making use of the (electric) dipole approximation $H_{\rm x}(t)$ is given by

$$H_{\rm x}(t) = -\sum_{\mu} A_{\mu}\,(t)\, X_{\mu}(t) \quad , \quad \mu = x, y, z \quad , \tag{19.5}$$

with $\mathbf{A}(t)$ being the displacement and $\mathbf{X}(t)$ the conjugated external force. In terms of $\mathbf{A}(t)$ the components of the current density $\mathbf{J}(t)$ are then given by

$$J_{\mu} = \frac{dA_{\mu}(t)}{dt} = \frac{i}{\hbar}\,[H_0,\, A_{\mu}(t)] \quad . \tag{19.6}$$

Within the so-called slowly varying envelope approximation a femtosecond pulse can be viewed as an amplitude modulated, quasimonochromatic plane wave propagating, e.g., along the z axis

$$\mathbf{E}(z,t) = \mathbf{e}\tilde{E}(t)\exp\left[i\,(q\,z)\right] = \boldsymbol{E}_0 E(t)\exp\left[i\,(q\,z - \omega_{\rm p} t)\right] \quad , \tag{19.7}$$

where $\mathbf{e}$ is the polarization unit vector, $\boldsymbol{E}_0$ a real amplitude, $\omega_{\rm p}$ the carrier frequency, and q refers to the corresponding (complex) wave vector.

Considering now that the total external electric field, $\mathbf{E}(\mathbf{r}, t)$ is simply given by the superposition of the pump and the probe pulses, see also the right part of Fig. (19.1),

$$\begin{aligned}\mathbf{E}(\mathbf{r},t) = {} & \mathbf{e}_{\rm pu} E_{\rm pu,0}\, E_{\rm pu}(t)\exp\left[i\,((\mathbf{q}_{\rm pu}\cdot\mathbf{r}) - \omega_{\rm pu} t)\right] \\ & + \mathbf{e}_{\rm pr}\, E_{\rm pr,0} E_{\rm pr}(t-\tau)\exp\left[i\,((\mathbf{q}_{\rm pr}\cdot\mathbf{r}) - \omega_{\rm pr} t)\right] \quad ,\end{aligned} \tag{19.8}$$

where

$\mathbf{e}_{\rm pu}, \mathbf{e}_{\rm pr}$	polarization unit vectors
$E_{\rm pu,0}, E_{\rm pr,0}$	(real) amplitudes
$E_{\rm pu}(t), E_{\rm pr}(t)$	time-dependent envelopes
$\mathbf{q}_{\rm pu}, \mathbf{q}_{\rm pr}$	propagation wave vectors
$\omega_{\rm pu}, \omega_{\rm pr}$	carrier frequencies
τ	delay time

such that a total (formally linear) dynamic conductivity can be formulated [1]

$$\sigma_{\mu\nu}(\omega_{\rm pr}, \omega_{\rm pu}, \omega; \tau) = \sigma^{(0)}_{\mu\nu}(\omega_{\rm pr}, \omega; \tau) + \sigma^{(1)}_{\mu\nu}(\omega_{\rm pr}, \omega_{\rm pu}, \omega; \tau) \quad , \tag{19.9}$$

$$\omega \in [\bar{\omega}_{\rm pr} - \Delta\omega,\, \bar{\omega}_{\rm pr} + \Delta\omega] \quad , \tag{19.10}$$

with $\bar{\omega}_{\rm pr}$ being the mean frequency of the probe pulse. In Eq. (19.9) the first term on the *rhs*, $\sigma^{(0)}_{\mu\nu}(\omega_{\rm pr},\omega;\tau)$, is the zero-th order and the second one, $\sigma^{(1)}_{\mu\nu}(\omega_{\rm pr},\omega_{\rm pu},\omega;\tau)$, the first order contribution.

In using only the zero-th order contribution Fig. 19.2 shows that of course the linear response of the layered system $Ni/Ni_{12}/Ni(100)$ to a (single) femtosecond laser pulse strongly depends on the pulse characteristics. In Fig. 19.3 the diagonal and off-diagonal elements of $\sigma^{(0)}_{\mu\nu}(\omega_{\rm pr},\omega;\tau)$, see Eq. (19.9), are displayed for two different delay times, namely 50 and 100 fs.

Usually, instead of a frequency-frequency representation of the dynamical optical conductivity tensor rather a frequency-time representation is used

$$\tilde{\sigma}^{(0)}_{\mu\nu}(\omega_{\rm pr},t;\tau) = \int_{\omega_{\rm min}}^{\omega_{\rm max}} \Big\{ w(\omega-\omega_{\rm pr};\omega_{\rm c})\ \tilde{\sigma}^{(0)}_{\mu\nu}(\omega_{\rm pr},\omega;\tau) \times \exp\left[-i(\omega-\omega_{\rm pr})\,t\right]\ d\omega \Big\} \quad , \qquad t \geq \tau > 0 \quad , \tag{19.11}$$

which can be obtained via a Fourier transformation in a symmetric interval $[\omega_{\rm pr}-\omega_{\rm c},\omega_{\rm pr}+\omega_{\rm c}]$ around $\omega_{\rm pr}$, where $\omega_{\rm c} = \min(\omega_{\rm pr}-\omega_{\rm min},\omega_{\rm max}-\omega_{\rm pr}) > 0$. In Eq. (19.11) a "window function" such as for example a "Gauss–window" is applied

$$w(\omega-\omega_{\rm pr};\omega_{\rm c}) = \exp\left[-\alpha\left(\pi\frac{\omega-\omega_{\rm pr}}{\omega_{\rm c}}\right)^2\right] \quad , \qquad \text{if} \quad |\omega-\omega_{\rm pr}| < \omega_{\rm c} \quad , \quad \alpha \in \mathbb{R} \quad . \tag{19.12}$$

This kind of representation is shown in Fig. 19.4 for Ni(100) considered as a layered system. As can be seen from this figure for a double exponential envelope function, the peak in the diagonal and off-diagonal elements of the conductivity tensor has a half-width of about 100 fs. Experimentally the width of this peak was found [2] to be about 80 fs, which proves that at least in this particular case the zero-th order term in Eq. (19.9) already gave a sufficiently accurate description of the occurring time-dependent processes. Whether or not the expression for this peak width used in the literature, namely *demagnetization time,* is really justified is questionable, since up-to-now no realistic calculations of the corresponding time-dependent magnetization density are available.

Augmented with an optical procedure similar to the one discussed in the previous chapter for the Kerr effect the example of Ni(100) shows that quite obviously not only a new type of Kerr spectroscopy with peaks lasting only a few femtoseconds is possible, but also that these short living peaks will have to be regarded as one of the main scientific and technological targets in magneto-optics.

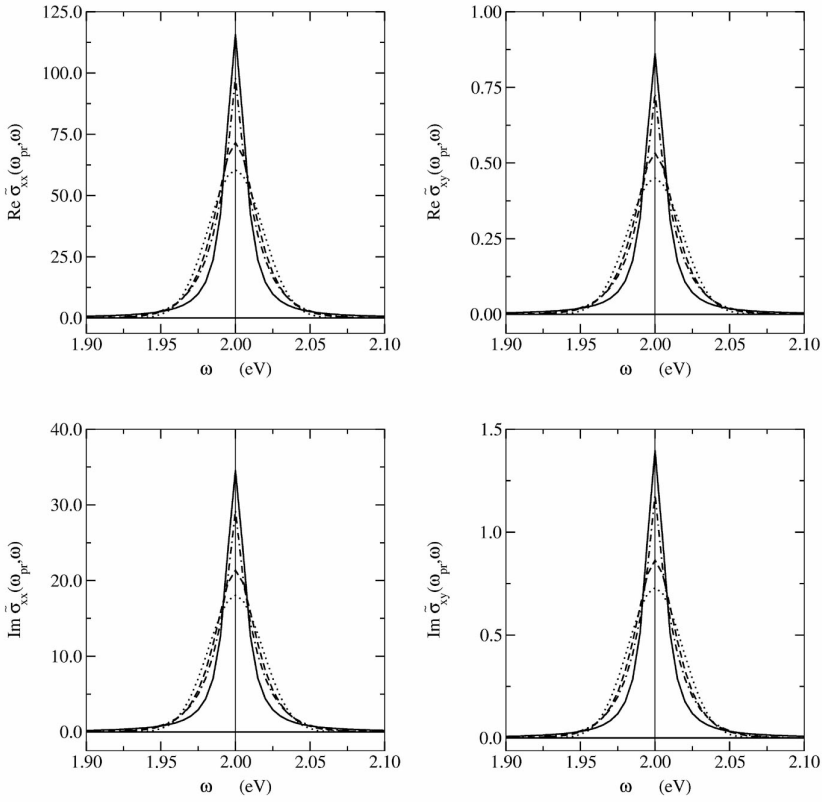

FIGURE 19.2: *Linear response to a femtosecond laser probe pulse shown as the dimensionless dynamic conductivity* $\tilde{\sigma}_{\mu\nu}(\omega_{\rm p},\omega)$ *for* $\mu\,,\nu = x\,,y$ *in the case of fcc Ni(100), when the pulse has a carrier frequency* $\omega_{\rm p} = 2$ *eV (marked by a thin vertical line), a duration time* 60 *fs (full width at half maximum, i.e. FWHM) and an envelope corresponding to a double exponential (full line), a Gaussian (dotted line), a hyperbolic secant (dashed line) and a Lorentzian shape (dot–dashed line), respectively. From Ref. [1].*

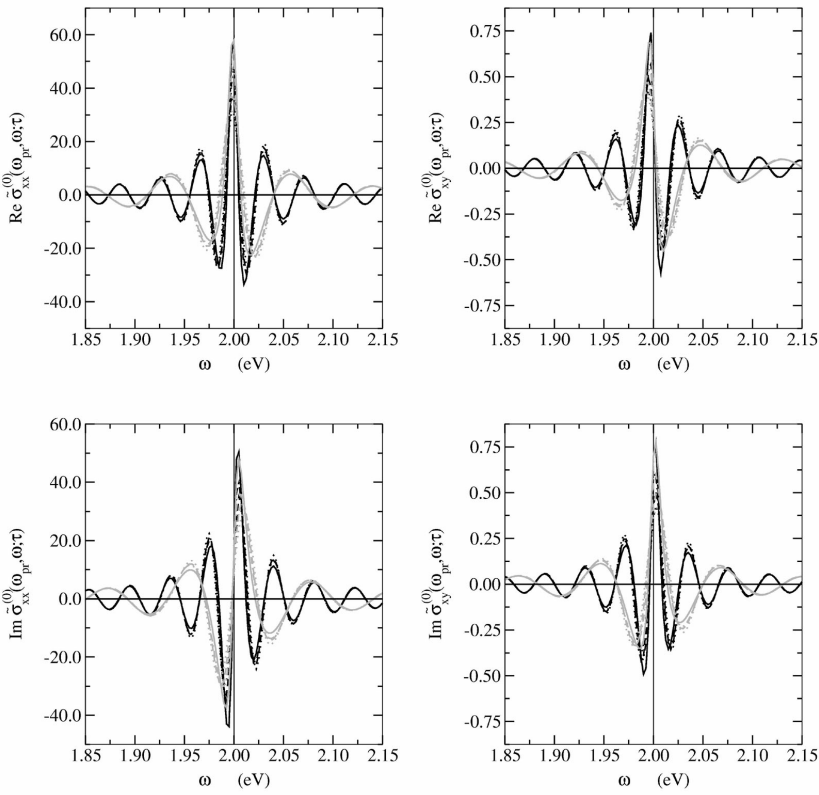

FIGURE 19.3: *Strictly linear, frequency– and delay time–dependent (grey: $\tau = 50$ fs, black: $\tau = 100$ fs) dimensionless zero-th order dynamic conductivity $\tilde{\sigma}^{(0)}_{\mu\nu}(\omega_{\rm pr}, \omega; \tau)$ in the case of fcc Ni(100), when the probe pulse has a carrier frequency $\omega_{\rm pr} = 2$ eV (marked by a thin vertical line), a duration time 60 fs (FWHM) and of an envelope corresponding to a double exponential (full line), a Gaussian (dotted line), a hyperbolic secant (dashed line) and a Lorentzian shape (dot–dashed line), respectively. From Ref. [1].*

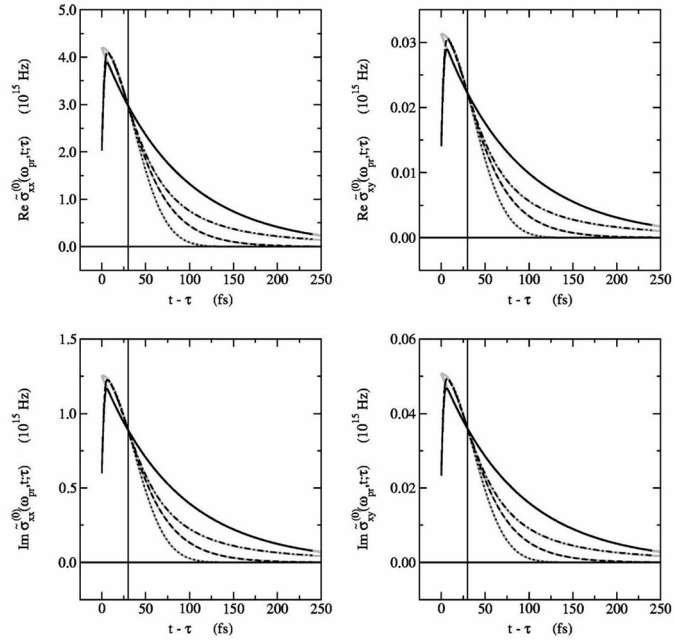

FIGURE 19.4: *Gauss–windowed (damping factor $\alpha = 3$), see Eq. (19.12), strictly linear, time– and delay time–dependent optical conductivity $\tilde{\sigma}^{(0)}_{\mu\nu}(\omega_{\rm pr}, t; \tau)$ as compared with $\tilde{E}_{\rm pr}(t-\tau)\tilde{\sigma}_{\mu\nu}(\omega_{\rm pr})$ shown in grey, where $\tilde{E}_{\rm pr}(t-\tau)$ is the envelope of the probe pulse (double exponential: full line, Gaussian: dotted line, hyperbolic secant: dashed line and Lorentzian: dot–dashed line) with a duration time of $\Delta t_{\rm FWHM} = 60$ fs (thin vertical lines marks $t - \tau = \Delta t_{\rm FWHM}/2$) and a carrier frequency of $\omega_{\rm pr} = 2$ eV. From [1].*

19.3 Pulsed electric fields

Another of these new time-resolved physical phenomena is switching of the orientation of the magnetization induced by short electric field pulses. Although a bit slower than most processes recorded in pump-probe experiments, namely occurring "only" on a time scale of nano- to picoseconds, so-called current-induced switching of spin valves and in particular current-driven domain wall motions [3, 4], seem to point in the direction of a completely new generation of technological devices. In Fig. 19.5 the experimental set-up (top) and result (bottom) of a domain wall motion in a permalloy nanowire induced by an electric field pulse are displayed. The middle row of this figure shows images of

the processes taking place in terms of Magnetic Force Microscopy (MFM). In Fig. 19.6 the corresponding time-resolved resistance measurements are shown. As can be seen the changes in resistance caused by driving a domain wall with electric field pulses through a section of the nanowire bordered by the contacts happen in time steps of about 20 - 50 ns.

19.4 Spin currents and torques

The theoretical requirements to describe the experimental evidence shown in Figs. (19.7) - (19.6) are two-fold: (1) the description has to be relativistic, otherwise resistances in magnetic alloys such as permalloy can not be evaluated, and (2) it has to be time-dependent. Since the 4×4 spin operator,

$$\mathbf{\Sigma} = \begin{pmatrix} \boldsymbol{\sigma} & 0 \\ 0 & \boldsymbol{\sigma} \end{pmatrix} \quad , \tag{19.13}$$

does not even commute with the field-free Dirac Hamiltonian,

$$\mathcal{H}_{\mathrm{D}} = c\boldsymbol{\alpha} \cdot \mathbf{p} + \beta m_{\mathrm{e}} c^2 \quad , \tag{19.14}$$

it was suggested by Bargmann and Wigner [6] to describe the spin-polarization of (moving) electrons in the presence of an electromagnetic field by means of the so-called four-component *polarization operator,*

$$T_\mu \equiv (\mathbf{T}, T_4) \quad , \tag{19.15}$$

$$\begin{cases} \mathbf{T} = \beta\, \mathbf{\Sigma} - i\Sigma_4 \dfrac{\boldsymbol{\pi}}{m_{\mathrm{e}} c} \\ \\ T_4 = i\, \mathbf{\Sigma} \cdot \dfrac{\boldsymbol{\pi}}{m_{\mathrm{e}} c} \end{cases} \quad , \tag{19.16}$$

where

$$\boldsymbol{\pi} = (\mathbf{p} - e\mathbf{A})\mathbf{I}_4 \quad , \tag{19.17}$$

and $\mathbf{A} = \mathbf{A}(\mathbf{r}, t)$ is the vector potential. It should be noted that both, Σ_μ

$$\Sigma_\mu \equiv (\mathbf{\Sigma},\, \Sigma_4) \quad , \quad \Sigma_4 = -i\, \gamma_5 \tag{19.18}$$

and T_μ are covariant axial four-vectors.

The time evolution of the polarization density $\mathcal{T}_\mu$,

$$\mathcal{T}_\mu \equiv \mathcal{T}_\mu(\mathbf{r}, t) = (\boldsymbol{\mathcal{T}}, \mathcal{T}_4) \tag{19.19}$$

$$\boldsymbol{\mathcal{T}} \equiv \boldsymbol{\mathcal{T}}(\mathbf{r}, t) = \psi^+ \mathbf{T} \psi \quad , \quad \mathcal{T}_4 \equiv \mathcal{T}_4(\mathbf{r}, t) = \psi^+ T_4 \psi \quad ,$$

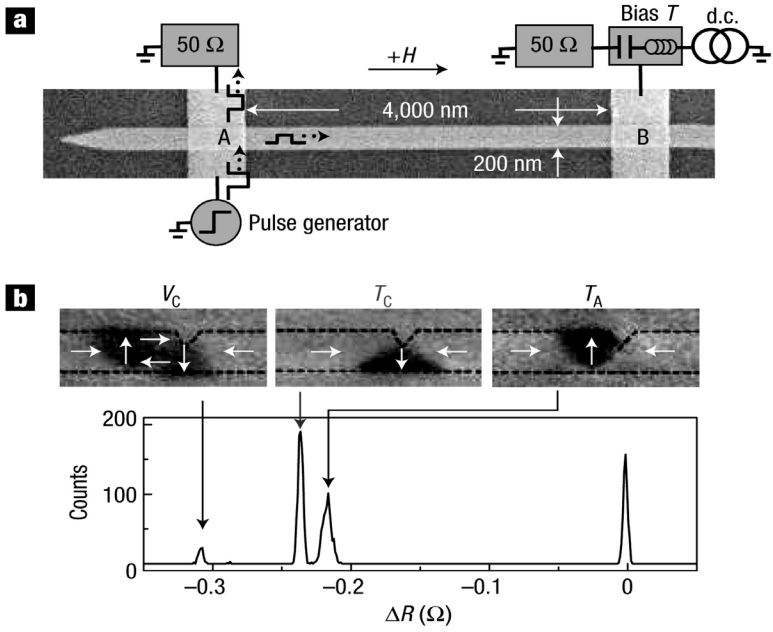

FIGURE 19.5: *Top (a) Experimental set-up and structure of injected domain walls at a notched pinning site, (b): Scanning electron microscopy image of a permalloy nanowire (horizontal) and its electrical contacts (vertical lines). Note that there is no notched pinning site in the nanowire shown in this image. A schematic illustration of the quasi-static resistance measurement set-up is overlaid on the image. Bottom: Histogram of R values measured in successive repeated experiments in which a domain wall is injected into the nanowire using a 2.5 V high, 10 ns long voltage pulse and is trapped at a notch located about 3 μm away from line A (see top entry). The notch is triangular, as shown in the MFM images above. R is the difference in the resistance of the nanowire before and after the domain wall injection. The MFM images show the magnetic configurations corresponding to each R peak. The white arrows denote the magnetization directions. By courtesy of the authors of Ref. [5].*

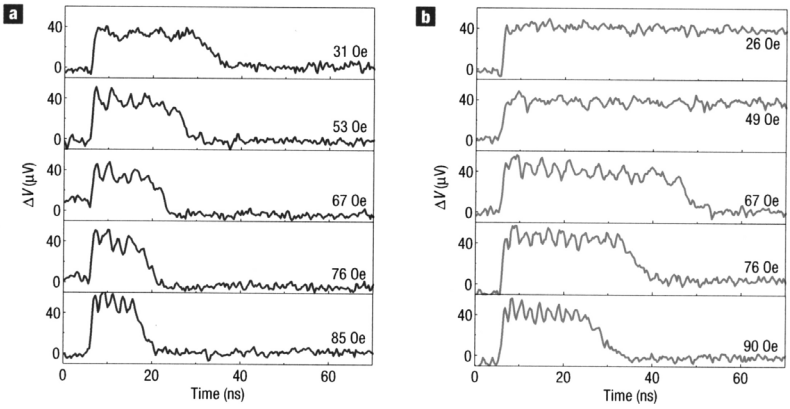

FIGURE 19.6: *Time-resolved resistance measurements of a propagating domain wall along a permalloy nanowire. Real-time measurements of the domain wall propagation along a nanowire obtained by averaging the temporal evolution of the nanowire resistance 16 000 times. Shown are the signal traces obtained by using (a) -2.8 V and (b) 2.6 V voltage pulses to inject a domain wall. By courtesy of the authors of Ref. [5].*

where $\psi = \psi(\mathbf{r}, t)$ is a solution of the time-dependent Dirac equation corresponding to a given scalar potential $V = V(\mathbf{r}, t)$,

$$\frac{\partial \psi}{\partial t} = \frac{1}{i\hbar}\mathcal{H}_{\rm D}\psi \quad , \quad \frac{\partial \psi^+}{\partial t} = -\frac{1}{i\hbar}\psi^+\mathcal{H}_{\rm D}^+ \quad , \tag{19.20}$$

$$\mathcal{H}_{\rm D} = \mathcal{H}_{\rm D}(\mathbf{r}, t) = c\boldsymbol{\alpha}\cdot\boldsymbol{\pi} + \beta m_{\rm e}c^2 + eV\mathbf{I}_4 \quad , \tag{19.21}$$

is then given by

$$\frac{d\mathcal{T}_\mu}{dt} = \frac{\partial \psi^+}{\partial t}T_\mu\psi + \psi^+\frac{\partial T_\mu}{\partial t}\psi + \psi_\mu^+ T_\mu\frac{\partial \psi}{\partial t} \quad , \tag{19.22}$$

or, by separating explicitly the vector and the scalar part, by

$$\frac{\partial \boldsymbol{T}}{\partial t} = \gamma_5\frac{e}{m_{\rm e}c}\frac{\partial \mathbf{A}}{\partial t} \, , \qquad \frac{\partial \mathcal{T}_4}{\partial t} = -\frac{ie}{m_{\rm e}c}\,\boldsymbol{\Sigma}\cdot\frac{\partial \mathbf{A}}{\partial t} \quad . \tag{19.23}$$

This equation can now be reformulated [7] in the following manner,

$$\frac{d\boldsymbol{T}}{dt} + \boldsymbol{\nabla}\cdot\mathbb{J} = \frac{e}{m_{\rm e}}\,\boldsymbol{S}\times\mathbf{B} - \frac{ie}{m_{\rm e}c}\,\mathbf{E}\,\mathcal{S}_4 \quad , \tag{19.24}$$

$$\frac{d\mathcal{I}_4}{dt} + \boldsymbol{\nabla}\cdot(\mathcal{J}_4' - \mathcal{J}_4'') = \frac{ie}{m_{\rm e}c}\,\boldsymbol{S}\cdot\mathbf{E} \quad , \tag{19.25}$$

where $\mathbf{B} = \mathbf{B}(\mathbf{r}, t)$ is the magnetic induction vector and $\mathbf{E} = \mathbf{E}(\mathbf{r}, t)$ the electric field intensity.

In Eqs. (19.24) and (19.25) the polarization-current density tensor elements are defined as

$$\mathbb{J}_{ij} = c\,\psi^{+}\,(\alpha_j T_i)\,\psi \quad , \quad (i, j = \mathrm{x}\,, \mathrm{y}\,, \mathrm{z}) \quad , \tag{19.26}$$

$$\mathcal{J}_4{}' = c\,\psi^{+}\,(T_4 \boldsymbol{\alpha})\,\psi \quad , \quad \mathcal{J}_4{}'' = \psi^{+}\left(2\,\frac{\boldsymbol{\pi}}{m_{\mathrm{e}}} \times \boldsymbol{\alpha}\right)\psi \quad , \tag{19.27}$$

such that

$$\boldsymbol{\nabla} \cdot \mathbb{J}\,|_i = \sum_j \partial_j \mathbb{J}_{ij} \quad . \tag{19.28}$$

The four-component density $\mathcal{S}_\mu \equiv (\boldsymbol{S},\, \mathcal{S}_4)$ in Eqs. (19.24) and (19.25),

$$\begin{aligned} \boldsymbol{S} &= \psi^{+} \boldsymbol{\Sigma}\, \psi \qquad , \qquad \mathcal{S}_4 = \psi^{+} \Sigma_4 \psi \quad , \\ \boldsymbol{S} &\equiv \boldsymbol{S}\,(\mathbf{r}, t) \qquad , \qquad \mathcal{S}_4 \;\equiv\; \mathcal{S}_4(\mathbf{r}, t) \quad , \end{aligned} \tag{19.29}$$

however, is also evolving in time. The corresponding equation of motion turns out [7] to be of the following form

$$\frac{d\boldsymbol{S}}{dt} - ic\,\nabla \mathcal{S}_4 = \frac{m_{\mathrm{e}} c}{\hbar} \mathcal{J}_4{}'' + i\,\boldsymbol{\nabla} \times \boldsymbol{J} \quad , \tag{19.30}$$

$$i\,\frac{d\mathcal{S}_4}{dt} - c \boldsymbol{\nabla} \cdot \boldsymbol{S} = i\,\frac{m_{\mathrm{e}} c}{\hbar} \mathcal{J}'' \quad , \tag{19.31}$$

where

$$\boldsymbol{J} = c\,\psi^{+} \boldsymbol{\alpha}\, \psi \tag{19.32}$$

is the relativistic probability current density and

$$\mathcal{J}'' = \psi^{+}\,(2c\;\beta \gamma_5)\,\psi \quad . \tag{19.33}$$

Very clearly the set of Eqs. (19.24), (19.25), (19.30) and (19.31) has to be solved now simultaneously.

In the absence of an electromagnetic field the polarization-current density $\mathbb{J}$ and the divergence in Eq. (19.28) have to be regarded as the relativistic generalization of the *conventional spin-current density* and the so-called *spin-transfer torque*, since then Eq. (19.24) reduces to a continuity equation for the polarization density and Eq. (19.31) to that for the magnetization density.

Clearly, having calculated $\mathbb{J}_{ij}$, $\mathcal{J}_4{}'$, see Eqs. (19.26) and (19.27), and $\boldsymbol{J}$ and $\mathcal{J}''$ in Eqs. (19.32) - (19.33) for a given vector potential $\mathbf{A}(\mathbf{r}, t)$, scalar potential $V(\mathbf{r}, t)$, magnetic induction $\mathbf{B}(\mathbf{r}, t)$ and electric field $\mathbf{E}(\mathbf{r}, t)$ at a particular time t, first the equation of motion for $\mathcal{S}_\mu$ and subsequently that for $\mathcal{T}_\mu$ can be determined, see the following table, from which all occurring time-dependencies can immediately be read.

property	quantity
tensor	$\mathbb{J}_{ij}(r,t) = \psi^{+}(r,t)\,[c\alpha_j T_i(r,t)]\,\psi(r,t)$
vector	$\mathcal{J}_4{}'(r,t) = \psi^{+}(r,t)\,[cT_4(r,t)\boldsymbol{\alpha}]\,\psi(r,t)$
vector	$\mathcal{J}_4{}''(r,t) = \psi^{+}(r,t)\left[2\,\dfrac{\boldsymbol{\pi}(r,t)}{m_e}\times\boldsymbol{\alpha}\right]\psi(r,t)$
scalar	$\mathcal{J}\,''(r,t) = \psi^{+}(r,t)\,[2c\beta\gamma_5]\,\psi(r,t)$
vector	$\boldsymbol{J}(r,t) = \psi^{+}(r,t)\,[c\boldsymbol{\alpha}\,]\,\psi(r,t)$
vector	$\boldsymbol{\pi}(r,t)) = (\mathbf{p} - e\mathbf{A}(r,t))$
components	$i,j = x\,,y\,,z$

Quite obviously in order to evaluate the various quantities in this table, the solutions of the time-dependent Dirac equation in Eq. (19.21) or equivalently the corresponding (time-dependent) Green's function have to be available, since all other "ingredients" are mostly given in terms of Dirac matrices or given functions (procedures).

19.5 Instantaneous resolvents & Green's functions

In principle the time-dependent Dirac equation ought to be solved in the context of the Time-Dependent-Density-Functional-Theory (TDDFT) [8, 9], which, however, applied to solid state systems still seems to be an unresolved issue. Even making the simplest possible approximation, namely the so-called Adiabatic Local Density Approximation (ALDA), for the exchange-correlation potential $V_{xc}(\mathbf{r},t;[n(\mathbf{r},t),\mathbf{m}(\mathbf{r};t)])$ and effective exchange field $\mathbf{B}(\mathbf{r},t;[n(\mathbf{r},t),\mathbf{m}(\mathbf{r};t)])$,

$$V_{xc}(\mathbf{r},t;[n(\mathbf{r},t),\mathbf{m}(\mathbf{r};t)]) = \frac{\delta E_{xc}[n(\mathbf{r};t),\mathbf{m}(\mathbf{r};t)]}{\delta n(\mathbf{r};t)} \quad , \tag{19.34}$$

$$\mathbf{B}(\mathbf{r},t;[n(\mathbf{r},t),\mathbf{m}(\mathbf{r};t)]) = \frac{e\hbar}{2mc}\frac{\delta E_{xc}[n(\mathbf{r};t),\mathbf{m}(\mathbf{r};t)]}{\delta \mathbf{m}(\mathbf{r};t)} \quad , \tag{19.35}$$

which are local both in space and time [10], approximate methods of solving the time-dependent Dirac equation have to be assumed, since it is virtually impossible to follow for a solid state system, in particular for those with a surface or interfaces, the time evolution of individual solutions $\psi(\mathbf{r},t)$ of Eq. (19.21).

Assuming that the system returns to the ground state after a certain period of time it was suggested [11] to use instantaneous time-dependent resolvents in order to evaluate directly the particle density $n(\mathbf{r},t)$ in Eq. (19.34) and the magnetization density $\mathbf{m}(\mathbf{r};t)$ in Eq.(19.35) for a given time-dependent process starting from a well-defined ground state.

19.5.1 Time-dependent resolvents

Suppose that the time-dependent Kohn-Sham-Dirac operator $\mathcal{H}(t)$ is defined as

$$\mathcal{H}(t) = \begin{cases} \mathcal{H}_0 + \mathcal{W}(t)\ , & t \geq t_0 \\ \\ \mathcal{H}_0 \qquad\quad , & t < t_0 \end{cases} \quad , \tag{19.36}$$

and that the following (time independent) initial eigenvalue equation applies

$$\mathcal{H}(t_0)\,\psi(t_0) = \mathcal{H}_0\psi(t_0) = E(t_0)\,\psi(t_0) \quad . \tag{19.37}$$

By introducing the resolvent of $\mathcal{H}(t)$ with t as a *parameter*,

$$G(z;t) = (z - \mathcal{H}(t))^{-1} \quad , \tag{19.38}$$

into the expression for the evolution operator corresponding to infinitesimal time steps,

$$U(t,t_0) = \frac{1}{2\pi i} \oint\limits_{C_-\cup C_+} dz\, \exp\left[-\frac{i}{\hbar} z\,(t-t_0)\right] G(z;t_0) \quad , \tag{19.39}$$

from Cauchy's residue theorem it immediately follows that

$$U(t,t_0) = \exp\left[-\frac{i}{\hbar}\mathcal{H}(t_0)\,(t-t_0)\right] \quad , \tag{19.40}$$

which in turn is identical to

$$U(t,t_0) = \exp\left[-\frac{i}{\hbar}\int\limits_{t_0}^{t} dt'\mathcal{H}(t')\right] \quad , \tag{19.41}$$

if and only if

$$\int\limits_{t_0}^{t} dt'\mathcal{W}(t') \simeq \mathcal{W}(t_0)\,(t-t_0) \quad . \tag{19.42}$$

In Eq. (19.39) C_+ (C_-) is a contour immediately above (below) the real axis followed from the right (left) to the left (right) such that for $t - t_0 > 0$ the contour C_- and for $t - t_0 < 0$ the contour C_+ yields vanishing contributions.

19.5.2 Time-evolution of densities

For the initial state, at $t = t_0$, the valence band particle density of a solid state system is given as usual by

$$n(\mathbf{r};t_0) = -\pi^{-1}\,\mathrm{Im}\int_{E_b}^{E_F(t_0)} \langle\mathbf{r}|\,G(z;t_0)\,|\mathbf{r}\rangle\,dz \quad , \tag{19.43}$$

where E_b denotes the band bottom and $E_F(t_0)$ is the Fermi energy of the equilibrium system. Similarly, assuming that – as already said – the time evolution of the system can be described by an instantaneous eigenvalue problem,

$$\mathcal{H}(t)\,\psi(t) = E(t)\,\psi(t) \quad , \tag{19.44}$$

by using $G(z;t)$, see Eq. (19.38), the density $n(\mathbf{r};t)$ at a given time t can be defined in terms of the following (contour) integration,

$$n(\mathbf{r};t) = -\pi^{-1}\,\mathrm{Im}\int_{E_b}^{E_F(t)} \langle\mathbf{r}|\,G(z;t)\,|\mathbf{r}\rangle\,dz \quad , \tag{19.45}$$

where $E_F(t)$ is now a "fictitious" Fermi energy at t, determined such that the below condition for a constant number of particles applies.

Suppose that at t_0 (well-defined initial state) the number of particles is N_0. The condition for a constant number of particles (one of the requirements of Density Functional Theory) then implies that

$$N(t) = N_0 \quad , \quad \forall t \quad , \tag{19.46}$$

with $N(t)$ being defined in terms of $n(\mathbf{r};t)$, see Eq. (19.45), as

$$N(t) = \int_{\Omega} n(\mathbf{r};t)d\mathbf{r} \quad . \tag{19.47}$$

Suppose further that at a particular t this condition was already fulfilled by closing the contour at a properly adjusted upper integral boundary $E_F(t)$; then correspondingly at $t' = t + \Delta t$ the contour has to be closed at $E_F(t')$,

$$N(t') = -\pi^{-1}\int_{\Omega}\left\{\mathrm{Im}\int_{E_b}^{E_F(t')} \langle\mathbf{r}|\,G(z;t')\,|\mathbf{r}\rangle\,dz\right\}d\mathbf{r} \quad , \tag{19.48}$$

such that Eq. (19.46) is met, i.e., $N(t') - N(t) = 0$. From fulfilling the condition in Eq. (19.46) it follows immediately that the time evolution of the

particle density maintaining a constant number of particles is given by

$$\frac{\delta n(\mathbf{r};t)}{\delta t} \simeq -\pi^{-1}\left\{ \mathrm{Im}\int_{E_b}^{E_F(t)} \langle\mathbf{r}|\,\frac{\delta G(z;t)}{\delta t}\,|\mathbf{r}\rangle\, dz \;+\; \mathrm{Im}\,\langle\mathbf{r}|\,G\left(E_F\left(t\right);t\right)|\mathbf{r}\rangle \right\} \quad . \tag{19.49}$$

Similarly, the time evolution of the magnetization density can easily be obtained from the below definition,

$$\mathbf{m}(\mathbf{r};t) = -\pi^{-1}\,\mathrm{Im}\,Tr\int_{E_b}^{E_F(t)} \langle\mathbf{r}|\,\beta\boldsymbol{\Sigma}G(z;t)\,|\mathbf{r}\rangle\, dz \quad , \tag{19.50}$$

where Tr denotes the trace in spin space. Imposing again particle conservation, this implies

$$\frac{\delta\mathbf{m}(\mathbf{r};t)}{\delta t} \simeq -\pi^{-1}\left\{ \mathrm{Im}\,Tr\int_{E_b}^{E_F(t)} \langle\mathbf{r}|\,\beta\boldsymbol{\Sigma}\frac{\delta G(z;t)}{\delta t}\,|\mathbf{r}\rangle\, dz \right.$$
$$\left. +\;\mathrm{Im}\,\langle\mathbf{r}|\;\beta\boldsymbol{\Sigma}G\left(E_F\left(t\right);t\right)|\mathbf{r}\rangle \right\} \quad . \tag{19.51}$$

From Eqs. (19.49) and (19.50) it is obvious that the time evolution of any other density such as the previously introduced polarization density can be evaluated in a similar manner.

19.6 Time-dependent multiple scattering

Since it can be shown that a time-dependent multiple scattering theory can be formulated by making use of a time independent resolvent $G^{(0)}(z)$ that corresponds to a given (time independent) reference Hamiltonian $\mathcal{H}_0$,

$$\mathcal{H}(t) = \mathcal{H}_0 + V + \mathcal{W}(t)\ ,\ G_0(z) = (z-\mathcal{H}_0)^{-1} \quad , \tag{19.52}$$

all the concepts introduced in Chapter 4 can be applied. In particular let a time-dependent Kohn-Sham-Dirac operator be defined as

$$\mathcal{H}(\mathbf{r};t) = \mathcal{H}^{(0)}(\mathbf{r}) + \mathcal{W}(\mathbf{r};t) \quad , \tag{19.53}$$

$$\mathcal{H}^{(0)}(\mathbf{r}) = c\boldsymbol{\alpha}\cdot\mathbf{p}\; + \beta mc^2 + V(\mathbf{r})I_4 + \beta\boldsymbol{\Sigma}\cdot\mathbf{B}(\mathbf{r}) \quad , \tag{19.54}$$

where $\mathcal{W}(\mathbf{r};t)$ is of the form

$$\mathcal{W}(\mathbf{r};t) = \sum_{\Lambda>0} W_\Lambda(r;t)Y_\Lambda(\hat{\mathbf{r}}) \quad , \quad \Lambda=(l,m) \quad , \tag{19.55}$$

such as, e.g., for an interaction with a laser pulse in the dipole approximation,

$$\begin{aligned}\mathcal{W}(\mathbf{r};t) &= eE_0E(t)\cos(\omega_0 t)\,(\mathbf{r}\cdot\mathbf{e}) \\ &= eE(t)\,|\mathbf{r}|\,[Y_{11}(\hat{\mathbf{r}})e_x + Y_{1-1}(\hat{\mathbf{r}})e_y + Y_{10}(\hat{\mathbf{r}})e_z] \quad ,\end{aligned} \tag{19.56}$$

with e being the elementary charge, E_0 a real amplitude, $E(t)$ a real envelope function, ω_0 the carrier frequency and $\mathbf{e}$ the polarization unit vector. In viewing the last equation it is obvious that at a given time t the term $E_0E(t)\cos(\omega t)$ is a real scalar quantity that multiplies $(\mathbf{r}\cdot\mathbf{e})$. Assuming now that in accordance with the requirements for multiple scattering integrations in configurational space can be split up into integrations over non-overlapping cells Ω_n

$$\Omega = \sum_n \Omega_n \quad , \quad \int_\Omega d\mathbf{r} = \sum_n \int_{\Omega_n} d\mathbf{r}_n \quad , \tag{19.57}$$

then the previously introduced concept of multiple scattering can be applied straightforwardly.

19.6.1 Single-site scattering

For example, the Kohn-Sham-Dirac Hamiltonian corresponding to a particular cell (site) of an ensemble of atoms can be rewritten [12] as

$$\mathcal{H}(\mathbf{r};t) = c\boldsymbol{\alpha}\cdot\mathbf{p} + \beta mc^2 + \mathcal{U}(\mathbf{r};t) \quad , \tag{19.58}$$

with

$$\mathcal{U}(\mathbf{r};t) = \begin{pmatrix} \mathcal{U}^+(\mathbf{r};t) & 0 \\ 0 & \mathcal{U}^-(\mathbf{r};t) \end{pmatrix} \quad , \tag{19.59}$$

$$\mathcal{U}^+(\mathbf{r};t) = \mathcal{V}(\mathbf{r};t) + \sigma_z\,\mathcal{B}(r;t) \quad , \tag{19.60}$$

$$\mathcal{U}^-(\mathbf{r};t) = \mathcal{V}(\mathbf{r};t) - \sigma_z\,\mathcal{B}(r;t) \quad , \tag{19.61}$$

since initially – because of the properties of the local spin-density functional – only the z component of the spin operator $\boldsymbol{\Sigma}$ appears. The potential $\mathcal{V}(\mathbf{r};t)$ can now be expanded as follows

$$\begin{aligned}\mathcal{V}(\mathbf{r};t) &= V(\mathbf{r};t)\xi(\mathbf{r}) \\ &= \sum_{\Lambda\Lambda'\Lambda'',\ell'\le 1} C^{\Lambda}_{\Lambda'\Lambda''} V_{\Lambda'}(r;t)\xi_{\Lambda''}(r)\,Y_\Lambda(\hat{\mathbf{r}}) \quad ,\end{aligned} \tag{19.62}$$

with

$$V(\mathbf{r};t) = V(\mathbf{r}) + \mathcal{W}(\mathbf{r};t) = \sum_\Lambda V_\Lambda(r;t)Y_\Lambda(\hat{\mathbf{r}}) \quad , \tag{19.63}$$

where

$$V_\Lambda(r;t) = \begin{cases} \sqrt{4\pi}V(r)\,, & \Lambda = (0,0) \\ W_\Lambda(r;t)\,, & \Lambda \neq (0,0) \end{cases} \quad . \tag{19.64}$$

The functions $\xi(\mathbf{r})$ in Eq. (19.62) are so-called *shape functions* [12] that ensure that according to the conditions of multiple scattering the individual potentials $\mathcal{V}(\mathbf{r};t)$ do not overlap.

In using the form given in Eq. (19.56) and assuming the polarization $\mathbf{e}$ in Eq. (19.56) to point along the z axis, there are only two coefficients in Eq. (19.63), namely

$$\begin{aligned} V_{00}(r;t) &= \sqrt{4\pi}V(r) \quad , \\ V_{10}(r;t) &= E_0 E(t)\cos(\omega t)\,|\mathbf{r}|\,Y_{10}(\hat{\mathbf{r}}) \quad . \end{aligned} \tag{19.65}$$

Making the below ansatz for the wave functions

$$\psi_Q(\mathbf{r};t) = \sum_{Q'} \begin{pmatrix} g_{Q'Q}(r;t)\,\chi_{Q'}(\hat{\mathbf{r}}) \\ i f_{Q'Q}(r;t)\,\chi_{\bar{Q}'}(\hat{\mathbf{r}}) \end{pmatrix} \quad , \tag{19.66}$$

where $Q = (\kappa,\mu)$ and $\bar{Q} = (-\kappa,\mu)$, κ and μ being the relativistic angular momentum quantum numbers, one arrives at a system of coupled radial equations which can be solved directly and which in turn can be used to obtain the instantaneous single-site t-matrices $\mathbf{t}(z;t)$ and the regular and irregular scattering solutions $Z_Q(\mathbf{r},z;t)$, $J_Q(\mathbf{r},z;t)$, $z = \epsilon + i\delta$.

19.6.2 Multiple scattering

At a particular time t the instantaneous single-particle Green's function $G(\mathbf{r},\mathbf{r}',z;t)$,

$$\begin{aligned} G(\mathbf{r},\mathbf{r}',z;t) = G(\mathbf{r}_n + \mathbf{R}_n, \mathbf{r}'_m + \mathbf{R}_m, z;t) = \\ \mathbf{Z}^n(\mathbf{r}_n,z;t)\tau_{nm}(z;t)\mathbf{Z}^m(;\mathbf{r}'_m,z;t)^\times \\ - \delta_{nm}\left\{\mathbf{J}^n(\mathbf{r}_n,z;t)\mathbf{Z}^n(\mathbf{r}'_n,z;t)^\times\Theta((r_n - r'_n)\right. \\ \left. + \mathbf{Z}^n(\mathbf{r}_n,z;t)\mathbf{J}^n(\mathbf{r}'_n,z;t)^\times\Theta((r'_n - r_n)\right\} \quad , \end{aligned} \tag{19.67}$$

where the $\mathbf{R}_n$ denote sites, is then defined in terms of an instantaneous scattering path operator,

$$\tau(z;t) = \{\tau_{nm}(z;t)\} \tag{19.68}$$

$$\tau(z;t) = \left[\mathbf{t}^{-1}(z;t) - \mathbf{G}_0(z)\right]^{-1} \quad . \tag{19.69}$$

Note that the structure constants $\mathbf{G}_0(z)$ refer to the Green's function for a constant (zero) reference potential, i.e., remain constant in time and that $\mathbf{Z}^n(\mathbf{r}_n,z;t)$ and $\mathbf{J}^n(\mathbf{r}_n,z;t)$ refer to site $\mathbf{R}_n$.

19.6.3 Particle and magnetization densities

In using Eq. (19.67) the time-dependent particle and magnetization densities can now easily be evaluated,

$$n(\mathbf{r};t) = \sum_n n(\mathbf{r}_n;t) \ , \ m(\mathbf{r};t) = \sum_n m(\mathbf{r}_n;t) \quad , \tag{19.70}$$

$$\begin{aligned} n(\mathbf{r}_n;t) = -\pi^{-1}\,\mathrm{Im} \int_{E_b}^{E_F(t)} \{\mathbf{Z}^n(\mathbf{r}_n,z;t)\tau_{nn}(z;t) \\ \times \mathbf{Z}(;\mathbf{r}_n,z;t)^{\times} - \mathbf{J}^n(\mathbf{r}_n,z;t)\mathbf{Z}^n(\mathbf{r}_n,z;t)^{\times}\}\, dz \quad , \end{aligned} \tag{19.71}$$

$$\begin{aligned} \mathbf{m}(\mathbf{r};t) = -\pi^{-1}\,\mathrm{Im}\, Tr \int_{E_b}^{E_F(t)} \beta\mathbf{\Sigma}\,\{\mathbf{Z}^n(\mathbf{r}_n,z;t)\tau_{nn}(z;t) \\ \times \mathbf{Z}(;\mathbf{r}_n,z;t)^{\times} - \mathbf{J}^n(\mathbf{r}_n,z;t)\mathbf{Z}^n(\mathbf{r}_n,z;t)^{\times}\}\, dz \quad , \end{aligned} \tag{19.72}$$

where $E_F(t)$ refers to that energy on the real axis at which the contour must be closed such that the number of particles remains constant and n is the number of sites, whose volumes summed up define the characteristic volume, see also Eq. (19.57).

19.7 Physical effects to be encountered

Since up to now no calculations are available that make use of Eqs. (19.24) - (19.25) and (19.30) - (19.31), only effects to be encountered can be sketched by taking the example of an atom, for which for matters of comparison also the more traditional time-dependent perturbation theory can be employed.

In describing for illustrative purposes for example an Fe atom corresponding to a spherically symmetric effective potential and an effective exchange field pointing along the z axis in terms of a time-dependent Kohn-Sham-Dirac Hamiltonian, see Eq. (19.53), when the polarization of the laser pulse $\mathbf{e}$ is parallel to the z axis, see Eq. (19.55), first of all a second-order Stark effect is encountered. This easily can be shown by considering in Eq. (19.55) only the amplitude of the electric field, i.e., $\mathcal{W}(\mathbf{r};t) = W_0 = ea_0E_0$, where a_0 is the Bohr radius. Fig. 19.7 clearly shows that the difference in (instantaneous) orbital energies, $\Delta E_B = E(W_0) - E(W_0 = 0)$, in a magnetic Fe atom (a) varies – as to be expected – quadratically with the magnitude of the electric field W_0, and (b) that apparently the $4p$ states of an Fe atom are more strongly affected by the external electric field than the more localized $3d$ states.

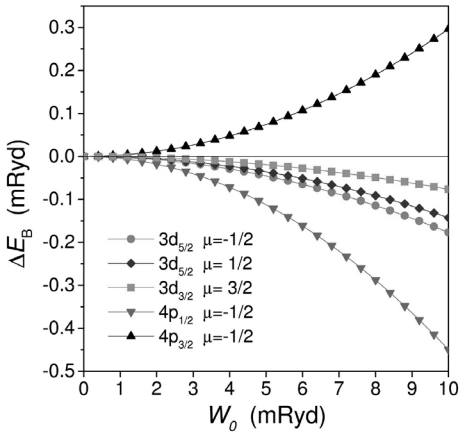

FIGURE 19.7: *Variation of* ΔE_B *with respect to* W_0 *for selected* 3*d and* 4*p states of an Fe atom. The labelling is according to the angular momentum component of the given state that contributes the most. From Ref. [11].*

As is well known from time-dependent perturbation theory, first order transition probabilities are given by

$$P_{if}\left(t\right)=\frac{1}{\hbar^{2}}\left|\int_{t_{0}}^{t}dt'\,\langle\psi_{i}^{0}|\mathcal{W}(t')|\psi_{f}^{0}\rangle\exp\left(i\omega_{if}t'\right)\right|^{2}\quad,\tag{19.73}$$

where $\mathcal{W}(t)$ starts at $t=t_0$, ψ_i^0 and ψ_f^0 are the initial and the final state wave functions of the unperturbed system corresponding to the eigenvalues E_i^0 and E_f^0, respectively, and $\omega_{if}=\left(E_i^0-E_f^0\right)/\hbar$. On the other hand, the first order transition probabilities can also be defined [11] as

$$P_{if}\left(t\right)=\left|\int_{t_{0}}^{t}dt'\,\langle\psi_{i}(t')|\frac{d}{dt'}\psi_{f}(t')\rangle\exp\left[i\int_{t_{0}}^{t'}dt''\,\omega_{if}(t'')\right]\right|^{2}\quad,\tag{19.74}$$

where $\psi_i(t)$ and $\psi_f(t)$ are the solutions of the instantaneous equation,

$$\mathcal{H}(t)\psi_{j}(t)=E_{j}(t)\psi_{j}(t)\quad,\quad(j=i,f)\quad,\tag{19.75}$$

and $\omega_{if}(t)=\left(E_i(t)-E_f(t)\right)/\hbar$.

In Fig. 19.8 the transition probability according to Eq. (19.73) as well as to Eq. (19.74) is displayed for an Fe atom caused by a double-exponential laser

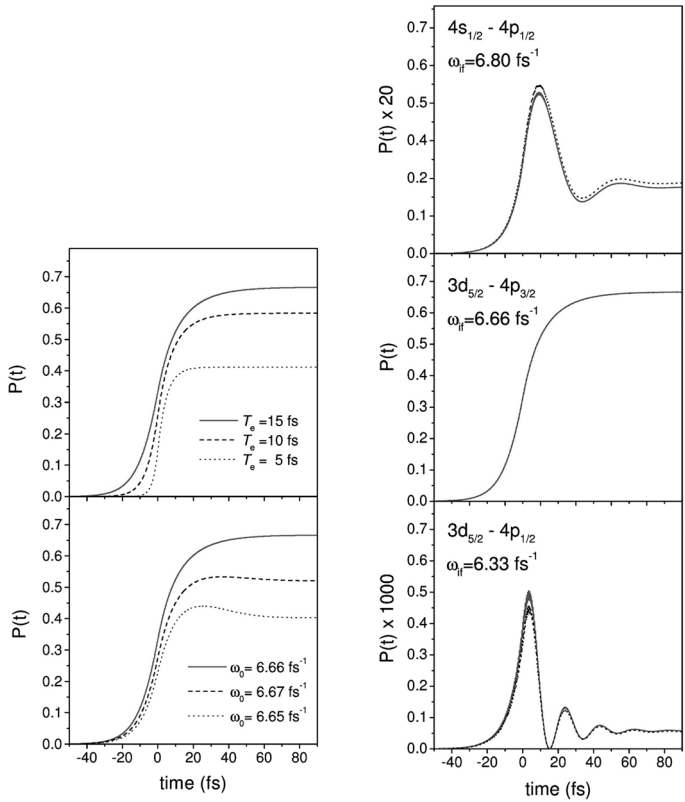

FIGURE 19.8: *Left: Calculated first order transition probabilities (solid line: Eq. (19.74), dotted line: Eq. (19.73)), for selected transitions in an Fe atom due to a double-exponential laser pulse with* $I = 6$ mJ/cm^2, $\omega_0 = 6.66$ fs^{-1} *and* $T_e = 15$ *fs. Right: Variation of the calculated transition probabilities with respect to the characteristics of a double exponential laser pulse, see Eq. (19.76), for a transition* $3d_{5/2}$–$4p_{3/2}$ ($\mu = -1/2$) *in an Fe atom. The upper panel refers to* ω_0=*6.66* fs^{-1}, *the lower one to* T_e=*15 fs. In all cases the intensity of the laser pulse was fixed to* I=*6* mJ/cm^2. *From Ref. [11].*

pulse, see Eq. (19.56),

$$E(t) = \exp\left(-\frac{|t|}{T_e}\right) \quad , \quad I = \epsilon_0 c T_e E_0^2 \quad , \tag{19.76}$$

with $I = 6$ mJ/cm^2, $T_e = 15$ fs and a carrier frequency $\omega_0 = 6.66$ fs^{-1}, that corresponds in energy to the transition $3d_{5/2}$– $4p_{3/2}$ ($\mu = -1/2$). In Eq. (19.76) T_e is a constant time characterizing the decay of the laser pulse and I the intensity (power density) with ϵ_0 being the vacuum permittivity and c the light velocity. As initial time $t_0 = -\,6T_e$ is chosen, which is the time at which the amplitude of the electric field is about 400 times smaller than at the center of the laser pulse.

The right half of Fig. 19.8, in which the zero of the time scale refers to the center of the laser pulse, shows the transition probabilities for three different transitions. Keeping in mind the different scales on the ordinates, it is fairly obvious that physically relevant processes occur only at or very close to the resonance. In particular the resonant transition (middle panel) proves that evaluating the instantaneous eigenstates of $\mathcal{H}(t)$ is a very useful numerical procedure. In the left half of this figure only one transition is considered, the $3d_{5/2}$–$4p_{3/2}$ ($\mu = -1/2$) transition. In keeping the intensity of the pulse at $I = 6$ mJ/cm^2, T_e (top) and ω_0 (bottom) is varied. As to be expected the transition probabilities are extremely sensitive to the carrier frequency: a relative change in ω_0 of only about 0.1% can decrease their magnitudes by about 20 - 40%.

19.8 Expectations

Clearly enough Figs. (19.7) - (19.8) served as illustrations only of possible effects to be encountered and as such have little in common with time-dependent phenomena in magnetic nanostructured matter. However, at least in the case of rather slow processes (nano- to picosecond scale) and almost square-like electric field pulses as used, e.g., to drive domain walls through nanowires, see Figs. (19.5) and (19.6), the use of instantaneous Green's functions might turn out to be of enormous help in evaluating the occurring spin currents and spin torques according to their definitions in section 19.4.

[1] A. Vernes and P. Weinberger, Phys. Rev. **B 71**, 165108 (2005).

[2] J. Hohlfeld, E. Matthias, R. Knorren, and K. H. Bennemann, Phys. Rev. Lett. **78**, 4861 (1997).

[3] S. S. P. Parkin, MRS Bulletin Vol. **31**, 389 (2006).

[4] R. Allenspach and P.-O. Jubert, MRS Bulletin Vol. **31**, 395 (2006).

[5] M. Hayashi, L. Thomas, C. Rettner, R. Moriya, and S. S. P. Parkin, Nature Physics **3**, 21 (2007).

[6] V. Bargmann and E. P. Wigner, Proc. Natl. Acad. Sci. U.S. **34**, 211 (1948).

[7] A. Vernes, B. L. Gyorffy, and P. Weinberger, Phys. Rev. B **76**, 012408 (2007).

[8] M. A. L. Marques and E. K. U. Gross, Annu. Rev. Phys. Chem. **55**, 427 (2004).

[9] E. Runge and E. K. U. Gross, Phys. Rev. Lett. **52**, 997 (1984).

[10] H. Appel and E. K. U. Gross, in *Quantum Simulations of Complex Many-Body Systems: From Theory to Algorithms*, NIC Series, Vol. 10, edited by J. Grotendorst, D. Marx and A. Muramatsu (John von Neumann Institute for Computing, Jülich, 2002), Chap.: *Static and time-dependent many-body effects via density-functional theory*, p. 255.

[11] A. Vernes, L. Szunyogh, and P. Weinberger, Phys. Rev. B., in press (2008).

[12] J. Zabloudil, R. Hammerling, L. Szunyogh and P. Weinberger, *Electron Scattering in Solid Matter*, Springer Berlin Heidelber New York, 2005.

Afterword

It must be a bit disturbing to find out that a book that starts out to "dot i's and cross t's" in the language colloquially used to describe parallel and antiparallel magnetic configurations suddenly ends up in *terra incognita*. This, however, is just the usual course in physics: whenever one manages to open one door, there is yet another one to be opened. After all physics ought to be "curiosity driven", driven by the desire to find out what is hidden behind the next door. It surely does not hurt if by the end of the day this kind of curiosity leads to technologically useful schemes.

Fortunately the topics sketched in the "*terra incognita*" chapter combine both aspects almost on equal footing, since the foreseeable end to standard device scaling requires radically different approaches in order to cope with the ever increasing needs of information technology, with the implications of Moore's law. As is well known, for this kind of purpose it does not make any sense to go below the nano-scale in length, below the "natural length scale" in solid state systems. New effects, up to now unknown or not fully appreciated phenomena and subsequently new types of devices can therefore only be found by reducing time scales, by exploiting the subtleties of time-dependent phenomena. Parts of the theoretical equipment to be taken along on such a discovery trip were described in this book.